Annai College of Arts & Science
Quality Education for Today & Tomorrow
Kovilacheri, Kumbakonam. 612 503. Ph: 0435 2453007
Accredited by NAAC with "B" Grade & Recognized by UGC under Section 2(f) & 12(B)
Affiliated to Bharathidasan University, Tiruchirappalli. E-Mail:acasdmn@gmail.com

ANNAI COLLEGE OF ARTS AND SCIENCE

BHARATHIDASAN UNIVERSITY

Supporting Document 3.3.2

RESEARCH PAPERS PER TEACHERS IN THE JOURNALS – 2020 to 2021

catalysts

MDPI

Article

One-Pot Synthesis of 7, 7-Dimethyl-4-Phenyl-2-Thioxo-2,3,4,6,7, 8-Hexahydro-1H-Quinazoline-5-OnesUsing Zinc Ferrite Nanocatalyst and Its Bio Evaluation

Tentu Nageswara Rao [1], Nalla Krishnarao [1], Faheem Ahmed [2,*], Suliman Yousef Alomar [3,*], Fadwa Albalawi [4], Panagal Mani [5], Abdullah Aljaafari [2], Botsa Parvatamma [6], Nishat Arshi [7] and Shalendra Kumar [2,8]

1 Department of Chemistry, Krishna University, Machilipatnam, Andhra Pradesh 521001, India; tnraochemistry@gmail.com (T.N.R.); nkrishnarao@gmail.com (N.K.)
2 Department of Physics, College of Science, King Faisal University, Hofuf, Al-Ahsa 31982, Saudi Arabia; aaljaafari@kfu.edu.sa (A.A.); sjagdish@kfu.edu.sa (S.K.)
3 Doping Research Chair, Zoology Dept, College of Science, King Saud University, Riyadh 11451, Saudi Arabia
4 Zoology Department, College of Science, King Saud University, Riyadh 11451, Saudi Arabia; Fadwa_saad@hotmail.com
5 Department of Biotechnology, Annai College of Arts&Science, Kumbakonam, Tamil Nadu 612503, India; master.maniji@gmail.com
6 Department of Organic Chemistry, GayathriP.G Courses, Gotlam, Vizianagaram 530045, India; Parvathi1787@rediffmail.com
7 Department of Basic Sciences, Preparatory Year Deanship, King Faisal University, Hofuf, Al-Ahsa 31982, Saudi Arabia; nshastri@kfu.edu.sa
8 Department of Physics, School of Engineering, University of Petroleum & Energy Studies, Dehradun 248007, India
* Correspondence: fahmed@kfu.edu.sa (F.A.); syalomar@ksu.edu.sa (S.Y.A.)

check for updates

Citation: Rao, T.N.; Krishnarao, N.; Ahmed, F.; Alomar, S.Y.; Albalawi, F.; Mani, P.; Aljaafari, A.; Parvatamma, B.; Arshi, N.; Kumar, S. One-Pot Synthesis of 7, 7-Dimethyl-4-Phenyl-2-Thioxo-2,3,4,6,7, 8-Hexahydro-1H-Quinazoline-5-OnesUsing Zinc Ferrite Nanocatalyst and Its Bio Evaluation. *Catalysts* **2021**, *11*, 431. https://doi.org/10.3390/catal11040431

Academic Editors: Maria Manuel B. Marques and Ana Sofia Santos

Received: 16 March 2021
Accepted: 24 March 2021
Published: 27 March 2021

Abstract: A simple and highly efficient protocol for the synthesis of derivatives 7, 7-dimethyl-4-phenyl-2-thioxo-2, 3, 4, 6, 7, 8-hexahydro-1H-quinazoline-5-one from 5, 5-dimethyl cyclohexane-1, 3-dione (**4a**–**4h**) (dimedone) has been described. The aryl aldehydes were substituted with thiourea in the presence of synthesized zinc ferrite nanocatalyst, which increased the yield under reflux through condensation, followed by cyclization to give desired products. The other advantages are that it is eco-friendly and economically affordable for large-scale production. Structural validation and characterization of all the newly synthesized compounds were evaluated by spectral analysis (mass spectrometry, proton nuclear magnetic resonance (^{1}HNMR), and Carbon-13 nuclear magnetic resonance(^{13}CNMR)spectroscopies. The structure of antibacterial and antifungal assays was performed with the newly synthesized compounds. The antimicrobial activity of title compounds possessing electron-withdrawing groups such as (**4e**–**4h**) (Cl, Br, and cyano group) exhibited more active potential than the electron-donating groups, C_6H_5,4-C_6H_4, 3-OC_2H_5-4OH-C_6H_3, etc., (**4a**–**4d**) containing moiety.

Keywords: dimedone; aryl aldehydes; zinc ferrite; bio evaluation; structural validation; NMR

1. Introduction

Multicomponent reaction (MCR) is the most powerful and efficient technique in modern synthetic organic chemistry. The advantages of these reactions in synthetic organic chemistry are the valuable characteristics such as constructing desired compounds, straightforward reaction design, atom economy, and the simple purification of target products. MCRs with heterocyclic moiety are particularly useful for the construction of drug-like molecules [1–3]. In the recent past, the six-membered heterocyclic compounds such as hexahydroquinazolinones in medicinal chemistry and synthetic organic chemistry are of special interest. The main focus on the synthesis of derivatives of 7,7-dimethyl-4-phenyl-2-thioxo-1,2,3,4,6,7,8-hexahydro-1H-quinazoline-5-ones has considerably attracted

attention in recent years due to their potential, antioxidant [4], antifungal, antibacterial, antitumor, and antitubercular activity [5] with wide applications, including anticonvulsant, sedative, tranquilizer, analgesic [6,7], antimicrobial, anesthetic [8], anticancer [9], antihypertensive [10], anti-inflammatory [11], diuretic [12], and muscle relaxant properties [13]. The various organic transformation reactions were employed by the use of trimethylsilyl chloride [14]. There are few reports for the synthesis of octa hydro quinazolinone derivatives using catalysts such as concentrated H_2SO_4 [15], Nafion-H [16], NH_4VO_3 [17], silica-sulfuric acid [18], and also in ionic liquids [HMIM] H_2SO_4 in presence of TMSCl [19], [BMIM]Br-[BMIM]BF_4 [20], and $ZrOCl_2$. $8H_2O$ [21]. This article tends to report the synthesis of 7, 7-dimethyl-4-phenyl-2-thioxo-2, 3, 4, 6, 7, 8-hexahydro-1H-quinazolin-5-ones using nanocatalyst. Lanthanum doped Ni0.6Zn0.2Fe2-XLaXO4 (x = 0.075) ferrite was developed by Amol et al. This ferrite has a spinal cubic structure and a lattice constant of 8.486. The Ferro-spinal sample was used as a magnetically recoverable heterogeneous catalyst [22]. Triethanolamine has a significant impact on the morphology of nano-ZnO catalyst. For the synthesis of coumarin derivatives, we developed an efficient, simple, and environmentally friendly synthetic methodology [23]. Catalytic reactions ensure high regio- and stereoselectivity of chemical transformations. In recent years, several novel catalytic systems were developed for the selective formation of carbon–heteroatom and carbon–carbon bonds [24]. The use of green nanocatalyst for the synthesis of various heterocycles has advantages such as short reaction time, high yield, inexpensive chemical usage, easy work-up procedure, and specific reaction [25]. The Michael addition reaction and cyclodehydration, followed by dimedone with various substituted aryl aldehydes and thioureain the presence of nanocatalystgive 7,7-dimethyl-4-phenyl-2-thioxo-2,3,4,6,7,8-hexahydro-1H-quinazolin-5-ones, were performed (Scheme 1). A pilot reaction using substituted aryl aldehyde (1), dimedone (2), and thiourea (3) in the presence of nanocatalyst and the structure and antagonistic properties of the synthesized compounds were also studied, in addition to studying the further development of derivatives.

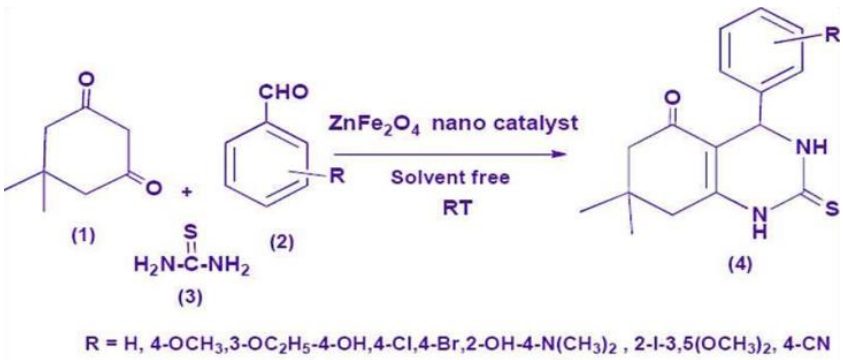

Scheme 1. Synthesisof 7, 7-dimethyl-4-phenyl-2-thioxo-2, 3,4,6,7, 8-hexahydro-1H-quinazolin-5-ones using zinc ferrite.

2. Results

2.1. XRD Pattern of $ZnFe_2O_4$ NPs

The X-ray diffraction (XRD) pattern of $ZnFe_2O_4$(Figure 1) shows clear diffraction peaks. The diffraction peak of the powder sample was indexed according to Joint Committee on Powder Diffraction Standards (JCPDS) card no. 22-1012. The material crystallized in a cubic unit cell with space group Fd-3m(Figure 2). The structure was refined by the Rietveld refinement method with the Fullprof software package using the single-phase Fd-3m diffraction data. The unit cell parameters (Table 1) of the crystallite size of the sample were calculated from the most intense diffraction by using Scherrer's formula. The Scherrer method (using full width at half maximum (FWHM)) calculates the ratio of the thickness's root-mean-fourthpower to its root-mean-square value. We illustrated that the Scherrer equation's calculation of crystallite size is accurate by comparing it to X-ray

diffraction peaks produced by the dynamical theory. In terms of crystalline size and Bragg angle, we also established the range of validity of the acceptable Scherrer equation.

$$D = \frac{K\lambda}{\beta cos\theta}, \quad (1)$$

where K is dimensionless shape factor and generally taken 0.94 for spherical particles, λ is the wavelength of X-ray used ($Cu - K_{\alpha}$ = 1.540 Å), and β and θ are the full widths of half maxima and diffraction angle of corresponding diffraction peak.

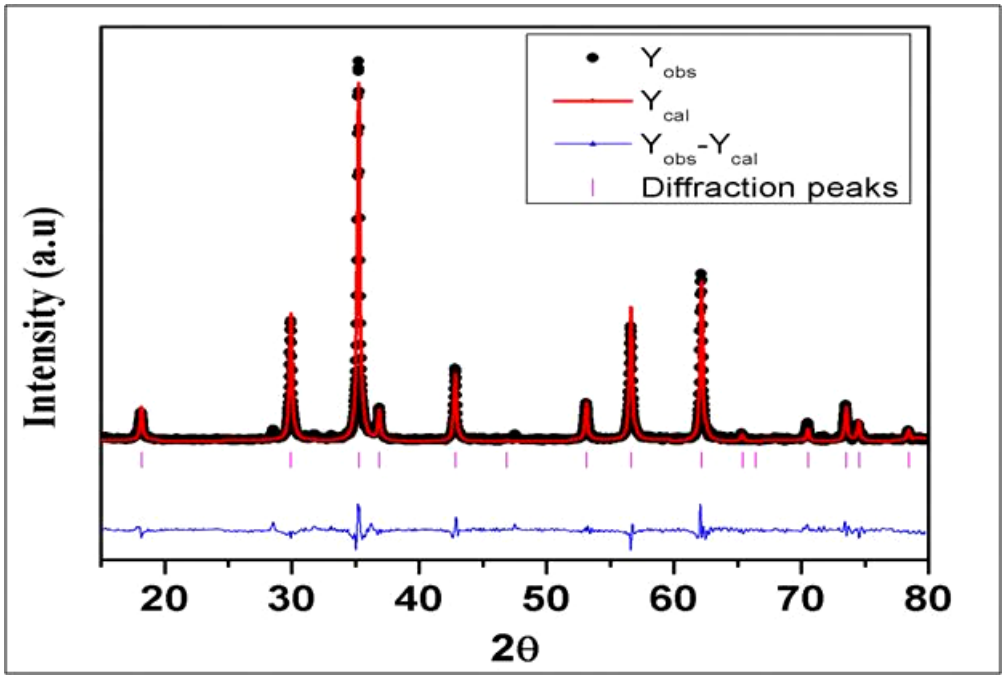

Figure 1. X-ray diffraction (XRD) pattern of ZnFe2O4 NPs.

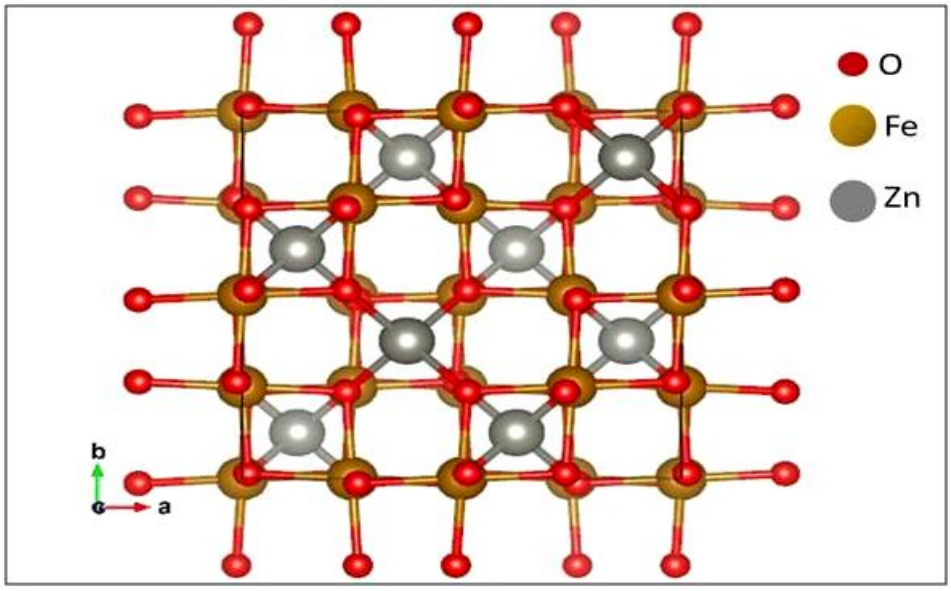

Figure 2. Crystalized in a cubic unit cell of $ZnFe_2O_4$ NPs.

Table 1. Refined unit cells parameters of $ZnFe_2O_4$ nanoparticles.

Atom	x	y	z	Occ.	B_{iso}	Site	Sym.
Zn	0.125	0.125	0.125	1	0.024	8a	43 m
Fe	0.5	0.5	0.5	1.035	0.009	16d	3 m
O	0.26335	0.26335	0.26335	1.038	0.016	32e	3 m
Unit cell Parameters	a = b = c = 8.43695 Å α = β = γ = 90°						
Unit cell Volume	600.559 $Å^3$						
R_p (%)	12.1						
R_{wp} (%)	18.3						
χ^2	2.02						
Fe-O	2.00295 Å						
Zn-O	2.02174 Å						

The average crystallite size of the powder sample was estimated in the close approximation of 39.16 nm. The difference between the calculated and observed data in the Rietveld refinement method elucidates the goodness of fit (χ^2) of the diffraction pattern. The minimal χ^2 value achieved for the synthesized $ZnFe_2O_4$ sample was 2.02, which is implicit in the observed XRD pattern. The lower χ^2 of refined XRD pattern indicates the single-phase and high purity of prepared $ZnFe_2O_4$ nanoparticles.

2.2. SEM Analysis of $ZnFe_2O_4$ NPs

The surface morphology of the acquired $ZnFe_2O_4$ (NPs) was documented using a scanning electron microscope (FESEM) (Figure 3). The FESEM image indicated that the $ZnFe_2O_4$ (NPs) have a smooth surface, and the agglomeration of NPs is also visible there.

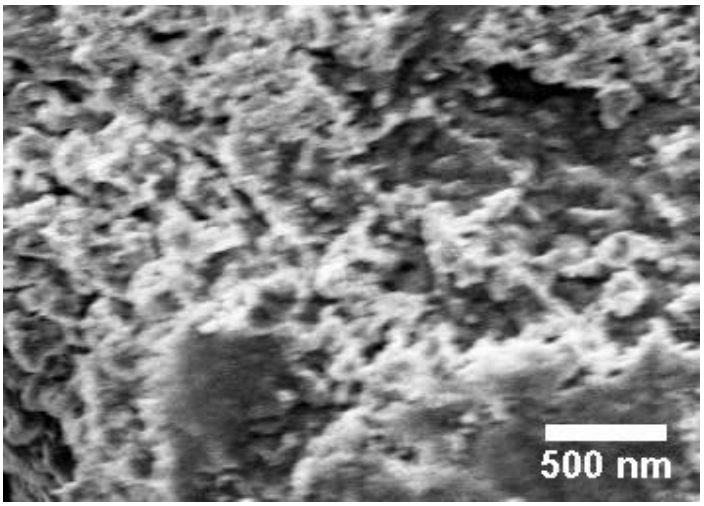

Figure 3. Field emission scanning electron microscopy (FESEM) image of $ZnFe_2O_4$ NPs.

2.3. HRTEM Analysis of $ZnFe_2O_4$ Nano Composite

The high-resolution transmission electron microscopy (HRTEM) images of $ZnFe_2O_4$ (NPs) are shown (Figure 4). The figure indicates that $ZnFe_2O_4$ NPs are uniform and cylindrical. The average particle size was calculated using Image-J software and the particle size is ranged about 50 nm.

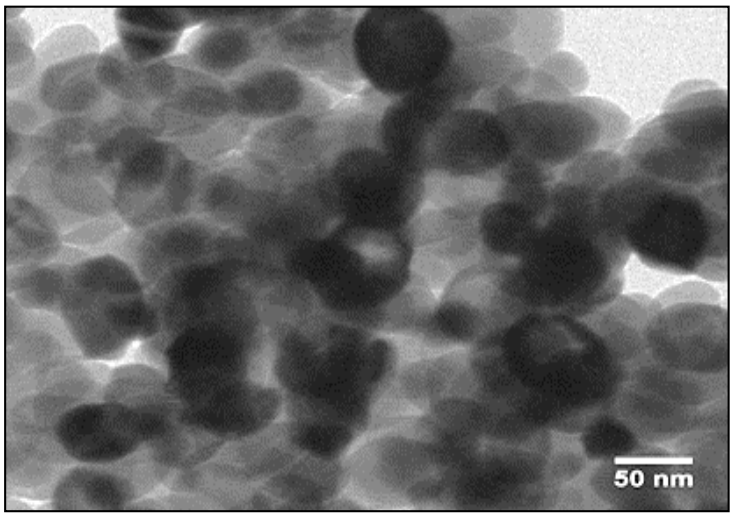

Figure 4. HRTEM Image of $ZnFe_2O_4$ NPs.

2.4. EDS Analysis of $ZnFe_2O_4$ NPs

The elemental composition of $ZnFe_2O_4$ NPs was studied by energy-dispersive X-ray spectroscopy (EDS), as shown in Figure 5. The $ZnFe_2O_4$ NPs exhibit three elemental peaks—one for zinc element located at 1.1 keV, one for oxygen element located at 0.5 keV, and two for iron element located at 0.65 and 6.4 keV. From the EDS data, the weight ratio of Zn:Fe:O is around 43.91:13.97:42.12. The sample consists of only O, Fe, and Znelements.

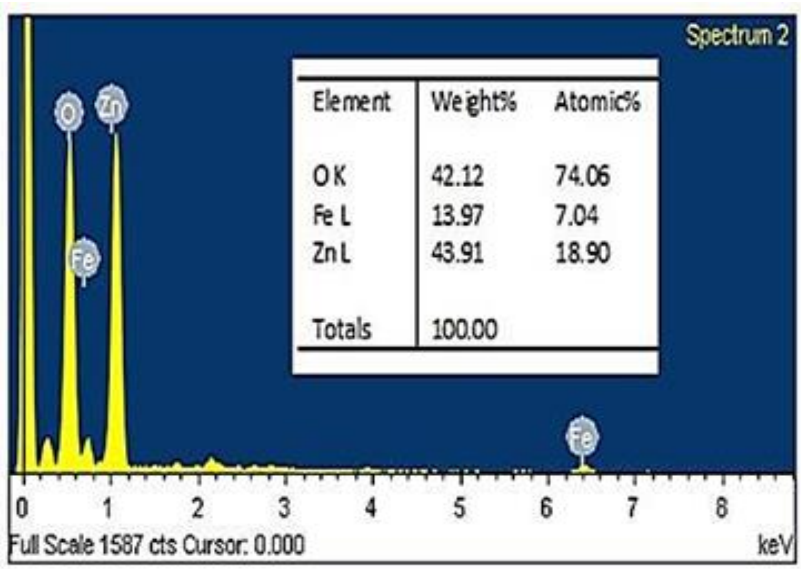

Figure 5. Energy-dispersive X-ray spectroscopy (EDS) pattern $ZnFe_2O_4$ nanoparticles.

2.5. Mass Spectra of Synthesized Compounds

The mass spectrum of **4a** revealed a molecular ion peak at m/z 286, which is consistent with the formula weight (285). This result confirmed the identity of the structure of **4a**. Similarly, the mass spectra of other compounds are also consistent with the proposed structures (for **4d**, m/z = 321, **4g**, m/z= 472 and **4h**, m/z= 310) (Figures S1–S4),

2.6. NMR Spectral Analysis

The ^{1}HNMR spectra of the compounds 7, 7-dimethyl-4-phenyl-2-thioxo-2, 3, 4, 6, 7, 8-hexahydro-1H-quinazolin-5-one from 5, 5-dimethyl cyclohexane-1, 3-diones (**4a**, **4d**, **4g**, **4h**) (Figures S5–S8) were assigned based on the observed chemical shift and relative

intensities of the signals. The ^{1}HNMR spectra of the compounds displayed sharp singlets owing to the two –NH protons in each compound at 9.52–10.36 ppm. ^{1}HNMR spectral values of –NH groups in quinazolones nucleus showed down fields, namely,10.23, 10.13, 10.29, 10.34 ppm (halogens and cyano group). The –NH-groups of quinazolones containing electron donating group (EDG) showed the ^{1}HNMR values in the upfield region such as 9.58, 9.73, 9.54, 9.74, 9.72, 9.84, and 9.52 ppm and also the showed–OH group at 10.24 ppm. The derivatives were obtained by the cyclization with the thiourea added. The two methyl group protons of the compounds fell at 0.92–1.15 ppm. A singlet at 3.57 ppm and a broad singlet at 3.66 ppm for **4b** and **4f** accounts for protons of *p*-methoxy (–OCH_3) and di-methoxy (3,5-OCH_3) groups, respectively. In the case of **4c** and **4d**, the hydroxy (–OH) protons were observed as singlets at 9.33 and 10.24 ppm, respectively. A singlet appeared at 2.74 ppm due to the N–Me proton in **4d**. The resonances due to aryl ring protons appeared in the range of 6.70–7.56 ppm. The quintets in 2.14–3.46 ppm and singlet around 2.40 ppm corresponded to methylene protons of dimedone ring.

The ^{13}CNMR spectra revealed the presence of the expected number of signals corresponding to different types of carbon atoms present in the compounds. The –OCH_3group absorbs at 55.25 (**4g**) and 55.30 (**4h**) ppm slightly downfield to the methyl group carbon due to the deshielding of the directly attached electronegative oxygen atom. The spectra of the compounds exhibit a strong band at 169.8–174.2 ppm and are assigned as C=S group. The ^{13}CNMR display signals in the range 112.4–151.7 ppm, which has been assigned to the aromatic carbon atoms. The signals due to the C attached to the methyl group resonate at 141.4–147.8 ppm. The resonance arising from the carbon attached to the hydroxyl (**4a** and **4d**) group is observed at 158.4 and 158.6 ppm, respectively. Values of downfield (195.2 ppm) compared with other groups (Figures S9–S12).

2.7. Antibacterial Activity

The antibacterial and antifungal activity of **4f**(4-(4-bromophenyl)-7,7-dimethyl-2-thioxo-2,3,4,6,7,8-hexahydro-1H-quinazolin-5-one) molecule showed high active potentials such as 20, 14,21,22,24 25 mm of inhibition, compared with **4e**(4-(4-chlorophenyl)-7,7-dimethyl-2-thioxo-2,3,4,6,7,8-hexahydro-1H-quinazolin-5-one) and **4g** (4-(2-iodo-3,5-dimethoxy phenyl)-7,7-dimethyl-2-thioxo-1,2,3,4,7,8-hexahydroquinazoline-5(6H)-one)molecules, which are also better than other compounds (Table 2). We observed that the important result in the investigation of the reaction of substituted aryl aldehydes, 5,5-dimethyl cyclohexane-1,3-dione(dimedone), and thiourea in the presence of nanocatalyst under solvent-free conditions at room temperature (Scheme 1).The advantages of using this catalyst for the reaction, which is responsible for easy work-up, include a short reaction time. Moderate-to-good yields, and purification of title compound by non-chromatographic methods. It is also identified that various substituted aryl aldehydes containing electron-withdrawing and electron-releasing substituents in para-positions lead better yield than ortho substituents. Therefore, we observed that the reaction of aryl aldehydes having an electron-withdrawing group was having a faster rate of reaction, compared to the reaction of aldehydes possessing electron releasing groups. In this reaction, halogen-substituted aryl aldehydes obtain a better yield than the electron-donating group containing aryl aldehyde. The reusability of this catalyst was investigated. The antimicrobial activity of title compounds possessing-electron withdrawing group (EWG) such as (**4e**–**4h**) (halogens and cyano group) exhibited more active potential than the EDG(**4a**–**4d**) containing moiety (Table 3).

Table 2. Synthesis of titled derivatives catalyzed by nanocatalyst solvent-free condition.

Entry	Ar(a)	Molecular Formula	Time [a] (min)	Yield [b] (%)	Molecular Weight (MW) g/mol	m.p (°C) Lit).
4a	C_6H_5	$C_{16}H_{18}N_2OS$	75	85	286.71	285–286 °C
4b	4-OH-C_6H_4	$C_{17}H_{20}N_2O_2$ S	130	87	317.53	274–276 °C
4c	3-OC_2H_5-4-OH-C_6H_3	$C_{18}H_{22}N_2O_3$ S.	150	87	365.22 (M-H).	273–274 °C
4d	4-Cl-C6H4	$C_{16}H_{17}ClN_2OS$	120	90	321.64	274–276 °C (Lit275–276 °C)
4e	4-Br-C_6H_4	$C_{16}H_{17}BrN_2OS$	120	91	366.16	284 °C
4f	2-OH-4-N$(CH_3)_2$-C_6H_3	$C_{18}H_{23}N_3O_2$ S	130	88	345.48	275–277 °C
4g	2-I-3,5-$(OCH_3)_2$-C_6H_3	$C_{18}H_{21}IN_2O_3S$.	150	90	472.29	275–276 °C
4h	4-CN-C_6H_4	$C_{17}H_{17}N_3OS$.	175	88	310.45 (M-H).	269–271 °C

[a] Reaction was continued until the Thin Layer Chromatography (TLC)shown the starting materials disappeared. [b] Isolated yield.

Table 3. In vitro antibacterial and antifungal screening study of the title compounds **4a**–**4h**.

S.No	Compound Code	Zone of Inhibition (mm)					
		Gram-Negative Bacteria		Gram-Positive Bacteria		Fungal Strains	
		E.coli	*P.aeruginosa*	*B.subtilis*	*B.megaterium*	*A.niger*	*C.albicans*
1	**4a**	16	13	21	15	15	16
2	**4b**	14	12	22	14	12	14
3	**4c**	16	15	14	16	13	16
4	**4d**	11	15	15	14	14	15
5	**4e**	19	17	20	20	23	24
6	**4f**	20	14	21	22	24	25
7	**4g**	19	20	21	21	23	24
8	**4h**	17	16	17	18	19	20
Control	**DMSO**		10			10	
Standard	**Streptomycin**	25	25	25	25		
	Fluconazole					30	30

3. Discussion

Dimedone also called 5, 5-dimethylcyclohexane-1, 3-dione is a cyclic diketone, which is used as a key sample molecule for the synthesis of the various moiety in synthetic organic chemistry. These are white to light yellow crystals in color and also have other names such asdimedone, Cyclomethicone, 5, 5-dimethyl-1,3-cyclohexanedione, dimethyl-dihydro resorcinol, and Methone. The molecular formula is $C_8H_{12}O_2$, and its molecular weight is 140.17968 g/mol with a melting point of 147–150 °C (420–423 K). It is stable under ambient conditions and soluble in organic solvents ($CHCl_3$, CC_4, toluene, etc.,) and in methanol, ethanol, and water. One-step reduction of dimedone to 3, 3-dimethylcyclohexanone compound with a yield of 69–73% (98–99% purity) by using Pd-catalyzed medium-pressure dimedone hydrogenation (1) in a solvent mixture of concentrated H_2SO_4 and propionic acid [26] was made. Dimedone and its derivatives have been previously documented to have various biological properties such as anticarcinogenic [27], antioxidant [28], antihistamine [29], and anticoagulant [30]. A three-component one-pot reaction of dimedone, 1, 3-cyclohexanedione, aromatic aldehydes, and malononitrile in the presence of D, L-proline under solvent-free conditions at ambient temperature to produce 2-amino-3-cyano-4-aryl-7,7-dimethyl-5,6,7 8-tetrahydrobenzopyrans has been reported [31].

The reaction proceeded at room temperature clearly shows to provide good yields for the products (ae = 94%). An efficient one-pot synthesis of 4H-benzopyrans via a three-component cyclo condensation of malononitrile using $CeCl_3 \cdot 7H_2O$ (10 mol percent) as a catalyst in a 1:2 mixture of water/ethanol under reflux conditions that yielded 70–94% within 1–2 h [32]. Sadehet al. (2017) [33] reported that in most organic transformations, dimedoneis a flexible and fascinating moiety. A wide variety of organic reactions, including one-pot multi-step syntheses, used the white to light yellow crystals of dimedone as a substrate. Dimedone has acidic properties in its methylene group, which is in harmony with its tautomericenol shape, making it possible to use them in various organic reactions. They are also used to evaluate the efficiency of some organic molecules, which have active pharmaceutical properties. Low-cost processing, ease of handling, low toxicity, easy accessibility, and moisture stability made it fascinating for use by synthetic organic chemists. Dimedone was concentrated in much of the reaction with a view to the media solvent. The temperature of the transformations in each segment has been subdivided, and this is used to achieve an organic transition based on green chemistry.

Leoa and Maryam (2018) [34] reported that the key peaks assigned to 200, 311, 400, 422, and 511 and Bragg reflection at 2 θ value of 27.36°, 36.03°, 46.18°, 56.77°, and 62.95° are according to the typical pattern for spinel-structured crystalline magnetite. The average nanoparticle diameter was around 73 nm, estimated from Debye–Scherrer's equation. It is also concluded that the chemical alteration process has not changed the magnetic nanoparticles' crystal structure, diameter, and structure. SEM images of $ZnFe_3O_4$ nanoparticles and $ZnFe_3O_4$@MSA were submitted. Fe_3O_4nano particles have a mean size of approximately 75 nm with good distribution according to SEM images. The SEM picture of Fe_3O_4@MSA shows that, due to the particle size of modified magnetite nanoparticles, the methane sulfonic acid layer attached to the nanoparticle surface is very thin because it is not larger than raw Fe_3O_4. These findings are in line with XRD trends [30].

Antibacterial activity was documented by Appaniet al. [35]. Electron withdrawing groups were demonstrated to have better behavior over aliphatic substituents among the various substituents on the C-2. Compounds with electron withdrawal substituents such as –Cl and–F showed increased activity over unsubstituted and electron releasing substituted moieties. As the most active compounds of the sequence, compounds 9a and 9h appeared to have the most potent activity against *P. Vulgaris* and *B*. Dimedone could be prepared from diethyl malonate and mesityl oxide, which is a safe compound with no or fewer hazards during usage. This dimedone is in equilibrium with its tautomericenol form in chloroform and the hydrogen bonding between the enolic structure results in the crystalline appearance. Dimedone and its analogs have been previously well documented with a wide spectrum of biological properties such as anticarcinogenic, antioxidant, antihistaminic, and anticoagulant [36].

The chemiluminescence property observed during the oxidation process belongs to 4-peroxydimedone radicals that are being synthesized from the first step of oxidation. Other applications of dimedone are colorimetry, crystallography, luminescence, and spectrophotometric analysis. Different types of reactions that include dimedone as a substrate have been presented and are classified based on the reaction media used. This is due to the importance of economical and green transformations in organic synthesis. The reaction could occur under solvent-free conditions, in aqueous media, and in the presence of various organic solvents. Some cases required heat to enhance them, and some others have taken place at room temperature. The above-discussed multiple properties of dimedone create a strong interest for utilizing them in different reactions by the synthetic chemists [37].

4. Materials and Methods

4.1. Materials

All the reagents, chemicals, and solvents (Merck, Mumbai, India) were procured and the melting points of the newly synthesized compounds were determined by using Agrawal 535 melting point apparatus. All the reactions were checked by thin-layer chromatography

using ethyl acetate and n-hexane (5:5) performed on percolated silica gel (Merck, Mumbai, India). The ^{1}HNMR spectra of these compounds were recorded on BRUKER 400 MHz spectrometers and ^{13}CNMR were recorded on BRUKER 100 MHz using $CDCl_3$ as the solvent and Tetramethylsilane as an internal standard. The molecular weight of compounds was determined by mass spectrometry.

4.2. Methods

4.2.1. Preparation of $ZnFe_2O_4$Nanoparticles (NPs)

The nanoparticles of zinc ferrite were prepared using both sol–gel techniques. As precursors, iron nitrate [$Fe(NO_3)_3 \cdot 9H_2O$] and zinc nitrate [$Zn(NO_3)_2 \cdot 6H_2O$] were used.

The precursors were dissolved in 50 mL ethylene glycol aliquot ($C_2H_6O_2$) and then agitated at room temperature for 2 h using a magnetic bead to form a homogenized aqueous solution (0.1 M). To evaporate all the material, the solution was dried for 6 h at 130 °C. Finally, the dry powder was annealed for crystallization at 500 °C for 1 h in the air.

4.2.2. Structural Characterization

The XRD profile at room temperature of the synthesized $ZnFe_2O_4$ (NPs) was obtained. The crystal structure and phase purity of the sample were evaluated, and the crystalline size was determined using the Debye–Scherrer equation. $ZnFe_2O_4$ (NPs) surface morphology was analyzed using the scanning electron microscope (SEM) (TESCAN, CZ/MIRA I LMH). Transmission electron microscope (TEM) (FEI, TECNAIG2TF20-ST) measured the particle size, and the elements present were analyzed by the energy dispersive x-ray analysis (EDS).

4.2.3. General Procedure for the Synthesis of 7, 7-Dimethyl-4-Phenyl-2-Thioxo-2, 3, 4, 6, 7, 8-Hexahydro-1H-Quinazolin-5-One

A mixture of substituted aryl aldehydes (1) (10 mmol), 5,5-dimethyl cyclohexane-1,3-dione(dimedone)(2) (10 mmol) and/thiourea (3) (15 mmol) with the nanocatalyst without solvent taken in a beaker (capacity 50 mL).The total mixture fitted on magnetic stirrer and reaction was proceeding. The completion of the reaction was monitored by TLC (ethyl acetate/hexane (5:5). The reaction mixture was then extracted with ethyl acetate and the catalyst was separated by the filtration. The organic layer was then washed with water and dried over anhydrous Na_2CO_3. The organic solvent was evaporated under reduced pressure and the solid compound was crystallized from absolute ethanol to lead the pure corresponding 7, 7-dimethyl-4-phenyl-2-thioxo-2, 3, 4, 6, 7, 8-hexahydro-1H-quinazolin-5-azones and its derivatives (**4a**–**4h**) in good yields.

7, 7-Dimethyl-4-phenyl-2-thioxo-2, 3, 4, 6, 7, 8-hexahydro-1H-quinazolin-5-one (**4a**):^{1}HNMR (400 MHz, CDCl3), δ ppm:1.02(s, 3H, CMe);1.11(s, 3H, CMe); 2.25 (q, *J* = 16.0 Hz, 2H, CH2); 2.31(s, 2H, CH2); 4.95 (d, *J* = 3.5 Hz,1H, CH); 7.12–7.32 (m, 5H, Ar); 9.66(s, 1H, NH); 10.22(s, 1H, NH); ^{13}CNMR (100 MHz, CDCl3): δ ppm: 193.7, 173.7, 147.8, 141.5, 128.9, 127.6, 125.8, 102.4, 51.5, 49.8, 32.6, 28.0, 26.4.

4-(4-Methoxyphenyl)-7,7-dimethyl-2-thioxo-2,3,4,6,7,8-hexahydro-1H-quinazolin-5-one (**4b**): ^{1}HNMR (400 MHz, CDCl3), δ ppm: 0.95(s, 3H, CMe); 1.11(s, 3H, CMe); 2.18(q, *J* = 16.2 Hz, 2H, CH2); 3.01(s, 2H, CH2); 3.57(s, 3H, OCH3), 5.10(d, *J* = 2.7 Hz, 1H, CH); 6.82(d, *J* = 8.4 Hz, 2H, Ar); 7.22(d, *J* = 8.8 Hz, 2H, Ar); 9.58(s, 1H, NH); 9.86(s,1H, NH); ^{13}CNMR (100 MHz, CDCl3): δppm: 193.4, 174.0, 158.2, 147.8,137.1,128.8,115.2,107.7, 100.8, 55.9, 52.4, 50.4, 32.9, 28.9, 26.8.

4-(3-ethoxy-4-hydroxyphenyl)-7,7-dimethyl-2-thioxo-1,2,3,4,6,7,8-hexahydro-1H-quinazolin-5-one (**4c**): ^{1}HNMR (400 MHz, CDCl3) δppm: 0.97(s, 3H, CMe); 1.11(s, 3H, CMe);1.25(t,3H,CH3); 3.46(q,2H,-CH2-), 2.22(q, =16.1 Hz, 2H, CH2); 2.39(s, 2H, CH2); 4.22(d, *J* = 3.6 Hz, 1H, CH); 6.70–7.51(m,34H, Ar); 9.33(s,1H,-OH); 9.73(s, 1H, NH); 9.94(s, 1H, NH); ^{13}CNMR (100 MHz, CDCl3): δppm:192.9,172.6,158.4,147.8,145.3,139.8,132.5,119.6,116.3,115.5,101.4, 60.9,50.4,47.8,36.9,30.6,26.3,13.7.

4-(4-Dimethylamino)-2-hydroxyphenyl)-7,7-dimethyl-2-thioxo-1,2,3,4,6,7,8-hexahydro-1H-quinazolin-5(6H)-one (**4d**): ^{1}HNMR (400 MHz,CDCl3) δppm: 1.05(s,3H,CMe); 1.15(s, 3H, CMe); 2.26(q, *J* = 16.2 Hz, 2H, CH2); 2.36(s, 2H, CH2); 2.74(s, 6H, NMe2), 4.94(d, *J* = 2.6 Hz, 1H, CH); 7.09–7.29 (m, 3H, Ar);9.15(s, 1H, NH);10.02(s,1H,-OH), 9.45(s, 1H, NH); ^{13}CNMR (100 MHz, CDCl3): δppm 193.9,174.2,158.6,151.6,149.2,131.4,126.7,122.9, 121.4,120.5,49.8,46.3, 38.6, 28.8, 26.9.

4-(4-Chlorophenyl)-7,7-dimethyl-2-thioxo-2,3,4,6,7,8-hexahydro-1H-quinazolin-5-one (**4e**): ^{1}HNMR (400 MHz, CDCl3)δppm: 0.94(s, 3H, CMe); 1.05(s, 3H, CMe); 2.19 (q, *J* = 16.5 Hz, 2H, CH2);2.40(s,2H,CH2);5.17(d, *J* = 3.6 Hz,1H,CH);7.36–7.15(m,4H,Ar);9.74(s,1H,NH);10.34(s,1H, NH); ^{13}CNMR(100 MHz,CDCl3) δppm: 194.5,174.2, 150.7, 141.4, 132.0, 129.7, 128.3, 127.4, 125.8, 104.4, 52.8, 50.6, 32.7, 28.9, 25.6.

4-(4-Bromophenyl)-7,7-dimethyl-2-thioxo-2,3,4,6,7,8-hexahydro-1H-quinazolin-5-one (**4f**): ^{1}HNMR (400 MHz, CDCl3) δppm: 0.98(s, 3H, CMe); 1.09(s, 3H, CMe); 2.14(q, *J* = 16.2 Hz, 2H, CH2); 2.35(s, 2H, CH2); 5.08(d, *J* = 2.7 Hz, 1H, CH); 7.20 (d, *J* = 8.4 Hz, 2H, Ar); 7.44(s, *J* = 7.6 Hz, 2H, Ar); 9.72(s, 1H, NH); 10.23(s, 1H, NH); ^{13}CNMR (100 MHz,CDCl3): δ 195.1, 173.6, 147.4, 141.7, 132.7, 130.2, 128.8, 121.5, 104.6, 52.0, 49.2, 32.4, 28.6, 25.9.

4-(2-iodo-3,5-dimethoxy phenyl)-7,7-dimethyl-2-thioxo-1,2,3,4,7,8-hexahydroquinazolne-5(6H)-one(**4g**):^{1}HNMR (400 MHz, CDCl3) δ ppm: 0.92(s, 3H, CMe); 1.13(s, 3H, CMe); 2.24(q, *J* = 16.4 Hz, 2H, CH2); 2.84(s, 2H, CH2); 3.66(s, 6H, (2OCH3), 5.07(d, *J* = 2.8 Hz, 1H, CH); 6.872(s, 1H, Ar); 7.02(s, 1H, Ar); 9.84(s, 1H, NH); 10.13(s, 1H, NH); 13CNMR (100 MHz, CDCl3): δppm: 194.6, 169.8, 156.7,151.7, 147.2, 119.8, 116.6, 115.3, 105.4,55.2,54.8, 51.3,48.7, 38.3, 28.6, 25.3. 8)4-(7,7-dimethyl-5-oxo-2-thioxo-1,2,3,4,7,8-ocatahydroquinazolne-4-yl) benzonitrile(**4h**) (400 MHz,CDCl3)δppm: 1.07(s,3H,CMe); 1.16(s, 3H, CMe); 2.32(q, *J* = 16.2 Hz, 2H, CH2); 2.43(s, 2H, CH2); 5.02(d, *J* = 2.8 Hz, 1H, CH); 7.39–7.56 (m, 4H, Ar);9.52(s,1H,NH); 10.29(s,1H,NH);^{13}CNMR(100 MHz,CDCl3)δppm:195.2,173.9,159.5,149.2,145.4,130.6,128.2, 120.8,112.4,104.7,52.3,49.2,38.6,29.4,29.4.

4.2.4. AntimicrobialAssays

Theantimicrobial activity of the titled compounds namely:7,7-dimethyl-4-phenyl-2-thioxo-2,3,4,6,7,8-hexahydro-1H-quinazolin-5-ones and its derivatives have been in vitro screened with both bacterial and fungal strains:

Gram-negative—*Escherichia coli, Pseudomonas aeruginosa*;

Gram-positive—*Bacillus subtilisin, Bacillus megaterium*;

Fungal strains—*Aspergillusniger and Candida albicans*.

The synthesized compounds were laid using agar plates containing nutrient broth for bacteria in vitro activities [8–11]. The antibacterial streptomycin and fluconazole were used as standards for antibacterial and antifungal assays, respectively. Dimethyl sulfoxide (DMSO) was used as solvent control. The antimicrobial inhibitions of test compounds were expressed as a zone of inhibition in standard units (mm). This marked antibacterial activity may be due to the presence of high hydrophobic content of this family of compounds and the quinazoline ring system. The compounds containing the quinazalone segment are more active against bacteria due to the strong interaction of the latter with the agar medium; this hinders their diffusion in the agar medium.

5. Conclusions

In conclusion, an efficient nanocatalyst is used for the synthesis of a series of7,7-dimethyl-4-phenyl-2-thioxo-2,3,4,6,7,8-hexahydro-1H-quinazolin-5-ones. The present methodology has very attractive features such as reduced reaction times and moderate-to-good yields, and the product was isolated efficiently. We believe that conducting this procedure in solvent-free conditions, along with easy recovery and reuse of catalyst, makethis method environmentally and economically valuable. Thederivativesof7, 7-dimethyl-4-phenyl-2-thioxo-2, 3, 4, 6, 7, 8-hexahydro-1H-quinazolin-5-ones have biological and medicinal significance.

Supplementary Materials: The following are available online at https://www.mdpi.com/article/10.3390/catal11040431/s1, Figure S1. Mass spectrum of 7, 7-Dimethyl-4-phenyl-2-thioxo-2, 3, 4, 6, 7, 8-hexahydro-1H-quinazolin-5-one (**4a**); Figure S2. Mass spectrum of 4-(4-Dimethylamino)-2-hydroxyphenyl)-7,7-dimethyl-2-thioxo-1,2,3,4,6,7,8-exahydro-1H-quinazolin-5(6H)-one (**4d**); Figure S3. Mass spectrum of 4-(2-iodo-3,5-dimethoxyphenyl)-7,7-dimethyl-2-thioxo-1,2,3,4,7,8-hexahydroquinazolne -5(6H)-one(**4g**); Figure S4. Mass spectrum of 4-(7,7-dimethyl-5-oxo-2-thioxo-1,2,3,4,7,8-ocatahydroquinazolne-4-yl) benzonitrile(**4h**); Figure S5. 1H NMR Spectrum of 7-Dimethyl-4-phenyl-2-thioxo-2, 3, 4, 6, 7, 8-hexahydro-1H-quinazolin-5-one (**4a**); Figure S6. 1H NMR Spectrum of 4-(4-Dimethylamino)-2-hydroxyphenyl)-7,7-dimethyl-2-thioxo-1,2,3,4,6,7,8-exahydro-1H-quinazolin-5(6H)-one (**4d**); Figure S7. 1H NMR Spectrum of 4-(2-iodo-3,5-dimethoxyphenyl)-7,7-dimethyl-2-thioxo-1,2,3,4,7,8-hexahydroquinazolne-5(6H)-one(**4g**); Figure S8. 1H NMR Spectrum of 4-(7,7-dimethyl-5-oxo-2-thioxo-1,2,3,4,7,8-ocatahydroquinazolne-4-yl) benzonitrile(**4h**); Figure S9. 13C NMR Spectrum of 7, 7-Dimethyl-4-phenyl-2-thioxo-2, 3, 4, 6, 7, 8-hexahydro-1H-quinazolin-5-one (**4a**); Figure S10. 13C NMR Spectrum of 4-(4-Dimethylamino)-2-hydroxyphenyl)-7,7-dimethyl-2-thioxo-1,2,3,4,6,7,8-exahydro-1H-quinazolin-5(6H)-one (**4d**); Figure S11. 13C NMR Spectrum of 4-(2-iodo-3,5-dimethoxyphenyl)-7,7-dimethyl-2-thioxo-1,2,3,4,7,8-hexahydroquinazolne-5(6H)-one(**4g**); Figure S12. 13C NMR Spectrum of 4-(7,7-dimethyl-5-oxo-2-thioxo-1,2,3,4,7,8-ocatahydroquinazolne-4-yl) benzonitrile(**4h**).

Author Contributions: S.Y.A. conceived and designed the experiments and supervised the research work; T.N.R. performed the experiments and wrote the paper; N.K. measured the characterizations; F.A. (Faheem Ahmed) and N.A. contributed reagents/materials/analysis tools. Visualization by F.A. (Fadwa Albalawi). and S.K. and data curation by P.M., A.A. and B.P. All authors have read and agreed to the published version of the manuscript.

Funding: The authors are grateful to the Deanship of Scientific Research, King Saud University, for funding through Vice Deanship of Scientific Research Chairs.

Data Availability Statement: Data is contained within the article and Supplementary Material.

Conflicts of Interest: The authors declare no conflict of interest.

References

1. Lednicer, D.; Mitscher, L.A. *The Organic Chemistry of Drug Synthesis*; Wiley InterscienceePubl: New York, NY, USA, 1977; Volume 1, pp. 338–342.
2. Lednicer, D.; Mitscher, L.A. *The Organic Chemistry of Drug Synthesis*; Wiley InterscienceePubl: New York, NY, USA, 1980; Volume 2, p. 361.
3. Kershaw, S.; Stables, J.P.; Jatav, V.; Mishra, P. Synthesis and CNS depressant activity of some derivatives of novel 3-[5-substituted-1, 3,4-thiadiazole-2-yl]-2-styrylquinazolin-4-(3H)-one. *Eur. J. Med. Chem.* **2008**, *43*, 135–141.
4. Sayed, R.E.; Wasfy, A.F. Synthesis of heterocycles having double character: As antimicrobial. *J. Chinesechem. Soc.* **2005**, *52*, 129–135.
5. Tyagi, M.; Pathak, U.S.; Rathod, R.S. Synthesis of 3-monosubstitutedquinazolin-4-(3H)-ones. *Ind. J. Chem.* **1995**, *2*, 617–623.
6. Thierry, B.A.; Jerome, G.; Charles, W.R. Multistepsynthesis of thiazoloquinazolines-under microwave irradiation in solution. *Tetrahedron Lett.* **2020**, *41*, 1027–1030.
7. Bahl, B.S.; Bahl, A.A. *Text Book of Organic Chemistry*; Chand and Company Ltd.: New Delhi, India, 1997; Volume 14, p. 735.
8. Guiry, P.J.; Connolly, D.J.; Cusack, D. Synthesis of quinazolinones and quinazoline. *Tetrahedron* **2005**, *737*, 10153–10202.
9. Feng, L.; Meng, Q.; Feng, Y. An efficient construction of Quinazoline-4-(3H)-ones under microwave irradiation. *ARKIVOC* **2007**, *I*, 40–50.
10. Meyyanathan, S. ASEAN review of biodiversity and environmental conversation. *ABEC* **1998**, *2*, 4–10.
11. Alexandra, P.B.; Thierry, B.; Corinne, F. Diaryliodoniums Salts as Coupling Partners for Transition-Metal Catalyzed C- and N-Arylation of Heteroarenes. *Catalysts.* **2000**, *10*, 1–34.
12. Lidstrom, P.; Tierney, J.; Westman, J. Microwaveassistedorganic synthesis—A review. *Tetrahedron* **2001**, *57*, 9225–9283. [CrossRef]
13. Lottie, B.; Thomas, H. Microwave enhanced decarboxylation of aromatic carboxylic acid, improved potential. *J. Chem. Res.* **2000**, *2*, 42–46.
14. Canevari, S.; Bantu, R.; Nagarapu, L. TMSCl mediated highly efficient one-pot synthesis of octa hydro quinazolinone and 1,8-dioxo-octa hydro xanthene derivatives. *Arkivoc* **2006**, *XVI*, 136–148.
15. Hassani, Z.; Islami, M.R.; Kalantari, M. An efficient one-pot synthesis of octa hydro quinazolinone derivatives using a catalytic amount of H_2SO_4 in the water. *Bioorganic Med. Chem. Lett.* **2006**, *16*, 4479. [CrossRef] [PubMed]
16. Lin, H.; Zhao, Q.; Xu, B.; Wang, X. Nafion-H catalysed cyclocondensation reaction for the synthesis of octa hydro quinazolinone derivatives. *J. Mol. Catal. A: Chem.* **2007**, *268*, 1–2. [CrossRef]
17. Niralwad, K.S.; Shingate, B.; Shingare, M.S. Microwave-assisted one-pot synthesis of octa hydro quinazolinone derivatives using ammonium metavanadate under solvent-free condition. *Tetrahedron Lett.* **2010**, *51*, 3616. [CrossRef]

18. Mobinikhaledi, A.; Foroughifar, N.; Khodaei, H. Synthesis of octa hydro quinazolinone-derivatives using silica sulfuric acid as an efficient catalyst. *Eur. J.Chem.* **2010**, *1*, 291. [CrossRef]
19. Kefayati, H.; Asghari, F.; Khanjanian, R. 1-Methylimidazolium hydrogen sulfate/chlorotrimethylsilane: An effective catalytic system for the synthesis of 3, 4-dihydropyridine-2(1H)-ones and hydroquinazolinone-2,5-diones. *J. Mol. Liq.* **2012**, *172*, 147. [CrossRef]
20. Khurana, J.M.; Kumar, S. Ionic liquids: An efficient and recyclable medium for the synthesis of octa hydro quinazolinone and biscoumarin derivatives. *Montashefte Fur Chem.* **2010**, *141*, 561. [CrossRef]
21. Karami, S.; Karami, B.; Khodabakhshi, S. Solvent-free synthesis of novel and known octahydroquinazolinones/thione by the use of $ZrOCl_2.8H_2O$ as a highly efficient and reusable catalyst. *J. Chin. Chem.Soc.* **2013**, *60*, 22. [CrossRef]
22. Pachpinde, A.M.; Langade, M.M. A simple one pot synthesis of 5-Acetyl-3,4-Dihydro-4-Phenylpyrimidin-2(1H)-one, by using magnetically recoverable heterogeneous nickel substituted nanoferro-spinel catalyst. *Int. J. Res. Appl. Sci. Biotechnol.* **2019**, *6*, 23–26. [CrossRef]
23. Kumar, B.V.; Naik, H.S.B.; Girija, D. ZnO nanoparticle as catalyst for efficient green one-pot synthesis of coumarins through Knoevenagel condensation. *J. Chem. Sci.* **2011**, *123*, 615–621. [CrossRef]
24. Beletskaya, I.; Tyurin, V. Recyclable Nanostructured Catalytic Systems in Modern Environmentally Friendly Organic Synthesis. *Molecules* **2010**, *15*, 4792–4814. [CrossRef]
25. Hemalatha, K.; Madhumitha, G.; Kajbafvala, A.; Anupama, N.; Sompalle, R.; Roopan, S.M. Function of nanocatalyst in chemistry of organic compounds revolution: An overview. *J. Nanomater.* **2013**, *2013*, 1–23. [CrossRef]
26. Cormier, R.A. A convenient synthesis of 3,3-dimethylcyclohexanone. *Synth. Commun.* **1981**, *11*, 295–298. [CrossRef]
27. Singletary, K.; MacDonald, C.; Iovinelli, M.; Fisher, C.; Wallig, M. Effect of the β-diketonesdiferuloylmethane (curcumin) and dibenzoylmethane on rat mammary DNA adducts and tumors induced by 7,12-dimethylbenz[a] anthracene. *Carcinogenesis* **1998**, *19*, 1039–1043. [CrossRef]
28. Rasmussen, H.B.; Christensene, S.B.; Kirs, L.P.; Karazmi, A. A simple and efficient separation of the curcumins, the antiprotozoal constituents of Curcuma longa. *Planta Med.* **2000**, *66*, 396–397. [CrossRef] [PubMed]
29. Matsuzaki, T.; Koiwai, A. Antioxidative-Diketones in stigma lipids of tobacco. *Agric. Biol. Chem.* **1988**, *52*, 2341–2342. [CrossRef]
30. Francis, L.E.; Douglas, D.E. Some observations on the antihistamine activity in the guinea pig of aliphatic 2,4diketones, a new class of physiological tissue components. *Res. Commun. Chem. Patel. Pharmacol.* **1977**, *17*, 357–364.
31. Guo, S.B.; Wang, S.X.; Li, J.T.D. L-Proline-catalyzed one-pot synthesis of Pyrans and Pyrano[2,3c]Pyrazole derivatives by a grinding method under solvent, free conditions. *Synth. Commun.* **2007**, *37*, 2111–2120. [CrossRef]
32. Sabitha, G.; Arundhathi, K.; Sudhakar, K.; Sastry, B.S.; Yadav, J.S. A concise study on dimedone: A versatile molecule in multicomponent reactions, an outlook to the green reaction media. *Synth. Commun.* **2009**, *39*, 433–440. [CrossRef]
33. Sadeh, F.N.; Fatahpour, M.; Hazeri, N.; Maghsoodlou, M.T.; Lashkari, M. One-pot condensation approach for the synthesis of some 1,8-dioxooctahydroxanthenes and 14-aryl-14hdibenzo[a,j]xanthenes using lactic acid as an efficient and eco-friendly catalyst. *Acta Chem. Iasi.* **2017**, *25*, 24–37. [CrossRef]
34. Leila, M.; Maryam, T. Green synthesis of 3,4-dihydropyrimidinones using nanoFe3O4@meglumine sulfonic acid as a new efficient solid acid catalyst under microwave irradiation. *J. Saudi Chem. Soc.* **2018**, *22*, 66–75.
35. Ramgopal, A.; Baburao, B.; Kiran, G. *Synthesis and Antibacterial Activity of 3-(Substituted)-2-(4-oxo2-Phenylquinazolin-3(4H)-Arylamino) Quinazolin-4(3H)-One*; Hindawi Publishing Corporation Scientifica: Cairo, Egypt, 2016; Volume 124, p. 5.
36. Kobra, N.F.; Molaei, F. A concise study on dimedone: A versatile molecule in multicomponent reactions, an outlook to the green reaction media. *J. Saudi Chem. Soc.* **2018**, *22*, 715–741.
37. Wang, G.W.; Lu, Q.Q.; Xia, J.J. Synthesis of N-substituted Acridinediones and Polyhydroquinoline derivatives in refluxing water. *Eur. J. Org. Chem.* **2011**, 4429–4438. [CrossRef]

Am J Cancer Res 2021;11(5):1828-1844
www.ajcr.us /ISSN:2156-6976/ajcr0127404

Review Article

Anti-ovarian cancer potential of phytocompound and extract from South African medicinal plants and their role in the development of chemotherapeutic agents

Chella Perumal Palanisamy[1], Bo Cui[1], Hongxia Zhang[1], Mani Panagal[2], Sivagurunathan Paramasivam[3], Uma Chinnaiyan[3], Selvaraj Jeyaraman[4], Karthigeyan Murugesan[5], Mauricio Rostagno[6], Vijayakumar Sekar[7], Srinivasa Prabhu Natarajan[8]

[1]State Key Laboratory of Biobased Material and Green Papermaking, College of Food Science and Engineering, Qilu University of Technology, Shandong Academy of Science, Jinan 250353, China; [2]Department of Biotechnology, Annai College of Arts and Science, Kovilacheri, Tamil Nadu, India; [3]Department of Microbiology, Faculty of Science, Annamalai University, Tamil Nadu, India; [4]Department of Biochemistry, Saveetha University, Chennai, Tamil Nadu, India; [5]Department of Biotechnology, Arumugam Pillai SeethaiAmmal College, Tamil Nadu, India; [6]Laboratory of Functional Properties in Foods, School of Applied Sciences, University of Campinas, Limeria, Sao Paulo, Brazil; [7]Marine College, Shandong University, Weihai 264209, China; [8]Department of Biotechnology, Bharathidasan University, Tamil Nadu, India

Received December 1, 2020; Accepted February 26, 2021; Epub May 15, 2021; Published May 30, 2021

Abstract: Ovarian cancer (OC) accounts for the highest tumor-related mortality among the gynecologic malignancies. Most of the OC patients diagnosed with advanced-stage (III and IV) this situation creates panic and provokes an emergency to discover a new therapeutic strategy. Plants that possess medicinal properties are gaining attention as they are enriched with various chemical compounds that are potential to treat various diseases. It is a prolonged process to provide innovative and significant leads against a range of pharmacological targets for a human disease management system. Though challenges and difficulties are faced in the development of a new drug, the emergence of combinatorial chemistry is providing a new ray of hope and also, the executed effort in discovering the drug, and a chemical compound has been remarkably successful. This review discussed the role of medicinal plants that are native of South Africa in treating the Ovarian Cancer and in drug discovery.

Keywords: Ovarian cancer, south african medicinal plants, anti-ovarian cancer activity, drug development

Introduction

Plants with medicinal values have been a part of human culture and tradition [1]. It possesses significant nutrition and is prescribed for various therapeutic purposes [2]. World Health Organization (WHO) assessed that about 80% of the population primarily rely on plant medicines to stay healthy [3]. Also, 21,000 plant species are reported by WHO to possess to have therapeutic values to be used as medicines [4]. Plant chemicals are extracted and the compounds of interest are identified continuously till date and recently to standardize the herbal medicines (**Table 1**) and to elucidate analytical marker compounds drug discovery techniques are applied [5]. Discovering a drug is an interdisciplinary action where it includes various fields of science. Novel drug discovery is an extravagant, challenging process, it devours time as well. The important process (**Figure 1**) involved in identifying New Chemical Entities (NCEs) which possess characteristic features such as effective druggability and medicinal chemistry [6]. NCEs are synthesized synthetically using chemicals or obtained from a natural process by isolation, approximately it would take 12 years for a new drug to reach a clinic from its discovered stage, also the investment done for the drug discovery is 1 billion US$ [7]. Numerous examples have proven that natural sources (including semi-synthetic analogues) and its products have been the backbone of more than 80% of drug substances [8].

Table 1. Some of the natural compounds from the medicinal plants

S. No.	Plant-derived compound	Classification	Plant Name	Biological function	References
1	Aescin 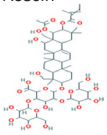	saponins	*Aesculus hippocastanum*	Anti-inflammatory, vasoconstrictor and vasoprotective effects	[113]
2	Ajmalicine 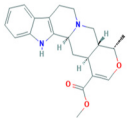	alkaloid	*Rauwolfia spp., Catharanthus roseus, and Mitragyna speciosa*	Antihypertensive drug used in the treatment of high blood pressure	[114]
3	Berberine 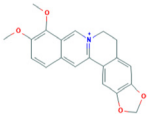	alkaloid	*Berberis vulgaris*	Treatment for bacillary dysentery	[115]
4	Colchicine 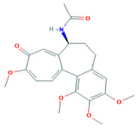	alkaloid	*colchicum autumnale*	Antitumor agent	[116]
5	Curcumin 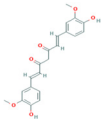	phenols	*Zingiberaceae*	dietary supplement	[117]
6	Emetine 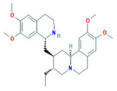	alkaloid	*Cephaelis ipecacuanha*	Amoebicide, emetic	[118]
7	Hesperidin 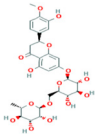	Flavonoid	*Citrus species*	Treatment for capillary fragility	[119]
8	Lapachol 	Phenols	*Handroanthus impetiginosus*	Anticancer activity	[120]
9	Nordihydroguaiaretic acid 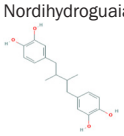	Phenols	*Larrea tridentata*	Antioxidant activity	[121]
10	Quinine 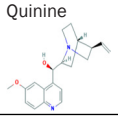	Alkaloid	*Cinchona officinalis*	Antimalarial drug	[122]

Cancer is referred to as the uncontrolled growth of abnormal cells anywhere in a body that can infiltrate normal body tissue and it is one of the leading fatal disease which leads to death worldwide [9]. The different types of cancer existence with histopathologies, genetic-epigenetic variations, and clinical outcomes are the challenges that persist in apprehending the mechanism of action of chemotherapeutics and in the development of innovative rehabilitations [10, 11]. Ovarian cancer cruelly affects the human population when compared with other gynaecological malignancies in worldwide. There is an urgent need for novel therapies to treat and prevent this life-threatening disease. Innovative research interest is illus-

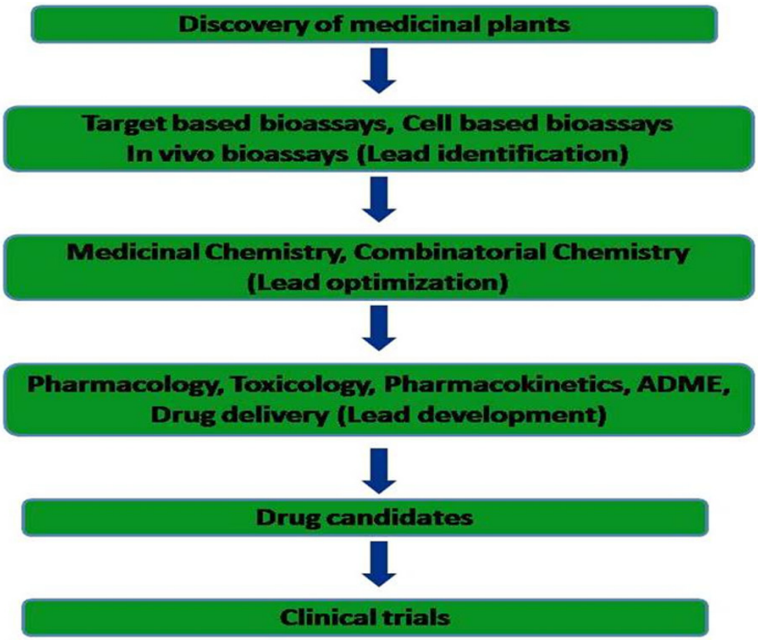

Figure 1. Modern drug discovery and development from the medicinal plant.

trating its attention towards naturally-derived compounds as they are considered to have less toxic side effects compared to current treatments such as chemotherapy, laser therapy, radiotherapy, gene therapy, hyperthermia and surgery. Plants produce secondary metabolites which are being investigated for their anti-ovarian cancer activities leading to the development of new clinical drugs. Development anti-ovarian cancer compounds from the medicinal plants have been utilized as staple drugs for treatment and prevention, the new technologies are emerging to expand the area further. Increasing demand for plant-derived drugs is putting pressure on high-value medicinal plants and risking their biodiversity. Plant-derived anti-ovarian cancer agents are effective inhibitors of cancer cells lines, making them in high demand [12].

Ovarian cancer and medicinal plants

Ovarian cancer (OC) stands seventh worldwide among the most commonly occurring types of cancer. Roughly it is estimated that twenty four hundred thousand females are diagnosed with the disease every year, this report depicts that 2% of all cancer cases around the world [13]. According to the World Cancer Research Fund International 2017, the highest incidence of OC occurs in Fiji (with estimated fifteen cases per hundred thousand), surprisingly very few cases are recorded in China and some parts of Africa (four cases among a hundred thousand female individuals) [14]. 1 in 70 women are prone to ovarian cancer risk. 150,000 deaths are recorded globally every year due to OC and this is considered as the fatal disease that leads to death when compared to other gynaecological malignancies. Due to poor diagnosis attributed to lack of symptoms at the early stages, as the symptoms appear at advanced stages (III and IV) [15]. The mortality is high comparatively. Chemotherapy, laser therapy, radiotherapy, gene therapy, hyperthermia, and surgery are few interventions practised or in trials to intervene in the growth of the cancer cells [16]. The medical aid includes a combined effort of incision, chemical treatments, and therapies which involves the action radiations [17]. Though there are pros in the procedures mentioned earlier the scientific community recognized that the interventions have disadvantages and limitations. Consequently, a development of drug that is capable of overcoming the obstacles and treating the disease effectively [18].

For centuries our ancestors were using plants to treat various human diseases and cancer is one among them [19-21]. Many medicinal plants have been reported to exhibit a variety of pharmacological and actions related to life functions namely antioxidant, antimicrobial, anticancer, antidiabetic properties and so on. Since plants acts as a store house of various phytochemicals they are capable of treating various ailments. these properties exhibited by plants [22-24]. The biologically important phytochemicals play a pivotal role in drug discovery [25-27] and the plant-derived biomolecules are recognized as an attractive and promising approach; possess high value in biomedical research for the development of drugs against cancer [28]. Interestingly in the recent past decades, plant that are medicinally important are been used to prepare drugs and the numbers are increasing comparatively. Inthe last twenty years a successful investigations are

done on natural products especially to treat cancer much effectively in most parts of the world [29, 30].

Anti-ovarian cancer activity of other medicinal plants

Several indigenous medicinal plants of Africa which include *Aframomum arundinaceum, Aframomum. alboviolaceum, Aframomum kayserianum, Aframomum polyanthum* [31], *Echinops giganteus, Xylopia aethiopica, Piper capense, Imperata cylindrical* [32, 33]. *Gladiolus quartinianus, Vepris soyauxii* [34], *Polygonum limbatum, Polycias fulva, Beilschmiedia acuta, Crinum zeylanicum, Dioscorea bulbifera, Elaoephorbia drupifera* [35], *Solanum aculeastrum, Albizia schimperiana, Zanthoxylum giletii* and *Strychnos usambarensis* are used in the treatment and management of malignancies such as cancer, etc. these plants also showed significant cytotoxicity effect against the regions that have developed an immune against the drugs and that are endowed with sensation [36].

In vitro studies were performed using Korean medicinal plants to study the anti-cancer activity, Ethyl Acetate fraction from the *Lespedeza cuneata* methanolic extract proved to possess a cell-poisoning effect on A2780 human ovarian carcinoma cells with the IC_{50} value of 77.25 ± 2.05 μg/mL. The lignanosides compound of (-)-9'-*O*-(α-l-rhamnopyranosyl) lyoniresinol from this plant possess *in vitro* antiproliferative activity on A2780 with an IC_{50} value of 77.24 ± 2.05 μM [37]. The seeds of tea (*Camellia sinensis*) which contains saponins exhibited cancer chemopreventive effects, this was identified and reported when an athymic mice study was performed for Anti-tumor efficacy in human SKOV3 ovarian cancer xenografts [38]. Curcumin is a polyphenol that occurs naturally in a plant species called *Curcuma longa* which also holds another compound called curcuminoid has a potency to inhibit IL 6 and IL 8 secretion that was induced by lysophosphatidic acid (LPA) and STAT 3 phosphorylation, where LPA is a bilipid which is found to stimulate the invasion of cancer cells, and cells that carry the infection from the infected part to various other parts of the body and STAT 3 phosphorylation that inhibits the motility of OC cells, as portrayed in PA and OVCAR3 [39]. In the past in Kwara and Lagos state, *Pistia stratiotes* was cited frequently to treat ovarian cancer. But a recent study has thrown light on another species called *Securidaca longipedunculata* which is now considered to be the commonly used botanical source in aiding ovarian cancer [40]. Notably, the above study focused only on the Ijebus, an ethnic Yoruba group. Similarly, different plants namely *Kigelia africana, P. stratiotes, Chenopodium ambrosioides, Nymphaea lotus, Parquetina nigrescens, Nicotiana tabacum, Alstonia congensis, Elaeis guineensis, Piper guineense, Aframomum melegueta, Petiveria alliacea* were been in practicein Ogun state by the natives, southwest Nigeria to treat cancer [41].

Anti-ovarian cancer activity of South African medicinal plants

Africa is enriched with flora, and the phytochemicals in plants exhibit structure that draws interest also along with the diverse biological activities they serve as a starting point for a development of a new drug [42]. South Africa holds rich biodiversity where 22,600 indigenous medicinal plants are present. The flora contributes about ten percent of the higher botanical species on Earth. The traditional medicinal and healthcare history of Africa is very long [43]. Although there is limited information about the anticancer activity of South African plants available in the literature, there are several pieces of evidence suggesting that some of these plants could be used for the development of new therapeutic drugs. The most relevant candidates are discussed below providing information or insights to their pharmacological potential [44].

Aspalathus linearis (Burm.f) R. Dahlgren: Aspalathus linearis is a bush that has legumes or pods (Rooibos) belongs to the family Fabaceae and the presence of legume is a characterstic feature of the family Fabaceae. It is native (**Figure 2A**) to the Cedarberg Mountains in the Western Cape region of South Africa. They are cultivated widely within the region as they are commercially useful from which herbal tea or tisane are produced [45, 46]. This beverage has its History from South Africa and now it is profoundly known in other countries as well [47]. The compounds such as various types of polyphenols, flavonoids present in the plants

Figure 2. Anti-ovarian cancer activity of South African medicinal plants.

are filled with medicinal properties also an added advantage is that caffeine and theaflavins are absent and hence it is used medicinally [48].

Table 2. Reported South African medicinal plants with anti-ovarian activity

S.No	Plant name	Type of Cell line	Extract with anti-ovarian action	References
1	*Aspalathus linearis*	Chinese hamster	Whole plant (Aqueous)	[50-52]
2	*Brachylaena rotundata*	OVCAR-5	Leaf (Dichloromethane)	[55]
3	*Catha edulis*	Chinese hamster	Leaf (Aqueous)	[59, 60]
4	*Centella asiatica*	SKOV3 and OVCAR-3	Whole plant (Aqueous)	[66]
5	*Dicoma anomala*	Chinese hamster	Root (Ethyl acetate)	[71]
6	*Dodonaea viscosa*	A2780 human	Root (ethanol)	[75]
7	*Drimia robusta*	OVCAR-3	Whole plant (methanol)	[55]
8	*Gomphocarpus fruticosus*	OVCAR-3	Root (Ethanol)	[55]
9	*Leyssera gnaphaloides*	Chinese hamster	Whole plant (Hexane)	[83]
10	*Parinari curatellifolia*	SW626 human	13-Methoxy-15-oxozoapatlin compound from the plant	[87]
11	*Pelargonium acraeum*	PA1 and OVCAR-3	Whole plant (Aqueous and methanol)	[55]
12	*Plumbago auriculata*	PA1	Whole plant (methanol)	[92]
13	*Solanum acanthoideum*	IGROV1	Root (methanol)	[55]
14	*Solanum nigrum*	ES-2, SKOV-3 and OVCAR-3	Whole plant (Aqueous)	[99, 100]
15	*Xanthium strumarium*	SKOV-3	Leaf	[111, 112]

Fantoukh et al. isolated 11 phytocompounds from methanolic extract of *Aspalathus linearis* such as Aspalathin (521 mg), Nothofagin (306 mg), Thermopsoside (23 mg), Isoorientin (90 mg), Vitexin (73 mg), Isovitexin (8 mg), Isoquercitrin (76 mg), Rutin (59 mg), Bioquercetin (136 mg), (R)/(S)-eriodictyol-6-C-β-D-glucopyranoside (68 mg) and Syringin (68 mg) which possess antioxidant, antimicrobial, anti-inflammatory, antidiabetic and anticancer activities [49, 50]. Rooibos extracts targe the premalignant cells present in the skin and inhibits the cell proliferation and thus intervenes in the growth of cancerous cells in the skin, it also induces apoptosis of tumor cells [51]. The efficacy of the extract has been revealed through various studies and it had shown significant anti-cancer effects against other types of cancer as well. An oral dose of this extract suppresses the activity of methylbenzlnitrosamine which induces the oesophageal squamous cell carcinogenesis in male F344rats [52]. B1 rats were given a dose of the Rooibos and this repressed the development of the fumonisin induced hepatocellular carcinoma [53].

Brachylaena rotundata (S.Moore): Brachylaena rotundata (Asteraceae) is a shrub or a small tree that grows up to 8 meters (**Figure 2B**). It also occurs in most Southern nations, particularly eastern Botswana, Transvaal, Mozambique, Zambia, and Zimbabwe, with presence in open woodland, on rocky koppies, and slopes, and on stream banks [54]. The dichloromethane extract of *Brachylaena rotundata* leaves (**Table 2**) has been found to reveal anti-ovarian cancer activity in OVCAR-5 ovarian cancer cell line with an IC_{50} value of 19.95 μg/ml [55].

Catha edulis (Vahl.) Endl.: Catha edulis (**Figure 2C**) is the South African medicinal plant belonging to the Celastraceae family. *Catha edulis* leaves contain phytochemicals and an indicative amount of vitamin C [56]. The worth of the foliage depends on the presence of cathinone contents [57]. Getasetegn (2016) reported the chemical composition of khat which possess 81 phytocompounds are classified into 7 major classes such as Phenylalkyl-amines ((+)-Cathine, (-)-Cathinone, 3,6-Dimethyl-2,5-diphenyl pyrazine, Merucathine, Merucathinone, (-)-Norephedrine, (-)-Norephedrine N-formyl, 1-Phenylpropane-1,2-dione and Pseudomerucathine), Cathedulins (Cathedulin E1-E6, Cathedulin K1, 2, 6, 12, 15, 17, 19 and 20, Cathedulin Y7-Y10, Cathidine A, B, D and Euonyminol), Flavonoids (Dihydromyricetin, Dihydromyricetin-3-O-rhamnoside, Kaempferol, Myricetin, Myricetin-3-O-b-D-galactoside, Myricetin-3-O-rhamnoside, Quercetin and Quercetin-3-O-b-D-galactoside), Sterol and Triterpenes (Celastrol, Friedeline, Iguesterin, Pristimerin, b-Sitosterol Tingenin A, B and b-Sitosterol glycoside), Volatiles (Fenchone, Linalool, Nerol, Ocimene, β-Phellandrene, α-Pinene, β-pinene, α–Terpineol, Terpinolene, α-Thujone and b-thujone), Amino acids and Vitamins (Vitamin C, B3, B2 and B1.) which hold unique biological activities in human disease management system [58].

The fresh leaf extract of *Catha edulis* exhibited the anti-ovarian cancer activity in the Chinese

hamster ovary cell line at the concentration of 50 μg/ml [59]. Alsanosy et al., (2020) examined the anti-ovarian cancer activity of Six different fractions from the extract of *Catha edulis* which exhibited the anti-ovarian cancer activity on A2780 with the significant IC_{50} values raging from 20.97 ± 5.03 to 53.78 ± 7.45 [60]. Elhag et al., (1999) isolated the phytocompound of 22b-hydroxytingenone from methanolic extract of *Catha edulis* and demonstrated their ovarian cancer activity in National Cancer Institute (USA) which showed the significant ED_{50} value of 2.35 μg/ml [61].

Centella asiatica (Linn.) Urb: Centella asiatica (Apiaceae), commonly called pennywort (**Figure 2D**) is a perennial creeper and the propagation is through stolons, they are commonly found in moist places. This plant has reported to have many medicinal values and the plant chemicals exhibit mitoprotective, antioxidant, anti-inflammatory, antioxidant, and anticancer properties [62-64]. It holds a very good healing property and this quality of the plant is assumed due to the presence of three active triterpenes such as Asiatic acid, madecassic acid and asiaticoside [65]. A triterpenoid compound of Asiatic acid was extracted from *Centella asiatica* and found to possess anti-ovarian cancer activity in SKOV3 and OVCAR-3 ovarian cancer cell lines (**Table 2**). At an intensity of 40 μg/mL of asiatic acid the practicability of the ovarian cancer cells was reduced to 50% and the colonization of the OC cells were also reduced by 25-30% at the concentration of 10 μg/mL of asiatic acid. Apoptosis of the tumor cells increased to 7-10 folds when the cells were treated with Asiatic acid and this also curbed the cell cycle at G_0/G_1 phase. Several molecular pathways were examined to study the asiatic-acid effect against ovarian cancer cells. The phosphorylation levels of P13, Akt, and mTOR were lowered in the asiatic-acid treated cells. The tumor cell cells are viable and constitutive overexpression of Akt reverses the cytotoxic effect of asiatic acid partially. The growth-suppressive activity of the acid was examined. The downregulation of Akt mimicked the activity of Asiatic acid in the repression of growth against tumor cells [66].

Dicoma anomala (Sond.): Dicoma anomala (**Figure 2E**) a member of Asteraceae Family and a resident of the South Africa known well for its medicinal values. It is an upright, partially bent, or an incumbent herb that bears a partially woody tuber which has a distinctive aroma at the base of a woody subterranean stem. This grassland species is widely distributed in sub-Saharan Africa [67]. There are many ethnomedical uses of *Dicoma anomala*. It is used in the treatment of cough and cold, fever, ulcer, dermatosis, venereal disease, labor pain, looseness of bowel, enternal parasite, abdominal pain, odontalgia and internal worm [68]. Its extracts also possess several pharmacological properties including anti-bacterial, anti-helminthic, anti-viral, anti-plasmodial, anti-spasmodic, wound healing, analgesic, anti-cancer, antioxidant, hepatoprotective, antidiabetic, cardioprotective, and anti-inflammatory activities [69]. Phytochemical investigations were done to identify various secondary metabolites and it revealed the presence of compounds such as acetylenic compounds, phenolic acids, flavonoids, sesquiterpene lactones, triterpenes, and phytosterols [70]. The compounds, Dehydrobrachylaenolide, and Chloroquine from Ethyl acetate extract of *Dicoma anomala* root have enormous cytotoxicity effects at the concentration (IC_{50} value) of 17.199 μM/ml and 35.800 μM/ml respectively on Chinese hamster ovary cell line [43].

Maroyi (2018) reported that different solvent extracts of (from non-polar to polar hexane, petroleum ether, chloroform, ethyl acetate, methanol and aqueous) leaf, root and twig of *Dicoma anomala* holds cytotoxicity activity on Chinese hamster ovary (CHO) cell line with moderate IC_{50} values from 0.44 μg/ml to 31.33 μg/ml. the isolated compound of (3aS, 5aS,9aR,9bS)-5amethyl3,9-dimethylidene-4,5,9a,9b-tetrahydro-3aHnaphtho[7,8-d]furan-2,8-dione from methanolic extract of *Dicoma anomala* showed the cytotoxicity against CHO cell line using the MTT assay with potential IC_{50} value of 4.2 μg/ml. The phytocompound of 3-oxoeudesma-1,4(15),11(13)-triene-12,6a-lide from *Dicoma anomala* showed the significant cytotoxicity against (CHO cell line using the MTT assay with an IC_{50} value of 17.2 μM [71].

Dodonaea viscosa (Jacq.) var. augustifolia (L.f) Benth: Dodonaea viscosa (Sapindaceae) is a blossoming plant (**Figure 2F**) in the soapberry family and it has a cosmopolitan distribution in tropical, subtropical, and warm temperate regions of South Africa. This shrub is extensive-

ly grown around the world. The roots bind the soil and thus are useful in sustaining stability in dunes and also curb the soil from getting eroded [72]. A variety of phytocompounds have been recorded with *Dodonaea viscosa,* such as flavonoids, fatty acids, and cyanolipids. A decoction was prepared from the leaf tips emerged newly to treat fever by the Cape settlers. In rural areas, *Dodonaea viscosa* var. *angustifolia* is still commonly used to treat colds, influenza, stomach trouble, and measles. Patients with a strep throat and oral infections caused by fungus gargle the decoction prepared using the leaves. The Khoi-Khoi used a concoction prepared from the roots and is used to treat colds and influenza [73]. Moreover, in Namaqualand, the extract prepared by boiling the leaves, this is then filtered, this extract is used for treating influenza, colds, and it also induces sweating. It is also used to relieve coughs and congested feeling typical of influenza, croup, and diphtheria. The same extract is considered to alleviate stomach ailments and fever [74]. The ethanolic root extract of *Dodonaea viscosa* exhibited a reproducible cell-perniciousness to A2780 ovarian cancer cell line (**Table 2**) with an IC_{50} value of 6.0 μg/ml. Cao et al., (2009) secluded the phytocompounds of two novel triterpenoid saponins from the root of *Dodonaea viscosa* (ethanolic extract) namely Dodonaeaside A and Dodonaeaside B which possess considerable antiproliferative activity on the ovarian cancer cell line of A2780 with IC_{50} values of 0.79 and 0.70 μM correspondingly [75].

Drimia robusta (Hyacinthaceae) is an important medicinal plant (**Figure 2G**) in South Africa because of its extensive usage [76]. The hot water infusions prepared using the pounded bulbs and leaves are used as enema by the Zulus as the leaves are diuretic in action which helps in cleaning the bladder and treat uterus related disease. It also exhibits anticancer, antimicrobial and antimicrobial activities due to the presence of aromatic compounds such as 4-hydroxy-3-methoxybenzoic acid, 3,4-dihydroxybenzoic acid and trans-3-(40-hydroxyphenyl)-2-propenoic acid, these compounds were isolated using ethyl acetate extraction of macerated bulbs [77]. Dichloromethane-methanol extract of *Drimia robusta* (Whole plant) possesses anti-ovarian cancer activity at the IC_{50} value of 1.05 μg/ml in OVCAR-3 cell line (**Table 2**) [55].

Gomphocarpus fruticosus (Linn.) Aiton f. (Apocynaceae), they have other few common names such as swan plant (**Figure 2H**), milkweed, or white cotton, is a perennial herb, spindly shrub, often with watery or milky sap. It is native to South Africa with a wide distribution in most Provinces, including Free State, Gauteng, KwaZulu-Natal, Mpumalanga, Cape (Eastern, Western, Northern), and North West [78]. *Gomphocarpus fruticosus* is used medicinally to treat headaches, stomach pain, tuberculosis, and as an emetic [79]. The acetone extract of *Gomphocarpus fruticosus* root possessed antigonoccol activity [80]. Similarly, the ethanolic extract of the root is reported to have anti-ovarian cancer activity with an IC_{50} value of 3.72 μg/ml in OVCAR-3 cell line (**Table 2**) [55].

Leyssera gnaphaloides (Linn.) L. (Fabaceae) is one of the South African medicinal plants (**Figure 2I**). It is used as a folk medicine medicine to treat various ailments including bronchitis, cough, diarrhoea, fever, and even tuberculosis [81, 82]. An extract was obtained using Hexane, bioactive fractions obtained from the extracts reveal that it possesses cytotoxic effects, however, more than 50% of the ovarian cells of Chinese hamster sustained even at a very high concentration. This result implies that the extract seems to be harmless to the Chinese hamster ovarian cells [83].

Parinari curatellifolia (Planch) ex. Benth. (Chrysobalanaceae) is a tree and is semi-circular in shape almost resembles a mushroom in its canopy and the hues are in blue-green and grey colour (**Figure 3A**). It is an evergreen, medium to large tree, that grows up to thirteen meters, but a height of twenty three-twenty six m also been recorded in certain areas [84]. The leaf extracts and bark are used for treating the symptoms of pneumonia, and eye/ear ailments. Many traditional healers incorporate the bark of *Parinari curatellifolia* in the formulation of their mixture or medicine [85]. The roots are soaked in water for about an hour or six in gelid water, it is used to aid cataract and earache respectively. This roots soaked water are used as eye and ear drops [86]. The bioactive compound, 13-Methoxy-15-oxozoapatlin from the plant, has significant cytotoxic activity against SW626 human ovarian adenocarcinoma cell line (**Table 2**) with the IC_{50} value of 0.6 μM/ml [87].

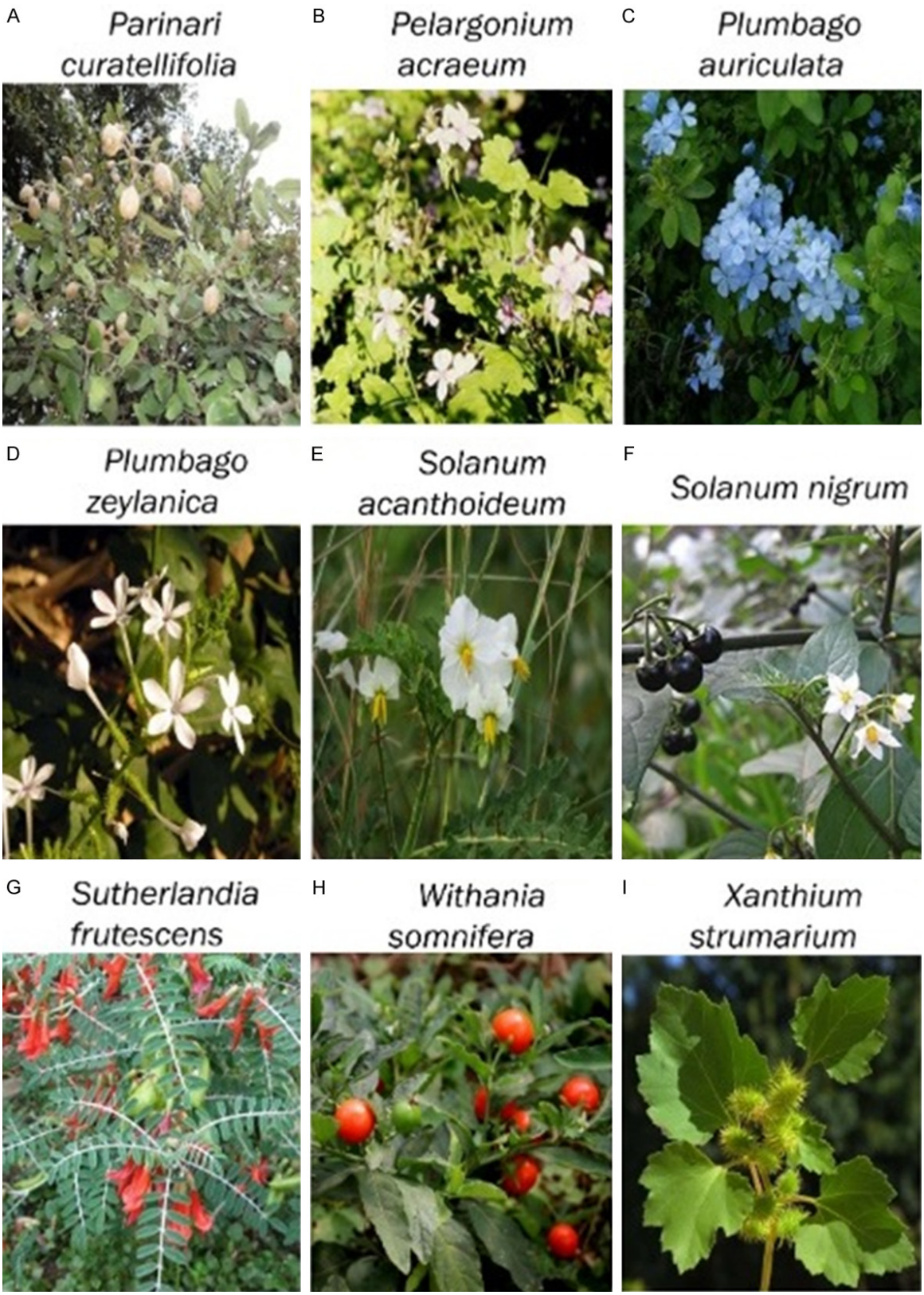

Figure 3. Anti-ovarian cancer potential of South African medicinal plants.

Pelargonium acraeum R.A.Dyer (Geraniaceae) is a small shrub (**Figure 3B**) of South African origin that grows up to 1 m, or occasionally 2 m high. The whole plant extract of *Pelargonium acraeum* has been reported to have anticancer activity. The genus *Pelargonium* is endowed with varieties of flavonoids and alkaloids characterized by antioxidant, antimicrobial, anti-inflammatory, and anticancer activities [88]. The methanolic extract of *Pelargonium acraeum* showed minimum cytotoxic activity with the IC_{50} value of 10 μg/ml and 60 μg/ml in PA1 ovarian cancer cell line after 24 hr and 48 hr respectively of exposure. Additionally, the aqueous extract of this plant showed better anti-ovarian cancer activity with the lowest IC_{50} value of 6.92 μg/ml on OVCAR-3 cell line (**Table 2**) [55].

Plumbago auriculata (Lam.) (Plumbaginaceae) is a medicinal plant and an ornamental shrub with clusters of light blue flowers (**Figure 3C**). it is commonly found in South Africa [89]. It is a rich source of alkaloids such as plumagain (2-methyl-5-hydroxyl, 4-naphthoquinone which could be used as an anti-cancer agent while also exhibiting antibacterial, antioxidant, antifungal, anti-inflammatory and anticoagulant potentials against various diseases such as rheumatism, piles, diarrhoea and skin diseases [90, 91]. The methanolic extract had a minimal cytotoxic activity at 10 μg/ml (24 hr) and 60 μg/ml (48 hr) on PA1 cell lines of human ovarian cancer. Consequently, of note is the significant morphological changes also observed in PA1 cancer cells (**Table 2**) by nuclear staining (4',6-diamidino-2-phenylindole) method [92].

Plumbago zeylanica (Linn.) (Plumbaginaceae) is a perennial herb (**Figure 3D**) commonly distributed across South Africa [93]. The entire plant is used to prepare a variety of folk medicines in Africa, but the roots hold an effective bioactive compound called Plumbagin, it had shown to have anti-malarial, anti-obese, anti-ulcer, antimicrobial, anticancer, anti-inflammatory, antioxidant properties etc. [94]. The chemotherapeutic potential of Plumbagin acts as an anticancer agent in BRCA1-mutated ovarian cancer patients. The mitochondrial membrane is lost, the nucleus gets condensed, DNA gets fragmented and other morphological changes are induced by Plumbagin in ovarian cancer cells. Moreover, it binds to the active site of ER-α and inhibits the classical ER-α signaling pathway in ovarian cancer [95].

Solanum acanthoideum Drege ex Dunal (Solanaceae) is also a medicinal plant (**Figure 3E**) of South African origin traditionally used to treat fever, intestinal infections, asthma, and to heal sores. It is similarly used to stimulate milk production in cows and treat cattle that are affected by gall sickness [79]. The root extract is reported to have anticancer activity in cancer cell lines. Intriguingly, the methanolic root extract of the plant has been reported in a study to possess anti-ovarian cancer activity with the IC_{50} value at 18.62 μg/ml using IGROV1 ovarian cancer cell line (**Table 2**) [55].

Solanum nigrum (Linn.) (Solanaceae) is one of the prominent species (**Figure 3F**) in the genus Solanum regarded as a common, important and one of the largest genera, that comprises about 84 families and 3000 species [96]. South Africa, Eurasia are its native and introduced to America, Australia and Asia. It is also known as black nightshade [97]. The ripe berries are used as food by the natives, while other plant parts are used as traditional medicine. Traditionally, it is used as an analgesic, antispasmodic, antiseptic, antibacterial, antibiofilm, anti dysenteric, antinarcotic, emollient, diuretic, tonic, soporific, laxative, anticancer, antiulcer and also to treat the disarrays of the neuro-vegetative system, etc. All these curative dispositions exhibited by the plant attributed to the alkaloid contents in them [98]. Aqueous extract of *Solanum nigrum* possess an anti-ovarian cancer activity in ovarian cancer cell lines of ES-2, SKOV-3 and OVCAR-3 (**Table 2**) with the significant IC_{50} values of 1.052, 1.779 and 2.000 mg/ml respectively [99, 100].

Sutherlandia frutescens (Linn.) Goldblath & J.C. Manning

Sutherlandia frutescens (**Figure 3G**) were newly referred to as *Lessertia frutescens* subsp. *frutescens* belong to the Fabaceae family, it is the third-largest family of flowering plants. These plants are the habitat of dry areas and are commonly found in South Western and Northern Provinces of Cape [101]. The plant can also be found in other areas of Southern Africa, especially Botswana, Zimbabwe, and Namibia [102]. *Sutherlandia frutescens* enhancing well-being, provide immune support for tuberculosis (TB),

and acquired immune deficiency syndrome (AIDS) as well as in the treatment of cancer; hence, the name cancer bush [103]. Pharmacologically, it is established to have antioxidant, anti-inflammatory, anti-ovarian cancer, and anti-diabetic activities [104].

Withania somnifera (L.) Dunal (Solanaceae) is widespread but not common in all (**Figure 3H**) the Provinces of South Africa but also distributed in Namibia, Botswana, Swaziland, and Lesotho. It grows in a large number of vegetation types from dry areas to areas with reasonably high rainfall, such as coastal vegetation and or grassland [105]. It possesses chemical compounds that exceeds 80 notably alkaloids and steroids (withanolides) are present in *W.somnifera*. Many studies have been performed and the studies disclose the truth about the pivotal deeds namely antibiotic, anti-inflammatory, cytotoxic, anti-tumor, and cholesterol-lowering deeds of these compounds, which are predominantly acquired from leaves and roots [106]. In a study, the supplementation of plant extract reduces the progression of ovarian cancer in the animal model. Moreover, Withaferin A, is a bioactive compound that has been isolated from this plant inhibits the activity of ovarian epithelial cancer cell line (A2780) by 70-80%, also the tumor growth is reduced and metastasis inhibition is also a part of the function of the isolated compound when compared to untreated controls in nude mice [107, 108].

Xanthium strumarium (Linn.) (Asteraceae) is a South African medicinal plant (**Figure 3I**) with global distribution found in abundance in Eurasia and America [109]. The entire plant has been used in the traditional medicine to treat the infections caused by bacteria, high-sugar, itching of the skin, and inflammatory diseases like coryza and rheumatoid arthritis. It has been used included in traditional Chinese medicine for anti-cancer treatment [110]. The fruit extract of the plant contains 3, 4-dihydroxybenzaldehyde investigated to inhibit malignant tumors in human. Two xanthanolide sesquiterpene lactones, 8-epi-xanthatin, and 8-epi-xanthatin-5b-epoxide have been isolated from leaves to inhibit ovarian cancer cell line of SK-OV-3 (**Table 2**) [111, 112].

Conclusion

The role of Medicinal plants in treating Ovarian Cancer is inevitable. Only a very few numbers of plants were been explored and phytochemical studies have been performed among 270,000 plant species. Though there many synthetic medicines are involved to treat various diseases about 3/4th community of the population adhere to the traditional medicines for their primary healthcare needs; however, only a few indigenous medicinal plants of South African have been investigated to their full potential in terms of commercialization. The opportunity for bioprospecting of the medicinal plants and their compounds for novel pharmaceuticals remain largely untapped. This paper addressed the anti-ovarian cancer activity of some of these South African medicinal plants and their bioactive compounds with a view that these medicinal plants are the real sources with less or no side-effect in treating a disease, especially they would create a revolution in combating against the Disease Ovarian Cancer by developing novel leads. This would help an individual to sustain their life.

Acknowledgements

The financial supports received from National Key Research & Development Program in China (Grant No. 2019YFD1002704), Shandong major projects of independent innovation (Grant No. 2019JZZY010722), the Key Research and Development Program of Shandong Province (Grant No. 2017YYSP024), Funds for Innovation Team of Jinan (Grant No. 2018GXRC004), and Special Funds for Taishan Scholars project are acknowledged. Authors also express our thankful to the Department of Plant Sciences, Faculty of Natural and Agricultural Sciences, University of the Free State, QwaQwa, South Africa for completion of this work in fine fulfillment.

Disclosure of conflict of interest

None.

Address correspondence to: Dr. Bo Cui, State Key Laboratory of Biobased Material and Green Papermaking, College of Food Science and Engineering, Qilu University of Technology, Shandong Academy of Science, Jinan 250353, China. Tel: +86-186-60811718; E-mail: cuibopaper@163.com

References

[1] Perumal PC, Sophia D, Raj CA, Ragavendran P, Starlin T and Gopalakrishnan VK. In vitro antioxidant activities and HPTLC analysis of etha-

nolic extract of Cayratia trifolia (L.). Asian Pac J Trop Dis 2012; 2: S952-S956.
[2] Hassan BAR. Medicinal plants (Importance and uses). Pharmaceut Anal Acta 2012; 3: e139.
[3] Ramaswamy L and Kanmani MG. Phytonutrient profile, health benefits and culinary applications of selected edible foliages. Int J Ayurvedic Herb Med 2012; 2: 469-476.
[4] Chakraborty P. Herbal genomics as tools for dissecting new metabolic pathways of unexplored medicinal plants and drug discovery. Biochim Open 2018; 6: 9-16.
[5] Perumal PC, Sowmya S, Pratibha P, Vidya B, Anusooriya P, Starlin T, Ravi S and Gopalakrishnan VK. Isolation, structural characterization and *in silico* drug-like properties prediction of a natural compound from the ethanolic extract of Cayratia trifolia (L.). Pharmacognosy Res 2015; 7: 121-125.
[6] Katiyar C, Gupta A, Kanjilal S and Katiyar S. Drug discovery from plant sources: an integrated approach. AYU (An Int Q J Res Ayurveda) 2012; 33: 10-19.
[7] Harvey AL. Natural products in drug discovery. Drug Discov Today 2008; 13: 894-901.
[8] Cragg GM and Newman DJ. Natural products: a continuing source of novel drug leads. Biochim Biophys Acta 2013; 1830: 3670-3695.
[9] Perumal PC, Sowmya S, Velmurugan D, Sivaraman T and Gopalakrishnan VK. Assessment of dual inhibitory activity of epifriedelanol isolated from Cayratia trifolia against ovarian cancer. Bangladesh J Pharmacol 2016; 11: 545-551.
[10] Ferreira D, Adega F and Chaves R. The Importance of cancer cell lines as in vitro models in cancer methylome analysis and anticancer drugs testing. Oncogenomics and Cancer Proteomics-Novel Approaches in Biomarkers Discovery and Therapeutic Targets in Cancer 2013; 139-166.
[11] Vargo-Gogola T and Rosen JM. Modelling breast cancer: one size does not fit all. Nat Rev Cancer 2007; 7: 659-672.
[12] Greenwell M and Rahman PK. Medicinal plants: their use in anticancer treatment. Int J Pharm Sci Res 2015; 6: 4103-4112.
[13] Coburn SB, Bray F, Sherman ME and Trabert B. International patterns and trends in ovarian cancer incidence, overall and by histologic subtype. Int J Cancer 2017; 140: 2451-2460.
[14] Cortez AJ, Tudrej P, Kujawa KA and Lisowska KM. Advances in ovarian cancer therapy. Cancer Chemother Pharmacol 2018; 81: 17-38.
[15] Torre LA, Trabert B, DeSantis CE, Miller KD, Samimi G, Runowicz CD, Gaudet MM, Ahmedin Jemal A and Siegel RL. Ovarian cancer statistics, 2018. CA Cancer J Clin 2018; 68: 284-296.
[16] Ruibin J, Bo J, Danying W, Chihong Z, Jianguo F and Linhui G. Therapy effects of wogonin on ovarian cancer cells. Biomed Res Int 2017; 2017: 9381513.
[17] Senapati S, Mahanta AK, Kumar S and Maiti P. Controlled drug delivery vehicles for cancer treatment and their performance. Signal Transduct Target Ther 2018; 3: 7.
[18] Chandra A, Pius C, Nabeel M, Nair M, Vishwanatha JK, Ahmad S and Basha R. Ovarian cancer: current status and strategies for improving therapeutic outcomes. Cancer Med 2019; 8: 7018-7031.
[19] Palanisamy CP and Ashafa AOT. Analysis of novel C-X-C Chemokine receptor type 4 (CXCR4) inhibitors from hexane extract of Euclea crispa (Thunb.) Leaves by chemical fingerprint identification and molecular docking analysis. J Young Pharm 2018;10: 173-177.
[20] Poornima K, Perumal PC and Gopalakrishnan VK. Protective effect of ethanolic extract of Tabernaemontana divaricata (L.) R. Br. against DEN and Fe NTA induced liver necrosis in Wistar Albino rats. Biomed Res Int 2014; 2014: 240243.
[21] Guru D, Perumal PC, Kumar K and Gopalakrishnan VK. Dietary evaluation, antioxidant and cytotoxic activity of crude extract from chia seeds (Salvia hispanica L) against human prostate cancer cell line (PC-3). Int J Pharmacogn Phytochem Res 2016; 8: 1358-1362.
[22] Poornima K, Palanisamy CP, Sundaram S and Kanniappan GV. Chromatographic fingerprinting analysis of secondary metabolites present in ethanolic extract of Tabernaemontana divaricata (L.) R. Br. by HPTLC technique. Anal Chem Lett 2017; 7: 20-29.
[23] Sowmya S, Perumal PC, Anusooriya P, Vidya B, Pratibha P and Gopalakrishnan VK. In vitro antioxidant activity, in vivo skin irritation studies and HPTLC analysis of Cayratia trifolia (L.) Domin. Int J Toxicol Pharmacol Res 2015; 7: 1-9.
[24] Palanisamy CP, Kanakasabapathy D and Ashafa AOT. In vitro antioxidant potential of Euclea crispa (Thunb.) leaf extracts. Pharmacognosy Res 2018; 10: 296-300.
[25] Malarvizhi D, Anusooriya P, Meenakshi P, Sowmya S, Perumal PC, Oirere EK and Gopalakrishnan VK. Antioxidant properties and analysis of bioactive compounds present in n-hexane root extract of Zaleya decandra. Int J Pharm Sci Rev Res 2015; 34: 118-123.
[26] Palanisamy CP, Selvarajan R, Balogun FO, Kanakasabapathy D and Ashafa AOT. Antioxidant and antimicrobial activities of (6E, 10E)-2, 6, 24-trimethyl pentacosa-2, 6, 10-triene from Euclea crispa leaves. South African J Bot 2019; 124: 311-319.
[27] Balogun FO, Ashafa AOT, Sabiu S, Ajao AA, Perumal PC, Kazeem MI and Adedeji AA. Pharma-

cognosy: importance and drawbacks. Pharmacogn Med Plants 2019; 1-18.
[28] Palanisamy CP and Ashafa AOT. Screening of potential phytocompounds from Euclea crispa (Thunb.) leaves targeting human epidermal growth factor receptor 2 (HER2) signaling pathway. J Pharm Bioallied Sci 2019; 11: 155-161.
[29] Palanirajan A, Raj CA, Perumal PC, Sundaram S, Balu V, Prabhakaran P and Gopalakrishnan VK. Screening of novel CXC chemokine receptor 4 inhibitors from ethyl acetate extract of alpinia purpurata using GC-MS analysis and its molecular docking studies. Int J Pharmacogn Phytochem Res 2015; 7: 480-488.
[30] Perumal PC, Pratibha P, Sowmya S, Oirere EK, Anusooriya P, Vidya B, Malarvizhi D, Poornima K, Ramkumar S and Gopalakrishnan VK. Discovery of novel inhibitors for HER2 from natural compounds present in Cayratia trifolia (l.): an in silico analysis. Int J Curr Pharm Rev Res 2015; 6: 164-168.
[31] Kuete V, Ango PY, Yeboah SO, Mbaveng AT, Mapitse R, Kapche GD, Ngadjui BT and Efferth T. Cytotoxicity of four Aframomum species (A. arundinaceum, A. alboviolaceum, A. kayserianum and A. polyanthum) towards multi-factorial drug resistant cancer cell lines. BMC Complement Altern Med 2014; 14: 340.
[32] Kuete V, Sandjo LP, Wiench B and Efferth T. Cytotoxicity and modes of action of four Cameroonian dietary spices ethno-medically used to treat cancers: echinops giganteus, xylopia aethiopica, imperata cylindrica and piper capense. J Ethnopharmacol 2013; 149: 245-253.
[33] Kuete V and Efferth T. Pharmacogenomics of Cameroonian traditional herbal medicine for cancer therapy. J Ethnopharmacol 2011; 137: 752-766.
[34] Kuete V, Fankam AG, Wiench B and Efferth T. Cytotoxicity and modes of action of the methanol extracts of six cameroonian medicinal plants against multidrug-resistant tumor cells. Evid Based Complement Alternat Med 2013; 2013: 285903.
[35] Kuete V, Voukeng IK, Tsobou R, Mbaveng AT, Wiench B, Beng VP and Efferth T. Cytotoxicity of Elaoephorbia drupifera and other Cameroonian medicinal plants against drug sensitive and multidrug resistant cancer cells. BMC Complement Altern Med 2013; 13: 250.
[36] Omosa LK, Midiwo JO, Masila VM, Gisacho BM, Munayi R, Francisca-Kamakama, Chemutai KP, Elhaboob G, Saeed ME, Hamdoun S, Kuete V and Efferth T. Cytotoxicity of 91 Kenyan indigenous medicinal plants towards human CCRF-CEM leukemia cells. J Ethnopharmacol 2016; 179: 177-196.
[37] Baek J, Lee D, Lee TK, Song JH, Lee JS, Lee S, Yoo SW, Kang KS, Moon E, Lee S and Kim KH. (-)-9'-O-(α-L-Rhamnopyranosyl)lyoniresinol from Lespedeza cuneata suppresses ovarian cancer cell proliferation through induction of apoptosis. Bioorganic Med Chem Lett 2018; 28: 122-128.
[38] Zhao W, Li N, Zhang X, Wang W, Li J and Si Y. Cancer chemopreventive theasaponin derivatives from the total tea seed saponin of Camellia sinensis. J Funct Foods 2015; 12: 192-198.
[39] Seo JH, Jeong KJ, Oh WJ, Sul HJ, Sohn JS, Kim YK, Cho DY, Kang JK, Park CG and Lee HY. Lysophosphatidic acid induces STAT3 phosphorylation and ovarian cancer cell motility: their inhibition by curcumin. Cancer Lett 2010; 288: 50-56.
[40] Segun PA, Ogbole OO and Ajaiyeoba EO. Medicinal plants used in the management of cancer among the ijebus of southwestern Nigeria. J Herb Med 2018; 14: 68-75.
[41] Olujimi OO, Bamgbose O, Arowolo T, Steiner O and Goessler W. Elemental profiles of herbal plants commonly used for cancer therapy in Ogun State, Nigeria. Part I. Microchem J 2014; 117: 233-241.
[42] Ntie-Kang F, Onguéné PA, Lifongo LL, Ndom JC, Sippl W and Mbaze LM. The potential of antimalarial compounds derived from African medicinal plants, part II: a hpharmacological evaluation of non-alkaloids and non-terpenoids. Malar J 2014; 13: 81.
[43] Becker JV, Van Der Merwe MM, Van Brummelen AC, Pillay P, Crampton BG, Mmutlane EM, Parkinson C, Heerden FR, Crouch NR, Smith PJ, Mancama DT and Maharaj VJ. In vitro antiplasmodial activity of dicoma anomala subsp. gerrardii (asteraceae): identification of its main active constituent, structure-activity relationship studies and gene expression profiling. Malar J 2011; 10: 295.
[44] Babiaka SB, Ntie-Kang F, Lifongo LL, Ndingkokhar B, Mbah JA and Yong JN. The chemistry and bioactivity of Southern African flora I: a bioactivity versus ethnobotanical survey of alkaloid and terpenoid classes. RSC Adv 2015; 5: 43242-43267.
[45] Khorombi T, Fouché G, Kolesnikova N, Maharaj V, Nthambeleni R and Merwe M. Investigation of South African plants for anti cancer properties. Pharmacologyonline 2006; 3: 494-500.
[46] McKay DL and Blumberg JB. A review of the bioactivity of South African herbal teas: Rooibos (Aspalathus linearis) and honeybush (Cyclopia intermedia). Phyther Res 2007; 21: 1-16.
[47] Van-Wyk BE. The potential of South African plants in the development of new medicinal products. South African J Bot 2011; 77: 812-829.
[48] Joubert E and De-Beer D. Rooibos (Aspalathus linearis) beyond the farm gate: from herbal tea

to potential phytopharmaceutical. South African J Bot 2011; 77: 869-886.
[49] Fantoukh OI, Dale OR, Parveen A, Hawwal MF, Ali Z, Manda VK, Khan SI, Chittiboyina AG, Viljoen A and Khan IA. Safety assessment of phytochemicals derived from the globalized South African rooibos tea (Aspalathus linearis) through interaction with CYP, PXR, and P-gp. J Agric Food Chem 2019; 67: 4967-4975.
[50] Johnson R, Shabalala S, Louw J, Kappo AP and Muller CJF. Aspalathin reverts doxorubicin-induced cardiotoxicity through increased autophagy and decreased expression of p53/mTOR/p62 signaling. Molecules 2017; 22: 1589.
[51] Marnewick J, Joubert E, Joseph S, Swanevelder S, Swart P and Gelderblom W. Inhibition of tumour promotion in mouse skin by extracts of rooibos (Aspalathus linearis) and honeybush (Cyclopia intermedia), unique South African herbal teas. Cancer Lett 2005; 224: 193-202.
[52] Sissing L, Marnewick J, De Kock M, Swanevelder S, Joubert E and Gelderblom W. Modulating effects of rooibos and honeybush herbal teas on the development of esophageal papillomas in rats. Nutr Cancer 2011; 63: 600-610.
[53] Marnewick JL, van der Westhuizen FH, Joubert E, Swanevelder S, Swart P and Gelderblom WC. Chemoprotective properties of rooibos (Aspalathus linearis), honeybush (Cyclopia intermedia) herbal and green and black (Camellia sinensis) teas against cancer promotion induced by fumonisin B1 in rat liver. Food Chem Toxicol 2009; 47: 220-229.
[54] Thomas AD and Dougill AJ. Distribution and characteristics of cyanobacterial soil crusts in the Molopo Basin, South Africa. J Arid Environ 2006; 64: 270-283.
[55] Fouche G, Cragg GM, Pillay P, Kolesnikova N, Maharaj VJ and Senabe J. In vitro anticancer screening of South African plants. J Ethnopharmacol 2008; 119: 455-461.
[56] Wabe NT. Chemistry, pharmacology, and toxicology of khat (catha edulis forsk): a review. Addict Heal 2011; 3: 137-149.
[57] Al-Alimi KR, Abdul Razak AA, Saub R and Alabsi AM. Tannins acid, ascorbic acid and fluoride from khat chewing plant. Int J Dent Oral Heal 2017; 3: 4.
[58] Getasetegn M. Chemical composition of Catha edulis (khat): a review. Phytochem Rev 2016; 15: 907-920.
[59] Al-Zubairi AS. Genotoxicity assessment of fresh Khat leaves extract in Chinese hamster ovary cell lines. J Med Sci 2017; 17: 126-132.
[60] Alsanosy R, Alhazmi HA, Sultana S, Abdalla AN, Ibrahim Y, Al Bratty M, Banji D, Khardali I and Khalid A. Phytochemical screening and cytotoxic properties of ethanolic extract of young and mature khat leaves. J Chem 2020; 2020: 7897435.
[61] Elhag H, Mossa JS and El-olemy MM. Antimicrobial and cytotoxic activity of the extracts of khat callus cultures. Perspect new crop new uses 1999; (Mic): 463-466.
[62] Oyedeji OA and Afolayan AJ. Chemical composition and antibacterial activity of the essential oil of Centella asiatica growing in South Africa. Pharm Biol 2005; 43: 249-252.
[63] Yao CH, Yeh JY, Chen YS, Li MH and Huang CH. Wound-healing effect of electrospun gelatin nanofibres containing Centella asiatica extract in a rat model. J Tissue Eng Regen Med 2017; 11: 905-915.
[64] Naidoo DB, Phulukdaree A, Anand K, Sewram V and Chuturgoon AA. Centella asiatica fraction-3 suppresses the nuclear factor erythroid 2-related factor 2 anti-oxidant pathway and enhances reactive oxygen species-mediated cell death in cancerous lung A549 cells. J Med Food 2017; 20: 959-968.
[65] Somboonwong J, Kankaisre M, Tantisira B and Tantisira MH. Wound healing activities of different extracts of Centella asiatica in incision and burn wound models: an experimental animal study. BMC Complement Altern Med 2012; 12: 103.
[66] Ren L, Cao QX, Zhai FR, Yang SQ and Zhang HX. Asiatic acid exerts anticancer potential in human ovarian cancer cells via suppression of PI3K/Akt/mTOR signalling. Pharm Biol 2016; 54: 2377-2382.
[67] Balogun FO, Tshabalala NT and Ashafa AOT. Antidiabetic medicinal plants used by the basotho tribe of eastern free state: a review. J Diabetes Res 2016; 2016: 4602820.
[68] Asfaw N and Demissew S. Handbook of African medicinal plants. Econ Bot 1994; 1-508.
[69] Balogun FO and Ashafa AOT. Aqueous root extracts of Dicoma anomala (Sond.) extenuates postprandial hyperglycaemia in vitro and its modulation on the activities of carbohydrate-metabolizing enzymes in streptozotocin-induced diabetic Wistar rats. South African J Bot 2017; 112: 102-111.
[70] Bohlmann F, Singh P and Jakupovic J. New germacranolides and other sesquiterpene lactones from Dicoma species. Phytochemistry 1982; 21: 2029-2033.
[71] Maroyi A. *Dicoma anomala* sond.: a review of its botany, ethnomedicine, phytochemistry and pharmacology. Asian J Pharm Clin Res 2018; 11: 70-77.
[72] Lawal D and Yunusa I. *Dodonea viscosa* linn: its medicinal, pharmacological and phytochemical properties. Int J Innov Appl Stud 2013; 2: 477-483.

[73] Getie M, Gebre-Mariam T, Rietz R and Neubert RH. Evaluation of the release profiles of flavonoids from topical formulations of the crude extract of the leaves of *Dodonea viscosa* (Sapindaceae). Pharmazie 2002; 57: 320-322.
[74] Colodel EM, Traverso SD, Seitz AL, Correa A, Oliveira FN, Driemeier D and Gava A. Spontaneous poisoning by *Dodonea viscosa* (Sapindaceae) in cattle. Vet Hum Toxicol 2003; 45: 147-148.
[75] Cao S, Brodie P, Callmander M, Randrianaivo R, Razafitsalama J, Rakotobe E, Rasamison VE, Dyke KT, Shen Y, Suh EM and Kingston DG. Antiproliferative triterpenoid saponins of *Dodonaea wiscosa* from the madagascar dry forest. J Nat Prod 2009; 72: 1705-1707.
[76] Ngugi GW, Jäger AK and Van-Staden J. *In vitro* propagation of *Drimia robusta* Bak. South African J Bot 1998; 64: 266-268.
[77] Xego S, Kambizi L and Nchu F. Threatened medicinal plants of South Africa: case of the family hyacinthaceae. African J Tradit Complement Altern Med 2016; 13: 169-180.
[78] van-Wyk BE. A broad review of commercially important southern African medicinal plants. J Ethnopharmacol 2008; 119: 342-355.
[79] Scott LC. The medicinal and poisonous plants of Southern Africa. Am J Trop Med Hyg 1933; 2: 112.
[80] Goyder DJ and Nicholas A. A revision of *Gomphocarpus* R. Br. (Apocynaceae: Asclepiadeae). Kew Bull 2001; 56: 769-836.
[81] Green E, Samie A, Obi CL, Bessong PO and Ndip RN. Inhibitory properties of selected South African medicinal plants against Mycobacterium tuberculosis. J Ethnopharmacol 2010; 130: 151-157.
[82] Tsichritzis F and Jakupovic J. Diterpenes from *Leyssera gnaphaloides*. Phytochemistry 1991; 30: 211-213.
[83] Bamuamba K, Gammon DW, Meyers P, Dijoux-Franca MG and Scott G. Anti-mycobacterial activity of five plant species used as traditional medicines in the Western Cape Province (South Africa). J Ethnopharmacol 2008; 117: 385-390.
[84] Ogbonnia SO, Adekunle A, Olagbende-Dada SO, Anyika EN, Enwuru VN and Orolepe M. Assessing plasma glucose and lipid levels, body weight and acute toxicity following oral administration of an aqueous ethanolic extract of *Parinari curatellifolia* Planch, (Chrysobalanaceae) seeds in alloxan-induced diabetes in rats. African J Biotechnol 2008; 7: 2998-3003.
[85] Lee IS, Shamon LA, Chai HB, Chagwedera TE, Besterman JM, Farnsworth NR, Gordell GA, Pezzuto JM and Kinghorn AD. Cell-cycle specific cytotoxicity mediated by rearranged entkaurene diterpenoids isolated from *Parinari curatellifolia*. Chem Biol Interact 1996; 99: 193-204.
[86] Olaleye MT, Amobonye AE, Komolafe K and Akinmoladun AC. Protective effects of *Parinari curatellifolia* flavonoids against acetaminophen-induced hepatic necrosis in rats. Saudi J Biol Sci 2014; 21: 486-492.
[87] Mi Q, Lantvit D, Reyes-Lim E, Chai H, Zhao W, Lee IS, Peraza-Sánchez S, Ngassapa O, Kardono LBS, Riswan S, Hollingshead GM, Mayo JG, Farnsworth NR, Cordell GA, Kinghorn AD and Pezzuto JM. Evaluation of the potential cancer chemotherapeutic efficacy of natural product isolates employing *in vivo* hollow fiber tests. J Nat Prod 2002; 65: 842-850.
[88] Williams CA, Harborne JB, Newman M, Greenham J and Eagles J. Chrysin and other leaf exudate flavonoids in the genus Pelargonium. Phytochemistry 1997; 46: 1349-1353.
[89] Karishma S, Yougasphree N and Baijnath H. A comprehensive review on the genus plumbago with focus on plumbago (Plumbaginaceae). Afr J Tradit Complement Altern Med 2018; 15: 199-215.
[90] Min Y, Wang J, Yang J and Liu W. Chemical constituents of *Plumbago zeylanica* L. In: Advanced Materials Research. 2011; 310: 1662-1664.
[91] Dorni AIC, Vidyalakshmi KS, Vasanthi HR and Rajamanickam GV. HPTLC Method for the quantification of plumbagin in three plumbago species. Res J Phytochem 2007; 1: 46-51.
[92] Lakshmanan G, Bupesh G, Vignesh A, Sathiyaseelan A and Murugesan K. Micropropagation and anticancer activity of methanolic extract of *Plumbago auriculata* Lam. Int J Adv Biotechnol Res 2016; 7: 2001-2011.
[93] Chauhan M. A review on Morphology, Phytochemistry and Pharmacological activities of medicinal herb *Plumbago Zeylanica* Linn. J Pharmacogn Phytochem 2014; 3: 95-118.
[94] Ankita Sharma and Nimali Singh. A multifarious potent herb*: plumbago zeylanica* - a mini review. Int J Recent Sci Res 2015; 6: 4825-4829.
[95] Thasni KA, Rakesh S, Rojini G, Ratheeshkumar T, Srinivas G and Priya S. Estrogen-dependent cell signaling and apoptosis in BRCA1-blocked BG1 ovarian cancer cells in response to plumbagin and other chemotherapeutic agents. Ann Oncol 2008; 19: 696-705.
[96] Huang HC, Syu KY and Lin JK. Chemical composition of *Solanum nigrum* linn extract and induction of autophagy by leaf water extract and its major flavonoids in AU565 breast cancer cells. J Agric Food Chem 2010; 58: 8699-8708.
[97] Shokrzadeh M, Azadbakht M, Ahangar N, Hashemi A and Saravi SS. Cytotoxicity of hydro-

alcoholic extracts of Cucurbita pepo and *Solanum nigrum* on HepG2 and CT26 cancer cell lines. Pharmacogn Mag 2010; 6: 176-179.
[98] Malaikozhundan B, Vijayakumar S, Vaseeharan B, Jenifer AA, Chitra P, Prabhu NM and Kannapiran E. Two potential uses for silver nanoparticles coated with *Solanum nigrum* unripe fruit extract: biofilm inhibition and photodegradation of dye effluent. Microb Pathog 2017; 111: 316-324.
[99] Tai CJ, Wang CW, Chen CL, Wang CK, Chang YJ, Jian JY, Lin CS, Tai CJ and Tai CJ. Cisplatin-, doxorubicin-, and docetaxel-induced cell death promoted by the aqueous extract of solanum nigrum in human ovarian carcinoma cells. Integr Cancer Ther 2015; 14: 546-555.
[100] Lee SJ, Oh PS, Ko JH, Lim K and Lim KT. A 150-kDa glycoprotein isolated from Solanum nigrum L. has cytotoxic and apoptotic effects by inhibiting the effects of protein kinase C alpha, nuclear factor-kappa B and inducible nitric oxide in HCT-116 cells. Cancer Chemother Pharmacol 2004; 54: 562-572.
[101] Aboyade OM, Styger G, Gibson D and Hughes G. Sutherlandia frutescens: the meeting of science and traditional knowledge. J Altern Complement Med 2014; 20: 71-76.
[102] Vuuren SF. Antimicrobial activity of South African medicinal plants. J Ethnopharmacol 2008; 119: 462-472.
[103] Tai J, Cheung S, Chan E and Hasman D. In vitro culture studies of Sutherlandia frutescens on human tumor cell lines. J Ethnopharmacol 2004; 93: 9-19.
[104] Chinkwo KA. Sutherlandia frutescens extracts can induce apoptosis in cultured carcinoma cells. J Ethnopharmacol 2005; 98: 163-170.
[105] Mishra LC, Singh BB and Dagenais S. Scientific basis for the therapeutic use of Withania somnifera (ashwagandha): a review. Altern Med Rev 2000; 5: 334-346.
[106] Rodríguez-Burford C, Barnes MN, Berry W, Partridge EE and Grizzle WE. Immunohistochemical expression of molecular markers in an avian model: a potential model for preclinical evaluation of agents for ovarian cancer chemoprevention. Gynecol Oncol 2001; 81: 373-379.
[107] Barua A, Bradaric MJ, Bitterman P, Abramowicz JS, Sharma S, Basu S, Lopez H and Bahr JM. Dietary supplementation of ashwagandha (Withania somnifera, Dunal) enhances NK cell function in ovarian tumors in the laying hen model of spontaneous ovarian cancer. Am J Reprod Immunol 2013; 70: 538-550.
[108] Kakar SS, Ratajczak MZ, Powell KS, Moghadamfalahi M, Miller DM, Batra SK and Singh SK. Withaferin a alone and in combination with cisplatin suppresses growth and metastasis of ovarian cancer by targeting putative cancer stem cells. PLoS One 2014; 9: e107596.
[109] McMillan C, Chavez PI, Plettman SG and Mabry TJ. Systematic implications of the sesquiterpene lactones in the "strumarium" morphological complex (Xanthium strumarium, Asteraceae) of Europe, Asia and Africa. Biochem Syst Ecol 1975; 2: 181-184.
[110] Panda SK and Luyten W. Antiparasitic activity in Asteraceae with special attention to ethnobotanical use by the tribes of Odisha, India. Parasite 2018; 25: 10.
[111] Al-Mekhlafi FA, Abutaha N, Mashaly AMA, Nasr FA, Ibrahim KE and Wadaan MA. Biological activity of Xanthium strumarium seed extracts on different cancer cell lines and Aedes caspius, Culex pipiens (Diptera: Culicidae). Saudi J Biol Sci 2017; 24: 817-821.
[112] Sánchez-Lamar A, Piloto-Ferrer J, Fiore M, Stano P, Cozzi R, Tofani D, Cundari E, Francisco M, Romero A, Gonzalez ML and Degrassi F. Xanthium strumarium extract inhibits mammalian cell proliferation through mitotic spindle disruption mediated by xanthatin. J Ethnopharmacol 2016; 194: 781-788.
[113] Gallelli L. Escin: a review of its anti-edematous, antiinflammatory, and venotonic properties. Drug Des Devel Ther 2019; 13: 3425-3437.
[114] León F, Habib E, Adkins JE, Furr EB, McCurdy CR and Cutler SJ. Phytochemical characterization of the leaves of Mitragyna speciosa grown in USA. Nat Prod Commun 2009; 4: 907-910.
[115] Neag MA, Mocan A, Echeverría J, Pop RM, Bocsan CI, Crisan G and Buzoianu AD. Berberine: Botanical Occurrence, traditional uses, extraction methods, and relevance in cardiovascular, metabolic, hepatic, and renal disorders. Front Pharmacol 2018; 9: 557.
[116] Kumar A, Sharma PR and Mondhe DM. Potential anticancer role of colchicine-based derivatives: an overview. Anticancer Drugs 2017; 28: 250-262.
[117] Kaliyadasa E and Samarasinghe BA. A review on golden species of Zingiberaceae family around the world: genus Curcuma. Afr J Agric Res 2019; 14: 519-531.
[118] Akinboye ES and Bakare O. Biological Activities of Emetine. Open Nat Prod J 2011; 4: 8-15.
[119] Mahmoud AM, Bautista RJ, Sandhu MA and Hussein OE. Beneficial effects of citrus flavonoids on cardiovascular and metabolic health. Oxid Med Cell Longev 2019; 2019: 5484138.
[120] Pires TC, Dias MI, Calhelha RC, Carvalho AM, Queiroz MJ, Barros L and Ferreira IC. Bioactive properties of Tabebuia impetiginosa-based phytopreparations and phytoformulations: a comparison between extracts and dietary supplements. Molecules 2015; 20: 22863-22871.

[121] Rahman S, Ansari RA, Rehman H, Parvez S and Raisuddin S. Nordihydroguaiaretic acid from creosote bush (Larrea tridentata) mitigates 12-O-tetradecanoylphorbol-13-acetate-induced inflammatory and oxidative stress responses of tumor promotion cascade in mouse skin. Evid Based Complement Alternat Med 2011; 2011: 734785.

[122] Achan J, Talisuna AO, Erhart A, Yeka A, Tibenderana JK, Baliraine FN, Rosenthal PJ and Alessandro UD. Quinine, an old anti-malarial drug in a modern world: role in the treatment of malaria. Malar J 2011; 10: 144.

catalysts

MDPI

Article

One-Pot Synthesis of 7, 7-Dimethyl-4-Phenyl-2-Thioxo-2,3,4,6,7, 8-Hexahydro-1H-Quinazoline-5-OnesUsing Zinc Ferrite Nanocatalyst and Its Bio Evaluation

Tentu Nageswara Rao [1], Nalla Krishnarao [1], Faheem Ahmed [2,*], Suliman Yousef Alomar [3,*], Fadwa Albalawi [4], Panagal Mani [5], Abdullah Aljaafari [2], Botsa Parvatamma [6], Nishat Arshi [7] and Shalendra Kumar [2,8]

1 Department of Chemistry, Krishna University, Machilipatnam, Andhra Pradesh 521001, India; tnraochemistry@gmail.com (T.N.R.); nkrishnarao@gmail.com (N.K.)
2 Department of Physics, College of Science, King Faisal University, Hofuf, Al-Ahsa 31982, Saudi Arabia; aaljaafari@kfu.edu.sa (A.A.); sjagdish@kfu.edu.sa (S.K.)
3 Doping Research Chair, Zoology Dept, College of Science, King Saud University, Riyadh 11451, Saudi Arabia
4 Zoology Department, College of Science, King Saud University, Riyadh 11451, Saudi Arabia; Fadwa_saad@hotmail.com
5 Department of Biotechnology, Annai College of Arts&Science, Kumbakonam, Tamil Nadu 612503, India; master.maniji@gmail.com
6 Department of Organic Chemistry, GayathriP.G Courses, Gotlam, Vizianagaram 530045, India; Parvathi1787@rediffmail.com
7 Department of Basic Sciences, Preparatory Year Deanship, King Faisal University, Hofuf, Al-Ahsa 31982, Saudi Arabia; nshastri@kfu.edu.sa
8 Department of Physics, School of Engineering, University of Petroleum & Energy Studies, Dehradun 248007, India
* Correspondence: fahmed@kfu.edu.sa (F.A.); syalomar@ksu.edu.sa (S.Y.A.)

check for updates

Citation: Rao, T.N.; Krishnarao, N.; Ahmed, F.; Alomar, S.Y.; Albalawi, F.; Mani, P.; Aljaafari, A.; Parvatamma, B.; Arshi, N.; Kumar, S. One-Pot Synthesis of 7, 7-Dimethyl-4-Phenyl-2-Thioxo-2,3,4,6,7, 8-Hexahydro-1H-Quinazoline-5-OnesUsing Zinc Ferrite Nanocatalyst and Its Bio Evaluation. *Catalysts* **2021**, *11*, 431. https://doi.org/10.3390/catal11040431

Academic Editors: Maria Manuel B. Marques and Ana Sofia Santos

Received: 16 March 2021
Accepted: 24 March 2021
Published: 27 March 2021

Abstract: A simple and highly efficient protocol for the synthesis of derivatives 7, 7-dimethyl-4-phenyl-2-thioxo-2, 3, 4, 6, 7, 8-hexahydro-1H-quinazoline-5-one from 5, 5-dimethyl cyclohexane-1, 3-dione (**4a**–**4h**) (dimedone) has been described. The aryl aldehydes were substituted with thiourea in the presence of synthesized zinc ferrite nanocatalyst, which increased the yield under reflux through condensation, followed by cyclization to give desired products. The other advantages are that it is eco-friendly and economically affordable for large-scale production. Structural validation and characterization of all the newly synthesized compounds were evaluated by spectral analysis (mass spectrometry, proton nuclear magnetic resonance (^{1}HNMR), and Carbon-13 nuclear magnetic resonance(^{13}CNMR)spectroscopies. The structure of antibacterial and antifungal assays was performed with the newly synthesized compounds. The antimicrobial activity of title compounds possessing electron-withdrawing groups such as (**4e**–**4h**) (Cl, Br, and cyano group) exhibited more active potential than the electron-donating groups, C_6H_5,4-C_6H_4, 3-OC_2H_5-4OH-C_6H_3, etc., (**4a**–**4d**) containing moiety.

Keywords: dimedone; aryl aldehydes; zinc ferrite; bio evaluation; structural validation; NMR

1. Introduction

Multicomponent reaction (MCR) is the most powerful and efficient technique in modern synthetic organic chemistry. The advantages of these reactions in synthetic organic chemistry are the valuable characteristics such as constructing desired compounds, straightforward reaction design, atom economy, and the simple purification of target products. MCRs with heterocyclic moiety are particularly useful for the construction of drug-like molecules [1–3]. In the recent past, the six-membered heterocyclic compounds such as hexahydroquinazolinones in medicinal chemistry and synthetic organic chemistry are of special interest. The main focus on the synthesis of derivatives of 7,7-dimethyl-4-phenyl-2-thioxo-1,2,3,4,6,7,8-hexahydro-1H-quinazoline-5-ones has considerably attracted

attention in recent years due to their potential, antioxidant [4], antifungal, antibacterial, antitumor, and antitubercular activity [5] with wide applications, including anticonvulsant, sedative, tranquilizer, analgesic [6,7], antimicrobial, anesthetic [8], anticancer [9], antihypertensive [10], anti-inflammatory [11], diuretic [12], and muscle relaxant properties [13]. The various organic transformation reactions were employed by the use of trimethylsilyl chloride [14]. There are few reports for the synthesis of octa hydro quinazolinone derivatives using catalysts such as concentrated H_2SO_4 [15], Nafion-H [16], NH_4VO_3 [17], silica-sulfuric acid [18], and also in ionic liquids [HMIM] H_2SO_4 in presence of TMSCl [19], [BMIM]Br-[BMIM]BF_4 [20], and $ZrOCl_2$. $8H_2O$ [21]. This article tends to report the synthesis of 7, 7-dimethyl-4-phenyl-2-thioxo-2, 3, 4, 6, 7, 8-hexahydro-1H-quinazolin-5-ones using nanocatalyst. Lanthanum doped Ni0.6Zn0.2Fe2-XLaXO4 (x = 0.075) ferrite was developed by Amol et al. This ferrite has a spinal cubic structure and a lattice constant of 8.486. The Ferro-spinal sample was used as a magnetically recoverable heterogeneous catalyst [22]. Triethanolamine has a significant impact on the morphology of nano-ZnO catalyst. For the synthesis of coumarin derivatives, we developed an efficient, simple, and environmentally friendly synthetic methodology [23]. Catalytic reactions ensure high regio- and stereoselectivity of chemical transformations. In recent years, several novel catalytic systems were developed for the selective formation of carbon–heteroatom and carbon–carbon bonds [24]. The use of green nanocatalyst for the synthesis of various heterocycles has advantages such as short reaction time, high yield, inexpensive chemical usage, easy work-up procedure, and specific reaction [25]. The Michael addition reaction and cyclodehydration, followed by dimedone with various substituted aryl aldehydes and thioureain the presence of nanocatalystgive 7,7-dimethyl-4-phenyl-2-thioxo-2,3,4,6,7,8-hexahydro-1H-quinazolin-5-ones, were performed (Scheme 1). A pilot reaction using substituted aryl aldehyde (1), dimedone (2), and thiourea (3) in the presence of nanocatalyst and the structure and antagonistic properties of the synthesized compounds were also studied, in addition to studying the further development of derivatives.

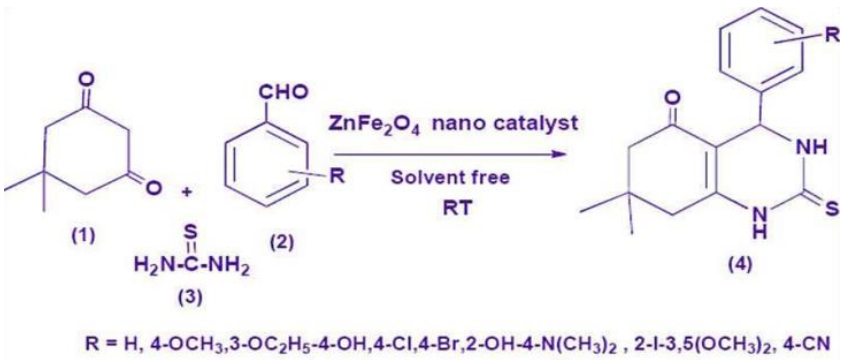

Scheme 1. Synthesisof 7, 7-dimethyl-4-phenyl-2-thioxo-2, 3,4,6,7, 8-hexahydro-1H-quinazolin-5-ones using zinc ferrite.

2. Results

2.1. XRD Pattern of $ZnFe_2O_4$ NPs

The X-ray diffraction (XRD) pattern of $ZnFe_2O_4$(Figure 1) shows clear diffraction peaks. The diffraction peak of the powder sample was indexed according to Joint Committee on Powder Diffraction Standards (JCPDS) card no. 22-1012. The material crystallized in a cubic unit cell with space group Fd-3m(Figure 2). The structure was refined by the Rietveld refinement method with the Fullprof software package using the single-phase Fd-3m diffraction data. The unit cell parameters (Table 1) of the crystallite size of the sample were calculated from the most intense diffraction by using Scherrer's formula. The Scherrer method (using full width at half maximum (FWHM)) calculates the ratio of the thickness's root-mean-fourthpower to its root-mean-square value. We illustrated that the Scherrer equation's calculation of crystallite size is accurate by comparing it to X-ray

diffraction peaks produced by the dynamical theory. In terms of crystalline size and Bragg angle, we also established the range of validity of the acceptable Scherrer equation.

$$D = \frac{K\lambda}{\beta cos\theta}, \quad (1)$$

where K is dimensionless shape factor and generally taken 0.94 for spherical particles, λ is the wavelength of X-ray used ($Cu - K_{\alpha}$ = 1.540 Å), and β and θ are the full widths of half maxima and diffraction angle of corresponding diffraction peak.

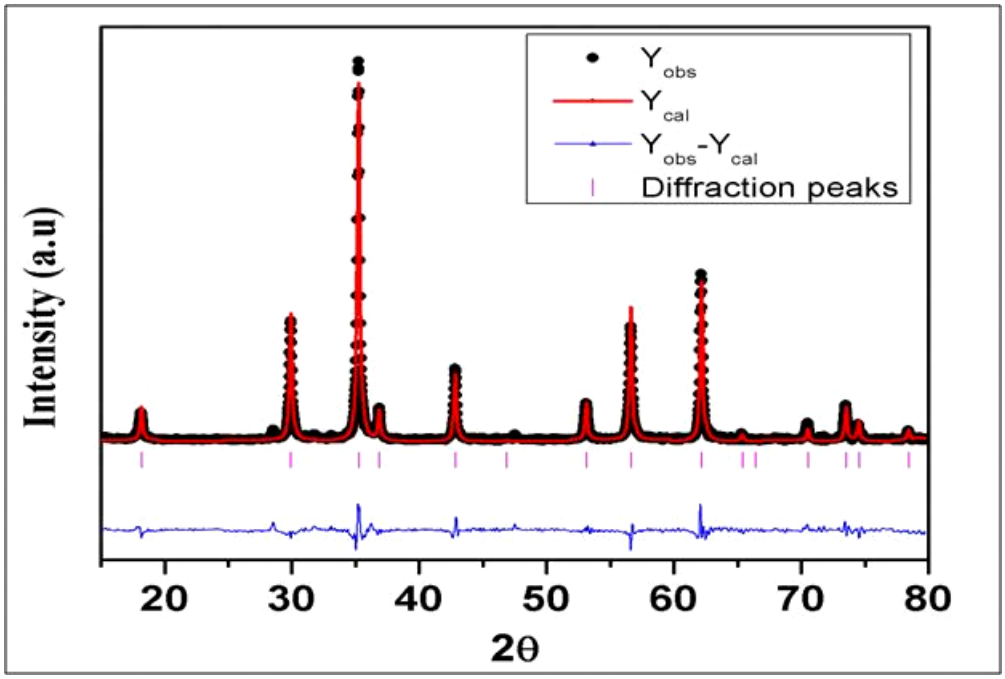

Figure 1. X-ray diffraction (XRD) pattern of ZnFe2O4 NPs.

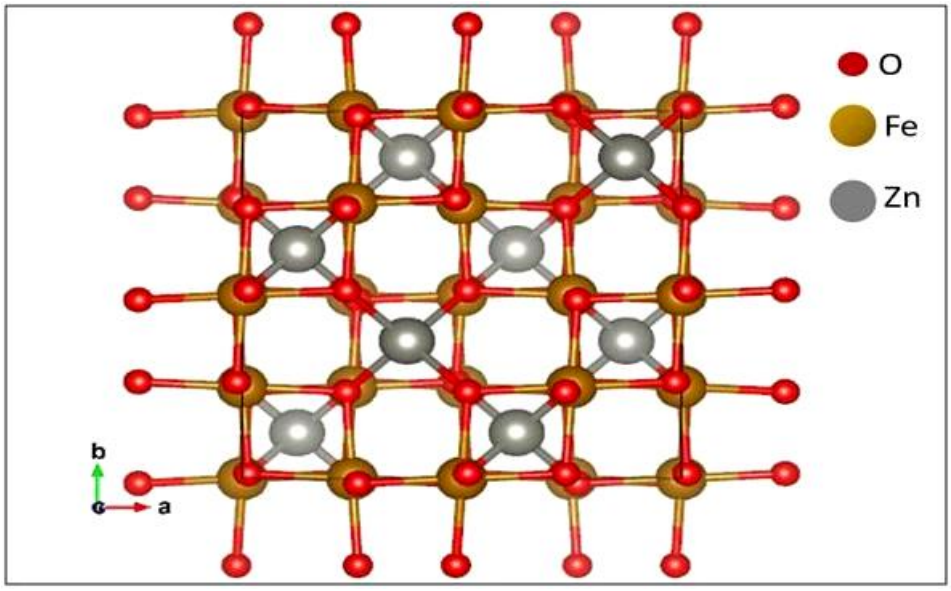

Figure 2. Crystalized in a cubic unit cell of $ZnFe_2O_4$ NPs.

Table 1. Refined unit cells parameters of $ZnFe_2O_4$ nanoparticles.

Atom	x	y	z	Occ.	B_{iso}	Site	Sym.
Zn	0.125	0.125	0.125	1	0.024	8a	43 m
Fe	0.5	0.5	0.5	1.035	0.009	16d	3 m
O	0.26335	0.26335	0.26335	1.038	0.016	32e	3 m
Unit cell Parameters	a = b = c = 8.43695 Å α = β = γ = 90°						
Unit cell Volume	600.559 $Å^3$						
R_p (%)	12.1						
R_{wp} (%)	18.3						
χ^2	2.02						
Fe-O	2.00295 Å						
Zn-O	2.02174 Å						

The average crystallite size of the powder sample was estimated in the close approximation of 39.16 nm. The difference between the calculated and observed data in the Rietveld refinement method elucidates the goodness of fit (χ^2) of the diffraction pattern. The minimal χ^2 value achieved for the synthesized $ZnFe_2O_4$ sample was 2.02, which is implicit in the observed XRD pattern. The lower χ^2 of refined XRD pattern indicates the single-phase and high purity of prepared $ZnFe_2O_4$ nanoparticles.

2.2. SEM Analysis of $ZnFe_2O_4$ NPs

The surface morphology of the acquired $ZnFe_2O_4$ (NPs) was documented using a scanning electron microscope (FESEM) (Figure 3). The FESEM image indicated that the $ZnFe_2O_4$ (NPs) have a smooth surface, and the agglomeration of NPs is also visible there.

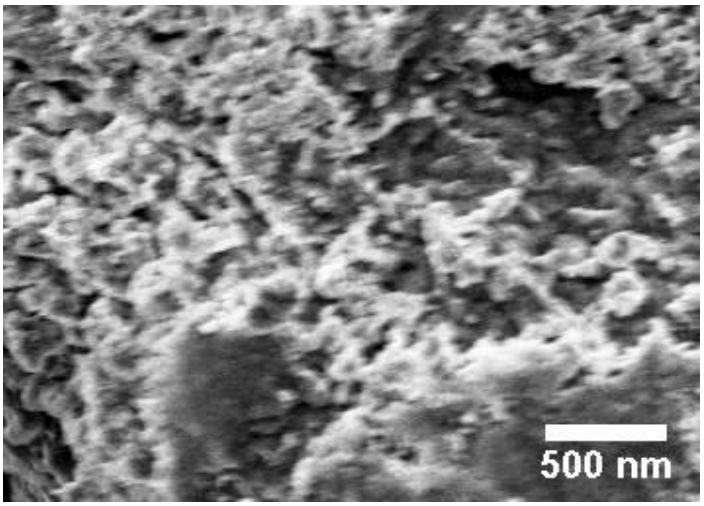

Figure 3. Field emission scanning electron microscopy (FESEM) image of $ZnFe_2O_4$ NPs.

2.3. HRTEM Analysis of $ZnFe_2O_4$ Nano Composite

The high-resolution transmission electron microscopy (HRTEM) images of $ZnFe_2O_4$ (NPs) are shown (Figure 4). The figure indicates that $ZnFe_2O_4$ NPs are uniform and cylindrical. The average particle size was calculated using Image-J software and the particle size is ranged about 50 nm.

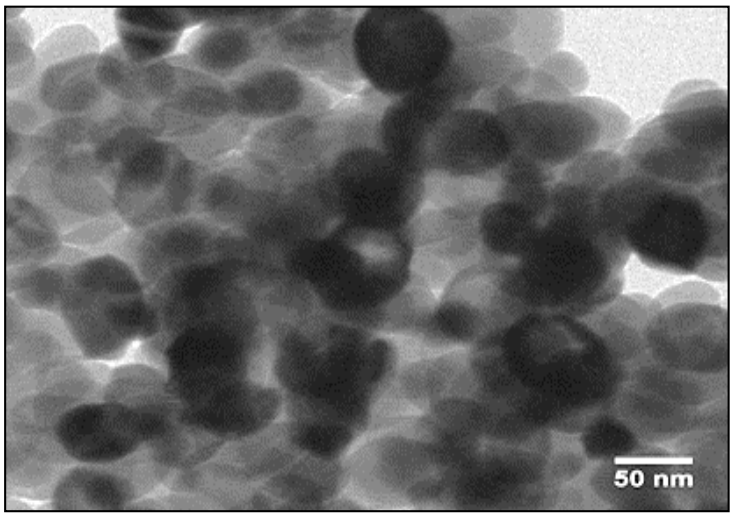

Figure 4. HRTEM Image of $ZnFe_2O_4$ NPs.

2.4. EDS Analysis of $ZnFe_2O_4$ NPs

The elemental composition of $ZnFe_2O_4$ NPs was studied by energy-dispersive X-ray spectroscopy (EDS), as shown in Figure 5. The $ZnFe_2O_4$ NPs exhibit three elemental peaks—one for zinc element located at 1.1 keV, one for oxygen element located at 0.5 keV, and two for iron element located at 0.65 and 6.4 keV. From the EDS data, the weight ratio of Zn:Fe:O is around 43.91:13.97:42.12. The sample consists of only O, Fe, and Znelements.

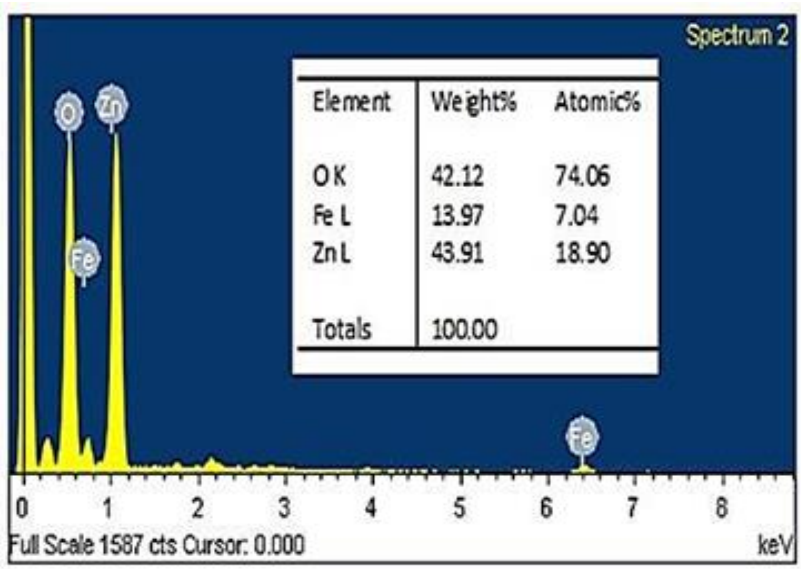

Figure 5. Energy-dispersive X-ray spectroscopy (EDS) pattern $ZnFe_2O_4$ nanoparticles.

2.5. Mass Spectra of Synthesized Compounds

The mass spectrum of **4a** revealed a molecular ion peak at m/z 286, which is consistent with the formula weight (285). This result confirmed the identity of the structure of **4a**. Similarly, the mass spectra of other compounds are also consistent with the proposed structures (for **4d**, m/z = 321, **4g**, m/z= 472 and **4h**, m/z= 310) (Figures S1–S4),

2.6. NMR Spectral Analysis

The ^{1}HNMR spectra of the compounds 7, 7-dimethyl-4-phenyl-2-thioxo-2, 3, 4, 6, 7, 8-hexahydro-1H-quinazolin-5-one from 5, 5-dimethyl cyclohexane-1, 3-diones (**4a**, **4d**, **4g**, **4h**) (Figures S5–S8) were assigned based on the observed chemical shift and relative

intensities of the signals. The ^{1}HNMR spectra of the compounds displayed sharp singlets owing to the two –NH protons in each compound at 9.52–10.36 ppm. ^{1}HNMR spectral values of –NH groups in quinazolones nucleus showed down fields, namely,10.23, 10.13, 10.29, 10.34 ppm (halogens and cyano group). The –NH-groups of quinazolones containing electron donating group (EDG) showed the ^{1}HNMR values in the upfield region such as 9.58, 9.73, 9.54, 9.74, 9.72, 9.84, and 9.52 ppm and also the showed–OH group at 10.24 ppm. The derivatives were obtained by the cyclization with the thiourea added. The two methyl group protons of the compounds fell at 0.92–1.15 ppm. A singlet at 3.57 ppm and a broad singlet at 3.66 ppm for **4b** and **4f** accounts for protons of *p*-methoxy (–OCH_3) and di-methoxy (3,5-OCH_3) groups, respectively. In the case of **4c** and **4d**, the hydroxy (–OH) protons were observed as singlets at 9.33 and 10.24 ppm, respectively. A singlet appeared at 2.74 ppm due to the N–Me proton in **4d**. The resonances due to aryl ring protons appeared in the range of 6.70–7.56 ppm. The quintets in 2.14–3.46 ppm and singlet around 2.40 ppm corresponded to methylene protons of dimedone ring.

The ^{13}CNMR spectra revealed the presence of the expected number of signals corresponding to different types of carbon atoms present in the compounds. The –OCH_3group absorbs at 55.25 (**4g**) and 55.30 (**4h**) ppm slightly downfield to the methyl group carbon due to the deshielding of the directly attached electronegative oxygen atom. The spectra of the compounds exhibit a strong band at 169.8–174.2 ppm and are assigned as C=S group. The ^{13}CNMR display signals in the range 112.4–151.7 ppm, which has been assigned to the aromatic carbon atoms. The signals due to the C attached to the methyl group resonate at 141.4–147.8 ppm. The resonance arising from the carbon attached to the hydroxyl (**4a** and **4d**) group is observed at 158.4 and 158.6 ppm, respectively. Values of downfield (195.2 ppm) compared with other groups (Figures S9–S12).

2.7. Antibacterial Activity

The antibacterial and antifungal activity of **4f**(4-(4-bromophenyl)-7,7-dimethyl-2-thioxo-2,3,4,6,7,8-hexahydro-1H-quinazolin-5-one) molecule showed high active potentials such as 20, 14,21,22,24 25 mm of inhibition, compared with **4e**(4-(4-chlorophenyl)-7,7-dimethyl-2-thioxo-2,3,4,6,7,8-hexahydro-1H-quinazolin-5-one) and **4g** (4-(2-iodo-3,5-dimethoxy phenyl)-7,7-dimethyl-2-thioxo-1,2,3,4,7,8-hexahydroquinazoline-5(6H)-one)molecules, which are also better than other compounds (Table 2). We observed that the important result in the investigation of the reaction of substituted aryl aldehydes, 5,5-dimethyl cyclohexane-1,3-dione(dimedone), and thiourea in the presence of nanocatalyst under solvent-free conditions at room temperature (Scheme 1).The advantages of using this catalyst for the reaction, which is responsible for easy work-up, include a short reaction time. Moderate-to-good yields, and purification of title compound by non-chromatographic methods. It is also identified that various substituted aryl aldehydes containing electron-withdrawing and electron-releasing substituents in para-positions lead better yield than ortho substituents. Therefore, we observed that the reaction of aryl aldehydes having an electron-withdrawing group was having a faster rate of reaction, compared to the reaction of aldehydes possessing electron releasing groups. In this reaction, halogen-substituted aryl aldehydes obtain a better yield than the electron-donating group containing aryl aldehyde. The reusability of this catalyst was investigated. The antimicrobial activity of title compounds possessing-electron withdrawing group (EWG) such as (**4e**–**4h**) (halogens and cyano group) exhibited more active potential than the EDG(**4a**–**4d**) containing moiety (Table 3).

Table 2. Synthesis of titled derivatives catalyzed by nanocatalyst solvent-free condition.

Entry	Ar(a)	Molecular Formula	Time [a] (min)	Yield [b] (%)	Molecular Weight (MW) g/mol	m.p (°C) Lit).
4a	C_6H_5	$C_{16}H_{18}N_2OS$	75	85	286.71	285–286 °C
4b	4-OH-C_6H_4	$C_{17}H_{20}N_2O_2$ S	130	87	317.53	274–276 °C
4c	3-OC_2H_5-4-OH-C_6H_3	$C_{18}H_{22}N_2O_3$ S.	150	87	365.22 (M-H).	273–274 °C
4d	4-Cl-C6H4	$C_{16}H_{17}ClN_2OS$	120	90	321.64	274–276 °C (Lit275–276 °C)
4e	4-Br-C_6H_4	$C_{16}H_{17}BrN_2OS$	120	91	366.16	284 °C
4f	2-OH-4-N$(CH_3)_2$-C_6H_3	$C_{18}H_{23}N_3O_2$ S	130	88	345.48	275–277 °C
4g	2-I-3,5-$(OCH_3)_2$-C_6H_3	$C_{18}H_{21}IN_2O_3S$.	150	90	472.29	275–276 °C
4h	4-CN-C_6H_4	$C_{17}H_{17}N_3OS$.	175	88	310.45 (M-H).	269–271 °C

[a] Reaction was continued until the Thin Layer Chromatography (TLC)shown the starting materials disappeared. [b] Isolated yield.

Table 3. In vitro antibacterial and antifungal screening study of the title compounds **4a**–**4h**.

S.No	Compound Code	Zone of Inhibition (mm)					
		Gram-Negative Bacteria		Gram-Positive Bacteria		Fungal Strains	
		E.coli	*P.aeruginosa*	*B.subtilis*	*B.megaterium*	*A.niger*	*C.albicans*
1	**4a**	16	13	21	15	15	16
2	**4b**	14	12	22	14	12	14
3	**4c**	16	15	14	16	13	16
4	**4d**	11	15	15	14	14	15
5	**4e**	19	17	20	20	23	24
6	**4f**	20	14	21	22	24	25
7	**4g**	19	20	21	21	23	24
8	**4h**	17	16	17	18	19	20
Control	**DMSO**		10			10	
Standard	**Streptomycin**	25	25	25	25		
	Fluconazole					30	30

3. Discussion

Dimedone also called 5, 5-dimethylcyclohexane-1, 3-dione is a cyclic diketone, which is used as a key sample molecule for the synthesis of the various moiety in synthetic organic chemistry. These are white to light yellow crystals in color and also have other names such asdimedone, Cyclomethicone, 5, 5-dimethyl-1,3-cyclohexanedione, dimethyl-dihydro resorcinol, and Methone. The molecular formula is $C_8H_{12}O_2$, and its molecular weight is 140.17968 g/mol with a melting point of 147–150 °C (420–423 K). It is stable under ambient conditions and soluble in organic solvents ($CHCl_3$, CC_4, toluene, etc.,) and in methanol, ethanol, and water. One-step reduction of dimedone to 3, 3-dimethylcyclohexanone compound with a yield of 69–73% (98–99% purity) by using Pd-catalyzed medium-pressure dimedone hydrogenation (1) in a solvent mixture of concentrated H_2SO_4 and propionic acid [26] was made. Dimedone and its derivatives have been previously documented to have various biological properties such as anticarcinogenic [27], antioxidant [28], antihistamine [29], and anticoagulant [30]. A three-component one-pot reaction of dimedone, 1, 3-cyclohexanedione, aromatic aldehydes, and malononitrile in the presence of D, L-proline under solvent-free conditions at ambient temperature to produce 2-amino-3-cyano-4-aryl-7,7-dimethyl-5,6,7 8-tetrahydrobenzopyrans has been reported [31].

The reaction proceeded at room temperature clearly shows to provide good yields for the products (ae = 94%). An efficient one-pot synthesis of 4H-benzopyrans via a three-component cyclo condensation of malononitrile using $CeCl_3 \cdot 7H_2O$ (10 mol percent) as a catalyst in a 1:2 mixture of water/ethanol under reflux conditions that yielded 70–94% within 1–2 h [32]. Sadehet al. (2017) [33] reported that in most organic transformations, dimedoneis a flexible and fascinating moiety. A wide variety of organic reactions, including one-pot multi-step syntheses, used the white to light yellow crystals of dimedone as a substrate. Dimedone has acidic properties in its methylene group, which is in harmony with its tautomericenol shape, making it possible to use them in various organic reactions. They are also used to evaluate the efficiency of some organic molecules, which have active pharmaceutical properties. Low-cost processing, ease of handling, low toxicity, easy accessibility, and moisture stability made it fascinating for use by synthetic organic chemists. Dimedone was concentrated in much of the reaction with a view to the media solvent. The temperature of the transformations in each segment has been subdivided, and this is used to achieve an organic transition based on green chemistry.

Leoa and Maryam (2018) [34] reported that the key peaks assigned to 200, 311, 400, 422, and 511 and Bragg reflection at 2 θ value of 27.36°, 36.03°, 46.18°, 56.77°, and 62.95° are according to the typical pattern for spinel-structured crystalline magnetite. The average nanoparticle diameter was around 73 nm, estimated from Debye–Scherrer's equation. It is also concluded that the chemical alteration process has not changed the magnetic nanoparticles' crystal structure, diameter, and structure. SEM images of $ZnFe_3O_4$ nanoparticles and $ZnFe_3O_4$@MSA were submitted. Fe_3O_4nano particles have a mean size of approximately 75 nm with good distribution according to SEM images. The SEM picture of Fe_3O_4@MSA shows that, due to the particle size of modified magnetite nanoparticles, the methane sulfonic acid layer attached to the nanoparticle surface is very thin because it is not larger than raw Fe_3O_4. These findings are in line with XRD trends [30].

Antibacterial activity was documented by Appaniet al. [35]. Electron withdrawing groups were demonstrated to have better behavior over aliphatic substituents among the various substituents on the C-2. Compounds with electron withdrawal substituents such as –Cl and–F showed increased activity over unsubstituted and electron releasing substituted moieties. As the most active compounds of the sequence, compounds 9a and 9h appeared to have the most potent activity against *P. Vulgaris* and *B*. Dimedone could be prepared from diethyl malonate and mesityl oxide, which is a safe compound with no or fewer hazards during usage. This dimedone is in equilibrium with its tautomericenol form in chloroform and the hydrogen bonding between the enolic structure results in the crystalline appearance. Dimedone and its analogs have been previously well documented with a wide spectrum of biological properties such as anticarcinogenic, antioxidant, antihistaminic, and anticoagulant [36].

The chemiluminescence property observed during the oxidation process belongs to 4-peroxydimedone radicals that are being synthesized from the first step of oxidation. Other applications of dimedone are colorimetry, crystallography, luminescence, and spectrophotometric analysis. Different types of reactions that include dimedone as a substrate have been presented and are classified based on the reaction media used. This is due to the importance of economical and green transformations in organic synthesis. The reaction could occur under solvent-free conditions, in aqueous media, and in the presence of various organic solvents. Some cases required heat to enhance them, and some others have taken place at room temperature. The above-discussed multiple properties of dimedone create a strong interest for utilizing them in different reactions by the synthetic chemists [37].

4. Materials and Methods

4.1. Materials

All the reagents, chemicals, and solvents (Merck, Mumbai, India) were procured and the melting points of the newly synthesized compounds were determined by using Agrawal 535 melting point apparatus. All the reactions were checked by thin-layer chromatography

using ethyl acetate and n-hexane (5:5) performed on percolated silica gel (Merck, Mumbai, India). The ^{1}HNMR spectra of these compounds were recorded on BRUKER 400 MHz spectrometers and ^{13}CNMR were recorded on BRUKER 100 MHz using $CDCl_3$ as the solvent and Tetramethylsilane as an internal standard. The molecular weight of compounds was determined by mass spectrometry.

4.2. Methods

4.2.1. Preparation of $ZnFe_2O_4$Nanoparticles (NPs)

The nanoparticles of zinc ferrite were prepared using both sol–gel techniques. As precursors, iron nitrate [$Fe(NO_3)_3 \cdot 9H_2O$] and zinc nitrate [$Zn(NO_3)_2 \cdot 6H_2O$] were used.

The precursors were dissolved in 50 mL ethylene glycol aliquot ($C_2H_6O_2$) and then agitated at room temperature for 2 h using a magnetic bead to form a homogenized aqueous solution (0.1 M). To evaporate all the material, the solution was dried for 6 h at 130 °C. Finally, the dry powder was annealed for crystallization at 500 °C for 1 h in the air.

4.2.2. Structural Characterization

The XRD profile at room temperature of the synthesized $ZnFe_2O_4$ (NPs) was obtained. The crystal structure and phase purity of the sample were evaluated, and the crystalline size was determined using the Debye–Scherrer equation. $ZnFe_2O_4$ (NPs) surface morphology was analyzed using the scanning electron microscope (SEM) (TESCAN, CZ/MIRA I LMH). Transmission electron microscope (TEM) (FEI, TECNAIG2TF20-ST) measured the particle size, and the elements present were analyzed by the energy dispersive x-ray analysis (EDS).

4.2.3. General Procedure for the Synthesis of 7, 7-Dimethyl-4-Phenyl-2-Thioxo-2, 3, 4, 6, 7, 8-Hexahydro-1H-Quinazolin-5-One

A mixture of substituted aryl aldehydes (1) (10 mmol), 5,5-dimethyl cyclohexane-1,3-dione(dimedone)(2) (10 mmol) and/thiourea (3) (15 mmol) with the nanocatalyst without solvent taken in a beaker (capacity 50 mL).The total mixture fitted on magnetic stirrer and reaction was proceeding. The completion of the reaction was monitored by TLC (ethyl acetate/hexane (5:5). The reaction mixture was then extracted with ethyl acetate and the catalyst was separated by the filtration. The organic layer was then washed with water and dried over anhydrous Na_2CO_3. The organic solvent was evaporated under reduced pressure and the solid compound was crystallized from absolute ethanol to lead the pure corresponding 7, 7-dimethyl-4-phenyl-2-thioxo-2, 3, 4, 6, 7, 8-hexahydro-1H-quinazolin-5-azones and its derivatives (**4a**–**4h**) in good yields.

7, 7-Dimethyl-4-phenyl-2-thioxo-2, 3, 4, 6, 7, 8-hexahydro-1H-quinazolin-5-one (**4a**):^{1}HNMR (400 MHz, CDCl3), δ ppm:1.02(s, 3H, CMe);1.11(s, 3H, CMe); 2.25 (q, *J* = 16.0 Hz, 2H, CH2); 2.31(s, 2H, CH2); 4.95 (d, *J* = 3.5 Hz,1H, CH); 7.12–7.32 (m, 5H, Ar); 9.66(s, 1H, NH); 10.22(s, 1H, NH); ^{13}CNMR (100 MHz, CDCl3): δ ppm: 193.7, 173.7, 147.8, 141.5, 128.9, 127.6, 125.8, 102.4, 51.5, 49.8, 32.6, 28.0, 26.4.

4-(4-Methoxyphenyl)-7,7-dimethyl-2-thioxo-2,3,4,6,7,8-hexahydro-1H-quinazolin-5-one (**4b**): ^{1}HNMR (400 MHz, CDCl3), δ ppm: 0.95(s, 3H, CMe); 1.11(s, 3H, CMe); 2.18(q, *J* = 16.2 Hz, 2H, CH2); 3.01(s, 2H, CH2); 3.57(s, 3H, OCH3), 5.10(d, *J* = 2.7 Hz, 1H, CH); 6.82(d, *J* = 8.4 Hz, 2H, Ar); 7.22(d, *J* = 8.8 Hz, 2H, Ar); 9.58(s, 1H, NH); 9.86(s,1H, NH); ^{13}CNMR (100 MHz, CDCl3): δppm: 193.4, 174.0, 158.2, 147.8,137.1,128.8,115.2,107.7, 100.8, 55.9, 52.4, 50.4, 32.9, 28.9, 26.8.

4-(3-ethoxy-4-hydroxyphenyl)-7,7-dimethyl-2-thioxo-1,2,3,4,6,7,8-hexahydro-1H-quinazolin-5-one (**4c**): ^{1}HNMR (400 MHz, CDCl3) δppm: 0.97(s, 3H, CMe); 1.11(s, 3H, CMe);1.25(t,3H,CH3); 3.46(q,2H,-CH2-), 2.22(q, =16.1 Hz, 2H, CH2); 2.39(s, 2H, CH2); 4.22(d, *J* = 3.6 Hz, 1H, CH); 6.70–7.51(m,34H, Ar); 9.33(s,1H,-OH); 9.73(s, 1H, NH); 9.94(s, 1H, NH); ^{13}CNMR (100 MHz, CDCl3): δppm:192.9,172.6,158.4,147.8,145.3,139.8,132.5,119.6,116.3,115.5,101.4, 60.9,50.4,47.8,36.9,30.6,26.3,13.7.

4-(4-Dimethylamino)-2-hydroxyphenyl)-7,7-dimethyl-2-thioxo-1,2,3,4,6,7,8-hexahydro-1H-quinazolin-5(6H)-one (**4d**): ^{1}HNMR (400 MHz,CDCl3) δppm: 1.05(s,3H,CMe); 1.15(s, 3H, CMe); 2.26(q, *J* = 16.2 Hz, 2H, CH2); 2.36(s, 2H, CH2); 2.74(s, 6H, NMe2), 4.94(d, *J* = 2.6 Hz, 1H, CH); 7.09–7.29 (m, 3H, Ar);9.15(s, 1H, NH);10.02(s,1H,-OH), 9.45(s, 1H, NH); ^{13}CNMR (100 MHz, CDCl3): δppm 193.9,174.2,158.6,151.6,149.2,131.4,126.7,122.9, 121.4,120.5,49.8,46.3, 38.6, 28.8, 26.9.

4-(4-Chlorophenyl)-7,7-dimethyl-2-thioxo-2,3,4,6,7,8-hexahydro-1H-quinazolin-5-one (**4e**): ^{1}HNMR (400 MHz, CDCl3)δppm: 0.94(s, 3H, CMe); 1.05(s, 3H, CMe); 2.19 (q, *J* = 16.5 Hz, 2H, CH2);2.40(s,2H,CH2);5.17(d, *J* = 3.6 Hz,1H,CH);7.36–7.15(m,4H,Ar);9.74(s,1H,NH);10.34(s,1H, NH); ^{13}CNMR(100 MHz,CDCl3) δppm: 194.5,174.2, 150.7, 141.4, 132.0, 129.7, 128.3, 127.4, 125.8, 104.4, 52.8, 50.6, 32.7, 28.9, 25.6.

4-(4-Bromophenyl)-7,7-dimethyl-2-thioxo-2,3,4,6,7,8-hexahydro-1H-quinazolin-5-one (**4f**): ^{1}HNMR (400 MHz, CDCl3) δppm: 0.98(s, 3H, CMe); 1.09(s, 3H, CMe); 2.14(q, *J* = 16.2 Hz, 2H, CH2); 2.35(s, 2H, CH2); 5.08(d, *J* = 2.7 Hz, 1H, CH); 7.20 (d, *J* = 8.4 Hz, 2H, Ar); 7.44(s, *J* = 7.6 Hz, 2H, Ar); 9.72(s, 1H, NH); 10.23(s, 1H, NH); ^{13}CNMR (100 MHz,CDCl3): δ 195.1, 173.6, 147.4, 141.7, 132.7, 130.2, 128.8, 121.5, 104.6, 52.0, 49.2, 32.4, 28.6, 25.9.

4-(2-iodo-3,5-dimethoxy phenyl)-7,7-dimethyl-2-thioxo-1,2,3,4,7,8-hexahydroquinazolne-5(6H)-one(**4g**):^{1}HNMR (400 MHz, CDCl3) δ ppm: 0.92(s, 3H, CMe); 1.13(s, 3H, CMe); 2.24(q, *J* = 16.4 Hz, 2H, CH2); 2.84(s, 2H, CH2); 3.66(s, 6H, (2OCH3), 5.07(d, *J* = 2.8 Hz, 1H, CH); 6.872(s, 1H, Ar); 7.02(s, 1H, Ar); 9.84(s, 1H, NH); 10.13(s, 1H, NH); 13CNMR (100 MHz, CDCl3): δppm: 194.6, 169.8, 156.7,151.7, 147.2, 119.8, 116.6, 115.3, 105.4,55.2,54.8, 51.3,48.7, 38.3, 28.6, 25.3. 8)4-(7,7-dimethyl-5-oxo-2-thioxo-1,2,3,4,7,8-ocatahydroquinazolne-4-yl) benzonitrile(**4h**) (400 MHz,CDCl3)δppm: 1.07(s,3H,CMe); 1.16(s, 3H, CMe); 2.32(q, *J* = 16.2 Hz, 2H, CH2); 2.43(s, 2H, CH2); 5.02(d, *J* = 2.8 Hz, 1H, CH); 7.39–7.56 (m, 4H, Ar);9.52(s,1H,NH); 10.29(s,1H,NH);^{13}CNMR(100 MHz,CDCl3)δppm:195.2,173.9,159.5,149.2,145.4,130.6,128.2, 120.8,112.4,104.7,52.3,49.2,38.6,29.4,29.4.

4.2.4. AntimicrobialAssays

Theantimicrobial activity of the titled compounds namely:7,7-dimethyl-4-phenyl-2-thioxo-2,3,4,6,7,8-hexahydro-1H-quinazolin-5-ones and its derivatives have been in vitro screened with both bacterial and fungal strains:

Gram-negative—*Escherichia coli, Pseudomonas aeruginosa*;

Gram-positive—*Bacillus subtilisin, Bacillus megaterium*;

Fungal strains—*Aspergillusniger and Candida albicans*.

The synthesized compounds were laid using agar plates containing nutrient broth for bacteria in vitro activities [8–11]. The antibacterial streptomycin and fluconazole were used as standards for antibacterial and antifungal assays, respectively. Dimethyl sulfoxide (DMSO) was used as solvent control. The antimicrobial inhibitions of test compounds were expressed as a zone of inhibition in standard units (mm). This marked antibacterial activity may be due to the presence of high hydrophobic content of this family of compounds and the quinazoline ring system. The compounds containing the quinazalone segment are more active against bacteria due to the strong interaction of the latter with the agar medium; this hinders their diffusion in the agar medium.

5. Conclusions

In conclusion, an efficient nanocatalyst is used for the synthesis of a series of7,7-dimethyl-4-phenyl-2-thioxo-2,3,4,6,7,8-hexahydro-1H-quinazolin-5-ones. The present methodology has very attractive features such as reduced reaction times and moderate-to-good yields, and the product was isolated efficiently. We believe that conducting this procedure in solvent-free conditions, along with easy recovery and reuse of catalyst, makethis method environmentally and economically valuable. Thederivativesof7, 7-dimethyl-4-phenyl-2-thioxo-2, 3, 4, 6, 7, 8-hexahydro-1H-quinazolin-5-ones have biological and medicinal significance.

Supplementary Materials: The following are available online at https://www.mdpi.com/article/10.3390/catal11040431/s1, Figure S1. Mass spectrum of 7, 7-Dimethyl-4-phenyl-2-thioxo-2, 3, 4, 6, 7, 8-hexahydro-1H-quinazolin-5-one (**4a**); Figure S2. Mass spectrum of 4-(4-Dimethylamino)-2-hydroxyphenyl)-7,7-dimethyl-2-thioxo-1,2,3,4,6,7,8-exahydro-1H-quinazolin-5(6H)-one (**4d**); Figure S3. Mass spectrum of 4-(2-iodo-3,5-dimethoxyphenyl)-7,7-dimethyl-2-thioxo-1,2,3,4,7,8-hexahydroquinazolne -5(6H)-one(**4g**); Figure S4. Mass spectrum of 4-(7,7-dimethyl-5-oxo-2-thioxo-1,2,3,4,7,8-ocatahydroquinazolne-4-yl) benzonitrile(**4h**); Figure S5. 1H NMR Spectrum of 7-Dimethyl-4-phenyl-2-thioxo-2, 3, 4, 6, 7, 8-hexahydro-1H-quinazolin-5-one (**4a**); Figure S6. 1H NMR Spectrum of 4-(4-Dimethylamino)-2-hydroxyphenyl)-7,7-dimethyl-2-thioxo-1,2,3,4,6,7,8-exahydro-1H-quinazolin-5(6H)-one (**4d**); Figure S7. 1H NMR Spectrum of 4-(2-iodo-3,5-dimethoxyphenyl)-7,7-dimethyl-2-thioxo-1,2,3,4,7,8-hexahydroquinazolne-5(6H)-one(**4g**); Figure S8. 1H NMR Spectrum of 4-(7,7-dimethyl-5-oxo-2-thioxo-1,2,3,4,7,8-ocatahydroquinazolne-4-yl) benzonitrile(**4h**); Figure S9. 13C NMR Spectrum of 7, 7-Dimethyl-4-phenyl-2-thioxo-2, 3, 4, 6, 7, 8-hexahydro-1H-quinazolin-5-one (**4a**); Figure S10. 13C NMR Spectrum of 4-(4-Dimethylamino)-2-hydroxyphenyl)-7,7-dimethyl-2-thioxo-1,2,3,4,6,7,8-exahydro-1H-quinazolin-5(6H)-one (**4d**); Figure S11. 13C NMR Spectrum of 4-(2-iodo-3,5-dimethoxyphenyl)-7,7-dimethyl-2-thioxo-1,2,3,4,7,8-hexahydroquinazolne-5(6H)-one(**4g**); Figure S12. 13C NMR Spectrum of 4-(7,7-dimethyl-5-oxo-2-thioxo-1,2,3,4,7,8-ocatahydroquinazolne-4-yl) benzonitrile(**4h**).

Author Contributions: S.Y.A. conceived and designed the experiments and supervised the research work; T.N.R. performed the experiments and wrote the paper; N.K. measured the characterizations; F.A. (Faheem Ahmed) and N.A. contributed reagents/materials/analysis tools. Visualization by F.A. (Fadwa Albalawi). and S.K. and data curation by P.M., A.A. and B.P. All authors have read and agreed to the published version of the manuscript.

Funding: The authors are grateful to the Deanship of Scientific Research, King Saud University, for funding through Vice Deanship of Scientific Research Chairs.

Data Availability Statement: Data is contained within the article and Supplementary Material.

Conflicts of Interest: The authors declare no conflict of interest.

References

1. Lednicer, D.; Mitscher, L.A. *The Organic Chemistry of Drug Synthesis*; Wiley InterscienceePubl: New York, NY, USA, 1977; Volume 1, pp. 338–342.
2. Lednicer, D.; Mitscher, L.A. *The Organic Chemistry of Drug Synthesis*; Wiley InterscienceePubl: New York, NY, USA, 1980; Volume 2, p. 361.
3. Kershaw, S.; Stables, J.P.; Jatav, V.; Mishra, P. Synthesis and CNS depressant activity of some derivatives of novel 3-[5-substituted-1, 3,4-thiadiazole-2-yl]-2-styrylquinazolin-4-(3H)-one. *Eur. J. Med. Chem.* **2008**, *43*, 135–141.
4. Sayed, R.E.; Wasfy, A.F. Synthesis of heterocycles having double character: As antimicrobial. *J. Chinesechem. Soc.* **2005**, *52*, 129–135.
5. Tyagi, M.; Pathak, U.S.; Rathod, R.S. Synthesis of 3-monosubstitutedquinazolin-4-(3H)-ones. *Ind. J. Chem.* **1995**, *2*, 617–623.
6. Thierry, B.A.; Jerome, G.; Charles, W.R. Multistepsynthesis of thiazoloquinazolines-under microwave irradiation in solution. *Tetrahedron Lett.* **2020**, *41*, 1027–1030.
7. Bahl, B.S.; Bahl, A.A. *Text Book of Organic Chemistry*; Chand and Company Ltd.: New Delhi, India, 1997; Volume 14, p. 735.
8. Guiry, P.J.; Connolly, D.J.; Cusack, D. Synthesis of quinazolinones and quinazoline. *Tetrahedron* **2005**, *737*, 10153–10202.
9. Feng, L.; Meng, Q.; Feng, Y. An efficient construction of Quinazoline-4-(3H)-ones under microwave irradiation. *ARKIVOC* **2007**, *I*, 40–50.
10. Meyyanathan, S. ASEAN review of biodiversity and environmental conversation. *ABEC* **1998**, *2*, 4–10.
11. Alexandra, P.B.; Thierry, B.; Corinne, F. Diaryliodoniums Salts as Coupling Partners for Transition-Metal Catalyzed C- and N-Arylation of Heteroarenes. *Catalysts.* **2000**, *10*, 1–34.
12. Lidstrom, P.; Tierney, J.; Westman, J. Microwaveassistedorganic synthesis—A review. *Tetrahedron* **2001**, *57*, 9225–9283. [CrossRef]
13. Lottie, B.; Thomas, H. Microwave enhanced decarboxylation of aromatic carboxylic acid, improved potential. *J. Chem. Res.* **2000**, *2*, 42–46.
14. Canevari, S.; Bantu, R.; Nagarapu, L. TMSCl mediated highly efficient one-pot synthesis of octa hydro quinazolinone and 1,8-dioxo-octa hydro xanthene derivatives. *Arkivoc* **2006**, *XVI*, 136–148.
15. Hassani, Z.; Islami, M.R.; Kalantari, M. An efficient one-pot synthesis of octa hydro quinazolinone derivatives using a catalytic amount of H_2SO_4 in the water. *Bioorganic Med. Chem. Lett.* **2006**, *16*, 4479. [CrossRef] [PubMed]
16. Lin, H.; Zhao, Q.; Xu, B.; Wang, X. Nafion-H catalysed cyclocondensation reaction for the synthesis of octa hydro quinazolinone derivatives. *J. Mol. Catal. A: Chem.* **2007**, *268*, 1–2. [CrossRef]
17. Niralwad, K.S.; Shingate, B.; Shingare, M.S. Microwave-assisted one-pot synthesis of octa hydro quinazolinone derivatives using ammonium metavanadate under solvent-free condition. *Tetrahedron Lett.* **2010**, *51*, 3616. [CrossRef]

18. Mobinikhaledi, A.; Foroughifar, N.; Khodaei, H. Synthesis of octa hydro quinazolinone-derivatives using silica sulfuric acid as an efficient catalyst. *Eur. J.Chem.* **2010**, *1*, 291. [CrossRef]
19. Kefayati, H.; Asghari, F.; Khanjanian, R. 1-Methylimidazolium hydrogen sulfate/chlorotrimethylsilane: An effective catalytic system for the synthesis of 3, 4-dihydropyridine-2(1H)-ones and hydroquinazolinone-2,5-diones. *J. Mol. Liq.* **2012**, *172*, 147. [CrossRef]
20. Khurana, J.M.; Kumar, S. Ionic liquids: An efficient and recyclable medium for the synthesis of octa hydro quinazolinone and biscoumarin derivatives. *Montashefte Fur Chem.* **2010**, *141*, 561. [CrossRef]
21. Karami, S.; Karami, B.; Khodabakhshi, S. Solvent-free synthesis of novel and known octahydroquinazolinones/thione by the use of $ZrOCl_2.8H_2O$ as a highly efficient and reusable catalyst. *J. Chin. Chem.Soc.* **2013**, *60*, 22. [CrossRef]
22. Pachpinde, A.M.; Langade, M.M. A simple one pot synthesis of 5-Acetyl-3,4-Dihydro-4-Phenylpyrimidin-2(1H)-one, by using magnetically recoverable heterogeneous nickel substituted nanoferro-spinel catalyst. *Int. J. Res. Appl. Sci. Biotechnol.* **2019**, *6*, 23–26. [CrossRef]
23. Kumar, B.V.; Naik, H.S.B.; Girija, D. ZnO nanoparticle as catalyst for efficient green one-pot synthesis of coumarins through Knoevenagel condensation. *J. Chem. Sci.* **2011**, *123*, 615–621. [CrossRef]
24. Beletskaya, I.; Tyurin, V. Recyclable Nanostructured Catalytic Systems in Modern Environmentally Friendly Organic Synthesis. *Molecules* **2010**, *15*, 4792–4814. [CrossRef]
25. Hemalatha, K.; Madhumitha, G.; Kajbafvala, A.; Anupama, N.; Sompalle, R.; Roopan, S.M. Function of nanocatalyst in chemistry of organic compounds revolution: An overview. *J. Nanomater.* **2013**, *2013*, 1–23. [CrossRef]
26. Cormier, R.A. A convenient synthesis of 3,3-dimethylcyclohexanone. *Synth. Commun.* **1981**, *11*, 295–298. [CrossRef]
27. Singletary, K.; MacDonald, C.; Iovinelli, M.; Fisher, C.; Wallig, M. Effect of the β-diketonesdiferuloylmethane (curcumin) and dibenzoylmethane on rat mammary DNA adducts and tumors induced by 7,12-dimethylbenz[a] anthracene. *Carcinogenesis* **1998**, *19*, 1039–1043. [CrossRef]
28. Rasmussen, H.B.; Christensene, S.B.; Kirs, L.P.; Karazmi, A. A simple and efficient separation of the curcumins, the antiprotozoal constituents of Curcuma longa. *Planta Med.* **2000**, *66*, 396–397. [CrossRef] [PubMed]
29. Matsuzaki, T.; Koiwai, A. Antioxidative-Diketones in stigma lipids of tobacco. *Agric. Biol. Chem.* **1988**, *52*, 2341–2342. [CrossRef]
30. Francis, L.E.; Douglas, D.E. Some observations on the antihistamine activity in the guinea pig of aliphatic 2,4diketones, a new class of physiological tissue components. *Res. Commun. Chem. Patel. Pharmacol.* **1977**, *17*, 357–364.
31. Guo, S.B.; Wang, S.X.; Li, J.T.D. L-Proline-catalyzed one-pot synthesis of Pyrans and Pyrano[2,3c]Pyrazole derivatives by a grinding method under solvent, free conditions. *Synth. Commun.* **2007**, *37*, 2111–2120. [CrossRef]
32. Sabitha, G.; Arundhathi, K.; Sudhakar, K.; Sastry, B.S.; Yadav, J.S. A concise study on dimedone: A versatile molecule in multicomponent reactions, an outlook to the green reaction media. *Synth. Commun.* **2009**, *39*, 433–440. [CrossRef]
33. Sadeh, F.N.; Fatahpour, M.; Hazeri, N.; Maghsoodlou, M.T.; Lashkari, M. One-pot condensation approach for the synthesis of some 1,8-dioxooctahydroxanthenes and 14-aryl-14hdibenzo[a,j]xanthenes using lactic acid as an efficient and eco-friendly catalyst. *Acta Chem. Iasi.* **2017**, *25*, 24–37. [CrossRef]
34. Leila, M.; Maryam, T. Green synthesis of 3,4-dihydropyrimidinones using nanoFe3O4@meglumine sulfonic acid as a new efficient solid acid catalyst under microwave irradiation. *J. Saudi Chem. Soc.* **2018**, *22*, 66–75.
35. Ramgopal, A.; Baburao, B.; Kiran, G. *Synthesis and Antibacterial Activity of 3-(Substituted)-2-(4-oxo2-Phenylquinazolin-3(4H)-Arylamino) Quinazolin-4(3H)-One*; Hindawi Publishing Corporation Scientifica: Cairo, Egypt, 2016; Volume 124, p. 5.
36. Kobra, N.F.; Molaei, F. A concise study on dimedone: A versatile molecule in multicomponent reactions, an outlook to the green reaction media. *J. Saudi Chem. Soc.* **2018**, *22*, 715–741.
37. Wang, G.W.; Lu, Q.Q.; Xia, J.J. Synthesis of N-substituted Acridinediones and Polyhydroquinoline derivatives in refluxing water. *Eur. J. Org. Chem.* **2011**, 4429–4438. [CrossRef]

Carbohydrate Polymer Technologies and Applications 2 (2021) 100037

Contents lists available at ScienceDirect

Carbohydrate Polymer Technologies and Applications

journal homepage: www.elsevier.com/locate/carpta

A study on structural comparisons of α-chitin extracted from marine crustacean shell waste

K. Mohan[a,*], T. Muralisankar[b], R. Jayakumar[c], C. Rajeevgandhi[d]

[a] PG and Research Department of Zoology, Sri Vasavi College, Erode, Tamil Nadu, 638 316, India
[b] Aquatic Ecology Laboratory, Department of Zoology, School of Life Sciences, Bharathiar University, Coimbatore, Tamil Nadu, 641 046, India
[c] Department of Molecular Medicine, Faculty of Medicine, University of Malaya, Kuala Lumpur 50603, Malaysia
[d] Department of Physics, Annai College of Arts and Science, Kumbakonam, Tamil Nadu, 612503, India

ARTICLE INFO

Keywords:
Crustacean shell waste
Shrimp
Crab
α-Chitin
Structural comparison

ABSTRACT

In the present study, chitin was extracted from marine crustacean shell waste (shrimp, crab, squilla and lobster) using traditional chemical methods (deproteinisation and demineralization) and its physicochemical and structural properties were characterized. The chitin content of crustacean shell waste ranged from 17.50% to 23.75% on a dry weight basis. The molecular weight analyses revealed that the crustacean chitin showed low molecular weight. The results of X-ray diffraction analysis (XRD), Fourier transform infrared spectroscopy (FT-IR), Energy dispersive X-ray analysis (EDAX), scanning electron microscopy (SEM) and thermogravimetry/differential thermal analysis (TG/DTA) confirmed that the α-chitins isolated from crustacean shell waste were similar to commercial crustacean chitin. The crystalline index value of the extracted chitin varied from 80.3% to 80.8%. The infrared spectroscopy analysis of the crustacean chitin exhibited two bands at around 1660 and 1620 cm^{-1}. SEM analysis of the extracted chitin showed the nanofibre and nanopore structures. Additionally, thermal stability of the crustacean chitin was close to that of the commercial chitin. Therefore, the results of this study confirmed that the extracted chitin is in α-form.

1. Introduction

Chitin is the second most abundant structural aminopolysaccharide next to cellulose in nature. It is an insoluble linear biopolymer comprising of 1,4-linked β-D-N-acetyl-glucosamine units (Fig. 1) and mostly occurs in crustacean shells (Kumari et al., 2017; Haripriya et al., 2018), insects (Waśko et., 2016; Kaya et al., 2016; Kim et al., 2017; Ibitoye et al., 2018), fungal species (Kaya et al., 2015a; Ospina Álvarez et al., 2014; Hassainia et al., 2017), mollusks (Rasti et al., 2016; Mohan et al., 2019) fish scales (Alabaraoye et al., 2017; Rumengan et al., 2017), coralline algae (Rahman & Halfar, 2014), polyzoa (Kaya et al., 2015b), freshwater sponge (Ehrlich et al., 2013) and black coral (Bo et al., 2012). The non-toxic, biodegradable and biocompatible properties of chitinous products such as chitosan and chitooligosaccharides have been used in biomedical field, textiles processing, waste water treatment and agricultural applications (Hirano, 1996; Nguyen et al., 2016).

The crustacean processing industries produces large number of by-products such as crustacean shells that accounts for 50–70% of raw materials. The improper disposal of crustaceans shells results in severe environmental problems such as off odour and sedimentation of minerals in landfill. Hence, conversion of the shell waste material into valuable products is one strategy to mitigate its environmental problems. The principal components of crustacean (shrimp, crab, lobster, squilla and krill) shells are chitin (15–40%), protein (20–40%), calcium and magnesium carbonate (20–50%), together with other minor components such as lipid, astaxanthin and minerals (Khoushab & Yamabhai, 2010). The removal of other substances (protein, lipid and other impurities) are essential to produce chitin. The chitin and its derived products are used to produce cost-effective aquatic feed and biofertilizers.

The chemical extraction of chitin from crustacean shells includes demineralization using strong acid and deproteinization using strong alkali; this process eliminates $CaCO_3$ and proteins (Shimahara & Takiguchi, 1988). The acid concentration and the time of treatment depends on the sources of chitin. High temperature is an undesirable factor that degrades the polymers (Roberts, 1992). In the present study, the α-chitin was extracted from marine crustacean shell waste. The percentage of chitin content in the crustacean shells was determined and the chemical and physical properties were characterized using XRD, FT-IR, EDAX, SEM and TG/DTA techniques.

* Corresponding author.
E-mail address: kmohanphd@gmail.com (K. Mohan).

https://doi.org/10.1016/j.carpta.2021.100037
Received 19 May 2020; Received in revised form 5 January 2021; Accepted 21 January 2021
Available online 23 January 2021

2. Materials and Methods

2.1. Source of Marine Crustacean Shell Waste

The shells of crustacean including shrimp (*Litopenaeus vannamei* and *Penaeus monodon*), crab (*Portunus sanguinolentus* and *Scylla serrata*), squilla (*Oratosquilla nepa* and *Harpiosquilla harpax*) and lobster (*Panulirus homarus* and *Thenus orientalis*) were collected from Annankoil, Mudasalodai and Pazhayar fish landing centre, Tamil Nadu and washed in neutral running water to remove impurities. The washed shells were boiled in water for 30 min to eliminate tissues by scraping and dried in a hot air oven at 100 °C for 60 min and ground into a fine powder using laboratory blender for chitin extraction.

2.2. Chitin Extraction

The shell powder (25 g) of each crustacean was used for chitin extraction. Demineralization was performed using HCl (2 M) at 60 °C for 150 min with continuous stirring. After decalcification, the shell powders were filtered and thoroughly washed using distilled water until the pH was neutral. Deproteinization was carried out by using 3M NaOH (for 120 min at 80 º C). Decolourisation of the demineralized and deproteinized products was done using 1:2:4 ratios of chloroform, methanol and distilled water and the decoloured products were kept in a hot air oven for 24 h at 60 °C. The final extracted chitin was stored in a refrigerator until further use. The schematic extraction method is shown in the Fig. 2 (No & Meyers, 2000; Kaya et al., 2013). The commercial chitin (Source: Shrimps, Pcode: 98507) was obtained from Sisco Research Laboratories (SRL), India and used for comparison with crustacean chitin.

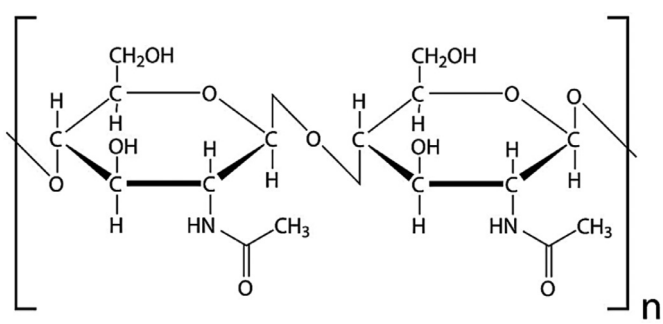

Fig. 1. Chemical structure of extracted chitin

2.3. Physico-Chemical Properties of Extracted Chitin

2.3.1. Yield, Moisture and Ash Levels

The chitin yield of each crustacean shell was expressed as a percentage of the weight of the raw material. The ash and moisture contents were determined according to the previous standard AOAC (1990) methods.

2.3.2. Degree of Acetylation Measurement

The degree of acetylation (DA) was performed using the acid-base titration method (Domard & Rinaudo, 1983) with some alterations. In short, 0.25 g of each of the extracted chitin samples were dissolved in 30 ml of 0.1 mol/l HCl aqueous solution at 24 °C, followed by stirring for 50 min to dissolve the chitin and cooled at 24 °C. To this suspension, methyl orange (5 to6 drops) was added. The chitin solution was titrated against 0.1 mol/l of NaOH until the color turned from red to orange (Domard & Rinaudo, 1983). The DA was calculated as follows

$$NaOH + HCl \rightarrow NaCl + H_2O \quad (1)$$

$$\text{Concentration of standard HCl aqueous solution(mol/l)} = (\text{volume of standard NaOH solution consumed during titration(ml)} \times \text{NaOH(mol/l)})/\text{volume of the standard HCl aqueous solution used to dissolve chitin(ml)} \quad (2)$$

$$\text{No of moles of HCl reacted with chitin} (\text{Concentration of standard HCl aqueous solution(mol/l)} \times \text{volume of the standard HCl aqueous solution used to dissolve chitin(ml)})/1000 \quad (3)$$

$$\text{Chitin mass} = \text{no of moles chitin} \times \text{molar mass of chitin}$$

$$\text{DA(\%)of chitin} = (\text{Mass of chitin(g)}/\text{Mass of the sample(g)}) \times 100 \quad (4)$$

2.3.3. Solubility of Chitin

Precisely, 0.1 g of each crustacean shell was dissolved in acetic acid (40 % v/v, 10 ml) with the help of an incubator shaker (12 × g at 25 °C for 30 min). Further, the suspension was submerged in a boiling water bath for 10 min and cooled at 25 °C. The cooled suspension was centrifuged (20160 × g for 10 min) and discarded. The undissolved particles were washed in distilled water and dried at 60 °C for 24 h. The dried particles were weighed and the solubility was calculated using the formula of Brine & Austin (1981):

$$\text{Solubility}(\%) = \left[(W2 - W1/W2)\right] \times 100 \quad (5)$$

Where,

W1 is the weight (g) of the insoluble chitin, and W2 is the total weight (g) of the chitin.

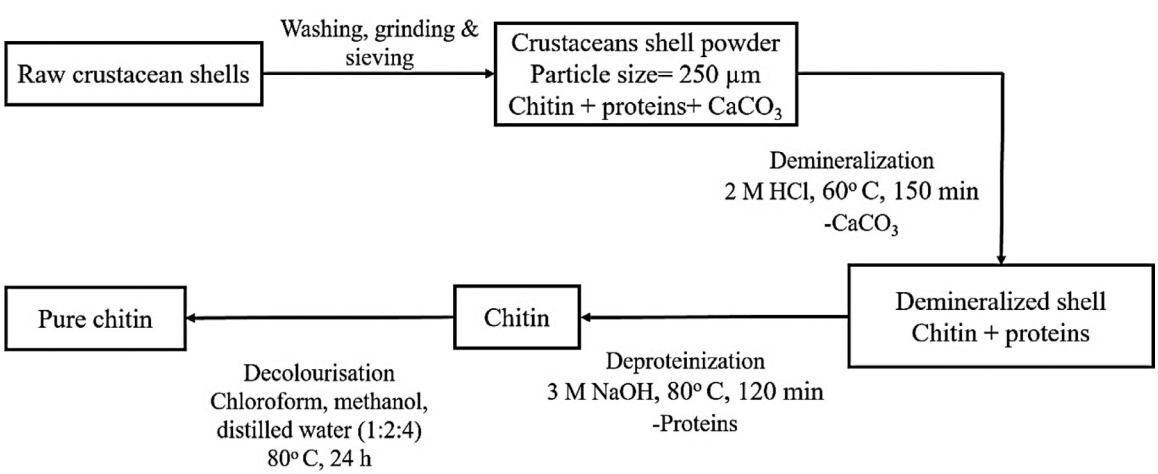

Fig. 2. Schematic representation of the production of chitin from crustacean shell waste

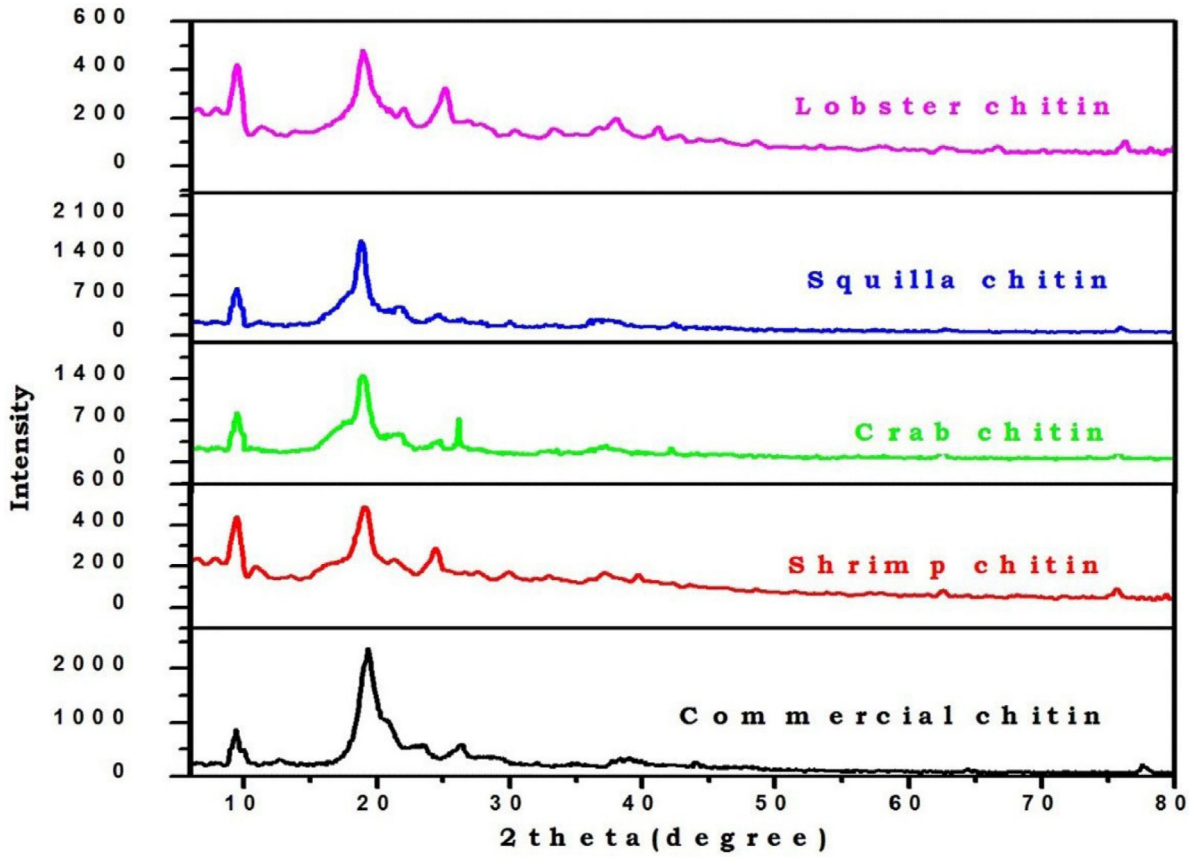

Fig. 3. XRD analysis of chitin from crustacean shell waste

2.3.4. Determination of Molecular Weight of Chitin

Each extracted chitin sample was dissolved in 5% w/v LiCl-DMAc and the viscosity-average molecular weight (Mv) determined using an Ubbelohde type dilution viscometer at 25°C. The Mv of each extracted chitin sample was determined by mark-Houwink mathematical equation described by Wang (1991).

$$[\eta] = kM^{\alpha} \tag{6}$$

k- Chosen solvent, M- Average Mv and α-function of polysaccharide type. Chitin and solvent, these values are 1.82×10^{-3} and 0.93 are the particular values and are not function of deacetylation degree (Terbojevidh & Cosani, 1997).

2.4. Structural Characterization of Extracted Chitin

2.4.1. X-Ray Diffraction Analysis (XRD)

The crystallinity of the extracted crustacean chitin was recorded with XRD (XRD 6000, Shimadzu). Data were collected at 2θ with a scan angle ranged between 5° and 45° and the crystalline index (CrI) was determined according to the formula of Liu et al. (2012).

$$\mathrm{CrI}\,100 = \left[(\mathrm{I110} - \mathrm{Iam}/\mathrm{I110})\right] \times 100 \tag{7}$$

Where, I_{110} is the maximum intensity of the (110) diffraction peak at $2\theta = 20^{\circ}$ and I_{am} is the amorphous diffraction signal at $2\theta = 16^{\circ}$ (Liu et al., 2012).

2.4.2. Fourier-Transform Infrared Spectroscopy Analysis (FT-IR)

Around 1 mg of each crustacean chitin was analyzed in FTIR spectrometer (IR Prestige 21, Shimadzu) with absorption between 4000 and 400 cm^{-1} to determine the IR bands.

2.4.3. Surface Morphology Analysis

Surface morphology of extracted chitin was studied using scanning electron microscope (JEOL JEM 6390). About 5 mg of each chitin sample was coated with gold using Gatan Precision Etching Coating System and kept in the goldcoating system for 25 s before SEM analysis.

2.4.4. Energy-Dispersive X-ray Spectroscopy (EDAX)

The elemental composition of each extracted crustacean chitin was analysed using EDAX, INCA energy 250 LN2 closed model.

2.4.5. Thermo Gravimetry/Differential Thermal (TG/DTA) Analysis

The thermal stability of the extracted crustacean chitin and commercial chitin was studied using TG/DTA analyser (DTG-60H, Shimadzu). For this analysis, 1 mg of each crustacean chitin samples was heated at 10 °C/min from 25 °C to 650 °C.

3. Results and Discussion

3.1. Extraction Yield

In the present study, it was observed that the dry weight of chitin extracted from shrimps (*L. vannamei* and *P. monodon*), crabs (*P. sanguinolentus* and *S. serrata*), squilla (*O. nepa* and *H. harpax*) and lobsters (*P. homarus* and *T. orientalis*) shell waste varied from 17.50 to 23.75% (Table 1). The chitin contents of the crustacean shell ranged from 7 to 40% and it varied from species to species (Tolaimate et al., 2003). The shell waste of crustaceans has been used for the manufacturing of commercial chitin due to the presence of high levels of chitin (19–27%) (Cortizo et al., 2008; Al Sagheer et al., 2009; Wang et al., 2013). The yield of chitin content from *Penaeus monodon*, house cricket, *Fomitopsis pinicola, Ganoderma lucidum, Agaricus bisporus, Conus inscriptus*, fish scales and *Plumatella repens* were 30%, 7.1%, 30.11%, 34%, 7.4%,

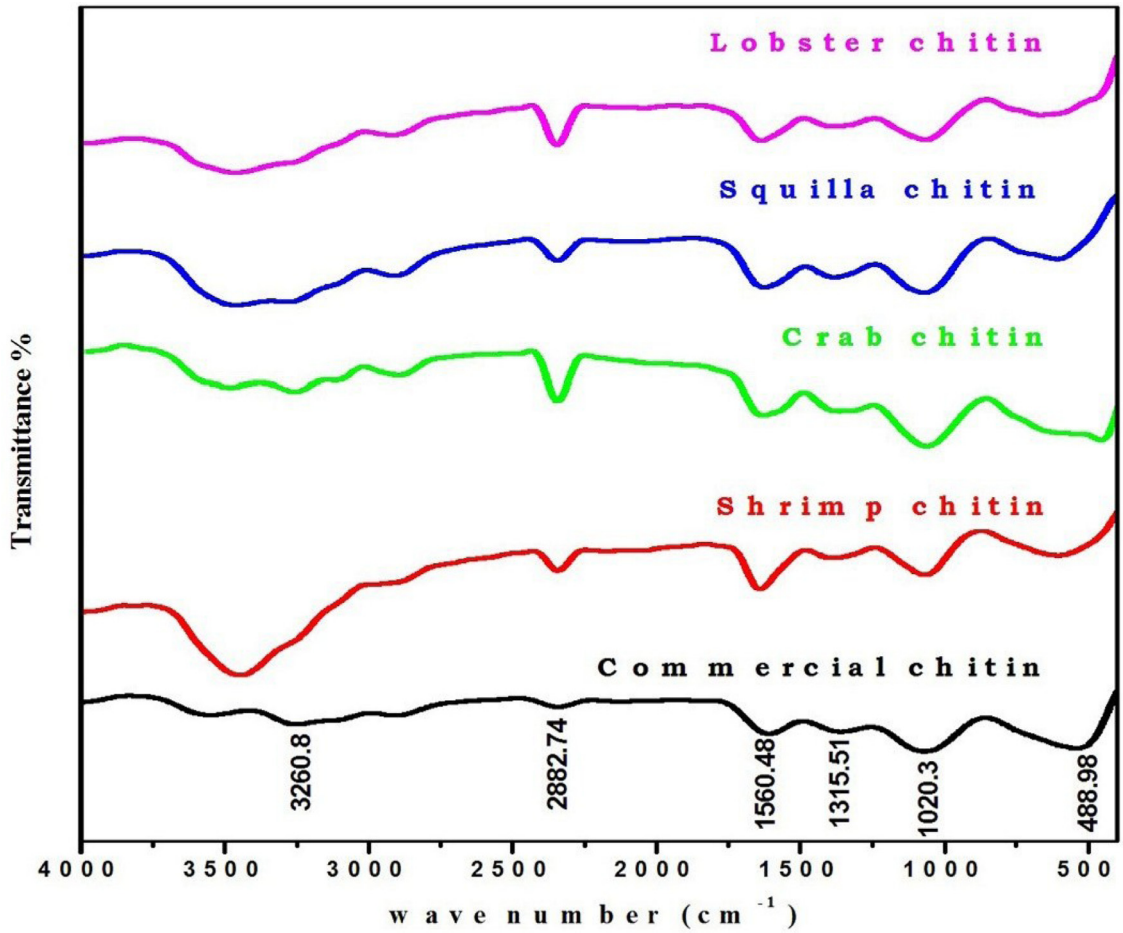

Fig. 4. FT-IR analysis of chitin from crustacean shell waste

Table 1
Yield of chitin (%) obtained from marine crustacean shell waste

Crustacean shell waste	Yield of chitin (%)
Commercial chitin	Not available
Shrimp shell waste	20.00
Crab shell waste	21.25
Squilla shell waste	23.75
Lobster shell waste	17.50

21.65%, 31.11% and 13.3% respectively (Haripriya et al., 2018; Ibitoye et al., 2018; Kaya et al., 2015a; Ospina Álvarez et al., 2014; Hassainia et al., 2017; Mohan et al., 2019; Alabaraoye et al., 2017; Kaya et al., 2015b). In the present study also a similar level of yield was obtained as reported in the earlier studies.

3.2. Physico-Chemical Properties of Extracted Chitin

3.2.1. Ash and Moisture Contents

The ash content of the chitin samples ranged from 1.08 to 5.54%, with shrimp chitin having the highest and squilla chitin the lowest ash (Table 2). Ash is the inorganic remains that form after entire degradation of chitin by heating in the presence of air. The quantification of ash in chitin is a vital indicator for the demineralization process. Generally, about 31% to 36% of ash can be removed from crustacean shell waste using demineralization process (Kaya et al., 2015a). Commercial-grade chitin should contain <1 % of ash content (Nessa et al., 2010). In the present study, the low level of ash content in squilla chitin shows that it is the better quality of chitin. The moisture content of chitin extracted from crustacean shell waste ranged from 5.35 to 7.50% (Table 2). The low amount of moisture content indicates a considerable amount of dry matter. The moisture content of the current study was less than the chitin isolated from shrimp, crab and squilla shell (8–9%) in earlier studies (Parthiban et al., 2017).

3.2.2. Determination of Degree Of Acetylation (DA)

The results of DA in this study showed that the chitin from the shrimp shell waste had the highest DA, followed by the chitin from other shells (Table 2). This might be due to the use of sodium hydroxide which leads to the enhancement of the DA. The DA is considered as one of the significant parameters as it influences the physicochemical properties of the chitin. In this study, the maximum DA was observed in the chitin extracted from shrimp shell waste than the chitin from other shells. Earlier studies reported that the DA values of marine seashell waste chitin varied from 51.61% to 91% (Alabaraoye et al., 2017).

3.2.3. Solubility

In this study, the chitin extracted from squilla showed better solubility; however, shrimp and crab chitin showed slightly lower solubility and lobster shell waste chitin had the least solubility (Table 2). The low ash content of the squilla shell chitin could be one of the reasons for its enhanced solubility. The lesser solubility of lobster, shrimp and crab chitin might be due to the strong inter and intramolecular bonds within the hydroxyl and acetamide group as noticed by Urbariczyk et al. (1997). Similarly, Alabaraoye et al. (2017) reported that the solubility of marine seashell waste chitin (mussel, oyster, prawn, crab, pang and silver scales) ranged from 58.33% to 85.71%.

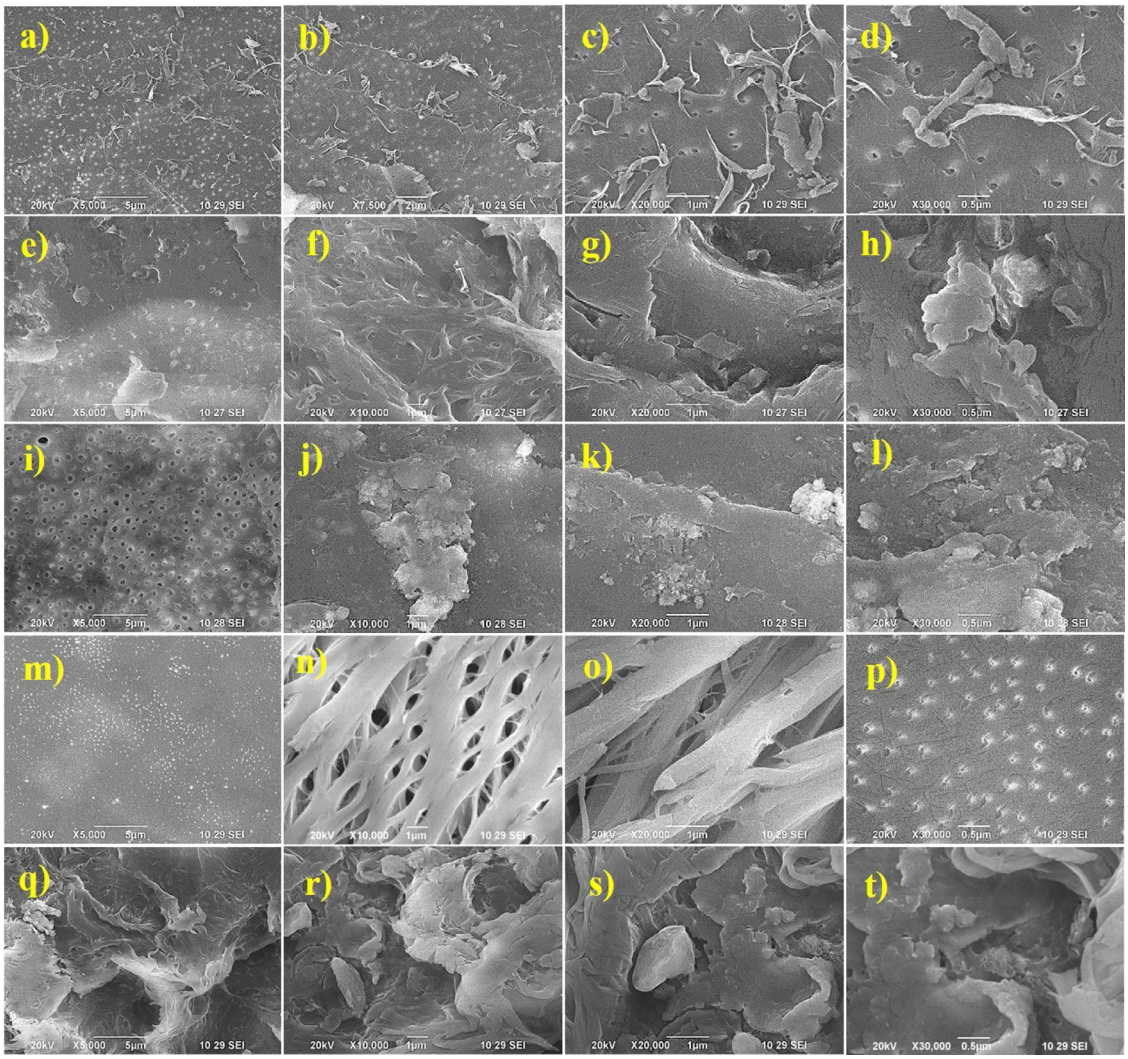

Fig. 5. SEM photographs of chitin from crustacean shell waste (a, b, c, d- commercial chitin; e, f, g, h-shrimp chitin; i, j, k, l-crab chitin; m, n, o, p-squilla chitin; and q, r, s, t-lobster chitin)

Table 2
Physicochemical properties of chitin extracted from crustacean shell waste

Crustacean shell waste chitin	Ash (%)	Moisture (%)	Molecular weight (kDa)	Degree of acetylation (DA %)	Solubility (%)	Appearance
Commercial chitin	2.00	10 (Max)	40	90	70	White
Shrimp chitin	5.54	7.50	25	79	58	Brownish white
Crab chitin	3.50	5.60	23	70	53	Brownish
Squilla chitin	1.08	6.20	21	68	65	White
Lobster chitin	4.15	5.35	20	65	46	Light brownish

3.2.4. Average Viscosity of Molecular Weight

The dilute solution viscometry (DSV) was used for calculating the viscosity-average molecular weight of the chitin extracted from the crustacean shell waste and commercial chitin. The Mv of the extracted chitin varied from 20 to 25 kDa (Table 2). In the present study, the chitin obtained from the crustacean shells showed lower Mv than the commercial chitin (40 kDa). It is challenging to determine the Mv of chitin as it possesses low solubility (Aranaz et al., 2009). There are number of research studies that have determined the Mv of chitin. Jang et al. (2004) used the average viscosity method to determine the Mv of alpha-chitin, beta-chitin and gamma-chitin. The low Mv of chitin extracted from shrimp shell waste was 2.8 kDa; it was also previously described by Salah et al. (2013). From this study it was found that the chitin extracted from crustacean shell has low Mv. In general, low Mv chitin has been classified as those that are below 50 kDa, medium Mv chitin ranges between 50 to 150 kDa and high Mv chitin have Mv higher than 150 kDa (Goy et al., 2009). The determination of Mv of chitin, chitosan and chitooligosaccharides have one of the important criteria in the manufacturing process (Dutta et al., 2004; Aranaz et al., 2009; Muzzarelli, 2011). The various Mv of chitin can be used in many useful areas. Salah et al. (2013) stated that low Mv chitin is the attractive targets for the chemo-drug carrier in cancer treatment.

3.3. Structural Characterization of Extracted Chitin

3.3.1. XRD analysis

The XRD peaks of chitin extracted from the crustacean shell waste are shown in Table 3. The broad peak of shrimp, crab and squilla chitin

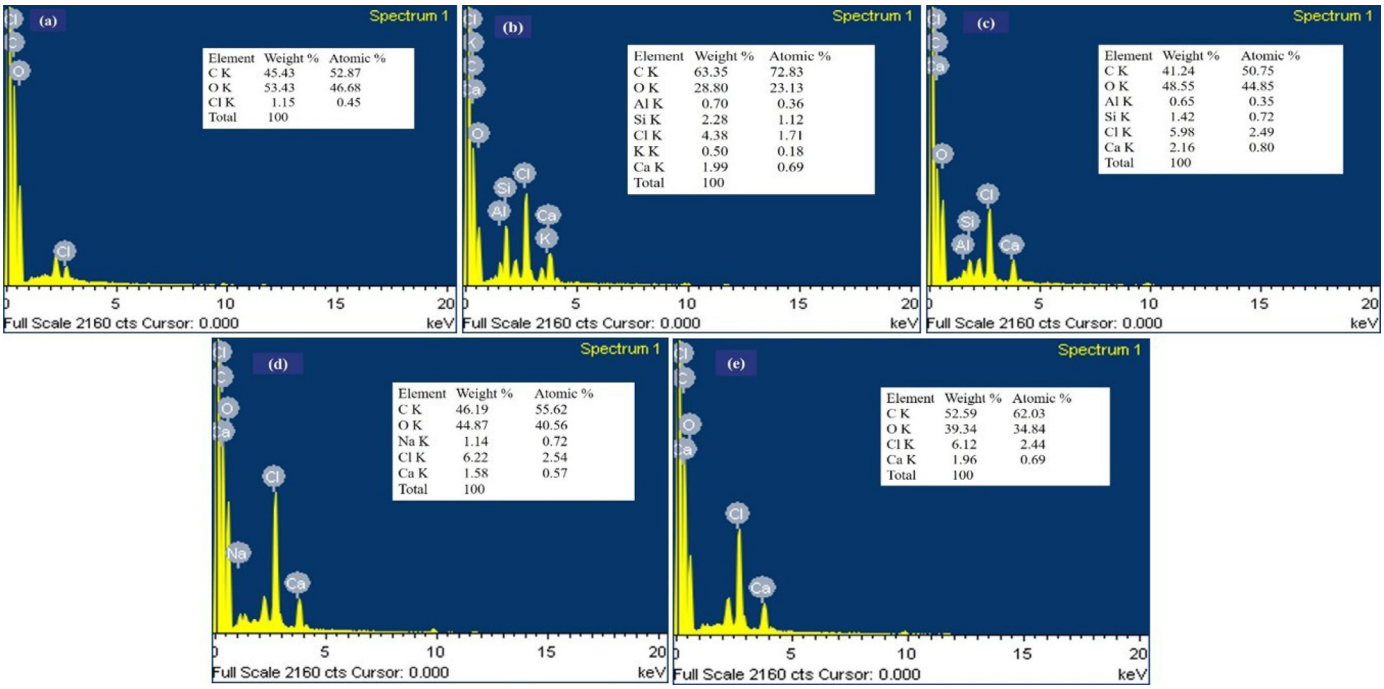

Fig. 6. Elemental (EDAX) analysis of chitin from crustacean shell waste (a. commercial chitin b. shrimp chitin c. crab chitin d. squilla chitin and e. lobster chitin)

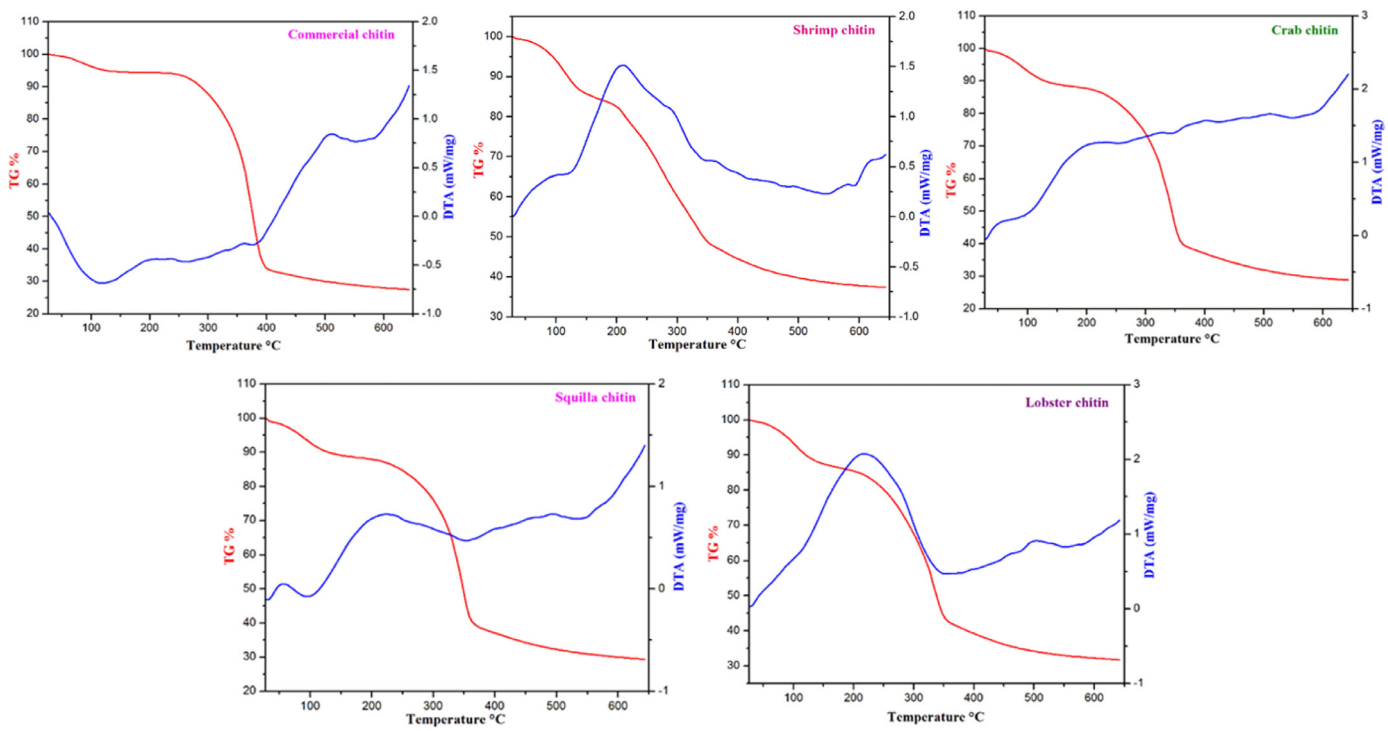

Fig. 7. TG/DTA analysis of chitin from crustacean shell waste

Table 3
XRD peaks and CrI values of chitin extracted from crustacean shell waste

Crustacean shell waste chitin	Crystalline peaks	CrI (%)
Commercial chitin	9.3, 13.3, 19.3, 21.1, 23.1, 26.1, 28.2, 39.0, 43.9, 77.6	80.7
Shrimp chitin	9.5, 13.1, 19.5, 21.1, 23.4, 26.4, 28.2, 39.1, 43.5, 77.4	80.5
Crab chitin	9.6, 13.2, 19.5, 21.0, 23.1, 26.1, 28.0, 39.0, 43.9, 77.5	80.8
Squilla chitin	9.4, 13.0, 19.5, 21.3, 23.4, 26.4, 28.1, 39.0, 44.1, 77.8	80.5
Lobster chitin	9.4, 13.6, 19.7, 21.2, 23.9, 26.8, 28.6, 39.7, 43.0, 78.0	80.3

Table 4
FT-IR bands of chitin extracted from crustacean shell waste and commercial chitin

Functional groups and vibration mode	Classification	Shrimp chitin	Crab chitin	Squilla chitin	Lobster chitin	Commercial chitin
O-H stretching	-	3442	3443	3445	3443	3260
N-H stretching	-	3261-3102	3260-3100	3260-3105	3263-3102	3261-3102
CH_3 sym. stretching and CH_2 sym. Stretch	Aliphatic compounds	2925	2927	2930	2935	2931
CH_3 sym. Stretch	Aliphatic compound	2879	2880	2881	2885	2882
C=O secondary amide stretch	Amide I	1658	1662	1665	1653	1663
C=O secondary amide stretch	Amide I	1620	1621	1621	1620	1622
N-H bend, C-N stretch	Amide II	1556	1560	1556	1549	1560
CH_2 ending and CH_3 deformation	-	1420	1415	1417	1416	1425
CH_2 bend, CH_3 sym. Deformation	-	1379	1379	1378	1376	1378
CH_2 wagging	Amide III, components of proteins	1308	1307	1307	1306	1315
C–O–C, C–O–P, P–O–P sym. stretch	Oligo and polysaccharide	1205	1204	1208	1205	1210
C-O-C asym. stretch in phase ring	Saccharide ring	1074	1075	1076	1074	1020
CH_3 wagging	Alone chain	951	952	954	950	955
CH ring stretching	Saccharide ring	885	886	885	886	890

showed similar crystalline structure, however, lobster chitin and commercial chitin were slightly differed. Four sharp and six weak peaks were observed in all the samples (Fig. 3). Yen et al. (2009) stated that the crystalline structural peaks at 9.1 and 20.3 are related to β-chitin, whereas the peaks at 9.6, 19.6, 21.1 and 23.7 represents α-chitin. In this study, the peaks detected in α-chitin that are extracted from crustacean shell waste was found to be similar to other organisms such as insects, crustaceans, anthozoans and fungi (Liu et al., 2012; Sajomsang & Gonil, 2010; Juárez-de La Rosa et al., 2012; Ifuku et al., 2011). The CrI values of the extracted chitin varied from 80.3% to 80.8% (Table 3). It has been revealed in earlier studies that CrI values of chitin varied from 47% to 91% according to species and extraction methods (Liu et al., 2012; Kaya et al., 2015a). Yen and Mau (2007) extracted the crab chitin using various extraction methods and found two crystal-like peaks at $2\theta = 9.3^o$ and 19.1^o in XRD analysis. Likewise, Cárdenas et al.(2004) reported that XRD analysis of α-chitin and β-chitin indicated their main characteristic peak at 19.2–19.3° and 19.3° respectively. In XRD of α-chitin structures, peaks at 26° were observed, related to those in this study (Cárdenas et al., 2004; Liu et al., 2012; Yen et al., 2009; Sajomsang & Gonil, 2010; Juárez-de La Rosa et al., 2012). Moreover, the intense peak of extracted chitin was broader than the commercial chitin, which shows the moderate purity of chitin extracted from crustacean shell waste.

3.3.2. FT-IR Analysis

The FT-IR spectra of chitin are shown in Fig. 4 and Table 4. The two bands around 1,650 and 1,620 cm^{-1} confirms the presences of amide I group. Whereas, in the β chitin, there was only one band around 1,650 cm^{-1} (Jang et al., 2004). FT-IR spectroscopy can determine the structure (α or β crystal) of the chitin molecule by referring the different hydrogen bonds. Chitin in the α -crystal form has two intermolecular hydrogen bonds (Cárdenas et al., 2004). The peaks in FT-IR spectrum significantly varied in the extracted chitin from crustacean shell waste than the commercial chitin (Fig. 4). Moreover, the absorption peak at 3620 cm^{-1}, which is attributed in the commercial chitin owing O-H vibration (Hydroxyl group). The FT-IR bands observed are closely matched with the previous reports (Acosta et al., 1993; Kumari et al., 2015). Brugnerotto et al. (2001) observed the bands at 3436 cm^{-1} of a hydroxyl group, 1661 and 1315 cm^{-1} for amide I and amide II bands, respectively. A similar kind of result has been reported by Zakaria et al. (2012) which explains that the band spectrum for hydroxyl group and $–NH_2$ at 3438 cm^{-1} and amide bands between 1639 and 1561 cm^{-1} are in close concurrence with the band spectrums obtained in this study. Moreover, the FT-IR bands of the chitin examined in this study are very similar to the FT-IR bands of α- chitin extracted from the shells of different organisms in previous studies (Liu et al., 2012; Kaya et al., 2015a; Juárez-de La Rosa et al., 2012; Ifuku et al., 2011; Al Sagheer et al., 2009; Wang et al., 2013). These results indicated that the chitin extracted from crustacean shell waste are in α-form.

3.3.3. SEM Analysis

The surface morphology of the extracted chitin was examined. The surface morphology varied among species (Fig. 5). The shrimp and crab shell waste chitin showed nanopore-based arrangements at lower magnification and nanofiber arrangements at higher magnification (Fig. 5 e-l). In case of squilla, the surface morphology was *vice versa*, nanofibre was observed at low magnification and nanopore at higher magnification (Fig. 5 m-p). However, only nanofibres were observed in lobster chitin (Fig. 5 q-t). The result of SEM analysis indicated that the commercial chitin had shown regularly arranged dense pores with irregularly arranged dense nanofibres on its surface (Fig. 5 a-d). The surface structure is one of the most significant properties of chitin which determines the effective use of chitin and its major derivative products (Aranaz et al., 2009). Synowiecki and Al-Khateeb (2003) stated that the number of pores in the chitin surface increases the chitin's capacity of the sorbent to absorb metal ions. The chitins with nanofibrous structure can be used in textiles processing. Moreover, the porous chitin structure has been used as a perfect material for tissue engineering and stem cell technologies (Aranaz et al., 2009). It could be seen from earlier studies that the surface morphology of chitin and its by-products acquired from crab, krill, insects and fungi are different (Al Sagheer et al., 2009; Wang et al., 2013; Paulino et al., 2006; Yen et al., 2007b). Liu et al. (2012) described that commercial chitin from shrimp has an uneven and thick surface with a clear arrangement in a microfibrillar crystalline structure.

3.3.4. Elemental (EDAX) Analysis

The elemental analysis of the crustacean shell waste and commercial chitin were proved in Fig. 6. The EDAX spectrum of crustacean shell waste chitin and commercial chitin showed the presence of carbon, oxygen, chlorine, sodium, calcium, potassium, aluminium and silicon (Fig. 6). The intensity of the peaks for elements were maximum for shrimp chitin followed by crab, squilla and lobster chitin (Fig 6 b, c, d, e), whereas commercial chitin showed minimal peak intensities (Fig. 6 a). In previous studies, the EDAX spectrum of chiton, conus, shrimp, fish and crayfish chitin and chitosan showed the highest carbon, oxygen content and a trace amount of minerals (calcium, sodium, iron and zirconium) (Kumari et al., 2016; Ghannam et al., 2016; Rasti et al., 2017; Mohan et al., 2019). Based on the previous studies, it was observed that the chitin extracted in this study is of high purity.

3.3.5. TG/DTA Analysis

The thermal stability analysis results showed that the decomposition of chitin extracted from crustacean shell proceeds in two major stages (Table 5 and Fig. 7). The degradation of shrimp chitin was 10% in the first stage and 38% in the second stage. The mass losses of crab, squilla and lobster chitin ranged from 8% to 10% in the first stage and ranged from 44% to 54% in the second stage respectively. The mass loss in

Table 5
TG/DTA analysis of chitin from crustacean shell waste

Crustacean shell waste chitin	% of the first mass loss	% of the second mass loss	DTA max (°C)	DTA Endothermic (°C)	DTA Exothermic (°C)
Commercial chitin	4	64	380	117	361
Shrimp chitin	10	38	351	118	209
Crab chitin	8	54	357	104	325
Squilla chitin	10	50	359	96	223
Lobster chitin	10	44	356	348	-

the first and second stages are due to the evaporation of water in the chitin structure and polymer degradation, respectively (Paulino et al., 2006). The maximum mass loss occurring in the second step was observed in the chitin extracted from crab shell waste, and the minimum mass loss was observed in the chitin extracted from shrimp shell waste. The results of the TGA analysis of chitin extracted from crab, shrimp and insects in earlier studies indicated that the mass losses appear in two different stages (Al Sagheer et al., 2009; Juárez-de La Rosa et al., 2012; Abdou et al., 2008). The maximum degradation temperature (DTGmax) of chitin extracted from shrimp, crab, squilla and lobster ranged from 351 °C to 359 °C. The DTGmax value of alpha chitin differed from 350 °C to 400 °C and this has been reported in previous studies (Paulino et al., 2006; Wang et al., 2013; Kaya et al., 2015a; Abdou et al., 2008; Juárez-de La Rosa et al., 2012; Jang et al., 2004; Aranaz et al., 2009). Wysokowski et al. (2015) reported that of chitin extracted from marine sponge possess very high thermal stability. In this study, the DTGmax temperatures of extracted chitin varied among the species and similar to previous studies (Paulino et al., 2006; Abdou et al., 2008; Wysokowski et al., 2015). The TG/DTA analysis of the crustacean chitin was almost similar to commercial chitin.

4. Conclusion

In this study, chitins were extracted from crustacean shell wastes in good yield and were structurally characterized. The results showed that all of the chitins were in the alpha form and of low molecular weight. Further, this study revealed that chitin extracted from the crustacean shell waste consists of nanoporous and nanofibre structures. Hence, the present study suggests that the selected crustaceans shell waste can be considered as a potential source of chitin for various applications.

Declaration of Competing Interest

The authors declare that they have no known competing financial interests or personal relationships that could have appeared to influence the work reported in this paper.

Acknowledgements

This research did not receive any specific grants from funding agencies in the public, commercial, or non-profit sectors. I sincerely thank Department of Zoology, Sri Vasavi College, Erode for supporting and providing essential infrastructure facilities needed for this study.

References

Abdou, E. S., Nagy, K. S., & Elsabee, M. Z. (2008). Extraction and characterization of chitin and chitosan from local sources. *Bioresource Technology, 99*, 1359–1367.
Acosta, N., Jiménez, C., Borau, V., & Heras, A. (1993). Extraction and characterization of chitin from crustaceans. *Biomass and Bioenergy, 5*, 145–153.
Alabaraoye, E., Achilonu, M., & Hester, R. (2017). Biopolymer (Chitin) from various marine seashell waste: isolation and characterization. *Journal of Polymers and the Environment, 26*, 2207–2218.
Al Sagheer, F. A., Al-Sughayer, M. A., Muslim, S., & Elsabee, M. Z. (2009). Extraction and characterization of chitin and chitosan from marine sources in Arabian Gulf. *Carbohydrate Polymers, 77*, 410–419.
Aranaz, I., Mengíbar, M., Harris, R., Paños, I., Miralles, B., Acosta, N., Galed, G., & Heras, Á. (2009). Functional characterization of chitin and chitosan. *Current Chemistry and Biology, 3*, 203–230.
Association of Official Analytical Chemists; In E. Horritz (Ed.), Official methods of analysis (15th ed.). Washington, 1990, DC:, method#930.15 p 69, method #942.05 p 70, method #962.09 p 80.
Bo, M., Bavestrello, G., Kurek, D., Paasch, S., Brunner, E., Born, R., Galli, R., Stelling, A. L., Sivkov, V. N., Petrova, O. V., & Vyalikh, D. (2012). Isolation and identification of chitin in the black coral *Parantipathes larix* (Anthozoa: Cnidaria). *International Journal of Biological Macromolecules, 51*, 129–137.
Brine, C. J., & Austin, P. R. (1981). Chitin isolates: species variation in residual amino acids. *Comparative Biochemistry and Physiology. Part B, Biochemistry & Molecular Biology, 70*, 173–178.
Brugnerotto, J., Lizardi, J., Goycoolea, F. M., Argüelles-Monal, W., Desbrieres, J., & Rinaudo, M. (2001). An infrared investigation in relation with chitin and chitosan characterization. *Polymer, 42*, 3569–3580.
Cárdenas, G., Cabrera, G., Taboada, E., & Miranda, S. P. (2004). Chitin characterization by SEM, FTIR, XRD, and 13C cross polarization/mass angle spinning NMR. *Journal of Applied Polymer Science, 93*, 1876–1885.
Cortizo, M. S., Berghoff, C. F., & Alessandrini, J. L. (2008). Characterization of chitin from *Illex argentinus* squid pen. *Carbohydrate Polymers, 74*, 10–15.
Domard, A., & Rinaudo, M. (1983). Preparation and characterization of fully deacetylated chitosan. *International Journal of Biological Macromolecules, 5*, 49–52.
Dutta, P. K., Dutta, J., & Tripathi, V. S. (2004). Chitin and chitosan: Chemistry, properties and applications. *Journal of Scientific & Industrial Research, 63*, 20–31.
Ehrlich, H., Kaluzhnaya, O. V., Brunner, E., Tsurkan, M. V., Ereskovsky, A., Ilan, M., Tabachnick, K. R., Bazhenov, V. V., Paasch, S., Kammer, M., & Born, R. (2013). Identification and first insights into the structure and biosynthesis of chitin from the freshwater sponge *Spongilla lacustris*. *Journal of Structural Biology, 183*, 474–483.
Ghannam, H. E., Talab, A. S., Dolgano, N. V., Husse, A., & Abdelmagui, N. M. (2016). Characterization of chitosan extracted from different crustacean shell wastes. *Journal of Applied Science, 16*, 454–461.
Goy, R. C., Britto, D. D., & Assis, O. B. (2009). A review of the antimicrobial activity of chitosan. *Polímeros, 19*, 241–247.
Haripriya, S., Kanayairam, V., & Ravichandran, R. (2018). Chitin and chitosan preparation from shrimp shells *Penaeus monodon* and its human ovarian cancer cell line, PA-1. *International Journal of Biological Macromolecules, 107*, 662–667.
Hassainia, A., Satha, H., & Boufi, S. (2017). Chitin from *Agaricus bisporus*: extraction and characterization. *Int. J. Biol. Macromol.* https://doi.org/10.1016/j.ijbiomac.2017.11.172.
Hirano, S. (1996). Chitin biotechnology applications. *Biotechnology Annual Review, 2*, 237–258.
Ibitoye, E. B., Lokman, I. H., Hezmee, M. N. M., Goh, Y. M., Zuki, A. B. Z., & Jimoh, A. A. (2018). Extraction and physicochemical characterization of chitin and chitosan isolated from house cricket. *Biomedical Materials, 13*, Article 025009.
Ifuku, S., Nomura, R., Morimoto, M., & Saimoto, H. (2011). Preparation of chitin nanofibers from mushrooms. *Materials, 4*, 1417–1425.
Jang, M. K., Kong, B. G., Jeong, Y. I., Lee, C. H., & Nah, J. W. (2004). Physicochemical characterization of α-chitin, β-chitin, and γ-chitin separated from natural resources. *Journal of Polymer Science A Polymer of Chemical, 42*, 3423–3432.
Juárez-de La Rosa, B. A., Quintana, P., Ardisson, P. L., Yáñez-Limón, J. M., & Alvarado-Gil, J. J. (2012). Effects of thermal treatments on the structure of two black coral species chitinous exoskeleton. *Journal of Materials Science, 47*, 990–998.
Kaya, M., Sargin, I., Tozak, K. Ö., Baran, T., Erdogan, S., & Sezen, G. (2013). Chitin extraction and characterization from *Daphnia magna* resting eggs. *International Journal of Biological Macromolecules, 61*, 459–464.
Kaya, M., Akata, I., Baran, T., & Menteş, A. (2015a). Physicochemical properties of chitin and chitosan produced from medicinal fungus (*Fomitopsis pinicola*). *Food Biophysics, 10*, 162–168.
Kaya, M., Baublys, V., Šatkauskienė, I., Akyuz, B., Bulut, E., & Tubelytė, V. (2015b). First chitin extraction from *Plumatella repens* (Bryozoa) with comparison to chitins of insect and fungal origin. *International Journal of Biological Macromolecules, 79*, 126–132.
Kaya, M., Sargin, I., Aylanc, V., Tomruk, M. N., Gevrek, S., Karatoprak, I., Colak, N., Sak, Y. G., & Bulut, E. (2016). Comparison of bovine serum albumin adsorption capacities of α-chitin isolated from an insect and β-chitin from cuttlebone. *Journal of Industrial and Engineering Chemistry, 38*, 146–156.
Khoushab, F., & Yamabhai, M. (2010). Chitin research revisited. *Marine Drugs., 8*, 1988–2012.
Kim, M. W., Song, Y. S., Han, Y. S., Jo, Y. H., Choi, M. H., Park, Y. K., Kang, S. H., Kim, S. A., Choi, C., & Jung, W. J. (2017). Production of chitin and chitosan from the exoskeleton of adult two-spotted field crickets (*Gryllus bimaculatus*). *Entomological Research, 47*, 279–285.
Kumari, S., Rath, P., Kumar, A. S. H., & Tiwari, T. N. (2015). Extraction and characterization of chitin and chitosan from fishery waste by chemical method. *Environment Technology Innovation., 3*, 77–85.

Kumari, S., Rath, P., & Kumar, A. S. H. (2016). Chitosan from shrimp shell (Crangon crangon) and fish scales (Labeorohita): extraction and characterization Suneeta. *African Journal of Biotechnology, 15*, 1258–1268.

Kumari, S., Annamareddy, S. H. K., Abanti, S., & Rath, P. K. (2017). Physicochemical properties and characterization of chitosan synthesized from fish scales, crab and shrimp shells. *International Journal of Biological Macromolecules, 104*, 1697–1705.

Liu, S., Sun, J., Yu, L., Zhang, C., Bi, J., Zhu, F., Qu, M., Jiang, C., & Yang, Q. (2012). Extraction and characterization of chitin from the beetle *Holotrichia parallela* motschulsky. *Molecules (Basel, Switzerland), 17*, 4604–4611.

Mohan, K., Ravichandran, S., Muralisankar, T., Uthayakumar, V., Chandirasekar, R., Rajeevgandhi, C., Rajan, D. K., & Seedevi, P. (2019). Extraction and characterization of chitin from sea snail Conus inscriptus (Reeve, 1843). *International Journal of Biological Macromolecules, 126*, 555–560.

Muzzarelli, R. A. (2011). Biomedical exploitation of chitin and chitosan via mechano–chemical disassembly, electrospinning, dissolution in imidazolium ionic liquids, and supercritical drying. *Marine Drugs., 9*, 1510–1533.

Nessa, F., Masum, S. M., Asaduzzaman, M., Roy, S. K., Hossain, M. M., & Jahan, M. S. (2010). A process for the preparation of chitin and chitosan from prawn shell waste. *Bangladesh Journal of Science Industries Reserve, 45*, 323–330.

Nguyen, T. T., Zhang, W., Barber, A. R., Su, P., & He, S. (2016). Microwave-intensified enzymatic deproteinization of Australian rock lobster shells (*Jasus edwardsii*) for the efficient recovery of protein hydrolysate as food functional nutrients. *Food Bioprocess Tech, 9*, 628–636.

No, H. K., & Meyers, S. P. (2000). Application of chitosan for treatment of wastewaters. *Reviews of Environmental Contamination and Toxicology, 163*, 1–27.

Ospina Álvarez, S. P., Ramírez Cadavid, D. A., Escobar Sierra, D. M., Ossa Orozco, C. P., Rojas Vahos, D. F., Zapata Ocampo, P., & Atehortúa, L. (2014). Comparison of extraction methods of chitin from *Ganoderma lucidum* mushroom obtained in submerged culture. *BioMed Res. Int.*, Article 169071.

Parthiban, F., Balasundari, S., Gopalakannan, A., Rathnakumar, K., & Felix, S. (2017). Comparison of the quality of chitin and chitosan from shrimp, crab and squilla waste. *Current World Environment, 12*, 672–679.

Paulino, A. T., Simionato, J. I., Garcia, J. C., & Nozaki, J. (2006). Characterization of chitosan and chitin produced from silkworm chrysalides. *Carbohydrate Polymers, 64*, 98–103.

Rahman, M. A., & Halfar, J. (2014). First evidence of chitin in calcified coralline algae: new insights into the calcification process of *Clathromorphum compactum*. *Scientific Reports, 4*, 6162. https://doi.org/10.1038/srep06162.

Rasti, H., Parivar, K., Baharara, J., Iranshahi, M., & Namvar, F. (2016). Chitosan extracted from the Persian Gulf chiton shells: Induction of apoptosis in liver cancer cell line. *Iran. Journal of Fishery and Science, 15*, 1362–1378.

Rasti, H., Parivar, K., Baharara, J., Iranshahi, M., & Namvar, F. (2017). Chitin from the mollusc Chiton: extraction, characterization and chitosan preparation, Iran. *Journal of Pharmaceutical Sciences, 16*, 366–379.

Roberts, G. A. F. (1992). *Chitin Chemistry* (pp. 54–61). London, UK: The Macmillan Press Ltd.

Rumengan, I. F. M., Suptijah, P., Wullur, S., & Talumepa, A. (2017). Characterization of chitin extracted from fish scales of marine fish species purchased from local markets in North Sulawesi, Indonesia. *IOP Conference of Series Earth Environment and Science, 89*, Article 012028.

Sajomsang, W., & Gonil, P. (2010). Preparation and characterization of α-chitin from cicada sloughs. *Material Science English C., 30*, 357–363.

Salah, R., Michaud, P., Mati, F., Harrat, Z., Lounici, H., Abdi, N., Drouiche, N., & Mameri, N. (2013). Anticancer activity of chemically prepared shrimp low molecular weight chitin evaluation with the human monocyte leukaemia cell line, THP-1. *International Journal of Biological Macromolecules, 52*, 333–339.

Shimahara, K., & Takiguchi, Y. (1988). Preparation of crustacean chitin. *In Methods in enzymology, Academic Press, 161*, 417–423.

Synowiecki, J., & Al-Khateeb, N. A. (2003). Production, properties, and some new applications of chitin and its derivatives. *Critical Reviews in Food Science and Nutrition, 43*, 145–171.

Terbojevidh, M., & Cosani, A. (1997). Molecular weight determination of chitin and chitosan. In R. A. A. Muzzarelli, & M. G. Peter (Eds.), *Chitin Handbook* (pp. 87–101). European Chitin Society.

Tolaimate, A., Desbrieres, J., Rhazi, M., & Alagui, A. (2003). Contribution to the preparation of chitins and chitosans with controlled physico-chemical properties. *Polymer, 44*, 7939–7952.

Urbariczyk, G. B., Lipp-Symonowicz, B., Jeziorny, A., Doran, K., Wrzosek, K., Urbaniak–Domagala, H., & Kowalska, W. S. (1997). Progress on chemistry and application of chitin and its derivatives. *Biomaterials, 3*, 186–187.

Wang, W., Bo, S., Li, S., & Qin, W. (1991). Determination of the Mark-Houwink equation for chitosans with different degrees of deacetylation. *International Journal of Biological Macromolecules, 13*, 281–285.

Wang, Y., Chang, Y., Yu, L., Zhang, C., Xu, X., Xue, Y., Li, Z., & Xue, C. (2013). Crystalline structure and thermal property characterization of chitin from Antarctic krill (*Euphausia superba*). *Carbohydrate Polymers, 92*, 90–97.

Waśko, A., Bulak, P., Polak-Berecka, M., Nowak, K., Polakowski, C., & Bieganowski, A. (2016). The first report of the physicochemical structure of chitin isolated from *Hermetia illucens*. *International Journal of Biological Macromolecules, 92*, 316–320.

Wysokowski, M., Petrenko, I., Stelling, A. L., Stawski, D., Jesionowski, T., & Ehrlich, H. (2015). Poriferan chitin as a versatile template for extreme biomimetics. *Polymers, 7*, 235–265.

Yen, M. T., Tseng, Y. H., Li, R. C., & Mau, J. L. (2007). Antioxidant properties of fungal chitosan from shiitake stipes. *LWT-Food Science Technology, 40*, 255–261.

Yen, M. T., Yang, J. H., & Mau, J. L. (2009). Physicochemical characterization of chitin and chitosan from crab shells. *Carbohydrate Polymers, 75*, 15–21.

Yen, M. T., & Mau, J. L. (2007). Physico-chemical characterization of fungal chitosan from shiitake stipes. *LWT-Food Science and Technology, 40*, 472–479.

Zakaria, Z., Izzah, Z., Jawaid, M., & Hassan, A. (2012). Effect of degree of deacetylation of chitosan on thermal stability and compatibility of chitosan-polyamide blend. *BioResources, 7*, 5568–5580.

Journal of Molecular Structure 1234 (2021) 130145

Contents lists available at ScienceDirect

Journal of Molecular Structure

journal homepage: www.elsevier.com/locate/molstr

Synthesis, spectral, stereochemical, biological, molecular docking and DFT studies of 3-alkyl/3,5-dialkyl-2r,6c-di(naphthyl)piperidin-4-one picrates derivatives

S. Savithiri [a,*], S. Bharanidharan [b], P. Sugumar [c], C. Rajeevgandhi [d], M. Indhira [e]

[a] Department of Chemistry, Karpagam Academy of Higher Education, Coimbatore, 641 021, Tamilnadu, India
[b] Department of Physics, PRIST University, Puducherry, 605 007, India
[c] Department of Physics, Dhaanish Ahmed College of Engineering, Tambaram, Chennai, 601 301, Tamilnadu, India
[d] Department of Physics, Annai College of Arts and Science, Kumbakonam, 612503, Tamilnadu, India
[e] Department of Physics, Vivekanandha College of Arts and Sciences for Women (Autonomous), Tiruchengode, 637 205, Tamilnadu, India

ARTICLE INFO

Article history:
Received 10 December 2020
Revised 6 February 2021
Accepted 12 February 2021
Available online 26 February 2021

Keywords:
Picrates
FT-IR
NMR
Biological activity
DFT and Molecular docking studies

ABSTRACT

A new series of 3-alkyl/3,5-dialkyl-2r,6c-di(naphthyl)piperidin-4-one picrates (**1-6**) were synthesized their chemical structures were confirmed by elemental analysis, FT-IR, ^{1}H and ^{13}C NMR and mass spectral techniques and for compound **4** was characterized by HOMOCOSY, HSQC, HMBC, NOESY, and DEPT NMR spectral techniques. From the NMR spectral data, the observed chemical shifts and coupling constants suggested that compounds (**1-6**) adopt a normal chair conformation with equatorial orientation of all the naphthyl groups at C-2 and C-6 and alkyl group at C-3 and C-5 and from the ^{1}H chemical shifts H-5a and H-3a have a higher magnitude than H-5e. This is due to 1,3 diaxial interaction between axial NH proton and axial protons at C-3 and C-5. The synthesized compounds were screened for their bacterial activity against *Escherichia coli, Staphylococcus aureus, Bacillus.subtilis, Vibreo cholerae and Pseudomonas aeruginosa* and fungal activity against *Candida albicans, Aspergillus niger, Aspergillus flavus and Trichophyton rubrum.* All the compounds showed good antibacterial and antifungal activities. The optimized molecular structure of the synthesized compounds (**1-6**) were studied by using DFT/B3LYP/6-311++G(d,p) basis set. The calculated electrical dipole moment (μ) and first hyperpolarizability (βo) values shows that all the molecules might have nonlinear optical (NLO) behavior. The HOMO-LUMO transition implies that intra-molecular charge transfer takes place within the molecule. Molecular electrostatic potential (MEP) surface is used to understand the reactive sites of a molecule. To establish information about the molecular interactions between protein and this novel compound theoretically, docking studies were carried out in detail.

1. Introduction

Heterocyclic compounds play a vital role in biological processes and are widespread as natural products. Synthetically produced heterocycles designed by organic chemists are used, for instance, as Agrochemicals and pharmaceuticals and play an important role in human life. Among the family of heterocyclic compounds, nitrogen containing heterocyclic compounds, especially piperidine-4-ones presumably gaining considerable importance owing to varied biological properties such as antibacterial [1], antifungal [2], antiviral [3], anti-tumor [4], analgesic [5], anti-inflammatory, local anesthetic [6], Central Nervous System (CNS) and depressant activities [7]. The relative chemical shift order of equatorial and axial protons in the normal chair conformation of cyclohexane and its derivatives (deq > dax) are considered as caused by the magnetic anisotropic effect of the C-C single bonds. The influence of substituents on the chemical shifts of protons attached to the adjacent carbons has been studied in detail [8–10]. The effect of protonation on the ^{1}H and ^{13}C chemical shifts in 2r,6c-diphenylpiperidin-4-one by examining carefully their picrates [11]. By investigating one picrate with the corresponding hydrochloride [12], they have shown that anions also could influence ^{1}H chemical shifts. Various addition complexes were prepared using different heterocyclic nitrogen complexes with picric acid that exhibit NLO properties owing to hydrogen bonding and π–π interactions [13,14]. Extensive effect is at present being expended to examine nonlinear optical materials that exhibit an array of potential applications in many fields of optical computing, telecommunications, optical power limiting, optical information processing and optical data storage [15-19]. Pi-

* Corresponding author.
E-mail address: savithiri.chem@gmail.com (S. Savithiri).

https://doi.org/10.1016/j.molstruc.2021.130145
0022-2860/

cric acid derivatives have charge transfer, due to the presence of phenolic OH favouring the formation of salts with various organic bases. Proton transfer complexes are intended for the development of first-order molecular hyperpolarizability (β) [20,21]. The bond formation process in picric acid complexes is due to the strength and nature of electron donor- acceptor type bonding. The linkage involves the formation of molecular complexes and electrostatic interactions. The formation of conjugated base, the picrates, and the value of molecular hyper polarizability is increased due to proton transfer [22]. In the present study, the synthesis of picrates characterized by spectral techniques and screens its anti-microbial activities and also has been carried out to identify the NLO property (first order hyperpolarizability), HOMO–LUMO energies and MEP analysis. In addition, molecular docking study has also been discussed in detail.

2. Experimental details

2.1. Materials and methods

All the solvents used were of spectral grade. The melting points of the compounds were measured in open capillaries and are uncorrected. IR spectra were recorded on an AVATAR-330 FT-IR spectrometer (Thermo Nicolet) using KBr (pellet form). ^{1}H NMR spectra were recorded at 400 MHz and ^{13}C NMR spectra at 100 MHz on a BRUKER model using DMSO-d6 as solvent for all the compounds. Tetramethylsilane (TMS) was used as internal reference for all NMR spectra, with chemical shifts reported in ((δ units parts per million) relative to the standard. ^{1}H NMR splitting patterns are designated as singlet (s), doublet (d), a doublet of doublet (dd), triplet (t), quartet (q) and multiplet (m). Coupling constants are expressed in Hertz (Hz). Mass spectra were recorded in VARIAN-SASTURAN 2200 GC–MS spectrometry using electron impact technique. The sample was prepared by dissolving about 1 mg in 5 ml of methanol. Microanalyses were performed on VarioMicro V2.2.0 CHN analyzer. Microbial screening studies were made at the Centre for biological sciences in Pondicherry.

2.2. Synthesis procedure of 3-alkyl/3,5-dialkyl-2r,6c-di(naphthyl) piperidin-4-one picrates

The piperidinium picrates (**1–6**) were prepared by mixing equimolar solutions of the corresponding 3-alkyl and 3,5-dialkyl-2r,6c-di(naphthyl)piperidin-4-one [23] with picric acid in ethanol and stirring the solution for 30 mins. The yellowish crystals formed were filtered. The yield of the product was found to be 95%. The harvested crystals were crystallized repeatedly to get excellent quality crystals.

2.2a. 3t-*methyl-2*r,6c-*di(naphthalene-1-yl)piperidin-4-one picrate (1)*

Yield 85%; m.p.: 176-178 (°C); MF: $C_{32}H_{26}N_4O_8$; Elemental analysis: Calcd (%): C, (64.64; H, 4.41; N, 9.42; Found (%): C, 64.59; H, 4.33; N, 9.41; IR (KBr) (cm^{-1}): 3435 (N-H stretching), 3077-2990 (aromatic C-H stretching), 2930-2855 (aliphatic C-H stretching), 1713 (C=O stretching), 1620 (C=C stretching), 1435 (C-O stretching), 1557, 1489 (NO_2 asymmetric stretching), 1329, 1269 (NO_2 symmetric stretching), 1078 (C-N stretching), 783-708 (aromatic C-H out of plane bending vibration), 663 (aromatic C-C out of plane bending vibration); ^{1}H NMR (400 MHz, DMSO-d_6, δ, ppm): 10.30 (d, 1H, Ax-NH, J = 7.6 Hz), 10.62 (d, 1H, Eq-NH, J = 8.0 Hz), 8.59 (s, 2H, picryl ring), 7.59-8.55 (m, 14H, Ar-H), 6.23 (t, 1H, H-6a, J_{6a5a} = 10.4 Hz), 5.99 (t, 1H, H-2a, J_{2a3a} = 10 Hz), 3.76 (t, 1H, H-3a & H-5a), 2.91 (d, 1H, H-5e, J_{5a5e} = 15.2 Hz), 0.81 (d, 3H, CH_3); ^{13}C NMR (100 MHz, DMSO-d_6, δ, ppm): 203.65 (C=O), 122.51-141.74 (Ar-C), 160.80 (C-O), 58.01 (C-2), 54.20 (C-6), 47.46 (C-3), 44.85 (C-5), 10.10 (CH_3). Mass (m/z)**:** 594.8

2.2b. 3t-*isopropyl-2*r,6c-*di(naphthalene-1-yl)piperidin-4-one picrate (2)*

Yield 87%; m.p.: 172-174 (°C); MF: $C_{34}H_{30}N_4O$; Elemental analysis: Calcd (%): C, 65.59; H, 4.86; N, 9.00; Found (%):C, 65.35; H, 4.78; N, 9.03; IR (KBr) (cm^{-1}): 3418 (N-H stretching), 3092-2967 (aromatic C-H stretching), 2934-2870 (aliphatic C-H stretching), 1711 (C=O stretching), 1626 (C=C stretching), 1437 (C-O stretching), 1555, 1491 (NO_2 asymmetric stretching), 1337, 1271 (NO_2 symmetric stretching), 1082 (C-N stretching), 787-710 (aromatic C-H out of plane bending vibration), 663(aromatic C-C out of plane bending vibration); ^{1}H NMR (400 MHz, DMSO-d_6, δ, ppm): 9.64 (d, 1H, Ax-NH, J = 10 Hz), 10.40 (d, 1H, Eq-NH, J = 9.2 Hz), 8.60 (s, 2H, picryl ring), 7.59-8.57 (m, 14H, Ar-H), 6.27 (t, 1H, H-6a, J_{6a5a} = 10.8 Hz), 6.12 (t, 1H, H-2a, J_{2a3a} = 10.4 Hz), 3.55 (t, 1H, H-3a & H-5a), 2.88 (d, 1H, H-5e, J_{5a5e} = 15.2 Hz), 1.66 (t, 1H, CH), 0.76 (d, 3H, CH_3), 1.02 (d, 3H, CH_3); ^{13}C NMR (100 MHz, DMSO-d_6, δ, ppm): 203.23 (C=O), 122.93-141.74 (Ar-C), 160.60 (C-O), 56.02 (C-2), 55.89 (C-6), 53.53 (C-3), 45.76 (C-5), 25.83 (CH), 20.53, 17.54 (CH_3).

2.2c. 3,5-*dimethyl-2*r,6c-*di(naphthalene-1-yl)piperidin-4-one picrate (3)*

Yield 75%; m.p.: 106-108 (°C); MF: $C_{33}H_{28}N_4O_8$; Elemental analysis: Calcd (%): C, 65.13; H, 4.64; N, 9.21; Found (%):C, 65.01; H, 4.53; N, 9.15; IR (KBr) (cm^{-1}): 3420 (N-H stretching), 3078-2992 (aromatic C-H stretching), 2926-2853 (aliphatic C-H stretching), 1713 (C=O stretching), 1622 (C=C stretching), 1446 (C-O stretching), 1549, 1489 (NO_2 asymmetric stretching), 1329, 1271 (NO_2 symmetric stretching), 1076 (C-N stretching), 783-712 (aromatic C-H out of plane bending vibration), 605 (aromatic C-C out of plane bending vibration); ^{1}H NMR (400 MHz, DMSO-d_6, δ, ppm): 9.55 (d, 1H, Ax-NH, J = 9.6 Hz), 10.33 (d, 1H, Eq-NH, J = 8.8 Hz), 8.59 (s, 2H, picryl ring), 7.58-8.44 (m, Ar-H), 5.96 (t, 1H, H-6a & H-2a, $J_{6a5a\ \&\ 2a3a}$ = 10.8 Hz), 3.69 (q, 1H, H-3a & H-5a, J = 11.6 Hz), 0.83 (d, 6H, CH_3); ^{13}C NMR (100 MHz, DMSO-d_6, δ, ppm): 205.28 (C=O), 122.80-141.75 (Ar-C), 160.76 (C-O), 57.71 (C-2 & C-6), 47.01 (C-3) & C-5), 10.46 (CH_3); Mass (m/z): 609.8 (m+1)

2.2d. 3t-*butyl-2*r,6c-*di(naphthalene-1-yl)piperidin-4-one picrate (4)*

Yield 80%; m.p.: 150–152 (°C); MF: $C_{35}H_{32}N_4O_8$; Elemental analysis: Calcd (%): C, 66.03; H, 5.07; N, 8.80; Found (%):C, 66.01; H, 4.99; N, 8.76; IR (KBr) (cm^{-1}): 3435 (N-H stretching), 3078-2957 (aromatic C-H stretching), 2928-2862 (aliphatic C-H stretching), 1721 (C=O stretching), 1611 (C=C stretching), 1433 (C-O stretching), 1559, 1489 (NO_2 asymmetric stretching), 1335, 1269 (NO_2 symmetric stretching), 1080 (C-N stretching), 777-710 (aromatic C-H out of plane bending vibration), 612 (aromatic C-C out of plane bending vibration); ^{1}H NMR (400 MHz, DMSO-d_6, δ, ppm): 9.77 (d, 1H, Ax-NH, J = 8.4 Hz), 10.34 (d, 1H, Eq-NH, J = 7.2 Hz), 8.59 (s, 2H, picryl ring), 7.60-8.47 (m, 14H, Ar-H), 6.23 (t, 1H, H-6a, J_{6a5a} = 10.8 Hz), 6.03 (t, 1H, H-2a, J_{2a3a} = 9.6 Hz), 3.44 (q, 1H, H-3a), 3.58 (q, 1H, H-5a, J_{5a5e} = 14.0 Hz), 2.91 (d, 1H, H-5e), 0.90-1.52 (m, 6H, CH_2), 0.56 (t, 3H, CH_3). ^{13}C NMR (100 MHz, DMSO-d_6, δ, ppm): 203.40 (C=O), 122.58-141.62 (Ar-C), 160.85 (C-O), 56.72 (C-2), 53.95 (C-6), 51.51 (C-3), 45.05 (C-5), 21.85-28.43 (CH_2), 13.30 (CH_3).

2.2e. 3t-*pentyl-2*r,6c-*di(naphthalene-2-yl)piperidin-4-one picrate (5)*

Yield 78%; m.p.: 156-158 (°C); MF: $C_{36}H_{28}N_4O_8$; Elemental analysis: Calcd (%): C, 66.45; H, 5.57; N, 8.61; Found (%):C, 66.35; H,

5.46; N, 8.57; IR (KBr) (cm^{-1}): 3429 (N-H stretching), 3084-2953 (aromatic C-H stretching), 2928-2860 (aliphatic C-H stretching), 1719 (C=O stretching), 1622 (C=C stretching), 1435 (C-O stretching), 1558, 1485 (NO_2 asymmetric stretching), 1329, 1269 (NO_2 symmetric stretching), 1078 (C-N stretching), 787-710 (aromatic C-H out of plane bending vibration), 664 (aromatic C-C out of plane bending vibration); ^{1}H NMR (400 MHz, DMSO-d_6, δ, ppm): 10.15 (s, 1H, Ax-NH), 10.15 (s, 1H, Eq-NH), 8.59 (s, 2H, picryl ring), 7.59-8.22 (m, Ar-H), 5.24 (t, 1H, H-6a, J_{6a5a} = 12.8 Hz), 4.97 (t, 1H, H-2a, J_{2a3a} = 9.6 Hz), 3.43 (t, 1H, H-3a), 3.68 (t, 1H, H-5a, J_{5a5e} = 14.4 Hz), 2.89 (d, 1H, H-5e), 1.06-1.47 (m, 8H, CH_2), 0.70 (t, 3H, CH_3); ^{13}C NMR (100 MHz, DMSO-d_6, δ, ppm): 203.30 (C=O), 124.38-141.73 (Ar-C), 160.74 (C-O), 63.38 (C-2), 59.00 (C-6), 50.43 (C-3), 44.53 (C-5), 21.56-31.13 (CH_2), 13.59 (CH_3).

2.2f. 3t-methyl-2r,6c-di(naphthalene-2-yl)piperidin-4-one picrate (6)

Yield 85%; m.p.: 182-184 (°C); MF: $C_{32}H_{26}N_4O_8$; Elemental analysis: Calcd (%): C, 64.64; H, 4.41; N, 9.42; Found (%):C, 64.20; H, 4.31; N, 9.28; IR (KBr) (cm^{-1}): 3426 (N-H stretching), 3084 (aromatic C-H stretching), 2928-2855 (aliphatic C-H stretching), 1707 (C=O stretching), 1624 (C=C stretching), 1433 (C-O stretching), 1559, 1487 (NO_2 asymmetric stretching), 1333, 1269 (NO_2 symmetric stretching), 1078 (C-N stretching), 777-708 (aromatic C-H out of plane bending vibration), 667 (aromatic C-C out of plane bending vibration), ^{1}H NMR (400 MHz, DMSO-d_6, δ, ppm): 9.76 (d, 1H, Ax-NH, J = 8.8 Hz), 10.11 (d, 1H, Eq-NH, J = 8.8 Hz), 8.58 (s, 2H, picryl ring), 7.69-8.18 (m, Ar-H), 5.24 (t, 1H, H-6a, J_{6a5a} = 10.0 Hz), 4.91 (q, 1H, H-2a, J_{2a3a} = 2.4 Hz), 3.52 (m, 1H, H-3a & H-5a), 2.93 (d, 1H, H-5e, J_{5a5e} = 14.4 Hz), 0.86 (d, 3H, CH_3); ^{13}C NMR (100 MHz, DMSO-d_6, δ, ppm): 203.41 (C=O), 122.24-141.73 (Ar-C), 160.73 (C-O), 64.45 (C-2), 58.78 (C-6), 45.79 (C-3), 43.88 (C-5), 10.44 (CH_3).

2.3a. Antibacterial activity by disc diffusion method

Nutrient agar plates were prepared under sterile conditions and incubated overnight to detect contamination. About 0.2 ml of working stock cultures was transferred into separate nutrient agar plates and spread thoroughly using a glass spreader. Whatmann No. 1 disc (6 mm in diameter) was impregnated with the test compounds dissolved in DMSO (200 mg/ml) for about half an hour. Commercially available drug disc (Ciprofloxacin 10 lg/disc) was used as positive reference standard. Negative controls were also prepared by impregnating the disc of the same size in DMSO solvent. The discs were placed on the inoculated agar plates and incubated at 37 ± 1°C for about 18–24 h. Antibacterial activity was evaluated by measuring the zone of inhibition against the test organism.

2.3b. Antifungal activity by disc diffusion method

Sabouraud's dextrose agar (SDA) medium was used for the growth of fungi and testing was done in Sabouraud's dextrose broth (SDB) medium. The subculture and the viable count were carried out by the same procedure used in antibacterial studies except the temperature, which was maintained at 28 ± 1°C for about 72 h. Similarly for disc diffusion method, the petri dishes were incubated at 28 ± 1°C for about 72 h. The same concentration of the test compound, solvent (DMSO) and Cetramazole (standard) prepared previously were used for the antifungal studies.

2.3c. Minimum inhibitory concentration (MIC)

The lowest concentration of the test compounds which caused apparently the inhibition of growth of organism, was taken as the minimum inhibitory concentration. The MIC was recorded by visual observation after 24 h (bacteria) and 72–96 h (fungi) of incubation. The sterile distilled water and DMSO did not show any inhibition.

2.4. Computational details

The Density Functional Theory (DFT) with B3LYP level theory using 6-311++G(d,p) basis set in Gaussian-09 have been used for theoretical calculations [24]. Following the geometry optimizations with B3LYP method, HOMO and LUMO energy values and energy gap for compounds **(1-6)** were calculated by using B3LYP method with 6-311++G(d,p) basis set. Molecular Electrostatic Potentials (MEPs) of compounds **(1-6)** were plotted in 3D by using optimized structures at B3LYP/6-311++G(d,p) level theory. Furthermore, in order to show nonlinear optical (NLO) activity of title molecule, the dipole moment, linear polarizability and first order hyperpolarizability were obtained from molecular polarizabilities based on theoretical calculations. Acetylcholinesterase (AChE), an enzyme present in the neuromuscular junctions and responsible for the hydrolysis of the neurotransmitter acetylcholine. Three-dimensional crystal structures of TcAChE complexes were retrieved from the RCSB (Research Collaboratory for Structural Bioinformatics) protein data bank under PDB ID: 1EVE [25]. The active site of TcAChE was defined as the collection of residues within 15.0 Å of the bound inhibitor present in the reference structure 1ACJ. The bound inhibitors were not included in the docking runs. Docking calculations were carried out on Acetylcholinesterase Inhibitors enzyme protein model [26]. Essential hydrogen atoms, Kollman united atom type charges, and solvation parameters were added with the aid of AutoDock tools [27].

3. Results and discussion

3-alkyl/3,5-dialkyl-2r,6c-di(naphthyl)piperidin-4-one picrates derivatives, according to the synthetic sequences of reactions illustrated in Scheme 1. The structures of all the synthesized compounds (**1-6**) are established on the basis of FT-IR, ^{1}H and ^{13}C NMR and mass spectral techniques and for compound **4** in addition to the 2D NMR (HOMOCOSY, HSQC, HMBC, NOESY, and DEPT) spectral studies were performed to make unambiguous configurationals and conformationals characterizations.

3.1. IR spectral analysis

In the IR spectrum of **4**, the prominent peaks around 3435 and 1721 cm^{-1} are attributed to NH and C=O vibrational modes, respectively. The C=C stretching vibration of the naphthyl ring appeared around 1611 cm^{-1}. The C-N stretching mode of the piperidine ring appeared around 1080 cm^{-1}. The peaks around 777-710 cm^{-1} are attributed to aromatic C-H out of plane bending vibrations. The NO_2 asymmetric stretching vibration of picryl group appeared around 1559-1489 cm^{-1}. The peaks around 1335-1269 cm^{-1} are due to NO_2 symmetric stretching, vibration modes of picryl group. The peak around 1433 cm^{-1} is attributed to C-O vibrational mode of picryl group. The FT-IR spectral data of compound **1-6** are given in Table 1. It is seen that the IR frequencies are influenced by the substitutes in the aromatic ring.

3.2. NMR spectral analysis

In the ^{1}H NMR spectrum of **4** is shown in Fig. 1, the two doublets at 9.77 ppm (J = 8.4 Hz) and 10.34 ppm (J = 7.2 Hz) are assigned to NH axial and equatorial protons of piperidinium amino group. The picryl protons at 8.59 ppm correspond to two proton

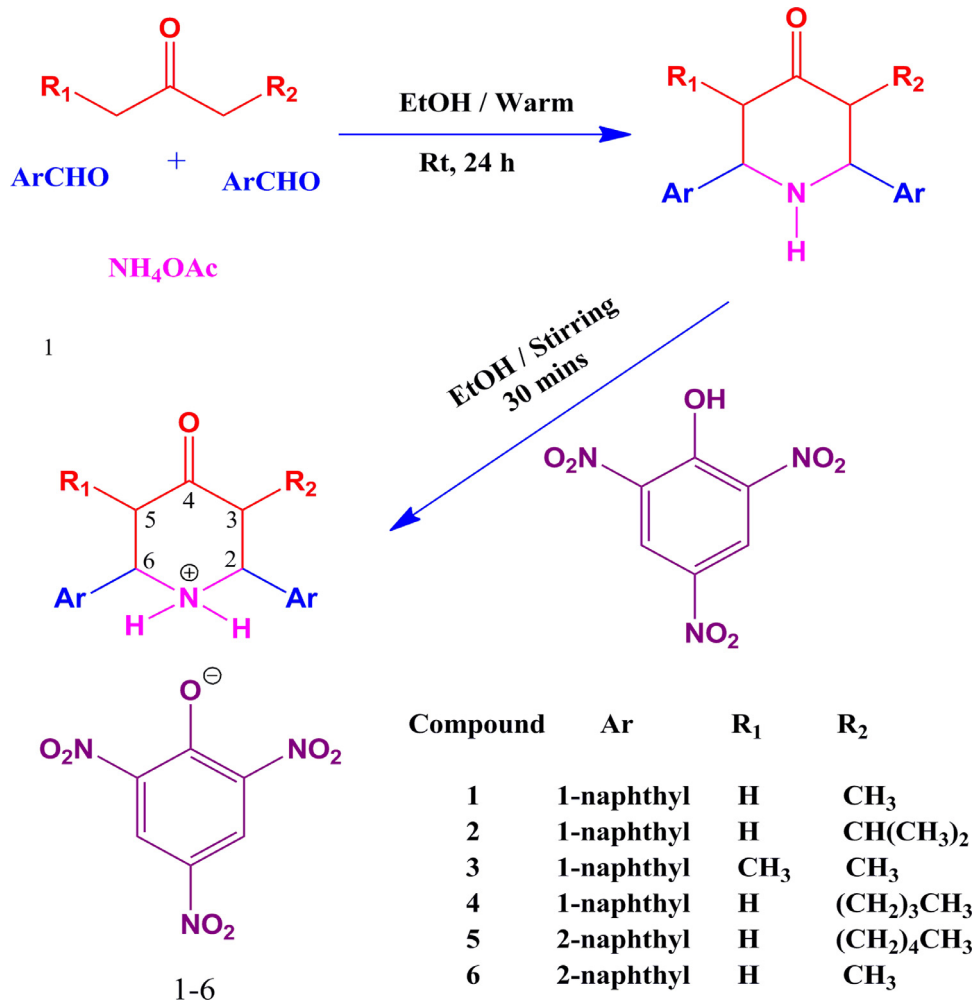

Scheme 1. Synthetic route for 3-alkyl /3,5-dialkyl-2r,6c-di(naphthyl)piperidin-4-one picrates derivatives.

Table 1
IR spectral data of compounds (1-6).

1	2	3	4	5	6	Assignments
3435	3418	3420	3435	3429	3426	NH
3077-2990	3092-2967	3078-2992	3078-2957	3084-2953	3084	C-H
2930-2855	2934-2870	2926-2853	2928-2862	2928-2860	2855	
1713	1711	1713	1721	1719	1707	C=O
1078	1082	1076	1080	1078	1078	C-N
1620	1626	1622	1611	1622	1624	C=C
1435	1437	1446	1433	1435	1433	C-O
1557	1555	1549	1559	1558	1559	NO_2 asymmetric stretching
1489	1491	1489	1489	1485	1487	
1329	1337	1329	1335	1329	1333	NO_2 symmetric stretching
1269	1271	1271	1269	1269	1269	
783-708	787-710	783-712	777-710	787-710	777-708	Aromatic C-H out of plane bending vibrations
663	663	605	612	664	667	Aromatic C-C out of plane bending vibrations

integral values. All the aromatic protons are observed in the region 7.59-8.47 ppm. The two triplets observed at 6.03 and 6.23 ppm are due to bezylic protons at C-2 and C-6 respectively. The axial methylene proton H-5a appears as a quartet at 3.58 ppm and the equatorial methylene proton H-5e is observed at 2.91 ppm. The axial methine proton H-3a appears as a quartet at 3.44 ppm. From the ^{1}H chemical shifts H-5a and H-3a have a higher magnitude than H-5e. This is due to 1,3 diaxial interaction between axial NH proton and the axial protons at C-3 and C-5. The signal at 0.81 ppm is due to methyl protons at C-3 of piperidone moiety. In the protonated piperidine-4-one derivatives, the axial NH bond experiences severe *syn* 1,3-diaxial interaction with the axial protons at C-5 and C-3 and due to these interactions the protons are deshielded to a greater extent than the corresponding C-3 and C-5 carbons which are shielded. The ^{1}H chemical shift values are summarized in Table 2. The assignments are further confirmed by HOMOCOSY and NOESY correlation spectra of compound **4**.

In order to determine the effect of protonation on chemical shifts, the chemical shifts of 2,6-dinaphthylpicrates **1** and **5** were compared with the corresponding piperidin-4-ones and 2,6-diphenylpicrates. Data in Table 5 reveals that picrate formation deshields H-2a and H-6a to a greater extent. In the picrate deriva-

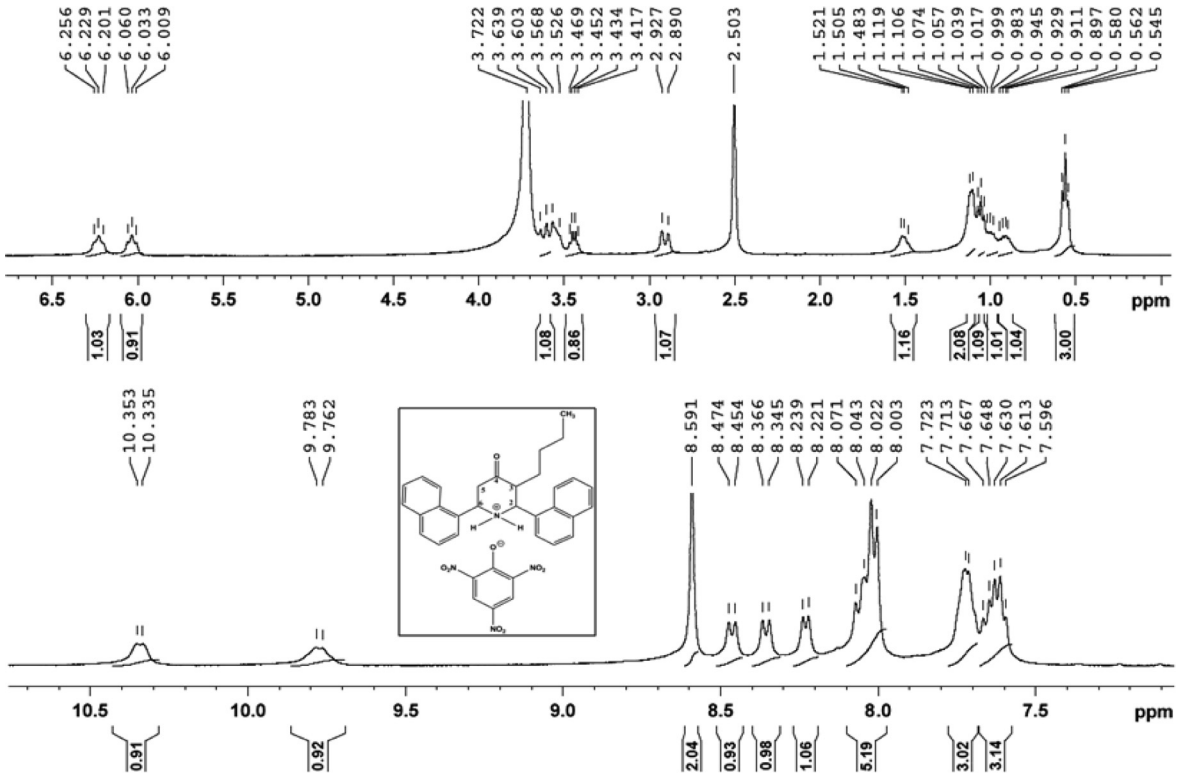

Fig. 1. ^{1}H NMR Spectrum of compound 4.

Table 2
^{1}H chemical shifts (ppm) of compounds (1–6).

Compound	H-2a	H-6a	H-5a	H-5e	H-3a	Ax-NH	Eq-NH	CH	CH_2	Picryl ring	CH_3	Aromatic Protons
1	5.99	6.23	3.76	2.91	3.76	10.30	10.62	-	-	8.59	0.81	7.59-8.55
2	6.12	6.27	3.55	2.88	3.55	9.64	10.40	1.66	-	8.60	0.76, 1.02	7.59-8.57
3	5.96	5.96	3.69	-	3.69	9.55	10.33	-	-	8.59	0.83	7.58-8.44
4	6.03	6.23	2.91	3.58	3.44	9.77	10.34	-	0.89-1.52	8.59	0.56	7.60-8.47
5	4.97	5.24	2.89	3.68	3.43	10.15	10.15	-	1.06-1.47	8.59	0.70	7.59-.822
6	4.91	5.24	3.52	2.93	3.52	9.76	10.11	-	-	8.58	0.86	7.69-8.18

tives the two protons at nitrogen occupy axial and equatorial orientations. The magnetic anisotropic effect of the axial N-H bond is responsible for the greater downfield shift observed on H-6a and H-2a in compound **4**. It is also seen that axial methylene proton H-5a is deshielded to a greater extent and it can be explained by syn 1,3-diaxial interaction. Picrate formation deshields the alkyl protons at C-3 also. NOESY spectrum of **4** is shown in Fig. 2. It is seen that NOE between H-2a and H-3a and that between H-6a and H-5 (i.e. H-5a and H-5e) are strong. The aromatic proton at 7.59 ppm should show strong NOE with H-3a and H-5a. Obviously, these protons must be the ortho protons of the naphthyl ring group at C-2 and C-6. Thus, the observed NOE of **4** supports the determined vicinal coupling constant. For compound **4** these assignments were confirmed by HSQC and HMBC spectra. The observed correlations in the HOMOCOSY, NOESY, HSQC and HMBC NOESY spectra are given in Table 4.

The compounds (**1-6**) should exist in chair conformation. In the chair conformation the aryl group alkyl group at C-3 are equatorial orientation. The coupling constant values and position of the chemical shifts were used to predict the conformation of the compound. The observation of large vicinal coupling constant values $^{3}J_{2a3a}$ = 9.6 and $^{3}J_{6a5a}$ = 10.8 Hz and small values of the vicinal coupling constant are not resolved. For the protons of C-6 and C-2 in **1-6** indicate that the six member heterocyclic rings adopts a normal chair conformation (Fig. 3) With equatorial orientation of aryl groups at C-2 and C-6 and alkyl group at C-3 and C-5. In compounds (**1-6**) the heterocyclic ring may be flattened or distorted about the (C-2)-(C-3) bond to decrease *gauche* interaction between the equatorial naphthyl groups and the equatorial alkyl group at C-2, C-6, C-3 and C-5 respectively.

In the ^{13}C NMR spectrum of compound **4** is shown in Fig. 4, the aromatic carbons are distinguished from other carbons by their characteristic absorptions at 122.58-141.62 ppm. The signal at 203.40 ppm in the most downfield is characteristic of carbonyl carbon. The signal in the downfield at 160.85 ppm is due to the C-O carbon of picryl group. The signals at 56.72 and 53.95 ppm are due to C-2 and C-6. The signals at 51.51 and 45.05 ppm are due to C-3 and C-5. The signal observed in the region 21.92-31.13 ppm are assigned to methylene carbons of butyl group at C-3 of piperidone ring and the most upfield signal at 13.30 ppm is assigned to methyl carbon of butyl group at C-3. The chemical shift values are reproduced in Table 3. It is clearly indicated that protonation shields all carbons. The shielding magnitude observed on C-3 and C-5 carbons is more that of C-2 and C-6 carbons. Due to protonation, the axial N-H bond experiences severe syn 1,3-diaxial interaction with axial hydrogens at C-3 and C-5 and due to these interactions butyl protons at C-3 and H-5a proton are shielded and the corresponding carbons are shielded. A ^{13}C NMR spectral study supported that the proposed chair conformation of the synthesized compounds with the equatorial orientation of the bulky aryl and

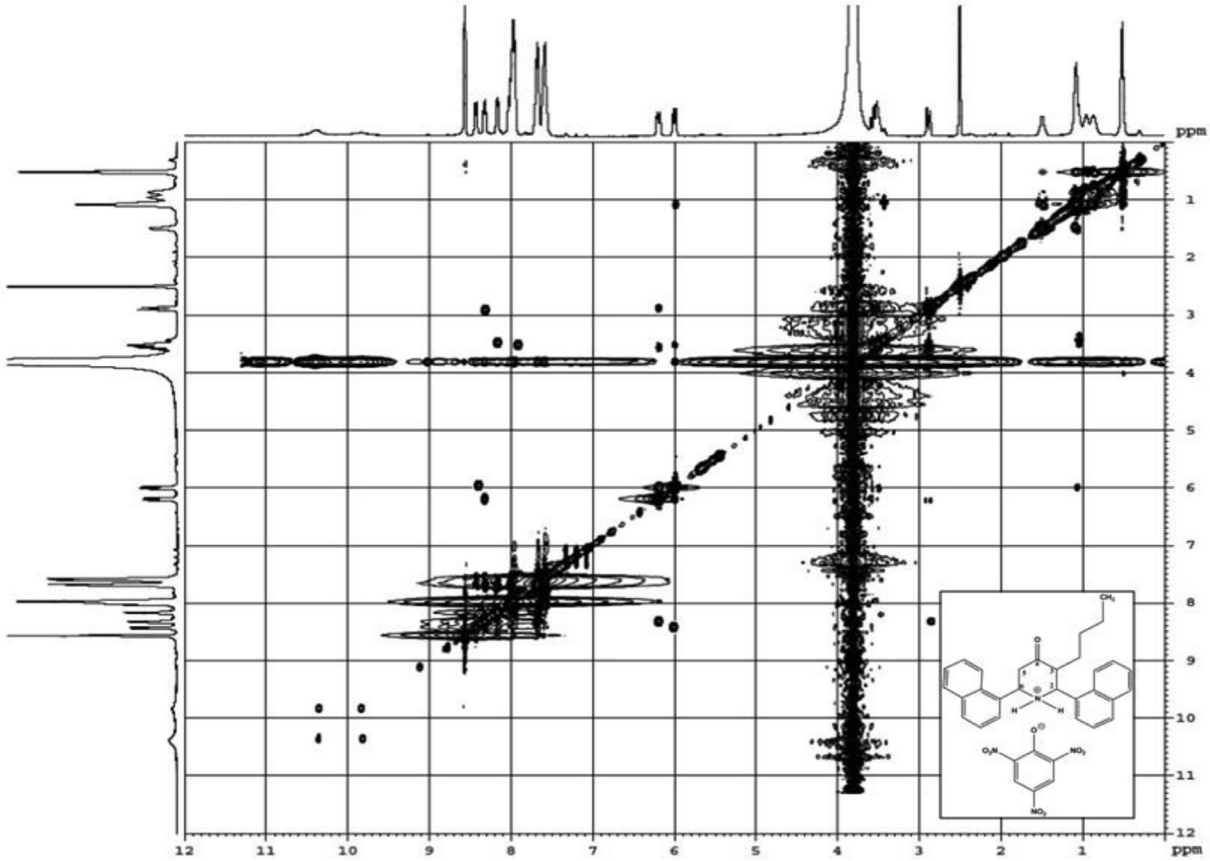

Fig. 2. NOESY Spectrum of compound 4.

Table 3
^{13}C chemical shifts (ppm) of compounds (1–6).

Compound	C-2	C-3	C-5	C-6	CH_2	CH	CH_3	C=O	C-O	Aromatic Carbons
1	58.01	47.46	44.85	54.20	-	-	10.10	203.65	160.80	122.51-141.74
2	56.02	53.53	45.76	55.89	-	25.83	20.53, 17.54	203.23	160.60	122.93-141.74
3	57.71	47.01	47.01	57.71	-	-	10.46	205.28	160.76	122.80-141.75
4	56.72	51.51	45.05	53.95	21.85-28.43	-	13.30	203.40	160.85	122.58-141.62
5	63.38	50.43	44.53	59.00	21.56-31.13	-	13.59	203.30	160.74	124.38-141.73
6	64.45	45.79	43.88	58.78	-	-	10.44	203.41	160.73	122.24-141.73

Table 4
Correlation in HOMOCOSY, NOESY, HSQC and HMBC spectra of compound 4 (δ, ppm).

^{1}H NMR Signal	Correlation in HOMOCOSY	Correlation in NOESY	Correlation in HSQC	Correlation in HMBC
6.23 (H-6a)	3.58 (H-5a), 2.91 (H-5e), 9.77 (Ax-NH)	3.58 (H-5a), 2.91 (H-5e), 7.59-8.47 (Aromatic Protons)	53.95 (C-6)	-
6.03 (H-2a)	3.44 (H-3a), 9.77 (Ax-NH)	3.44 (H-3a), 0.89-1.52 (CH_2), 7.59-8.47 (Aromatic Protons)	56.72 (C(2))	51.51 (C-3), α), 122.58-141.62 (Aromatic Carbons, α)
3.44 (H-3a)	0.89-1.52 (CH_2), 6.03 (H-2a)	0.89-1.52 (CH_2), 6.03 (H-2a), 7.59-8.47 (Aromatic Protons)	51.51 (C-3)	203.40 (C-4), α), 21.92-31.13 (CH_2, α), 122.58-141.62 (Aromatic Carbons, β)
3.58 (H-5a)	2.91 (H-5e), 6.23 (H-6a)	2.91 (H-5e), 6.23 (H-6a), 7.59-8.47 (Aromatic Protons)	45.05 (C-5)	53.95 (C-6), α), 203.40 (C-4), α), 122.58-141.62 (Aromatic Carbons, α)
2.91 (H-5e)	3.58 (H-5a), 6.23 (H-6a)	3.58 (H-5a), 6.23 (H-6a), 7.59-8.47 (Aromatic Protons)	45.05 (C-5)	203.40 (C-4), α)
0.56 (CH_3)	0.89-1.52 (CH_2),	0.89-1.52 (CH_2)	13.30 (CH_3)	21.92-31.13 (CH_2, α)
0.89-1.52 (CH_2)	0.89-1.52 (CH_2), 3.44 (H-3a)	0.89-1.52 (CH_2), 3.44 (H-3a), 6.03 (H-2a)	21.85-28.43 (CH_2)	21.85-28.43 (CH_2, α), 203.40 (C-4), β)
9.77 (Ax-NH)	10.34 (Eq-NH), 6.23 (H-6a), 6.03 (H-2a)	10.34 (Eq-NH), 3.58 (H-5a)	-	-
10.34 (Eq-NH)	9.77 (Ax-NH)	9.77 (Ax-NH), 3.58 (H-5a)	-	-
7.59-8.47 (Aromatic Protons)	7.59-8.47 (Aromatic Protons)	6.23 (H-6a), 6.03 (H-2a), 3.58 (H-5a), 2.91 (H-5e), 3.44 (H-3a),	122.58-141.62 (Aromatic carbons)	53.95 (C-6), α), 56.72 (C-2), α)

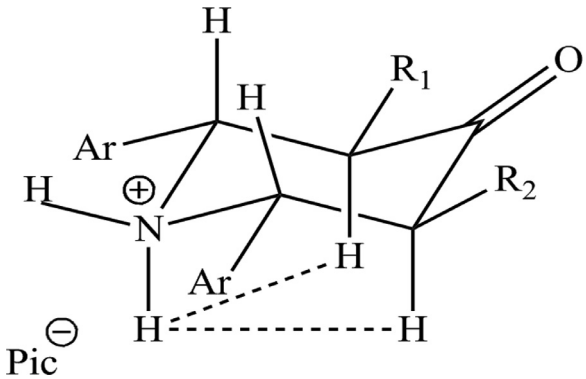

Fig. 3. Schematic representation of syn 1,3-diaxial interactions.

Table 5
^{1}H chemical shift difference between piperidones[a] and picrates (1) and phenyl picrates[b] and naphthyl picrates (5).

Compound 1 piperidones[a] and picrates		Compound 5 phenyl picrates[b] and naphthyl picrates
H(6)	0.26	-0.23
H(2)	-0.17	-0.23
H(5a)	-0.3	-0.04
H(3a)	-0.03	-0.45
H(5e)	0.4	-0.14
CH3	-0.01	0.04

[a] Taken from Ref. [28].
[b] Taken from Ref. [23].

alkyl groups. The ^{13}C chemical shifts of compounds **1** and **5** were compared with the corresponding piperidin-4-ones (Table 6). The assignments are further confirmed by using DEPT, HSQC and HMBC spectra.

Table 6
^{13}C chemical shift difference between piperidones[a] and picrates (1) and phenyl picrates[b] and naphthyl picrates (5).

Compound 1 piperidones[a] and picrates		Compound 5 phenyl picrates[b] and naphthyl picrates	
C(2)	0.80	C(2)	-0.37
C(3)	0.76	C(3)	-0.05
C(4)	0.68	C(4)	-0.16
C(5)	0.74	C(5)	-0.25
C(6)	-9.15	C(6)	-0.35
CH_3	0.49	CH_3	0.03

[a] Taken from Ref. [28].
[b] Taken from Ref. [23].

These compounds were further characterized by mass spectroscopy (Fig. S10 and Fig. S15) and the detected The mass spectra of compounds **1** and **3** were recorded and the observed m/z values are consistent with the proposed molecular formula of the respective compounds. The presence of peaks at m/z 594.8 and 609.8 are due to the molecular ion peaks of compounds **1** and **3**.

3.3. Antimicrobial activity

The preliminary antimicrobial activity of the compounds (**1-6**) was carried out using disc diffusion and two fold serial dilution methods. The bacterial strains viz., *Escherichia coli, Staphylococcus aureus, Bacillus.subtilis, Vibreo cholerae* and *Pseudomonas aeruginosa* and fungal strains viz., *Candida albicans, Aspergillus niger, Aspergillus flavus* and *Trichophyton rubrum* were used for this study. DMSO was used as control while *Ciprofloxacin* and *Amphotericin B* were used as standard drugs respectively for bacterial and fungal strains.

The zone of inhibition (mm) and minimum inhibitory concentrations (MIC in μg/mL) of the compounds **1-6** against the tested

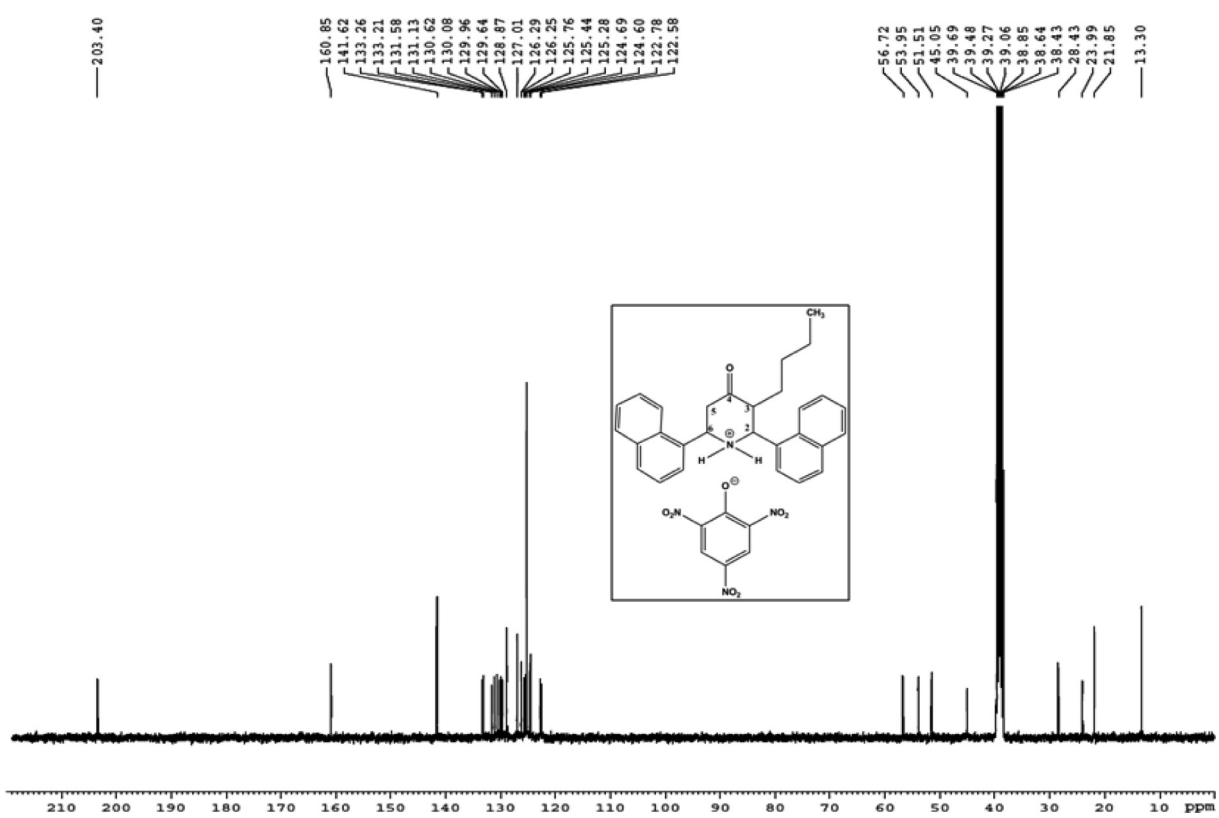

Fig. 4. ^{13}C NMR Spectrum of compound 4.

Table 7
Antibacterial and antifungal activities of compounds (1-6) by disc diffusion method.

Compound	Diameter of zone of inhibition (mm)								
	Bacterial strain					Fungal strain			
	E. coli	*S. aureus*	*B. subtilis*	*V. cholerae*	*P. aeruginosa*	*C. albicans*	*A. niger*	*A. flavus*	*T. Rubrum*
1	12	13	07	09	11	12	10	11	08
2	09	11	07	10	12	08	14	07	11
3	16	15	11	12	15	21	16	12	14
4	22	16	15	12	20	15	17	12	14
5	13	15	20	18	14	17	15	16	12
6	14	12	09	12	10	14	11	13	10
Ciprofloxacin	12	15	16	16	11	-	-	-	-
Amphotericin B	-	-	-	-	-	13	12	14	11

Table 8
Antibacterial and antifungal activities of compounds (1-6) by serial dilution method.

Compound	Minimum inhibitory concentration (μg/mL)								
	Bacterial strain					Fungal strain			
	E. coli	*S. aureus*	*B. subtilis*	*V. cholera*	*P. aeruginosa*	*C. albicans*	*A. niger*	*A. flavus*	*T. rubrum*
1	50	50	200	100	100	50	100	50	200
2	200	100	200	100	50	200	25	200	100
3	25	25	100	100	50	12.5	25	100	50
4	12.5	25	25	50	12.5	25	25	50	50
5	50	25	12.5	25	25	12.5	25	25	50
6	25	50	100	50	100	25	100	50	100
Ciprofloxacin	25	25	12.5	50	12.5	-	-	-	-
Amphotericin B	-	-	-	-	-	25	25	50	50

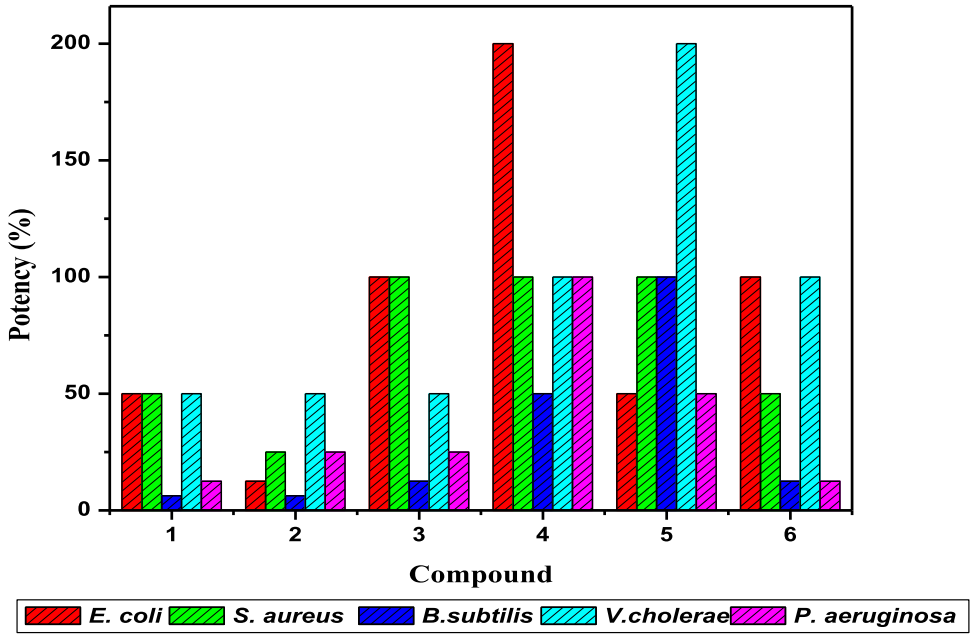

Fig. 5. Comparison of antibacterial potency of compounds (1–6).

bacterial strains are given in Tables 7 and 8. From the zone of inhibition, it is clear that the compounds **3, 4, 5** and **6** against *E. coli*, **3, 4** and **5** against *S. aureus* and *P. aeruginosa*, **5** against *B. subtilis* and *V. cholerea* is better in enhancing the anti-bacterial potency on the tested organisms than the others.

A close survey of the MIC values in Table 8 indicates that all the compounds exhibited a varied range 12.5-200 μg/mL of antibacterial activity against the tested bacterial strains. The compounds **1** and **2** were inactive against all the tested bacterial strains. The compound **3** with methyl groups at C-3 and C-5 positions of piperidone ring exhibited good activity against *E. coli* and *S. aureus* whereas against *B. subtilis, V. cholerae* and *P. aeruginosa* poor activity was noted. Introduction of butyl group at C-3 position of the piperdone moiety in **1** (compound **4**) exhibited excellent activity against all the tested bacterial strains except *B. subtilis*. Replacement of methyl groups by the pentyl group at C-3 and 1-naphthyl by the 2-naphthyl group in C-2 and C-6 positions of the piperidone ring in **1** (compound **5**) showed excellent activity against *S. aureus, B. subtilis* and *V. cholerae* while against *E. coli* and *P. aeruginosa* have registered poor activity. Substitution of the methyl group at C-3 and the 2-naphthyl group in C-2 and C-6 positions of the piperidone ring in **1** (compound **6**) displayed excellent activity against *E. coli* and *V. cholerae* but poor activity was noted against the rest of the tested bacterial strains.

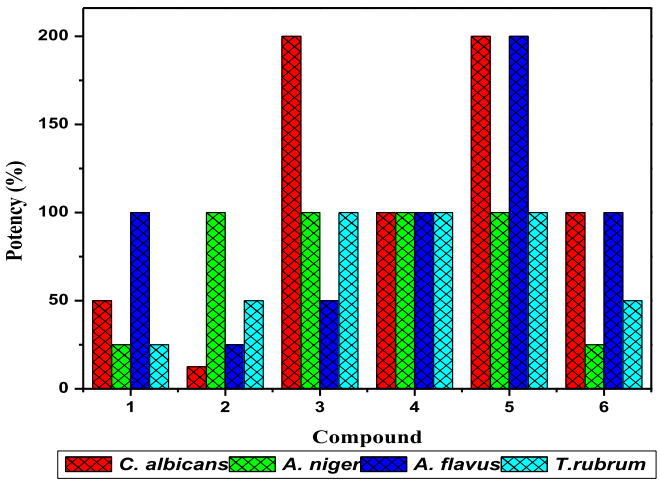

Fig. 6. Comparison of antifungal potency of compounds (1–6).

The zone of inhibition (mm) and minimum inhibitory concentrations (MIC in μg/mL) of the compounds (**1-6**) against the tested fungal strains are given in Tables 7 and 8. From the zone of inhibition, it is clear that the compounds **3, 4, 5** and **6** against *C. albicans* and *A. niger*, **5** against *A. flavus* and **3, 4, 5** against *T. rubrum* are found to be better in enhancing the antibacterial potency on the tested organisms than the others.

Table 8 shows the in vitro anti-fungal activities of compounds (**1-6**). Amphotericin B was used as standard drug on fungal strains such as *C. albicans, A. niger, A. flavus* and *T. rubrum*, whose activities were measured as the minimum inhibitory concentration (MIC in μg/mL). The compound with 1-naphthyl/2-naphthyl groups at C-2 and C-6 positions (**i.e. compounds 1-6**), compound **1** did not exert antifungal activity against *C. albicans, A. niger* and *T. rubrum* except *A. flavus*. Introduction of the isopropyl group at C-3 instead of the methyl group of piperidone moiety in **1**, (compound **2**) has good activity against *A. niger* whereas poor activity was noticed against all the tested fungal strains. However, further substitution of a methyl group at C-5 position in **1**, compound **3** has pronounced antifungal activity against *C. albicans, A. niger* and *T. rubrum* while against *A. flavus* poor activity was noted. Replacement of methyl groups by butyl group at C-3 position of piperidone moiety in **1** (compound **4**) showed excellent activity against all the tested fungal strains. Due to the incorporation of 2-naphthyl group at C-2 and C-6 and pentyl group at C-3 position of piperidone ring in **1** (compound **5**) exhibited excellent activity against all the fungal strains. Substitution of 2-naphthyl groups at C-2 and C-6 and further introduction of methyl group at C-5 position in **1** (compound **6**) has registered excellent activity against *C. albicans* and *A. flavus* while against *A. niger* and *T. rubrum* poor activity was noted.

The potency of synthesized compounds (**1-6**) against the tested bacterial and fungal strains was derived in comparison with the reference standards by using the following equation

$$\text{Potency (\%)} = \frac{\text{MIC } (\mu\text{g/mL}) \text{ of reference compound}}{\text{MIC } (\mu\text{g/mL}) \text{ of reference compound}} \times 100$$

The obtained results are also presented as shown in Figs. 5 and 6. On comparison with Ciprofloxacin, double the potency (200%) is noted for compound 4 against *E. coli* and compound **5** against *V. cholerae* while equal potency (100%) is noted for compounds **3** and **6** against *E. coli*, compound **5** against *B. subtilis*, **3, 4, 5** against

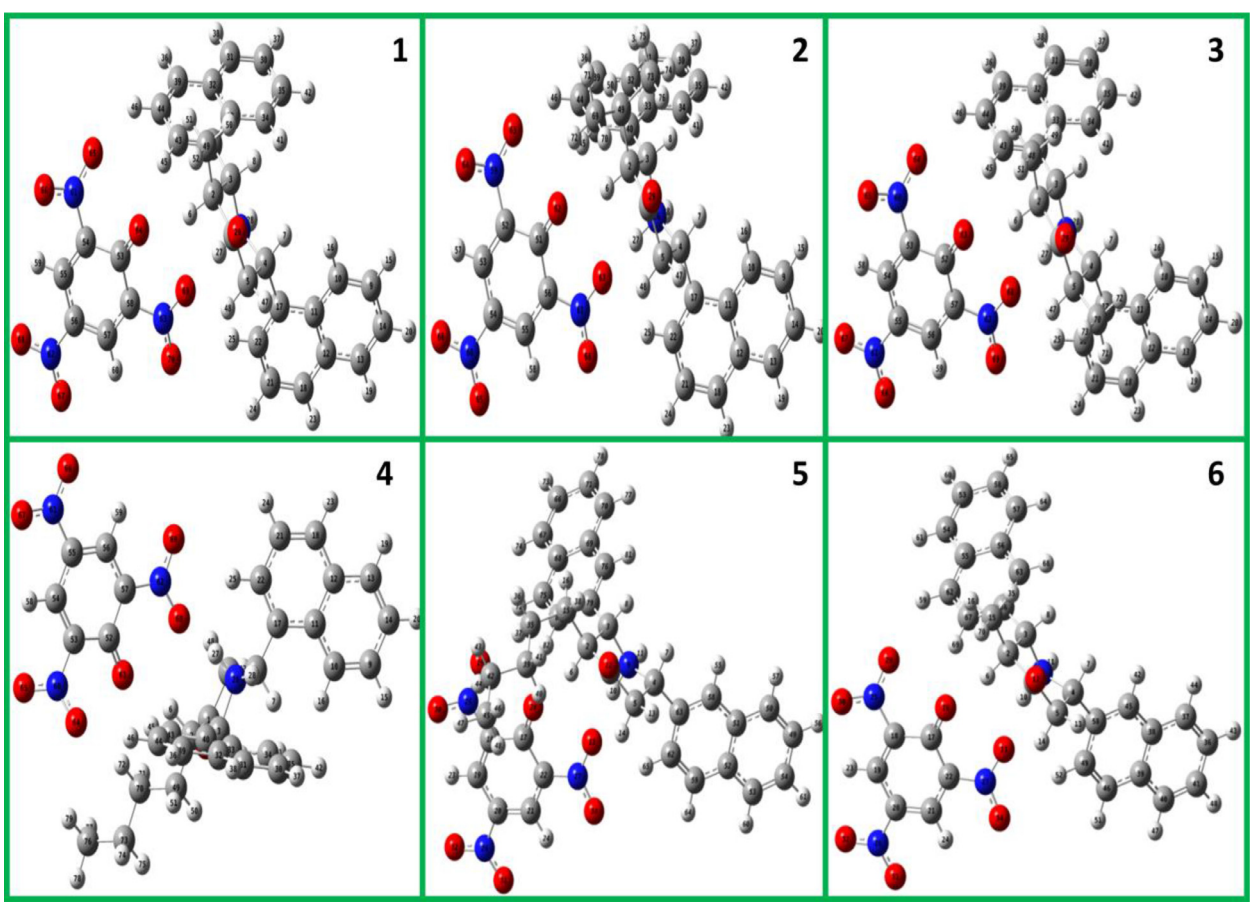

Fig. 7. Optimized molecular structures of compounds (1-6) by B3LYP/6-311++G(d,p) method.

Table 9
Selected bond lengths, bond angles and dihedral angles of compounds (1-6).

Bond Lengths (Å)	1	2	3	4	5	6
C1-C2	1.535	1.535	1.536	1.534	1.536	1.537
C2-C3	1.551	1.556	1.550	1.554	1.554	1.549
C3-N9	1.556	1.555	1.552	1.557	1.557	1.555
N9-C4	1.535	1.533	1.536	1.535	1.543	1.546
C4-C5	1.540	1.538	1.552	1.541	1.539	1.538
C1-C5	1.525	1.528	1.538	1.526	1.528	1.528
C17-O28	1.262	1.263	1.262	1.263	1.264	1.264
C17-C22	1.472	1.471	1.472	1.471	1.468	1.469
C17-C18	1.469	1.468	1.469	1.468	1.466	1.467
C22-C21	1.398	1.397	1.397	1.399	1.398	1.397
C18-C19	1.371	1.371	1.371	1.371	1.373	1.373
N9-H10	1.046	1.045	1.045	1.045	1.043	1.044
N9-H11	1.026	1.026	1.026	1.026	1.025	1.025
Bond Angles (°)	**1**	**2**	**3**	**4**	**5**	**6**
C2-C1-C5	117.92	117.93	118.53	117.48	117.42	118.09
C1-C2-C3	110.72	110.76	110.33	109.89	109.43	110.27
C1-C5-C4	112.03	112.58	109.71	111.30	111.90	112.66
C17-C22-C21	122.51	122.46	122.52	122.48	122.65	122.83
C17-C18-C19	123.77	123.75	123.75	123.73	123.65	123.61
C22-C17-C18	112.61	112.66	112.60	112.70	112.81	112.75
O33-N27-O34	120.12	120.19	120.17	120.19	120.13	119.96
O31-N26-O32	123.80	123.80	123.79	123.80	123.81	123.81
O29-N25-O30	123.60	123.65	123.58	123.59	123.50	123.36
Dihedral Angles (°)	**1**	**2**	**3**	**4**	**5**	**6**
N9-C4-C5-C1	-54.1	-54.1	-54.0	-54.9	-53.9	-52.5
C5-C1-C2-C15	-169.2	-170.7	-171.6	-173.0	-173.4	-169.1
N9-C3-C2-C15	173.5	177.2	173.9	175.3	178.9	177.7
N9-C3-C2-C1	49.8	49.0	50.6	50.9	53.7	53.3
C50-C4-C5-C1	-178.1	-178.0	-177.5	-179.0	-179.3	-178.8
C1-C2-C3-C66	172.9	171.1	173.4	173.0	173.2	173.0
H10-N9-C4-C5	-56.1	-56.1	-56.2	-56.7	-56.3	-55.5
H10-N9-C3-C2	57.7	58.0	58.3	58.3	55.2	55.6
H11-N9-C4-C5	-174.7	-174.6	-174.3	-175.0	-174.6	-173.5
H11-N9-C3-C2	175.2	175.3	175.5	175.5	175.0	175.5

S. aureus, **4, 6** against *V. cholerae*, **4** against *P. aeruginosa*. But, the remaining compounds exert lesser potentially in the range 6.25-50% than the standard drug. With reference to *Amphotericin B*, an equal potency is noted for compounds **4** and **6** against *C. albicans*, **2, 3, 4** and **5** against *A. niger*, **1, 4** and **6** against *A. flavus*, **3, 4** and **5** against *T. rubrum* while compounds **3** and **5** against *C. albicans* and **5** against *A. flavus* are doubly effective. But 12.5-50% potency is noted with the rest of the compound when compared to the standard drug.

3.4. DFT study

Geometry optimizations for the compounds (**1-6**) were carried out according to DFT/6-311++G(d,p) basis set by using Gaussian-09W program package [24]. The optimized molecular structures of (**1-6**) are shown in Fig. 7.

The selected bond lengths, bond angles and dihedral angles values are given in Table 9. In the picrate anion, the C-O bond distance of the anion shows characteristic value with O28-C17 (~1.26) Å) which is intermediate between single and double bond lengths. The loss of a proton from picric acid is confirmed by the lengthening of the C-C bond. The C17-C22 and C17-C18 bond length of ~1.47 Å deviate from the standard aromatic C-C bond lengths (1.40 Å). These differences are attributed to the loss of a hydroxyl proton of picric acid, leading to conversion from the neutral to the anionic state where the negative charge is constrained to lie in the ring.

The repulsive interactions of the deprotaneted oxygen atom with the electron withdrawing NO_2 groups attached to the *ortho* positions are responsible for the shortening of the C22-C21 ~1.39 Å and C18-C19 ~1.37 Å bonds as well as for the significant difference between the internal C-C-C angles within the ring. Both C-C-C angles joining the NO_2 groups C17-C22-C21, 122.83° and C17-C18-C19, 123.61° are significantly greater and C22-C17-C18, 112.75° angles joining the deprotonated hydroxyl group is significantly smaller than the expected angle (120°) for sp^2 hybridized carbon. On comparison, of bond lengths of C17-C22, ~1.47 Å, C17-C18, ~1.46 Å, C22-C21 ~1.39 Å, C18-C19 ~1.37 Å and C-O, ~1.26 Å with normal bond lengths of C-C, C=C and C-O, it is found that C17-C22, C17-C18 (1.4 Å) have single bond character and C22-C21,

Table 10
HOMO-LUMO energies and dipole moments of compounds (1-6).

Compound	HOMO-LUMO Energies (eV)			Dipole Moment			
	HOMO	LUMO	ΔE	μ_x	μ_y	μ_z	μ_{tot}
1	-6.5437	-3.4268	3.1169	15.3904	2.884	-3.8793	16.1317
2	-6.5557	-3.4268	3.1289	15.3634	2.1482	-4.2466	16.0836
3	-6.5220	-3.3768	3.1452	15.472	2.8185	-3.6523	16.1452
4	-6.5565	-3.4295	3.1270	15.2047	-2.3043	4.0525	15.9033
5	-6.4341	-3.4116	3.0225	13.8393	7.3006	-1.4985	15.7185
6	-6.4036	-3.3871	3.0165	13.6338	7.0495	-2.7717	15.5967

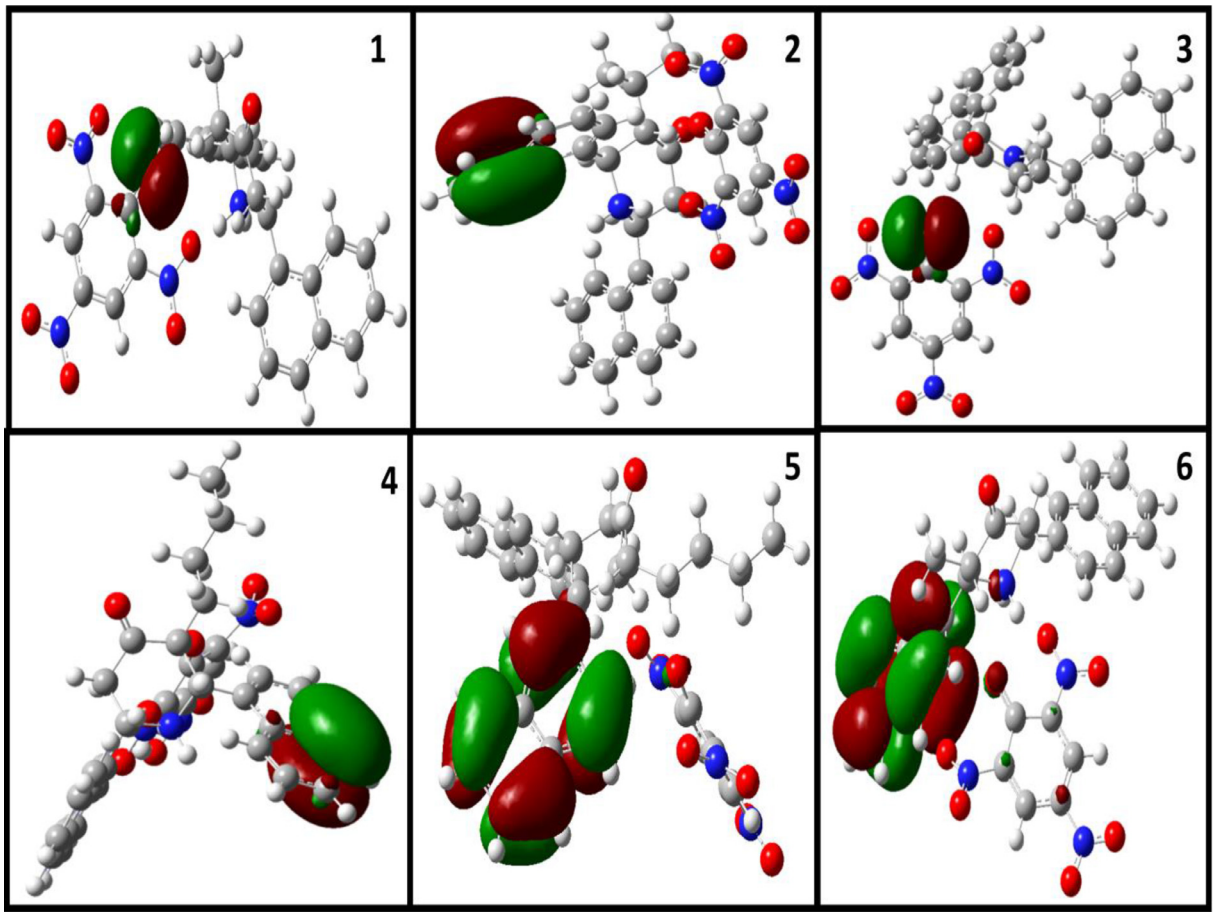

Fig. 8. HOMO energies of compounds (1-6).

C18-C19 (1.39 Å) have double bond character. The C-O (1.21 Å) also carries the double bond character. This indicates that the complex possesses more quinonoid than benzenoid character.

An equatorial orientation of the naphthyl group is witnessed by its torsional angles ~170.0° [C5-C1-C2-C15] and ~177.3° [N9-C3-C2-C15]. The torsional angles of the naphthyl groups on both sides of the amino group are -178.8° [C50-C4-C5-C1] and -173.0° [C1-C2-C3-C66], which support the equatorial orientation of the naphthyl groups. The N-atom of the piperidone molecule shows sp^3 hybridization, which can be noticed from the angles around that nitrogen. The N9-H10 group also adopts an equal disposition to the best plane of the piperdone ring, which is evidenced from the torsional angles H11-N9-C4-C5= -173.5° and H11-N9-C3-C2= 175.5° and H10-N9-C4-C5= -55.5° and H10-N9-C3-C2= 55.6°.

HOMO-LUMO energies have been determined theoretically according to DFT calculations using B3LYP/6-311++G(d,p) level of theory. From the HOMO-LUMO orbital picture (Figs. 8 and 9) it was found that in compounds **6** and **5**, the HOMO is located on the C-O$^-$ group in picric acid, whereas the LUMO is located on the Nitro group at the *para* position in picric acid. In compounds **1** and **3**, the HOMO is located on the naphthyl group attached to C1 carbon in piperidine moiety, whereas the LUMO is located on the Nitro group at the *para* position in picric acid. In compounds **2** and **4**, the HOMO is located on the naphthyl group attached to C1 in piperidine moiety, whereas the LUMO is located on the phenolic oxygen in picric acid. It is seen from Table 10, the replacement of 2-naphthyl group by1-naphthyl group at C1 and C5 in piperidine ring moiety increases the energy gap and bulkiness of alkyl group at C3 position also influences the energy gap. The HOMO-LUMO transition implies that intra-molecular charge transfer takes place within the molecule. All the synthesized compounds (**1-6**) with the lowering of HOMO- LUMO band gap and lower dipole moment exhibits higher bioactive properties of the molecule against the both tested bacterial and fungal strains.

In order to predict the electron density of nitrogen and oxygen performed by DFT calculations and obtained MEP for compounds **1-6**. MEP surface diagram (Fig. 10) Is used to understand the reactive sites in of a molecule. The MEP images of compounds **1-6** clearly suggest that oxygen and nitrogen atoms represent the nucleophilic center (dark red), whereas the protonated nitrogen bears positive charge. The MEP clearly confirms the existence of the electrophillic active centers characterized by red colour.

The density functional theory has been used to calculate the dipole moment (μ), mean polarizability (α) and the total first static hyperpolarizability (β_0) for **1-6** in terms of *x, y, z* components and is given by the following equations.

$$\mu = \left(\mu_x{}^2 + \mu_y{}^2 + \mu_z{}^2\right)^{1/2}$$

$$\alpha_{tot} = \frac{1}{3}(\alpha_{xx} + \alpha_{yy} + \alpha_{zz})$$

$$\Delta\alpha = \frac{1}{\sqrt{2}}\left[\left(\alpha_{xx} - \alpha_{yy}\right)^2 + \left(\alpha_{yy} - \alpha_{zz}\right)^2 + (\alpha_{zz} - \alpha_{xx})^2 + 6\left(\alpha_{xy}^2 + \alpha_{yz}^2 + \alpha_{xz}^2\right)\right]^{\frac{1}{2}}$$

$$\beta_0 = \left[(\beta_{xxx} + \beta_{xyy} + \beta_{xzz})^2 + (\beta_{yyy} + \beta_{xxy} + \beta_{yzz})^2 + (\beta_{zzz} + \beta_{xxz} + \beta_{yyz})^2\right]^{1/2}$$

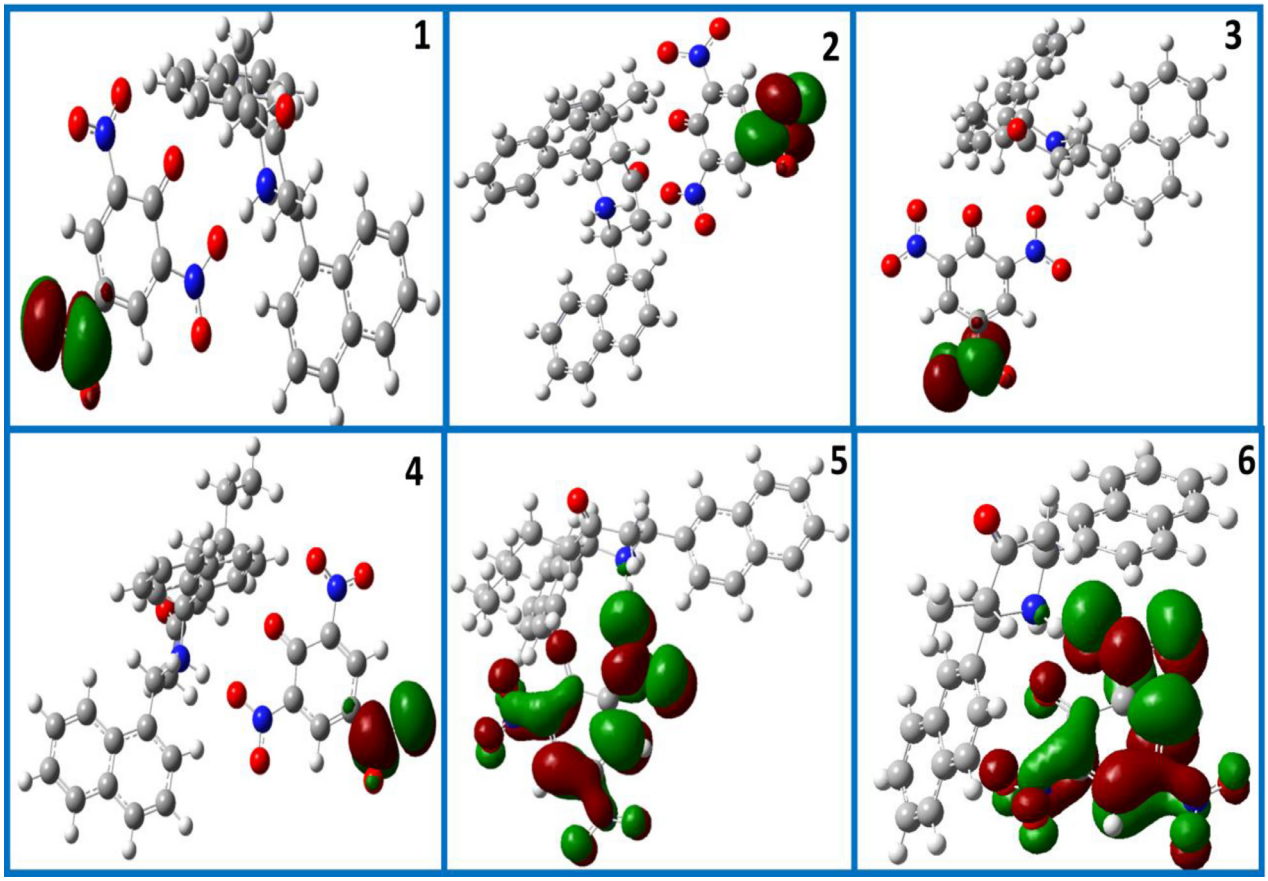

Fig. 9. LUMO energies of compounds (1-6).

Table 11
Polarizability and first hyperpolarizability of compounds (1-6).

Compound	1	2	3	4	5	6
α_{xx}	281.98	295.67	292.02	293.71	282.96	269.49
α_{yy}	256.82	276.34	262.46	295.76	291.72	263.16
α_{zz}	267.72	272.69	272.63	271.04	295.11	267.63
α_{xy}	-13.53	-16.95	-12.93	20.67	-13.65	-17.37
α_{xz}	-8.77	-8.37	-10.29	7.51	-10.60	-8.91
α_{yz}	-18.43	-18.14	-19.26	-18.34	-23.64	-15.79
α_o(x10^{-23}) (esu)	3.98	4.2	4.09	4.25	4.30	3.95
$\Delta\alpha$ (x10^{-24}) (esu)	6.73	7.55	7.20	8.49	7.74	6.47
β_{XXX}	645.3052	649.4835	650.8677	621.6441	514.2514	500.5509
β_{YYY}	42.1811	24.2724	47.4182	-59.8622	227.5143	221.4778
β_{ZZZ}	-87.1668	-97.1635	-72.0881	128.2878	-91.2742	-85.8137
β_{XYY}	131.0622	163.4085	123.7093	198.1327	164.6443	164.2975
β_{XXY}	53.6178	55.5242	64.07	-72.6862	60.0789	100.2613
β_{XXZ}	9.9549	9.7643	2.3299	-19.2332	16.2086	-42.7065
β_{XZZ}	-7.0948	-29.3598	3.9566	-51.7681	-24.9955	-30.4014
β_{YZZ}	34.0308	42.5668	24.866	-23.9767	69.1207	13.8675
β_{YYZ}	-37.8465	-25.0478	-36.882	-3.9599	30.3782	-3.467
β_{XYZ}	105.3365	82.8687	110.0518	38.2465	120.0581	118.7922
β_{tot} (x10^{-30}) (esu)	6.8100	6.92	6.8900	6.8300	6.4467	6.3048

All the electric dipole moments and first hyperpolarizabilities were calculated by taking the origin of the Cartesian coordinate system (x,y,z) = (0,0,0) at the center of mass of the compounds.

The dipole moment (μ), mean polarizability (α) and the total first static hyperpolarizability (β_0) are related directly to the non-linear optical efficiency of structures. The optical non-linearity of organic materials originates from the delocalized electron cloud of the substituent groups. All the compounds (**1-6**) are found to be polar molecules and have non-zero dipole moment components. Introduction of the smaller alkyl group at C3 slightly enhances the dipole moment, whereas bulky alkyl group decreases the dipole moment. Non – zero dipole moments result in large microscopic first hyperpolarizabilities and hence, have a good microscopic NLO behavior.

The calculated polarizabilities α_{tot} have non-zero values and are dominated by diagonal components. As seen from Table 11, β_{tot} values for 1-naphthyl substituted piperidone picrates (**1-4**) are higher than that of 2-naphthyl substituted derivatives (**5** and **6**). In compounds **5** and **6** as buliknes of alkyl group at C2 increases, β_{tot} values also increase, whereas in compounds (**1-4**), the NLO charac-

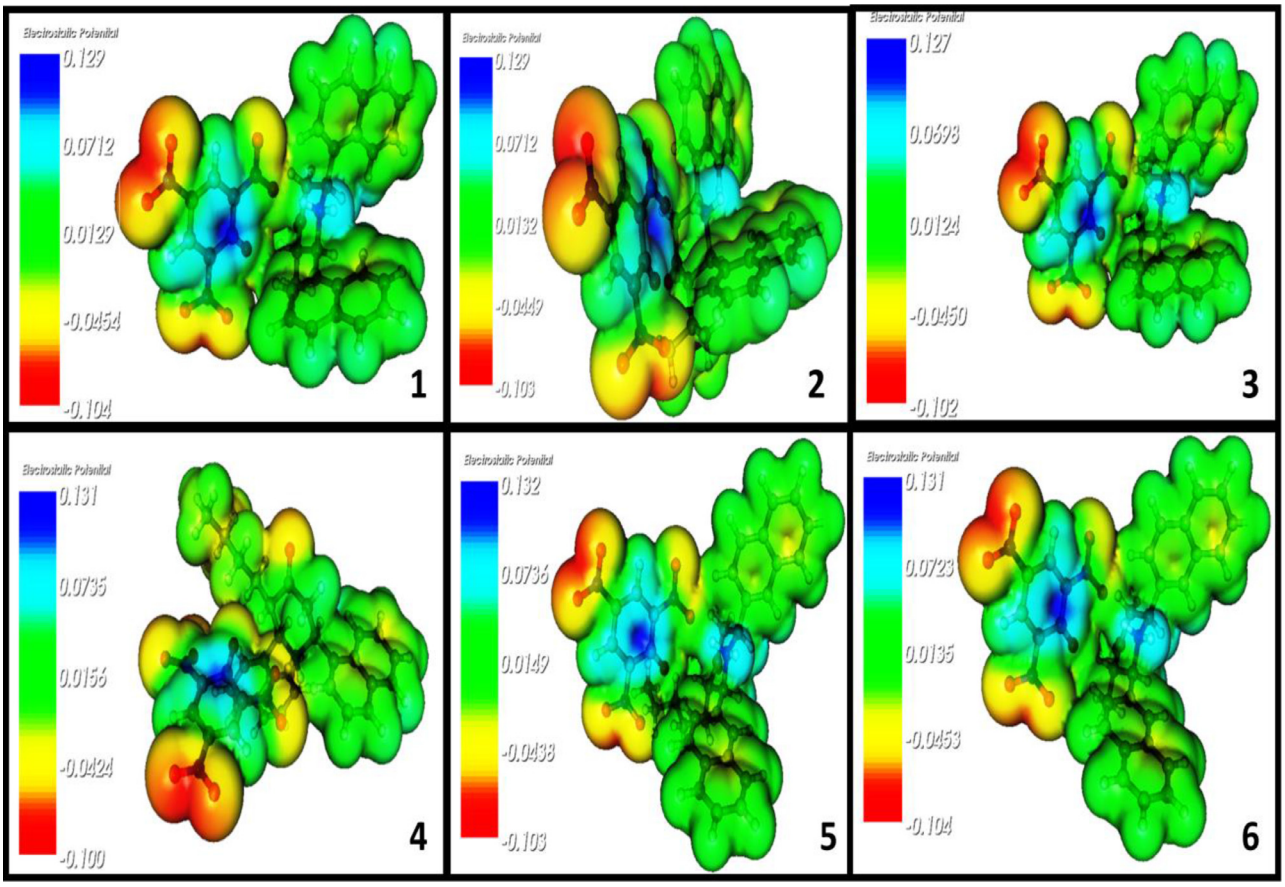

Fig. 10. MEP diagram of compounds (1-6).

Table 12
Hydrogen bond interactions of piperidone with amino acids at the active site of Acetylcholinesterase Inhibitors of compounds (1-6).

Compound	Docking Score	Hydrogen Bonding Interactions Donor	Acceptor	Distance (Å)
1	-14.1	-	-	-
2	-11.7	**TYR129(N-H…O)**	O*	2.9
3	-11.9	-	-	-
4	-10.6	**PHE287(O…H-N)PHE330(O-H…O)**	N*O*	3.13.3
5	-11.2	**TYR129(O-H…O)**	O*	2.8
6	-12.4	**ARG288(N-H…O)(O-H…O)ILE286(N-H…O)**	O*O*O*	3.33.22.8
Co-Crystal (**1-BENZYL-4-[(5,6-DIMETHOXY-1-INDANON-2-YL)METHYL]PIPERIDINE**)	-10.4	**THR129(O…H-N)**	N*	2.6

* Ligand

ter decreases according to the following order C2-CH$(CH_3)_2$ (**2**) > C2 & C4- CH_3 (**3**) > C2-CH_3 (**1**) > C2-$(CH_2)_3CH_3$ (**4**).

3.5. Molecular docking studies

The entire docking calculations were performed using the Autodock docking module program. It performs flexible protein-ligand docking and searches for favorable interactions between one typically small ligand molecule and a typically larger protein molecule. Docking process, wherein the protein preparation inhibited refinement is carried out with a maximum of 20 poses, wherein the side chains are optimized and refinement of residues takes place, if the ligand poses are within 5.0Å. The best docked structure was chosen by docking score and the number of amino acids matches (hydrogen bonds) with original drug complex.

The docked, glide energy and hydrogen bonding interactions of the compounds (**1-6**) and co-crystallized ligand is given in Table 12. A view of the X-ray crystal structure of the title compound in the Acetylcholinesterase Inhibitors Receptor active site showing the key hydrogen contacts between inhibitor and enzyme is depicted in Figs 11(a-f). The surface diagram showing the compounds (**1-6**) docked at the active site of Acetylcholinesterase Inhibitors Receptor is depicted in Fig. 12. Molecular analysis of compounds **(1-6)** indicated that hydrogen bond and hydrophobic are four major interactions (THR9, VAL12, GLN20) incorporating the attachment of this ligand to Acetylcholinesterase Inhibitors acceptor. The co-crystallized ligand also docked well and it shows better interactions with active residues. The results show that the compound **1** having better binding energy and the co-crystallized ligand have comparable interactions. It is indicated that compound **6** has better ligand protein interactions. X-ray crystal structures confirmed the expected binding mode, and consideration of binding orientation and electronic properties enabled optimization to Piperidone as a more potent second-generation lead.

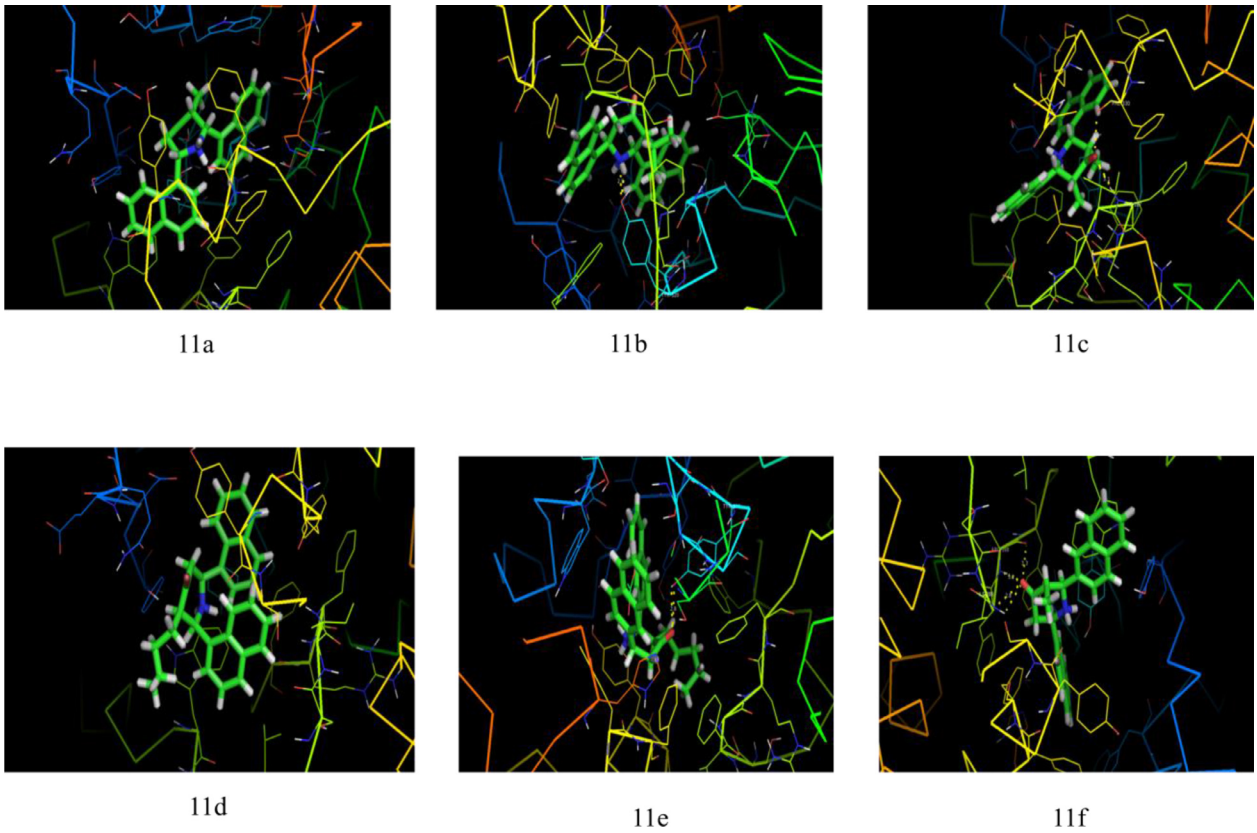

Fig. 11. (a-f) The title compounds (1-6) in the Acetylcholinesterase Inhibitors Receptor active site showing key hydrogen contacts between piperidone inhibitor and enzyme.

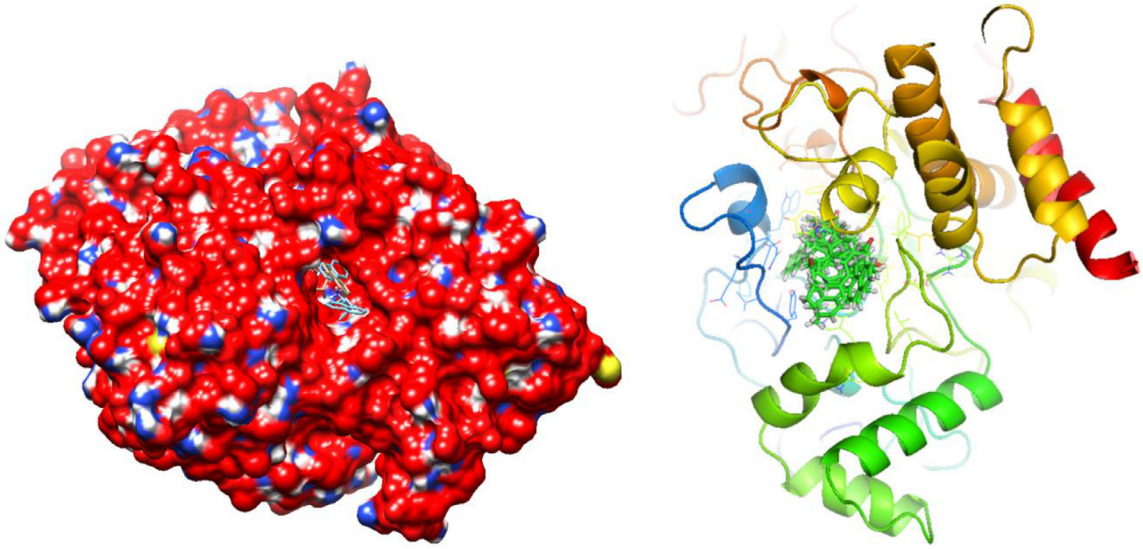

Fig. 12. Surface and Cartoon diagram showing the piperidone docked at the active site of Acetylcholinesterase Inhibitors.

4. Conclusions

A series of 3-alkyl/3,5-dialkyl-2r,6c-di(naphthyl)piperidin-4-one picrates have been synthesized successfully in appreciable yields and were characterized by elemental analysis, FT-IR, Mass, 1D (^{1}H and ^{13}C), and 2D (HOMOCOSY, HSQC, HMBC, NOESY, and DEPT) NMR spectral techniques. The NMR spectral data suggest that the title compounds (**1-6**) exist in normal chair conformation with equatorial orientation of all the substitutes. Due to protonation, the axial N-H bond experiences severe syn 1,3-diaxial interaction with axial hydrogens at C-3 and C-5 and due to these interactions the protons H-3a and H-5a are deshielded and corresponding carbons C-3 and C-5 shielded. The chemical shifts of the heterocyclic ring protons are influenced by the picrate anion. All the newly synthesized compounds were screened for their antibacterial and antifungal activities. Most of the compounds showed good antibacterial and antifungal activities. However, the antibacterial and antifungal activities are significantly influenced by the aromatic substituents. The geometry optimization have been obtained for the compounds (**1-6**) by using DFT/B3LYP/6-311++G(d,p) level. The lowering of

HOMO and LUMO energy gap clearly indicates the charge transfer taking place within the molecule. The MEP maps show that oxygen and nitrogen atoms are the negative potential sites and the positive potential sites are around the hydrogen atoms. The total dipole moment, polarizability and hyperpolarizability of the compounds were calculated and the results show that the molecule could be good NLO material. Docking results show that the compound **1** having better binding energy and the co-crystallized ligand have comparable interactions. It is indicated that compound **6** has better ligand protein interactions.

Author contribution statement

S. Savithiri: Conceived and designed the experiments; Performed the experiments; Analyzed and interpreted the data; Contributed reagents, materials, analysis tools or data; Wrote the paper.

S. Bharanidharan: Conceived and designed the experiments; Contributed reagents, materials, analysis tools or data.

P. Sugumar: Performed the experiments; Analyzed and interpreted the data.

C. Rajeevgandhi: Analyzed and interpreted the data.

M. Indhira: Analyzed and interpreted the data.

Declaration of Competing Interest

The authors declare no conflict of interest.

Supplementary materials

Supplementary material associated with this article can be found, in the online version, at doi:10.1016/j.molstruc.2021.130145.

References

[1] P. Parthiban, S. Balasubramanian, G. Aridoss, S. Kabilan, Spectrochim. Acta. A. 70 (2008) 1–24.
[2] C. Ramalingam, Y.T. Park, S. Kabilan, Eur. J. Med. Chem. 41 (2006) 683–696.
[3] I.G. Mokio, A.T. Soldatenkov, V.O. Federov, E.A. Ageev, N.D. Sergeeva, S. Lin, E.E. Stashenku, N.S. Prostakov, E.L. Andreeva, Khim Farm Zh 23 (1989) 421–427.
[4] P. Parthiban, G. Aridoss, P. Rathika, V. Ramkumar, S. Kabilan, Bioorg. Med. Chem. Lett. 19 (2009) 2981–2985.
[5] H.I. El-Subbagh, S.M. Abu-Zaid, M.A. Mahran, F.A. Badria, A.M. Al-Obaid, J. Med. Chem. 43 (2000) 2915–2921.
[6] A.A. Watsona, G.W.J. Fleet, N. Asano, R.J. Molyneux, R.J. Nugh, Phytochemistry 56 (2001) 265–295.
[7] G. Aridoss, S. Amirthaganesan, M.S. Kim, J.T. Kim, Y.T. Jeong, Eur. J. Med. Chem. 44 (2009) 4199–4210.
[8] E.L. Eliel, M.H. Gianni, T.H. Williams, J.B. Stothers, Tetrahedron Lett 3 (17) (1962) 741–747.
[9] N.S. Bhacca, D.H. Williams, Applications of NMR Spectroscopy in Organic Chemistry: Illustration from the Steroid Field, Holden-Day, 1964.
[10] H. Booth, J.H. Little, Tetrahedron 23 (1) (1967) 291–297.
[11] A. Manimekalai, J. Jayabharathi, Ind. J. Chem. 45B (2006) 1686–1691.
[12] V. Vimalraj, K. Pandiarajan, Magn. Reson. Chem. 49 (10) (2011) 682–687.
[13] Z. Dega-Szafran, G. Dutkiewicz, Z. Kosturkiewicz, M. Petryna, J. Mol. Struct. 708 (1-3) (2004) 15–21.
[14] V. Stilinović, B. Kaitner, Cryst. Growth & Design 11 (9) (2011) 4110–4119.
[15] B. Bashir, B. Zhang, S. Pan, Z. Yang, J. Alloys and Compounds 758 (2018) 85–90.
[16] C. Zhang, Y. Song, X. Wang, Coord. Chem. Rev. 251 (1-2) (2007) 111–141.
[17] T. Arivazhagan, S.S.B. Solanki, N.P. Rajesh, J. Cryst. Growth 496 (2018) 43–50.
[18] V. Ramesh, K. Rajarajan, Appl. Phy. B. 113 (1) (2013) 99–106.
[19] M.M. Chen, H.G. Xue, S.P. Guo, Coord. Chem. Rev. 368 (2018) 115–133.
[20] G.A. Babu, S. Sreedhar, S.V. Rao, P. Ramasamy, J. Cryst. Growth 312 (12-13) (2010) 1957–1962.
[21] B. Dhanalakshmi, S. Ponnusamy, C. Muthamizhchelvan, J. Cryst. Growth 313 (1) (2010) 30–36.
[22] S. Savithri, M. Arockia doss, G. Rajarajan, V. Thanikachalam, J. Mol. Struct. 1105 (2015) 225–237.
[23] S. Savithiri, M. Arockia doss, G. Rajarajan, V. Thanikachalam, J. Mol. Struct. 1075 (2014) 430–441.
[24] M.J. Frisch, G.W. Trucks, H.B. Schlegel, G.E. Scuseria, M.A. Robb, J.R. Cheeseman, G. Scalmani, V. Barone, B. Mennucci, G.A. Petersson, H. Nakatsuji, M. Caricato, X. Li, H.P. Hratchian, A.F. Izmaylov, J. Bloino, G. Zheng, J.L. Sonnenberg, M. Hada, M. Ehara, K. Toyota, R. Fukuda, J. Hasegawa, M. Ishida, T. Nakajima, Y. Honda, O. Kitao, H. Nakai, T. Vreven, J.A. Montgomery Jr., J.E. Peralta, F. Ogliaro, M. Bearpark, J.J. Heyd, E. Brothers, K.N. Kudin, V.N. Staroverov, T. Keith, R. Kobayashi, J. Normand, K. Raghavachari, A. Rendell, J.C. Burant, S.S. Iyengar, J. Tomasi, M. Cossi, N. Rega, J.M. Millam, M. Klene, J.E. Knox, J.B. Cross, V. Bakken, C. Adamo, J. Jaramillo, R. Gomperts, R.E. Stratmann, O. Yazyev, A.J. Austin, R. Cammi, C. Pomelli, J.W. Ochterski, R.L. Martin, K. Morokuma, V.G. Zakrzewski, G.A. Voth, P. Salvador, J.J. Dannenberg, S. Dapprich, A.D. Daniels, O. Farkas, J.B. Foresman, J.V. Ortiz, J. Cioslowski, D.J. Fox, Gaussian 09, 2010 Revision C.02, Gaussian Inc., Wallingford CT.
[25] G. Kryger, I. Silman, J.L. Sussman, Struct. 7 (1999) 297–307.
[26] Z. Bikadi, E. Hazai, J. Chem info. 1 (1) (2009) 15.
[27] G.M. Morris, D.S. Goodsell, R.S. Halliday, R. Huey, W.E. Hart, R.K. Belew, A.J. Olson, J. Comp. Chem. 19 (1998) 1639–1662.
[28] M. Arockia doss, S. Savithiri, S. Vembu, G. Rajarajan, V. Thanikachalam, Can. Chem. Trans. 3 (2015) 261–274.

J Mater Sci: Mater Electron

Enhancement of magnetic, supercapacitor applications and theoretical approach on cobalt-doped zinc ferrite nanocomposites

K. Sathiyamurthy[1], C. Rajeevgandhi[2,*], L. Guganathan[3], S. Bharanidharan[4], and S. Savithiri[5]

[1] Department of Physics, PRIST University, Vallam, Thanjavur, Tamilnadu 613 403, India
[2] Department of Physics, Annai College of Arts and Science, Kovilacheri, Kumbakonam, Tamilnadu 612 503, India
[3] Department of Physics, Annamalai University, Annamalainagar, Tamilnadu 608 002, India
[4] Department of Physics, PRIST University, Puducherry 605 007, India
[5] Department of Chemistry, Karpagam Academy of Higher Education, Coimbatore, Tamilnadu 641 021, India

Received: 22 December 2020
Accepted: 13 March 2021

ABSTRACT

Nanostructured zinc ferrite, cobalt ferrite, and cobalt-doped zinc ferrite were synthesized by using a simple co-precipitation method. Physico-chemical analyses were investigated by thermogravimetric and differential thermal analysis (TG/DTA) and X-ray diffraction (XRD) techniques. The TG/DTA study revealed the thermal transformation of metal hydroxide precursors. The XRD representation confirmed the cubic spinel structure of the cobalt-doped zinc ferrite nanoparticles. The Fourier-transform infrared spectrum, recorded to acquire the characteristic vibration mode of the metal oxides, was present in the composites. The analyzed morphology was confirmed by field-emission transmission electron microscopy and field-emission scanning microscopy, revealing a spherical structure with an agglomeration of nanocomposites. Analysis of the energy dispersive X-ray spectrum of the cobalt-doped zinc ferrite nanocomposites exposed the elemental features. The prepared nanocomposites were examined using a vibrating sample magnetometer, which showed the transformation of paramagnetic to ferromagnetic behavior. The specific capacitance of the three ferrites were calculated, and there was a noticeable enhanced specific capacitance of 218 Fg^{-1} in $Co_{0.5}Zn_{0.5}Fe_2O_4$ at the scan rate of 10mV/s. In the present work, the mixed spinel structure of the nanocomposites revealed the magnetic and electrochemical properties. The prepared nanocomposites can be used in energy storage devices. The theoretical part was calculated by the density functional theory method, which was employed to study the structural, nonlinear optics, and physico-chemical parameters of $CoZnFe_2O_4$ NPs.

Address correspondence to E-mail: rajeevphdphy@gmail.com

https://doi.org/10.1007/s10854-021-05764-2
Published online: 09 April 2021

1 Introduction

Nanocrystalline spinel ferrites are interesting materials that have many different uses in, for example, image recording tapes, permanent magnets, hard plate recording media, flexible record media, read–make heads, dynamic pieces of ferrofluids, concealing imaging, attractive refrigeration, an alluringly controlled vehicle of aggressive to illness drugs, interesting resolution imaging (X-ray) separate overhaul, attractive cell segments, etc. [1–3]. Electro-shock resistance–storage frameworks, i.e., batteries and supercapacitors are required to utilize them. The supercapacitor is the most significant property; it can yield high-control thickness, high-rate ability, and broad cycle life [4, 5]. $CoFe_2O_4$ is the inverse spinel structure, with Co^{2+} particles usually on octahedral (B) sites and Fe^{3+} particles equally positioned between octahedral (B) and tetrahedral (A) destinations [6]. $ZnFe_2O_4$ is assembled in normal spinel with each Fe^{3+} particle on octahedral (B) sites and each Zn^{2+} on tetrahedral (A) sites. In general, the mixed spinel structure of cobalt-doped zinc ferrite nanocomposites is attractive for numerous applications, such as supercapacitors [7, 8], microwave applications [9], recording media [10], magnetic fluids [11], gas sensors [12], and catalysts [13]. It has been specially designed in many fields of research because of its strong properties, high electric resistivity, and magnetic delicacy center [14, 15]. Different combination procedures are available for ferrite nanoparticles (NPs) such as sol–gel, co-precipitation, ball–milling, micro-emulsions, and electrospinning method [16–25]. Among these methods, the co-precipitation method has some crucial points, with the possibility of obtaining nanomaterials with greater homogeneity, reproducibility, and morphology. Although cobalt is more expensive than iron and zinc, mixed metal oxides may give attractive metal-based composites. In the current work, we examine the preparation of cobalt zinc ferrite nanoparticles in the ratio of ($x = 0.0$, 0.5, and 1.0). The prepared nanocomposites were characterized by morphological, magnetic, and electrochemical properties. Quantum chemical calculations were used to analyze the theoretical parameters of the title compound.

2 Experimental details

2.1 Synthesis procedure

Cobalt-doped zinc ferrite $Co_xZn_{1-x}Fe_2O_4$ ($x = 0.0$ to 1.0) NPs were prepared by the co-precipitation method from $Fe(NO_3)_3.9H_2O$, $Co(NO_3)_2.6H_2O$, $Zn(NO_3)_2.6H_2O$, and $C_6H_8O_7$, with NaOH as a precipitating agent. The value of x was varied from 0.0, 0.5, and 1.0 to achieve different levels of doping concentration. The chosen stoichiometric measure of each metal nitrate and citric were weighed and dissolved independently in bare minimum amounts of 20 ml deionized water. After complete dissolution, the metal nitrates were mixed together to maintain the Co + Zn/ferrite (Fe) relative amount of 1:2. The aqueous solution of metal nitrate and citric was mixed together in the proportion of 1:3. Next, the whole solution was kept with constant stirring at 500 rpm at 70 °C on a magnetic stirrer with an incorporated hot plate. Finally, an amount of NaOH solution was added as the precipitating agent, and it was established that the pH value was 9. The resulting combination was stirred magnetically for 3 h at 80 °C until a brown precipitate was produced, which was sanitized by de-ionized water and acetone a number of times to eliminate impurities. The final result was dried at 100 °C to in a hot air oven and further calcinated at 600 °C for 3 h.

2.2 Characterization

An X-ray powder diffraction (XRD) investigation was conducted using an X'pert PRO (PW3040/60) powder X-ray diffractometer with Cu-Kα radiation (operated at 40 kV and 30 mA). Thermogravimetric and differential thermal analysis (TG/DTA) was carried out at a heating rate of 10 °C min^{-1} under air atmosphere using a NETZSCH-STA 449 F3 JUPITER. Fourier-transform infrared (FT-IR) transmission spectra were taken on a Perkin Elmer Spectrum BX model infrared spectrophotometer in a range from 4000 to 400 cm^{-1}. Field-emission scanning microscopy (FE-SEM) and energy dispersive X-ray (EDAX) were performed using a ZEISS SUPRA 40 VP SEM, while elemental analysis was carried out with the help of EDAX. The morphology and size have determined by field-emission transmission electron microscopy (FE-TEM) analysis using a JEM 2100 F. Magnetic measurements were carried out with the

Quantum Design Model 7407 vibrating sample magnetometer, and parameters such as saturation magnetization (Ms), coercive force (Hc), remanence (Mr) and magnetic moment were evaluated. Cyclic voltammetry (CV) analysis was carried out to investigate the electrochemical properties of the $Co_xZn_{1-x}Fe_2O_4$ samples and investigated using an electrochemical workstation (Model CHI 660) at different scan rates of 10, 20, 30, and 50 mVs^{-1} operated between − 1.5 and + 1.6 V at 31 ± 2 °C. Furthermore, the electrochemical measurements were observed with 0.2 M tetra butyl ammonium perchlorate electrolyte with a standard three-electrode system comprising a working electrode where the sample was placed, an Ag/AgCl electrode as a reference electrode, and a high platinum wire, which was used as a counter electrode.

3 Results and discussion

3.1 Structural analysis

The powder XRD spectra of $Co_xZn_{1-x}Fe_2O_4$ samples with different concentrations (x = 0.0, 0.5, 1.0) of zinc ferrite, cobalt-doped zinc ferrite, and cobalt ferrite nanocomposites are shown in Fig. 1. The mixed spinel structure of the diffraction plane according to 2θ shows that the characteristic peaks at 29.6, 35.8, 42.3, 52.7, 56.9, and 62.5 match the planes (220), (311), (400), (422), (511) and (440), respectively, with the reflected arrangement due to the cubic spinel structure of $Co_xZn_{1-x}Fe_2O_4$ (x = 0.0, 0.5 and 1.0) NPs [26]. All the characteristic peaks were confirmed in agreement with the JCPDS Cards (#22-1086 for $CoFe_2O_4$ and #89-1012 for $ZnFe_2O_4$), which indicates the single cubic spinel structure [27]. The power of the planes (220) and (440) is very sensitive to the metal cations present inside the tetrahedral and octahedral destinations of the spinel ferrite [28]. Usually, the structure of zinc ferrite is dependent on the normal cubic phase due to the divalent cations Zn^{2+} possesses the tetrahedral site, and trivalent cations Fe^{3+} involve the octahedral site. Cobalt-doped zinc ferrite NPs have a mixed spinel structure. By doping with Co^{2+} ions, they especially occupy both the octahedral and tetrahedral destinations in the spinel structures [29]. The crystallite sizes of $Co_xZn_{1-x}Fe_2O_4$ (x = 0.0, 0.5, 1.0) was estimated by Scherrer's formula and were 24, 27, and 21 nm for zinc ferrite, cobalt-doped zinc ferrite, and cobalt ferrite, respectively. The structural parameters are presented in Table 1. The small variety of crystallite sizes show the effect of crystallization on the surface and the expanding atomic fixations that bring about granule development. The lattice parameter 'a' was determined for each example utilizing connection $a = d(h^2 + k^2 + l^2)^{½}$ [30], where h, k, and l are Miller indices of the planes. The cell parameter 'a' with the increasing Co complex can be connected with the variety in ionic radii of Co^{2+} (0.74 Å) [31] and Zn^{2+} (0.82 Å) [32] which found that the size of the zinc particles is more prominent than the size of the cobalt particle in $Co_xZn_{1-x}Fe_2O_4$, the changes of lattice parameter strongly recommended by Vagurd's law. These findings are now detailed in the literature, which rely in particular on the type of planning

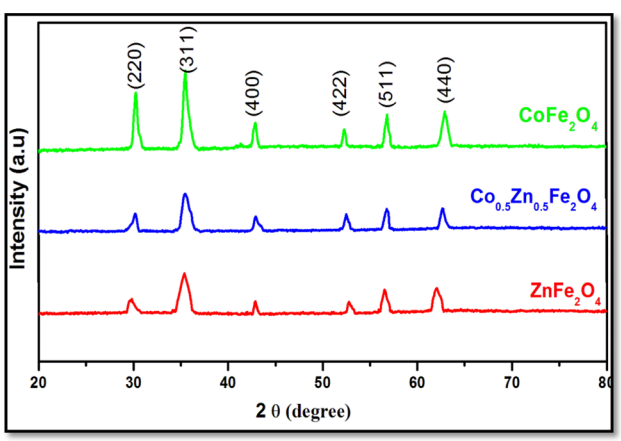

Fig. 1 XRD spectra of $Co_xZn_{1-x}Fe_2O_4$ NPs (x = 0.0, 0.5 and 1.0)

Table 1 Structural parameters of $Co_xZn_{1-x}Fe_2O_4$ NPs (x = 0.0, 0.5 and 1.0)

Composition	Crystallite size (D) nm	Lattice parameter (a) nm	Volume of cubic cell $(V)^3$ Å	X-ray density (dx) (gm/cm^3)
$ZnFe_2O_4$	24	8.49	590	5.32
$Co_{0.5}Zn_{0.5}Fe_2O_4$	27	8.41	585	5.40
$CoFe_2O_4$	21	8.38	580	5.58

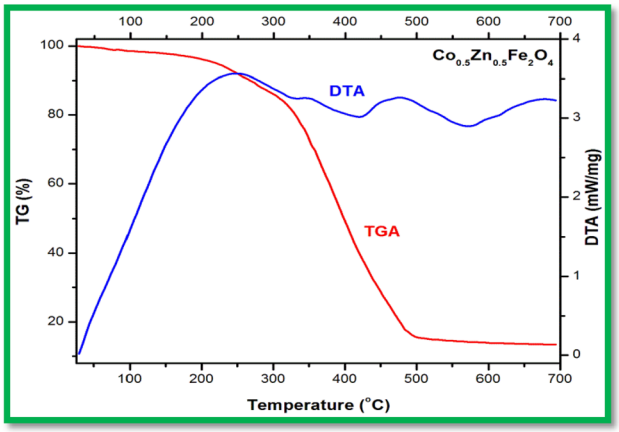

Fig. 2 TG/DTA curve of the $Co_{0.5}Zn_{0.5}Fe_2O_4$ sample

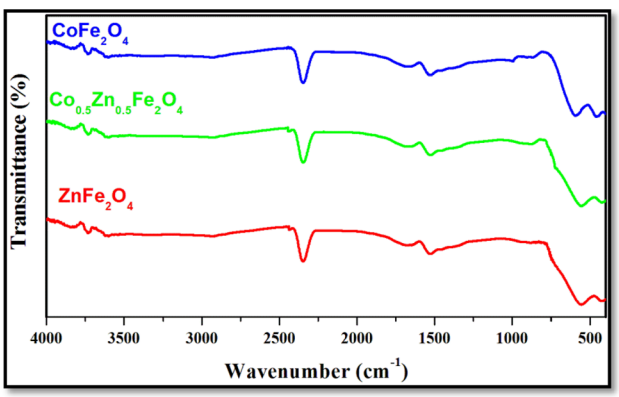

Fig. 3 FT-IR spectra of $Co_xZn_{1-x}Fe_2O_4$ NPs ($x = 0.0$, 0.5 and 1.0)

strategy, timing, circumstances, molar rate, and precursor [33, 34]. The reduction of the cross-section parameter with Co^{2+} expansion is recommended for the development of an essential homogenized structure with a strong arrangement [35]. This may be the explanation for the $ZnFe_2O_4$ nanostructure including the solid interatomic collaboration contrasting with the $Co_xZn_{1-x}Fe_2O_4$ structure. It could also be clarified as regards the appropriation of cations (Zn^{2+} and Fe^{3+}) by substitution of Co^{2+} particles in the interstitial sites of the spinel ferrite. The X-ray density of all the samples was additionally calculated using the connection [36] of $\rho X = 8$ M/NAV cell, where M is the sub-atomic weight, NA is Avogadro's number and V is the cell volume.

3.2 TG/DTA analysis

TG/DTA of the as-prepared $Co_xZn_{1-x}Fe_2O_4$ ($x = 0.5$) sample recorded from 35 °C to 700 °C is shown in Fig. 2. TG bends under latent air indicating that two-weight losses in the sample between 35 and 320 °C and 321 to 501 °C. The fundamental weight losses were identified with the weakening of the water molecules, while the second loss is because of a decrease of the inorganic templates [37, 38]. The DTA bend shows that one endothermic peak at 423 °C is owing to the required hydration and that there are two exothermic peaks at 252 and 475 °C ascribed to the decomposition of nitrates [39]. One progressive endothermic peak showing at 573 °C balances the breakdown of the citrate precursor to make cobalt zinc ferrite with the inferred development of CO, CO gas, and the formation of dissolved particles. After 500–700 °C, there is no weight loss in the current analysis confirming the phase transition of the NPs. This conclusion of the thermogravimetric examinations according to the conditions of the synthesis of the precursor powders was selected at 600 °C, being the ideal temperature for obtaining high crystalline stages.

3.3 Functional group analysis

Functional group studies confirmed by infrared spectroscopy were used to consider the change in the spinel precursors calcinated at 600 °C. Figure 3 shows the $Co_xZn_{1-x}Fe_2O_4$ ($x = 0.0$, 0.5, and 1.0) FT-IR analysis for zinc ferrite, cobalt-doped zinc ferrite, and cobalt ferrite NPs recorded in the 4000−400 cm^{-1} range. In the FT-IR of the metal hydroxide, $(M(OH)_2)$ groups developed in the 3600–3200 cm^{-1} range. The two absorption main groups by extending the vibration-stretching groups around 460−400 cm^{-1} are the tetrahedral sites (Fe-O), while the metal-stretching groups around 600−550 cm^{-1} are the octahedral sites [40–43]. In this work, the prepared sample was calcined at 600 °C due to distinct groups like M-O, and the assembly frequencies for NO_3-, OH- and H_2O have disappeared. The tetrahedral sites are occupied by the Zn^{2+} , while cobalt and iron have both tetrahedral and octahedral locations because they are divalent particles in the mixed Co_xZn_{1-x}-Fe_2O_4 spinel.

3.4 Morphological studies

3.4.1 FE-SEM

Morphological confirmation of the calcined samples was examined by FE-SEM. Figure 4a–c shows the FE-SEM micrographs of measurement at $x = 0.0$, 0.5, and 1.0 (zinc ferrite, cobalt zinc ferrite, and cobalt ferrite, respectively). All the micrographs show a spherical type with agglomerations in the same places. The prepared samples were calcinated at 600 °C and particle sizes were from 20 to 30 nm. The surface morphology compromises the agglomeration at a few places of the particles due to magnetic interaction or interfacial surface strain. The EDAX images of zinc ferrite, cobalt zinc ferrite, and cobalt ferrite reveal the quantities of Zn, Co, Fe, and O, as shown in Fig. 4d–f.

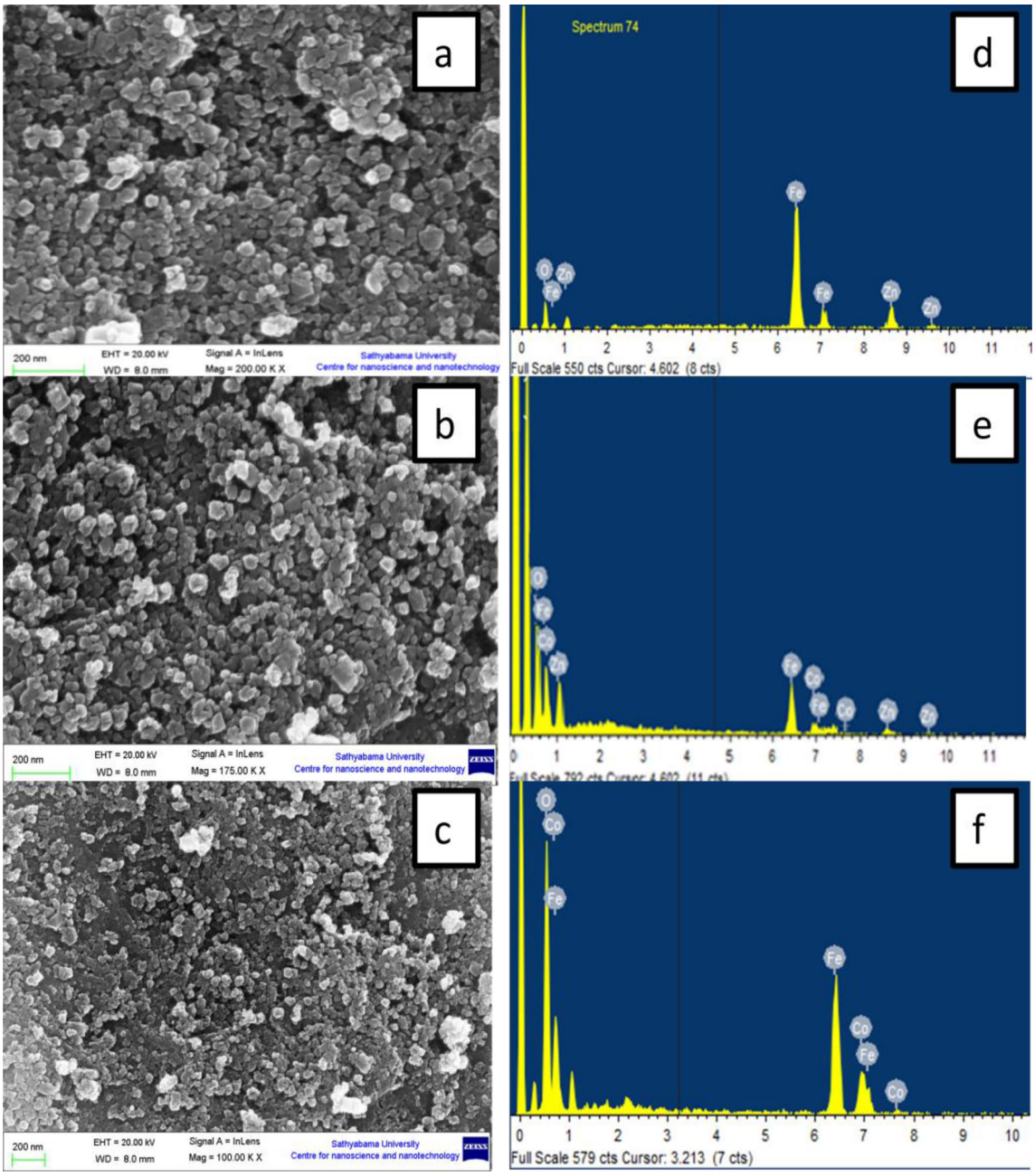

Fig. 4 **a–f** FE-SEM images with EDAX spectra for $Co_xZn_{1-x}Fe_2O_4$ NPs ($x = 0.0$, 0.5 and 1.0)

3.4.2 FE-TEM

Field emission transmission electron microscopy (FE-TEM) was used to explore the morphology of the calcinated samples. Figure 5a–c displays the FE-TEM micrographs of the zinc ferrite, cobalt-doped zinc ferrite, and cobalt ferrite samples at $x = 0.0$, 0.5, and 1.0. The micrographs of the calcinated NPs show the spherical shape with agglomerations [44]. The selected particle sizes measured with help of Image 'J' software found the particle sizes in the range of 20–24 nm. An agglomeration of NPs can have two reasons: first, the decision about the particular amalgamation process utilized, and second, the subsequent NPs undergo a magnetic interaction. The crystalline concept of the analysis has been visualized by the design of selected area electron diffraction (SAED), as shown in Fig. 5d–f. The SAED reveals the presence of good homogeneity, with sharp rings connected to different diffraction planes of the prepared NPs [18, 22, 28].

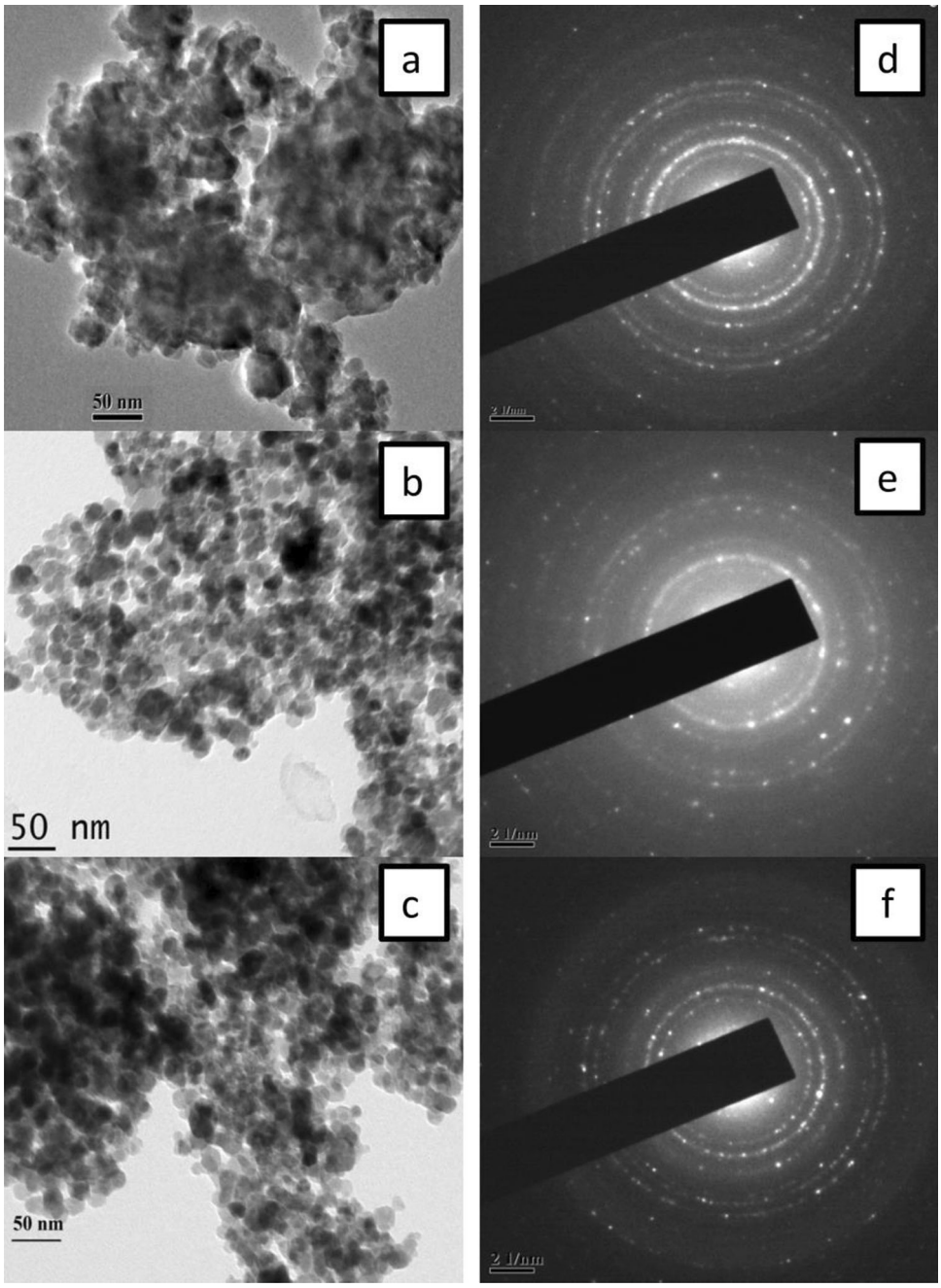

Fig. 5 **a–f** FE-TEM with SAED pattern of $Co_xZn_{1-x}Fe_2O_4$ NPs ($x = 0.0$, 0.5 and 1.0)

3.5 Magnetic properties

The magnetic properties of the prepared samples ($x = 0.0$, 0.5, and 1.0) of zinc ferrite, cobalt zinc ferrite, and cobalt ferrite were recorded at room temperature to recognize the magnetic term. The applied magnetic field was about − 15 G to + 15 G for the M–H graph, as shown in Fig. 6a–c. Sensitive magnetic parameters for $Co_xZn_{1-x}Fe_2O_4$ NPs such as saturation magnetization (Ms), coercivity (Hc) and remanent (Mr) have been recorded in Table 2. Without the magnetic field at room temperature, immersion, remanence, loading, and coercivity show that the prepared nanocomposite has a superparamagnetic character, in which loosening of their turns can be upset on the removal of the applied magnetic field to give a zero net magnetic moment [45]. The zinc ferrite NPs have a paramagnetic nature. The doping of the Co^{2+} particles contributes to the enhancement of the magnetic behavior in zinc ferrite due to the ferromagnetic order.

It is expected that the magnetic properties of the spinel ferrites by substitution of the nonmagnetic molecule, for instance, Zn, which inhabits a specific tetrahedral A site, leads to the diminishing of the exchange participation between the A and B sites [46]. The non-attendance of coercivity at room temperature could in like manner be ascribed to the event of Zn particles, or else the ferromagnetic cobalt ferrite phase, for the realistic creation [47, 48]. The observed variety in the immersion polarization and remanent charge are a direct result of explicit components, like cationic redistribution and surface blemishes that influence the net magnetic moments.

3.6 Cyclic voltammetry (CV)

Figure 7a–c shows the CV study of the $Co_xZn_{1-x}Fe_2O_4$ samples at different concentrations ($x = 0.0$, 0.5, and 1.0) for zinc ferrite, cobalt-doped zinc ferrite,

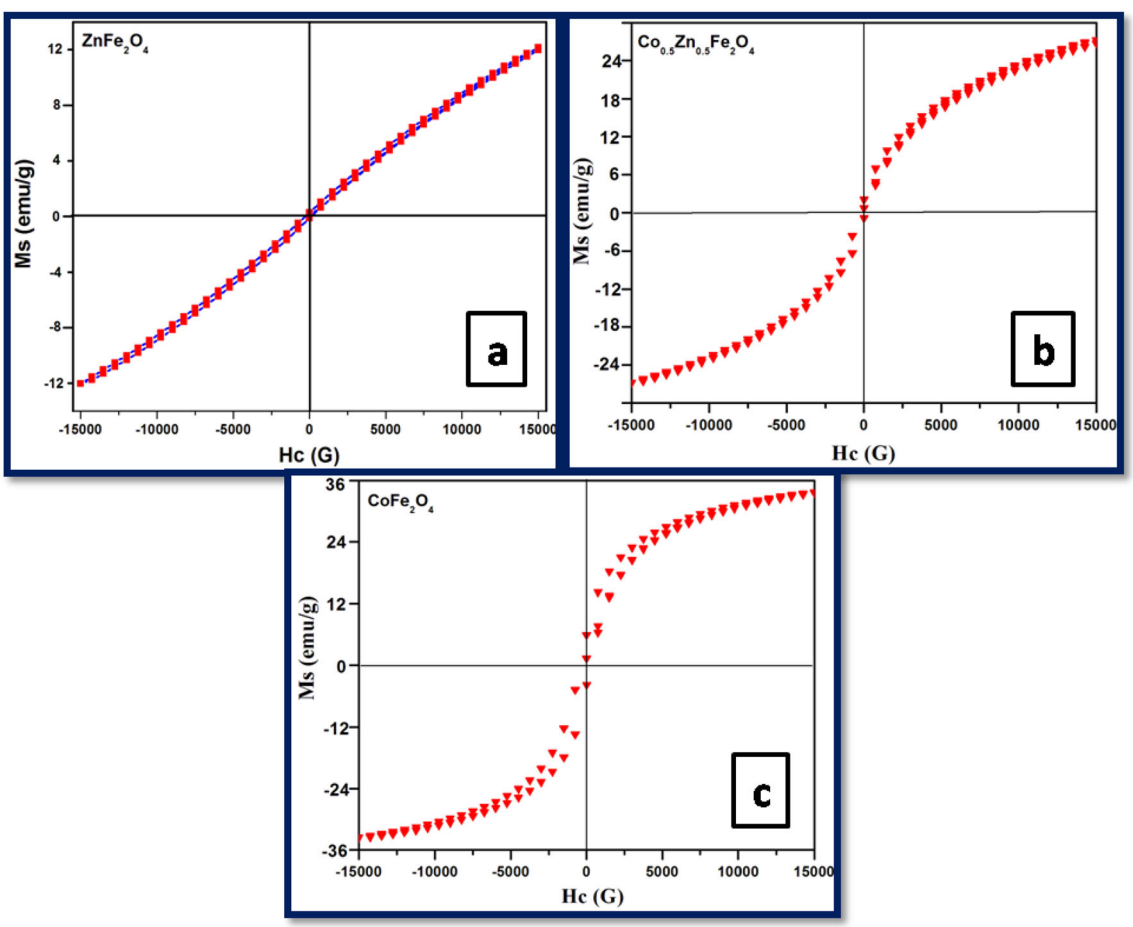

Fig. 6 **a–c** M–H loops of $Co_xZn_{1-x}Fe_2O_4$ NPs ($x = 0.0$, 0.5 and 1.0)

Table 2 Saturation value, remanance, coercivity, and magnetic moment for $Co_xZn_{1-x}Fe_2O_4$ NPs ($x = 0.0$, 0.5 and 1.0)

Composition	Saturation value Ms(emu/g)	Coercivity Hc (G)	Remanance Mr (emu/g)	Magnetic moment (μB)
$ZnFe_2O_4$	12.1	220.5	1.28	0.25
$Co_{0.5}Zn_{0.5}Fe_2O_4$	26.5	342.1	6.71	0.57
$CoFe_2O_4$	35.19	391.3	10.21	0.79

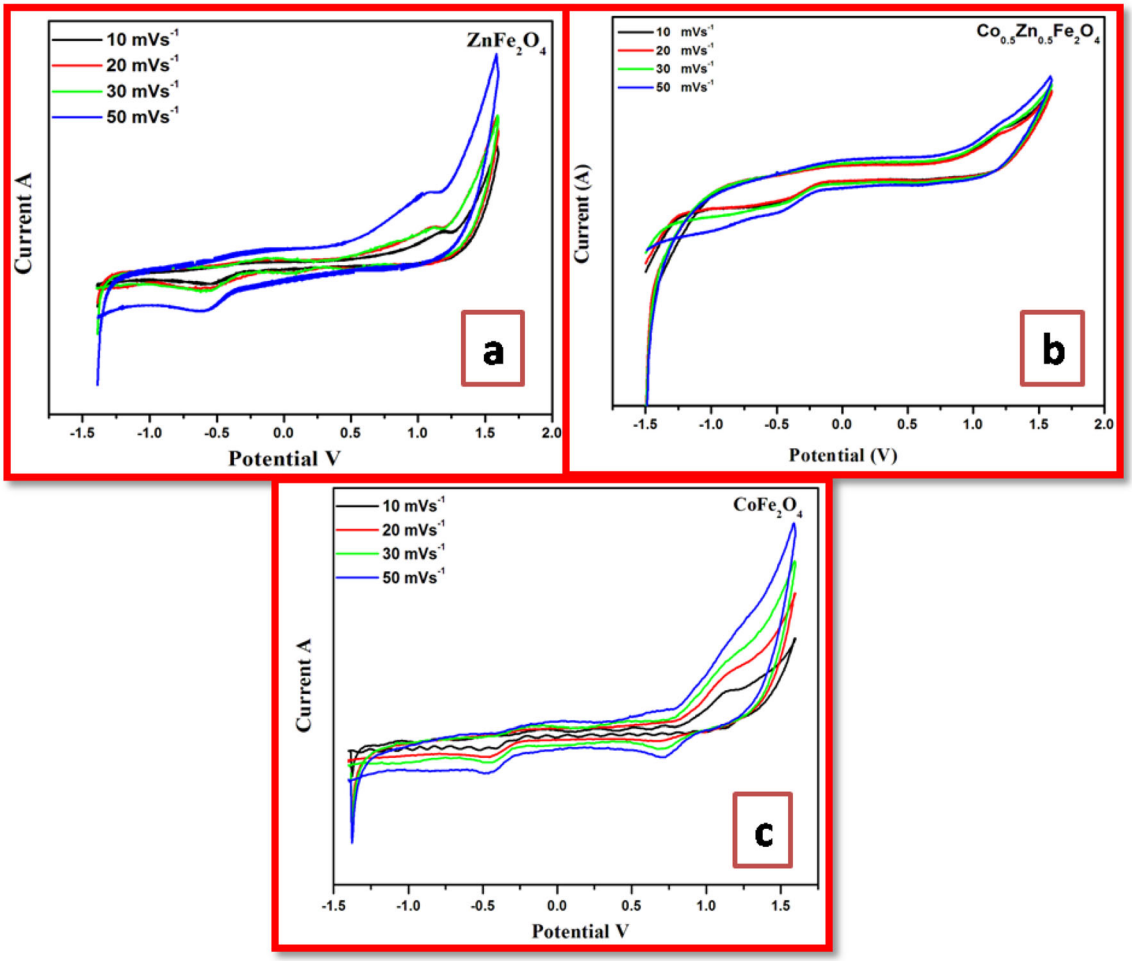

Fig. 7 **a–c** CV curves of $Co_xZn_{1-x}Fe_2O_4$ NPs ($x = 0.0$, 0.5 and 1.0)

and cobalt ferrite. The large redox response peaks in the CV curves of the samples show that the electrochemical capacity of the embedded samples is due to their pseudo-capacitive nature. Batteries and supercapacitors provide the backbone for electrochemical energy storage devices. While both are based on electrochemical processes, their charge storage mechanisms are unalike, ensuing from different energy and power densities. Materials of pseudocapacitors reveal that the storage charge in the battery is like redox reactions, but, at fast rates comparable to those of electrochemical double-layer capacitors. For these materials, for that motive, there is a pathway for accomplishing even high energy and high power densities. Materials that coalesce these properties are required for the increase of fast-charging electrochemical energy storage devices, competent in bringing high power for long periods of time. In the current work, the fundamental electrochemical properties of the pseudocapacitive materials have

been described, with a focus on the kinetics processed and distinctions between batteries and pseudocapacitive materials. Furthermore, we discuss the different types of pseudocapacitive materials, highlighting the differences between intrinsic and extrinsic materials, evaluating the applications of the devices, and examining future perspectives in the field. The CV curves have been completed at different output rates (10, 20, 30, and 50 mV/s). The specific capacitance (Cs) of the samples can be obtained from the condition $Cs = Q/\Delta V$ m. The adjustment in examining the rate shows that an expansion on the subject of redox peaks is because of the greatest current thickness with a diminishing explicit limit [49, 50]. The most outrageous specific capacitance is gained at a low sweep rate, which may emerge from the low Faradaic response. Table 3 provides the estimated specific capacitance of the samples for different output rates. The improved specific capacitance is about 218 F/g for the cobalt-doped zinc ferrite NPs with a scanning speed of 10 mV/s. The improvement of the specific capacitance in the Co-doped zinc ferrite spinel structure is due to trivalent Fe^{3+} particles with divalent zinc particles, which prompts the progression of oxygen on the outside of the working anode ($Co_xZn_{1-x}Fe_2O_4$) [51]. Higher specific capacitance at a low output rate is seen which demonstrates ionic diffusion in both the inner and outer surfaces, while the lower specific capacitance obtained at higher output rates show the ionic scattering in the outer surfaces. In the current work, the improved specific capacitancee stays in the zinc ferrite spinel structure while expanding the cobalt complex. In the present explorations, the attractive behavior of the electrochemical properties of the zinc ferrite NPs is less specific capacitance compared to the cobalt ferrite NPs. The doping of cobalt contributions in the zinc ferrite nanocomposites produces improved specific capacitance in the mixed cobalt-doped zinc ferrite NPs.

Table 3 Specific capacitance values of $Co_xZn_{1-x}Fe_2O_4$ NPs ($x = 0.0$, 0.5 and 1.0)

Scan rate (mVs^{-1})	Specific capacitance (Fg^{-1})		
	$ZnFe_2O_4$	$Co_{0.5}Zn_{0.5}Fe_2O_4$	$CoFe_2O_4$
10	146	218	172
20	58	92	78
30	27	45	37
50	12	21	19

4 Computational details

Quantum chemical calculations were performed at density functional theory (DFT) levels on a Pentium IV/3.02 GHz personal computer using the Gaussian 09 W [52] program package, invoking gradient geometry optimization [52, 53]. In this study, the density functional three-parameter hybrid model DFT/B3LYP/LANL2DZ basis set was used to calculate the bond parameters, NLO, and bandgap energy for the title molecule.

5 Results and discussion (DFT study)

5.1 Geometrical parameters

The optimized molecular structure of the $CoZnFe_2O_4$ molecule with an atom numbering scheme is shown in Fig. 8. The geometrical parameters (bond lengths, bond angles, and dihedral angles) of the title compound were calculated by the DFT method with the B3LYP/LANL2DZ basis set and are listed in Table 4. In the present study, the Co1-Zn2/2.399 Å bond length is a higher value compared to the Co-Fe, Fe-O, and O-O bonds. These results show that the title molecule is tightly bonded with metal–metal ions. In addition, the bond angles and dihedral angles were calculated at the same level of theory. The dihedral angles of O5-Co1-Fe4-O7 and O8-Co1-Fe4-O6 are

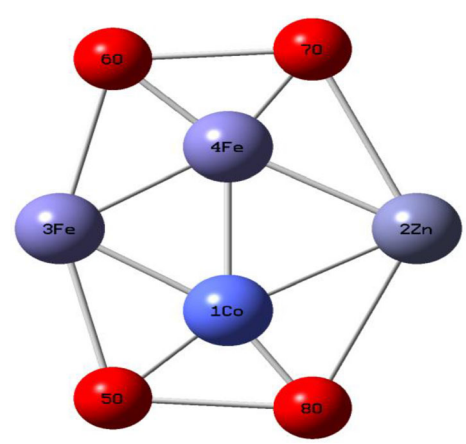

Fig. 8 The optimized molecular structure of $CoZnFe_2O_4$

Table 4 The bond parameters of $CoZnFe_2O_4$

Bond lengths (Å)	B3LYP/LANL2DZ	Bond lengths (Å)	B3LYP/LANL2DZ
Co1-Zn2	2.399	Zn2-O8	2.0416
Co1-Fe3	2.1748	Fe3-Fe4	2.1748
Co1-Fe4	2.3891	Fe3-O5	1.8104
Co1-O5	2.1409	Fe3-O6	1.8104
Co1-O8	1.8324	Fe4-O6	2.1409
Zn2-Fe4	2.399	Fe4-O7	1.8324
Zn2-O7	2.0416		
Bond angles (°)	**B3LYP/LANL2DZ**	**Bond angles (°)**	**B3LYP/LANL2DZ**
Zn2-Co1-Fe3	116.8209	Co1-Fe3-O6	130.8575
Zn2-Co1-O5	166.4192	Fe4-Fe3-O5	130.8575
Fe3-Co1-O8	172.5957	O5-Fe3-O6	164.9167
Fe4-Co1-O5	106.2825	Co1-Fe4-O6	106.2825
Fe4-Co1-O8	115.9116	Co1-Fe4-O7	115.9116
O5-Co1-O8	137.8059	Zn2-Fe4-Fe3	116.8209
Co1-Zn2-O7	107.6401	Zn2-Fe4-O6	166.4192
Fe4-Zn2-O8	107.6401	Fe3-Fe4-O7	172.5957
O7-Zn2-O8	155.5537	O6-Fe4-O7	137.8059
Dihedral angles (°)	**B3LYP/LANL2DZ**	**Dihedral angles (°)**	**B3LYP/LANL2DZ**
Fe3-Co1-Zn2-O7	0	O8-Co1-Fe4-O6	180
O5-Co1-Zn2-O7	0	O8-Co1-Fe4-O7	0
Zn2-Co1-Fe3-O6	0	O8-Zn2-Fe4-Fe3	0
O8-Co1-Fe3-O6	0	O8-Zn2-Fe4-O6	0
O5-Co1-Fe4-O6	0	O5-Fe3-Fe4-Zn2	0
O5-Co1-Fe4-O7	180	O5-Fe3-Fe4-O7	0

180°, which shows the linear and the planarity nature of the title molecule.

5.2 NLO property

The potential application of the title molecule in the field of nonlinear optics requires the investigation of its structural and bonding features. In this study, the B3LYP/LANL2DZ method has been used for the prediction of the first hyperpolarizability or second harmonic generation. Urea is the prototypical molecule utilized in the investigation of the NLO properties of the compound under investigation. For this reason, hyperpolarizability urea is often used as a threshold value for comparative purposes. The calculated first hyperpolarizability (β_0) and the total molecular dipole moment (μ) of $CoZnFe_2O_4$ are $2.2200533 \times 10^{-30}$ esu and 1.9409902 Debye, respectively. As the total dipole moment of the title, the compound is higher than and the β_0 value is six times greater than that of urea, and the molecule $CoZnFe_2O_4$ is expected to have considerable NLO activity. The μ, α_0, and β_0 values are listed in Table 5.

5.3 HOMO–LUMO analysis

The highest occupied molecular orbital (HOMO) and lowest unoccupied molecular orbital (LUMO) are very important parameters for chemical reactions. The HOMO is the orbital that primarily acts as an electron donor and the LUMO is the orbital that largely acts as the electron acceptor, and the gap between HOMO and LUMO characterizes the molecular chemical stability. The HOMO–LUMO energy gap is a critical parameter in determining the molecular electrical transport property, since it is a measure of electron conductivity. The HOMO and LUMO energies and band gap values evaluated at the DFT level using the B3LYP hybrid functional invoking the LANL2DZ basis set are listed in Table 6 and

Table 5 The NLO measurements of $CoZnFe_2O_4$

Parameters	B3LYP/LANL2DZ
Dipole moment (μ)	Debye
μ_x	− 0.1967524
μ_y	1.8244172
μ_z	0.6326401
μ	1.9409902 Debye
Polarizability (α_0)	$x10^{-30}$ esu
α_{xx}	251.7143228
α_{xy}	46.9713456
α_{yy}	174.5204769
α_{xz}	- 35.1823978
α_{yz}	- 28.3509192
α_{zz}	88.5219587
α_0	$0.4557421 \times 10^{-30}$ esu
Hyperpolarizability (β_0)	$x10^{-30}$esu
β_{xxx}	221.1293675
β_{xxy}	− 410.7548921
β_{xyy}	− 233.9148764
β_{yyy}	728.3927925
β_{xxz}	− 20.1142654
β_{xyz}	33.4094243
β_{yyz}	− 26.8284367
β_{xzz}	19.64168950
β_{yzz}	− 67.5012743
β_{zzz}	− 11.5293476
β_0	$2.2200533 \times 10^{-30}$ esu

Standard value for urea ($\mu = 1.3732$ Debye, $\beta_0 = 0.3728 \times 10^{-30}$ esu)

esu electrostatic unit

Table 6 The frontier molecular orbital energies of $CoZnFe_2O_4$

Orbitals	Energies (a.u.)	Energies (eV)
Homo	− 0.29145	− 7.93035
Lumo	− 0.16535	− 4.49917
Energy gap (H to L)	0.12610	3.43118
Homo-1	− 0.30495	− 8.29768
Lumo + 1	− 0.15900	− 4.32639
Energy gap (H-1 to L + 1)	0.14595	3.97129

illustrated in Fig. 9. HOMO and LUMO are located over the entire molecule and the charges are evenly distributed in $CoZnFe_2O_4$. The calculated HOMO, LUMO and bandgap are − 7.93035, − 4.49917, and 3.43118 eV, respectively. Hence, the title molecules which have large/small bandgaps are called hard/-soft molecules, respectively.

6 Conclusions

$Co_xZn_{1-x}Fe_2O_4$ concentrations ($x = 0.0$, 0.5, 1.0) of zinc ferrite, cobalt-doped zinc ferrite, and cobalt ferrite NPs were prepared by a simple co-precipitation method. The prepared samples were subject to characterization of the structural, morphological, functional, magnetic, and electrochemical properties of the NPs. XRD results revealed good crystallinity in frontier molecular orbital ferrite-based nanocomposites due to their cubic spinel-type. The functional groups at 460−400 and 600−550 cm^{-1} have a place with tetrahedral and octahedral sites. The groups of NO_3-, OH- and H_2O disappeared due to being calcined at 600 °C. The tetrahedral sites were occupied by the Zn^{2+} particles while the cobalt and iron possessed both the tetrahedral and octahedral sites, as they are divalent particles in $Co_xZn_{1-x}Fe_2O_4$ NPs. FE-SEM and FE-TEM with SAED revealed that the combined samples have spherical-type NPs. The magnetic properties, such as remanence (Mr), coercivity (Hc), and saturation magnetization (Ms), were resolved. The enhancements of the magnetic properties due to the effect of the cobalt ions has a major role in the mixed spinel of cobalt-doped zinc ferrite. From the electrochemical results, we acquired the specific capacitance of zinc ferrite, from 146 to 218 Fg^{-1} by the expansion of cobalt. The present investigation of cobalt-doped zinc ferrite nanocomposites has shown that it is a good potential material for supercapacitor applications.

The quantum chemical calculation study analyzed the theoretical parameters of the title compound. It can be used to find the structural behavior of the $CoZnFe_2O_4$ molecule. The geometrical bond parameters were calculated by using DFT method with the B3LYP/LANL2DZ level of theory. These bond parameters results concluded that the title molecule is tightly bonded with metal–metal ions. The β_0 value of $CoZnFe_2O_4$ is six times larger than the magnitude of urea, hence the molecule had a good NLO property. The title molecule has a small energy gap (3.43118 eV). Hence, the molecule with a small frontier orbital gap is generally associated with high chemical reactivity and low kinetic stability.

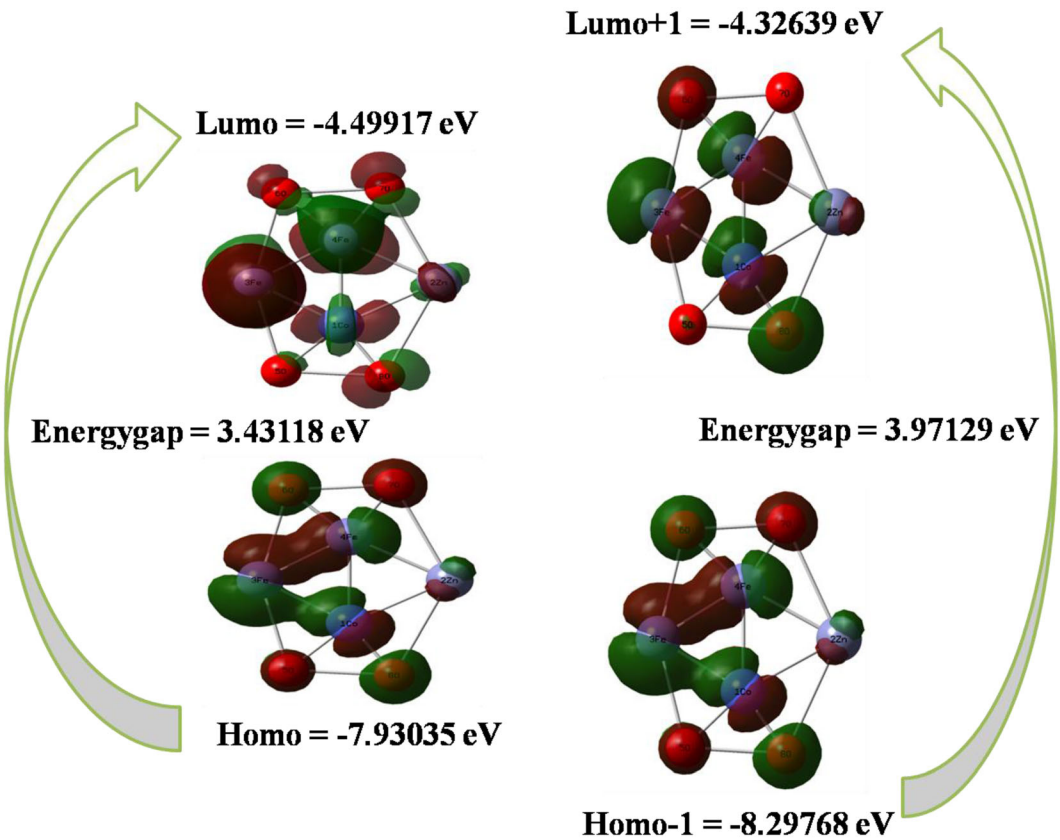

Fig. 9 The frontier molecular orbital of $CoZnFe_2O_4$

Acknowledgements

We express special thanks to the Chairman Dr. M. Anwar Kabir, Annai Group of Institutions, Kumbakonam, Tamilnadu, India, for providing financial support for the completion of this work.

Declarations

Conflict of interest The authors have declared that there is no conflict of interest.

References

1. G.D. Prasanna, H.S. Jayanna, A.R. Lamani, S. Dash, Polyaniline/$CoFe_2O_4$ nanocomposites: A novel synthesis, characterization and magnetic properties. Synthetic Metals **161**(21–22), 2306–2311 (2011)
2. K. Zhang, T. Holloway, A.K. Pradhan, Magnetic behavior of nanocrystalline $CoFe_2O_4$. J. Magn. Magn. Mater. **323**(12), 1616–1622 (2011)
3. X. Zhang, W. Jiang, D. Song, H. Sun, Z. Sun, F. Li, Salt-assisted combustion synthesis of highly dispersed superparamagnetic $CoFe_2O_4$ nanoparticles. J. Alloy. Compd. **475**(1–2), 34–37 (2009)
4. D. Chen, Q. Wang, R. Wang, G. Shen, Ternary oxide nanostructured materials for supercapacitors: a review. J. Mater. Chem. A **3**(19), 10158–10173 (2015)
5. P. Lavela, J.L. Tirado, $CoFe_2O_4$ and $NiFe_2O_4$ synthesized by sol–gel procedures for their use as anode materials for Li ion batteries. J. Power Sources **172**(1), 379–387 (2007)
6. N.V. Long, Y. Yang, T. Teranishi, C.M. Thi, Y. Cao, M. Nogami, Related magnetic properties of $CoFe_2O_4$ cobalt ferrite particles synthesised by the polyol method with $NaBH_4$ and heat treatment: new micro and nanoscale structures. RSC Adv. **5**(70), 56560–56569 (2015)
7. V.S. Kumbhar, A.D. Jagadale, N.M. Shinde, C.D. Lokhande, Chemical synthesis of spinel cobalt ferrite ($CoFe_2O_4$) nano-flakes for supercapacitor application. Appl. Surf. Sci. **259**, 39–43 (2012)
8. L. Lv, Q. Xu, R. Ding, L. Qi, H. Wang, Chemical synthesis of mesoporous $CoFe_2O_4$ nanoparticles as promising bifunctional electrode materials for supercapacitors. Mater. Lett. **111**, 35–38 (2013)

9. P. He, K. Yang, W. Wang, F. Dong, L. Du, Y. Deng, Reduced graphene oxide-$CoFe_2O_4$ composites for supercapacitor electrode. Russ. J. Electrochem. **49**(4), 359–364 (2013)
10. C. Zhou, A. Zhang, T. Chang, Y. Chen, Y. Zhang, F. Tian, W. Zuo, Y. Ren, X. Song, S. Yang, The phase diagram and exotic magnetostrictive behaviors in spinel oxide $Co(Fe_{1-x}Al_x)_2O_4$ system. Materials **12**(10), 1685 (2019)
11. K. Elayakumar, A. Manikandan, A. Dinesh, K. Thanrasu, K.K. Raja, R.T. Kumar, Y. Slimani, S.K. Jaganathan, A. Baykal, Enhanced magnetic property and antibacterial biomedical activity of Ce^{3+} doped $CuFe_2O_4$ spinel nanoparticles synthesized by sol-gel method. J. Magn. Magn. Mater. **478**, 140–147 (2019)
12. T. Sathitwitayakul, M.V. Kuznetsov, I.P. Parkin, R. Binions, The gas sensing properties of some complex metal oxides prepared by self-propagating high-temperature synthesis. Mater. Lett. **75**, 36–38 (2012)
13. M. Kooti, M. Afshari, Magnetic cobalt ferrite nanoparticles as an efficient catalyst for oxidation of alkenes. Sci. Iran. **19**(6), 1991–1995 (2012)
14. W. Fu, S. Liu, W. Fan, H. Yang, X. Pang, J. Xu, G. Zou, Hollow glass microspheres coated with $CoFe_2O_4$ and its microwave absorption property. J. Magn. Magn. Mater. **316**(1), 54–58 (2007)
15. P. Thakur, D. Chahar, S. Taneja, N. Bhalla, A. Thakur, A review on MnZn ferrites: Synthesis, characterization and applications. Ceram. Int. **46**(10), 15740–15763 (2020)
16. N.A.S. Nogueira, V.H.S. Utuni, Y.C. Silva, P.K. Kiyohara, I.F. Vasconcelos, M.A.R. Miranda, J.M. Sasaki, X-ray diffraction and Mossbauer studies on superparamagnetic nickel ferrite ($NiFe_2O_4$) obtained by the proteic sol–gel method. Mater. Chem. Phys. **163**, 402–406 (2015)
17. D.D. Andhare, S.R. Patade, J.S. Kounsalye, K.M. Jadhav, Effect of Zn doping on structural, magnetic and optical properties of cobalt ferrite nanoparticles synthesized via. Co-precipitation method. Physica B **583**, 412051 (2020)
18. Z.H. Yang, Z.W. Li, Y.H. Yang, Structural and magnetic properties of plate-like W-type barium ferrites synthesized with a combination method of molten salt and sol–gel. Mater. Chem. Phys. **144**(3), 568–574 (2014)
19. U. Kurtan, H. Erdemi, A. Baykal, H. Güngüneş, Synthesis and magneto-electrical properties of MFe_2O_4 (Co, Zn) nanoparticles by oleylamine route. Ceram. Int. **42**(12), 13350–13358 (2016)
20. J. Töpfer, A. Angermann, Nanocrystalline magnetite and Mn–Zn ferrite particles via the polyol process: Synthesis and magnetic properties. Mater. Chem. Phys. **129**(1–2), 337–342 (2011)
21. M.A. Noor Ismail, M. Hashim, A. Hajalilou, I. Ismail, M.M.M. Zulkimi, N. Abdullah, W.N.A. Rahman, M.S. Abdullah, M. Manap, Magnetic Properties of Mechanically Alloyed Cobalt-Zinc Ferrite Nanoparticles. J. Supercond. Novel Magn. **27**(5), 1293–1298 (2013)
22. J. Rehman, M.A. Khan, A. Hussain, F. Iqbal, I. Shakir, G. Murtaza, M.N. Akhtar, G. Nasar, M.F. Warsi, Structural, magnetic and dielectric properties of terbium doped NiCoX strontium hexagonal nano-ferrites synthesized via micro-emulsion route. Ceram. Int. **42**(7), 9079–9085 (2016)
23. S.J. Azhagushanmugam, N. Suriyanarayanan, R. Jayaprakash, Magnetic properties of zinc-substituted cobalt ferric oxide nanoparticles: Correlation with annealing temperature and particle size. Mater. Sci. Semicond. Process. **21**, 33–37 (2014)
24. A. Schütz, M. Günthner, G. Motz, O. Greißl, U. Glatzel, High temperature (salt melt) corrosion tests with ceramic-coated steel. Mater. Chem. Phys. **159**, 10–18 (2015)
25. X. Huang, J. Zhang, S. Xiao, G. Chen, The cobalt zinc spinel ferrite nanofiber: lightweight and efficient microwave absorber. J. Am. Ceram. Soc. **97**(5), 1363–1366 (2014)
26. M. Mozaffari, S. Manouchehri, M.H. Yousefi, J. Amighian, The effect of solution temperature on crystallite size and magnetic properties of Zn substituted Co ferrite nanoparticles. J. Magn. Magn. Mater. **322**(4), 383–388 (2010)
27. A.B. Kulkarni, S.N. Mathad, Variation in structural and mechanical properties of Cd-doped Co-Zn ferrites. Mater. Sci. Ener. Technol. **2**(3), 455–462 (2019)
28. S. Raghuvanshi, F. Mazaleyrat, S.N. Kane, $Mg_{1-x}Zn_xFe_2O_4$ nanoparticles: Interplay between cation distribution and magnetic properties. AIP Adv. **8**(4), 047804 (2018)
29. A. Manikandan, L.J. Kennedy, M. Bououdina, J.J. Vijaya, Synthesis, optical and magnetic properties of pure and Co-doped $ZnFe_2O_4$ nanoparticles by microwave combustion method. J. Magn. Magn. Mater. **349**, 249–258 (2014)
30. K.M. Batoo, G. Kumar, Y. Yang, Y. Al-Douri, M. Singh, R.B. Jotania, A. Imran, Structural, morphological and electrical properties of Cd^{2+} doped $MgFe_{2-x}O_4$ ferrite nanoparticles. J. Alloy. Compd. **726**, 179–186 (2017)
31. D. Varshney, K. Verma, A. Kumar, Substitutional effect on structural and magnetic properties of $A_xCo_{1-x}Fe_2O_4$ (A = Zn, Mg and x = 0.0, 0.5) ferrites. J. Mol. Struct. **1006**(1–3), 447–452 (2011)
32. K.A. Mohammed, A.D. Al-Rawas, A.M. Gismelseed, A. Sellai, H.M. Widatallah, A. Yousif, M.E. Elzain, M. Shongwe, Infrared and structural studies of $Mg_{1-x}Zn_xFe_2O_4$ ferrites. Physica B **407**(4), 795–804 (2012)
33. Y. Köseoğlu, A. Baykal, F. Gözüak, H. Kavas, Structural and magnetic properties of $Co_xZn_{1-x}Fe_2O_4$ nanocrystals synthesized by microwave method. Polyhedron **28**(14), 2887–2892 (2009)

34. G. Gnanaprakash, J. Philip, B. Raj, Effect of divalent metal hydroxide solubility product on the size of ferrite nanoparticles. Mater. Lett. **61**(23–24), 4545–4548 (2007)
35. R.D. Shannon, Revised effective ionic radii and systematic studies of interatomic distances in halides and chalcogenides. Acta Crystallogr. Sect. A **32**(5), 751–767 (1976)
36. A.M.M. Farea, S. Kumar, K.M. Batoo, A. Yousef, C.G. Lee, Alimuddin, Structure and electrical properties of $Co_{0.5}Cd_x$-$Fe_{2.5-x}O_4$ ferrites. J. Alloy. Compd. **464**(1–2), 361–369 (2008)
37. S. Ayyappan, G. Paneerselvam, M.P. Antony, J. Philip, Structural stability of $ZnFe_2O_4$ nanoparticles under different annealing conditions. Mater. Chem. Phys. **128**(3), 400–404 (2011)
38. S. Ayyappan, G. Panneerselvam, M.P. Antony, J. Philip, High temperature stability of surfactant capped $CoFe_2O_4$ nanoparticles. Mater. Chem. Phys. **130**(3), 1300–1306 (2011)
39. S.H. Xiao, W.F. Jiang, L.Y. Li, X.J. Li, Low-temperature auto-combustion synthesis and magnetic properties of cobalt ferrite nanopowder. Mater. Chem. Phys. **106**(1), 82–87 (2007)
40. Z. Chen, L. Gao, Synthesis and magnetic properties of $CoFe_2O_4$ nanoparticles by using PEG as surfactant additive. Mater. Sci. Engin. B **141**(1–2), 82–86 (2007)
41. Z. Li, Y. Xiong, Y. Xie, Selected-Control Synthesis of ZnO Nanowires and Nanorods via a PEG-Assisted Route. Inorg. Chem. **42**(24), 8105–8109 (2003)
42. H.H. Huang, X.P. Ni, G.L. Loy, C.H. Chew, K.L. Tan, F.C. Loh, J.F. Deng, G.Q. Xu, Photochemical Formation of Silver Nanoparticles in Poly(N-vinylpyrrolidone). Langmuir **12**(4), 909–912 (1996)
43. Y. Sun, Y. Xia, Large-scale synthesis of uniform silver nanowires through a soft, self-seeding, polyol process. Adv. Mater. **14**(11), 833–837 (2002)
44. G. Sathishkumar, C. Venkataraju, K. Sivakumar, Synthesis, structural and dielectric studies of nickel substituted cobalt-zinc ferrite. Mater. Sci. Appl. **01**(01), 19–24 (2010)
45. T.R. Tatarchuk, N.D. Paliychuk, M. Bououdina, B. Al-Najar, M. Pacia, W. Macyk, A. Shyichuk, Effect of cobalt substitution on structural, elastic, magnetic and optical properties of zinc ferrite nanoparticles. J. Alloy. Compd. **731**, 1256–1266 (2018)
46. A.I. Nandapure, S.B. Kondawar, P.S. Sawadh, B.I. Nandapure, Effect of zinc substitution on magnetic and electrical properties of nanocrystalline nickel ferrite synthesized by refluxing method. Physica B **407**(7), 1104–1107 (2012)
47. R.S. Yadav, J. Havlica, M. Hnatko, P. Šajgalík, C. Alexander, M. Palou, E. Bartoníčková, M. Boháč, F. Frajkorová, J. Masilko, M. Zmrzlý, L. Kalina, M. Hajdúchová, V. Enev, Magnetic properties of $Co_{1-x}Zn_xFe_2O_4$ spinel ferrite nanoparticles synthesized by starch-assisted sol–gel auto-combustion method and its ball milling. J. Magn. Magn. Mater. **378**, 190–199 (2015)
48. K.M. Batoo, E.H. Raslan, Y. Yang, S.F. Adil, M. Khan, A. Imran, Y. Al-Douri, Structural, dielectric and low temperature magnetic response of Zn doped cobalt ferrite nanoparticles. AIP Adv. **9**(5), 055202 (2019)
49. M.M. Vadiyar, S.C. Bhise, S.K. Patil, S.A. Patil, D.K. Pawar, A.V. Ghule, P.S. Patil, S.S. Kolekar, Mechanochemical growth of a porous $ZnFe_2O_4$ nano-flake thin film as an electrode for supercapacitor application. RSC Adv. **5**(57), 45935–45942 (2015)
50. B.J. Rani, G. Ravi, R. Yuvakkumar, V. Ganesh, S. Ravichandran, M. Thambidurai, A.P. Rajalakshmi, A. Sakunthala, Pure and cobalt-substituted zinc-ferrite magnetic ceramics for supercapacitor applications. Appl. Phys. A **124**(7), 1–12 (2018)
51. M.A. Maksoud, R.A. Fahim, A.E. Shalan, M. Abd Elkodous, S.O. Olojede, A.I. Osman, C. Farrell, H. Ala'a, A.S. Awed, A.H. Ashour, D.W. Rooney, Advanced materials and technologies for supercapacitors used in energy conversion and storage: a review. Environmental Chemistry Letters, 1–65 (2020)
52. M.J. Frisch, G.W. Trucks, H.B. Schlegel, G.E. Scuseria, M.A. Robb, J.R. Cheeseman, G. Scalmani, V. Barone, B. Mennucci, G. Petersson, H. Nakatsuji, *H. Gaussian 09, Revision d* (Gaussian. Inc., Wallingford, CT, 2009), p. 01
53. H.B. Schlegel, Optimization of equilibrium geometries and transition structures. J. Comput. Chem. **3**(2), 214–218 (1982)

Materials Today: Proceedings 43 (2021) 2117–2122

Contents lists available at ScienceDirect

Materials Today: Proceedings

journal homepage: www.elsevier.com/locate/matpr

Catalytic effect of nano cadmium phosphate catalyst on the synthesis of some (*E*)-3,4-dimethoxyphenylprop-2-en-1-ones

V. Mala [a], I. Muthuvel [b,c], G. Thirunarayanan [b,*], V. Usha [d]

[a] Department of Chemistry, Annai College of Arts and Science, Kovilacheri, Kumbakonam 612 503, India
[b] Department of Chemistry, Annamalai University, Annamalainagar 608 002, India
[c] Department of Chemistry, MR Government Arts College, Mannargudi 614 001, India
[d] Department of Chemistry, University College of Engineering, Panruti 607 106, India

ARTICLE INFO

Article history:
Received 3 July 2020
Received in revised form 2 November 2020
Accepted 22 November 2020
Available online 16 January 2021

Keywords:
Nano Cadmium phosphate
Micro wave irradiation
Aldol-Condensation
Dimethoxyphenyl enones
IR and NMR spectra
Solvent effects

ABSTRACT

Cadmium phosphate nanomaterial was applied for the synthesis of some (*E*)-3,4-dimethoxyphenylprop-2-en-1-ones through microwave irradiation. Investigations made by the authors for the study of catalytic action of the nano cadmium phosphate catalyst by means of obtained yields and reusability. In this method the obtained maximum yield was 90% and the catalyst effect was not appreciably changed up to 6th time. Influence of solvents on this process was studied using normal boiling technique. Reaction in ethanol medium gave high yield than other solvents but not more than microwave method. The synthesized (*E*)-3,4-dimethoxyphenylprop-2-en-1-ones were analyzed through spectroscopic technique, micro analysis, yields, and physical constants. These data are confirmed by the formation of the 2-propen-1-ones.

Selection and peer-review under responsibility of the scientific committee of the International Conference on Advanced Materials Behavior and Characterization.

1. Introduction

In recent decades, metal phosphates have been attractive and commonly used for their possible application in the fields of catalysis, biocompatibility, proton conductivity and ion exchange, adsorption as the most important inorganic materials. [1–3]. Different hierarchical metal phosphates were prepared in a controllable manner and shown interesting properties. Inductive effect enhances the photocatalytic activity of metal phosphates by means of efficiency of pairs of electrons-holes in the catalyst. Due to this character, this is employed for the photo degradation of organic contaminants and raw water purification [4,5]. A plentiful metal phosphates such as hydroxyapatite ($Ca(PO_4)_6(OH)_2$, $Ti_2O(PO_4)_2(H_2O)_2$), $Ag_3PO_4/Ca(PO_4)_6(OH)_2$), $BiCu_2PO_6$, $TiO_2/Ca(PO_4)_6(OH)_2$ and $Cu_2(OH)PO_4$ were used as innovative photocatalysts [6–9]. Cadmium metal based nano materials plays an important role in basic and applied science research i.e., degradation of organic pollutants including nano technology [7–11]. Ortiz-Islas *et al.* [12] reported the preparation of phosphate titania employing sol–gel method. Yi *et al.* [13] reported the photooxidation properties of orthophosphate semiconductor under visible-light irradiation. Guo *et al.*[14] reported, the $Ag_3PO_4/Cr\text{-}SrTiO_3$ catalyst was useful for the removal of gaseous organic pollutants through visible light radiation. Ahmed and his co-workers prepared an acidic solid catalyst $H_3PW_{12}O_{40}$ supported nano oxides of tin metal and they found this is a resourceful reagent for deriving 7-hydroxy-4-methylcoumarins. [15]. Feng et. al.,[16] investigated the efficient vapour phase oxidation of n-butane with H_3PO_4-treated ZrO_2 catalyst. Ghiaci et. al., [17] reported various organic reactions with phosphate catalysts. Numerous modified and unmodified phosphatic catalyst were employed for organic reactions such as $H_3PO_4/ZrO_2–TiO_2$ assisted Beckmann rearrangement and acylation of phenol[18], H_3PO_4/ZSM-5 assisted Fries reaction of phenyl acetate[19], toluene alkylation with propane-2-ol[20], phosphoric acid-MCM-41 mesoporous reagent assisted methylbenzene alkylation[21] and phosphoric acid-Al-MCM-41 mesoporous silicate assisted desiccation of cinnamaldoxime[22]. The efficient adsorption of organic matter on H_3PO_4-activated bentonite catalyst was reported by Khoualdia et al.,[23]. Abbaspourrad and his co-workers investigated the inspiration of reaction limitations on the discrimination and alteration of H_3PO_4/MCM-41 catalyst through toluene alkylation in alcoholic medium [24]. Enones are important organic compounds for further organic building blocks, possess numerous pharmacological effects and many industrial applications including non-corrosiveness [25,26]. Peer literature

* Corresponding author.
E-mail address: drgtnarayanan@gmail.com (G. Thirunarayanan).

https://doi.org/10.1016/j.matpr.2020.11.892
2214-7853/
Selection and peer-review under responsibility of the scientific committee of the International Conference on Advanced Materials Behavior and Characterization.

review shows that, there is no reports availed for the nano cadmium phosphate catalyzed microwave assisted organic synthesis. Herein, we report the catalytic effect of nano cadmium phosphate catalyst through the synthesis of some 2-propenones by aldol condensation by microwave as well as conventional methods. In this method, the effect of catalyst was investigated by means of obtained yield and reusability.

2. Experimental

2.1. Materials and methods

The ketone 1-(3,4-dimethoxyphenyl) ethanone was procured along with substituted aromatic aldehydes from Sigma Aldrich Chemical Company, Bengaluru-100. The basic nanocatalyst $Cd_3(PO4)_2$ was characterized by the surface analytical techniques reported in our earlier work [25]. Siemens D5005 diffractometer was employed for measuring XRD spectra with CuKα (K = 0.051418 nm) light. About10-80° of 2θ range along with 20 s counter time of individual locations adopted for recording diffractograms. Debye Scherrer equation was utilized for finding usual crystalline magnitudes. Thermo Nicolet IS5 FT-IR spectrophotometer (4000–400 cm^{-1}) used for infrared spectra with spectroscopic grade potassium bromide disc. Bruker RFS27 100 s^{-1} (1064 nm) spectrophotometer equipped with 1024 × 256 pixels liquefied nitrogen-cooled germanium detector used for measuring Raman spectra. Frequency double enhanced neodymium doped yttrium aluminium garnet (Nd:YAG) used for measurements. Kept the laser power not more than15 mW for the sample. Maintained 18 s as the acquisition time for each spectrum recording and kept ~ 2 cm^{-1} as the spectral resolution. The FEI quanta FEG 250 high resolution scanning electron microscope (Netherlands) utilized for measuring HR-SEM images. Sample mounted gold platforms used for measuring images at various magnifications. The EDX measure was performed on various points of sample surface for reducing any probable variances raising on the heterogeneous nature of the examined shallow. About 0.1% concentration applied for detection of elements.

Melting points of all compounds were measured in Raga tech electrical melting point apparatus and are uncorrected. IR spectra of all 2-propenones under investigation were measured using SHIMADZU 8400 FT-IR spectrophotometer. The ^1H and ^{13}C NMR Spectra of all 2-propenones under investigation were measured in BRUKER AVIII 500NMR spectrophotometers using 500 MHz for ^1H NMR spectra and 125.46 MHz for ^{13}C NMR spectra. Deuterated chloroform and dimethoxy sulfoxide as solvent with deuterated tetramethyl silane. Micro analysis 2-propenones were performed in Thermofennigan CHN analyzer. Shimaduz mass spectrometer utilized for measuring *m*/*z* ratios of all 2-propenones.

2.2. Synthesis of catalyst

Literature report methodology used for preparation of $Cd_3(PO_4)_2$ nano catalyst [27]. In a 50 mL conical flask, an aqueous solution (10 mL) of cadmium nitrate (0.1 M) and 10 mL of disodium hydrogen phosphate (0.1 M) were stirred an hour in a magnetic stirrer. The obtained cadmium phosphate was filtered, dried for 12 h at 100 °C after washed using double distilled water. Muffle furnace utilized for 3 h calcination of dried $Cd_3(PO_4)_2$ nano catalyst on 400 °C.

2.3. Synthesis of (E)-3,4-dimethoxyphenylprop-2-en-1-ones by nano cadmium phosphate assisted Aldol condensation

A mixture of equimolar quantities of benzaldehydes (1 mmol) and 3,4-dimethoxyphenylethanone (1 mmol), cadmium phosphate (0.35 g) and 3 mL of ethyl alcohol were taken in a 25 mL stoppered conical flask and shaken thoroughly. Microwave irradiation of this reaction blend was done for 3–5 min at 450 W (Scheme 1) (Samsung Grill, GW73BD Microwave oven, 230 V A/c, 50 Hz, 2450 Hz, 100–750 W (IEC–705). After the concluding the process, as checked through TLC, added 8 mL of dichloromethane. The organic layer and the insoluble catalyst were separated by simple filtration. Evaporation of organic layer afforded the products. The crude 2-propenones were further purified by crystallization with ethyl alcohol. The crystallized products were kept in a desiccator. The unsolvable catalytic reagent was re-used after the catalyst was washed with ethyl acetate(8 mL) and more than 1 h hot air drying at 125 °C in an oven. All synthesized compounds were analyzed employing their physico-chemical parameters and spectroscopic statistics data. The physico-chemical parameters, yields and mass spectral *m*/*z* measurements of the enones are given in Table 1. The infrared and nuclear magnetic spectroscopic data of all (*E*)-3,4-dimethoxyphe nylprop-2-en-1-ones were tabulated in Tables 2 and 3.

3. Results and discussion

3.1. Characterization of nano cadmium phosphate catalyst.

The prepared nano cadmium phosphate catalyst was characterized with literature data [27]. As obtained the XRD data for the prepared $Cd_3(PO_4)_2$ catalyst shows the appeared peaks of 2θ values of 22.18°, 23.51°, 27.41°, 28.57°, 31.95°, 36.34°, and 38.11°, were aggregable for $Cd_3(PO_4)_2$. The line peak obtained at 27.41° (1 3 1) resembles to $Cd_3(PO_4)_2$ [JCPDS Card No. 72–1959] [26]. From infrared spectra, the PO_4^{3-} stretches obtained at 947–1200 cm^{-1} and are aggregable for the catalyst[28]. Stretch modes obtained at 727, 650, 575, and 1057 cm^{-1} is dispensed to P–O stretches of PO_4^{3-} in $Cd_3(PO_4)_2$ [29]. From Raman spectra, appeared peak at 912 cm^{-1} is allocated for PO_4^{3-} stretching mode and the symmetric P = O vibration bands observed at 1010 and 1170 cm^{-1} [30].

From the HR-SEM image of $Cd_3(PO_4)_2$ showed the plate- or sheet-like structure. The EDX examination statistics of cadmium phosphate reveals the existence of P, Cd, C, and O elements. From DRS, the obtained optical band gaps ~ 4.95 eV of $Cd_3(PO_4)_2$ was good agreement with literature data. These data are strongly aggregable with earlier report and confirmed the nano structure of $Cd_3(PO_4)_2$ catalyst.

3.2. Effect of nano cadmium phosphate catalyst on synthesis of (E)-3,4-dimethoxyphenylprop-2-en-1-ones

In our synthetic organic chemistry research room, we attempt to synthesize some enones by nano cadmium phosphate catalyst catalyzed crossed Aldol condensation of 3,4-dimethoxyphenyl ketone and benzaldehydes with substitutions under microwave assisted method. As mentioned in the experimental section, we prepared some enones and observed the electron giving substituted benzaldehydes gave higher yield than the electron-withdrawing substituted benzaldehydes. In this experiment the maximum yield was obtained for benzaldehyde and 4-methoxy benzaldehyde and least yield was observed for fluoro- and nitro- substituted benzaldehydes. Nano cadmium phosphate is the basic nature material. This condensation follows base catalyzed reaction mechanism. First step consists of formation of carbanion by abstraction of proton from 3,4-dimethoxy acetophenone. Second step consists of the attack of carbonyl carbon of substituted benzaldehydes by the carbanion and carbonyl oxygen gets negative charge. Third step involves the protonation of oxygen and the negative charge was neutralized. Fourth step consists of removal of water through β-elimination gave the product as (*E*)-3,4-dimethoxyphenylprop-2-en-1-ones. The schematic diagram of the mechanism is shown in Fig. 1

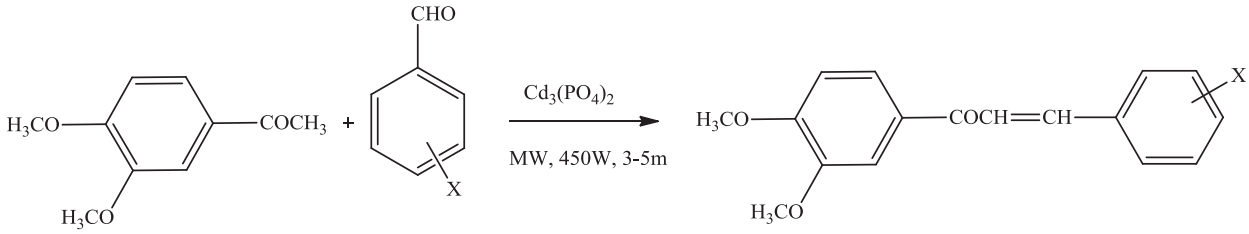

Scheme 1. Synthesis of (*E*)-3,4-dimethoxyphenylprop-2-en-1-ones by $Cd_3(PO_4)_2$ assisted aldol condensation.

Table 1
Physical constants, yields, micro analysis and mass fragments of (*E*)-3,4-dimethoxyphenylprop-2-en-1-ones.

Cpd. No.	X	M.F.	M. W.	Time (m)	Yield (%)	m. p. (° C)	Micro analysis (%)			Mass (*m*/*z*)
							C	H	N	
1	H	$C_{17}H_{16}O_3$	268	3.5	88	74–75	76.05 (76.10)	6.07 (6.01)	–	268[M$^+$], 237, 207, 178, 165, 137, 131,103, 91, 77, 54, 31, 28, 24.
2	3-Br	$C_{17}H_{15}BrO_3$	347	4	82	94–95	58.84 (58.81)	4.31 (4.35)	–	347[M$^+$], 349[M^{2+}], 315, 267, 209, 191, 181, 165, 137, 91, 79, 77, 54, 28, 24
3	4-Br	$C_{17}H_{15}BrO_3$	347	4	83	92–93	58.79 (58.81)	4.30 (4.35)	–	347[M$^+$], 349[M^{2+}], 315, 267, 209, 191, 181, 165, 137, 91, 79, 77, 54, 28, 24, 15
4	3-Cl	$C_{17}H_{15}ClO_3$	303	4.5	83	62–63	77.46 (77.44)	4.95 (4.99)	–	303[M$^+$], 305[M^{2+}], 267, 241, 191, 165,137, 111, 101, 91, 77, 54, 35, 31, 28, 24, 15
5	2-F	$C_{17}H_{15}FO_3$	286	4	80	75–76	71.36 (71.32)	5.23 (5.28)	–	286[M$^+$], 288[M^{2+}], 267, 191, 165, 149, 137, 121, 95, 106, 91, 77, 54, 31, 28, 24, 19, 15
6	4-F	$C_{17}H_{15}FO_3$	286	4	80	92–93	71.34 (71.32)	5.24 (5.28)	–	286[M$^+$], 288[M^{2+}], 267, 191, 165, 149, 137, 121, 95, 106, 91, 77, 54, 31, 28, 24, 19, 15
7	4-OCH_3	$C_{18}H_{18}O_4$	298	4.5	90	76–77	72.49 (72.47)	6.03 (6.08)	–	298[M$^+$], 267, 191, 165, 137, 133, 107, 91, 77, 54, 31, 28, 24, 15
8	4-CH_3	$C_{18}H_{18}O_3$	282	4	88	68–69	76.59 (76.57)	6.38 (6.43)	–	282[M$^+$], 267, 251, 221, 191, 165, 145, 137, 117, 104, 91, 77, 54, 31, 28, 24,15.
9	4-NO_2	$C_{17}H_{15}NO_5$	313	5	80	122–123	65.22 (65.17)	4.78 (4.83)	4.42 (4.47)	313[M$^+$], 282, 261, 252, 191, 176, 165, 148, 136, 122, 101, 91, 77, 54, 46, 28, 24, 15.

Table 2
Infrared spectroscopic data (ν, cm^{-1}) of (*E*)-3,4-dimethoxyphenylprop-2-en-1-ones.

Cpd. No.	X	$\nu CO_{s\text{-}cis}$	$\nu CO_{s\text{-}trans}$	νCH_{ip}	νCH_{op}	$\nu CH = CH_{op}$	$\nu C = C_{op}$
1	H	1664.23	1605.56	1164.20	759.11	979.83	487.94
2	3-Br	1653.25	1596.90	1145.62	787.02	1020.34	561.04
3	4-Br	1655.82	1600.36	1145.15	758.25	1019.67	591.63
4	3-Cl	1650.31	1577.65	1160.23	777.62	1021.53	563.49
5	2-F	1651.56	1597.54	1164.84	768.58	1021.96	585.29
6	4-F	1651.92	1576.43	1161.76	805.23	1017.54	507.52
7	4-CH_3	1654.76	1599.29	1149.52	805.09	1020.78	500.37
8	4-OCH_3	1650.47	1594.78	1161.34	796.18	1026.46	555.49
9	4-NO_2	1655.28	1597.52	1150.26	755.35	1018.39	594.82

Table 3
Nuclear magnetic resonance chemical shifts (δ, ppm) of (*E*)-3,4-dimethoxyphenylprop-2-en-1-ones.

Cpd. No	X	^{1}H NMR				^{13}C NMR				
		H_α(s)	H_β(s)	Ar-H (m)	OCH_3(s, s)	CO	C_α	C_β	Ar-C	OCH_3
1	H	7.563	7.814	6.926–7.837(8H)	1.69, 1.73	188.66	121.69	144.03	109.99–153.30	56.08, 56.14
2	3-Br	7.591	7.773	6.832–7.428(7H)	1. 72, 1.74	188.16	122.89	142.17	121.35–147.20	57.32, 57.36
3	4-Br	7.734	7.747	6.772–8.012(7H)	1.73, 1.74	196.92	122.16	142.57	124.39–146.92	58.02, 58.09
4	3-Cl	7.552	7.732	6.630–7.502(7H)	1.69, 1.71	188.18	124.85	142.26	125.32–148.98	58.12, 58.16
5	2-F	7.677	7.899	7.253–7.734(7H)	1.66, 1.69	188.64	124.49	149.29	122.93–148.62	58.91, 58.94
6	4-F	7.492	7.772	7.351–7.673(7H)	1.68, 1.70	188.40	123.03	142.70	121.09–145.23	58.89, 58.93
7	4-CH_3	7.521	7.804	7.543–7.708(7H)	1.62, 1.64	188.77	122.98	144.13	123.73–145.98	54.66, 54.68
8	4-OCH_3	7.447	7.791	7.532–7.768(7H)	1.58, 1.59	188.66	122.86	143.86	121.98–146.34	52.68, 52.74
9	4-NO_2	7.51	7.66	7.573–7.621(7H)	7.77, 1.79	196.26	123.37	140.74	122.56–144.37	59.73, 59.78

nCdP = Nano cadmium phosphate; x = substituents

The effect of nano cadmium phosphate catalyst was studied on the synthesis of (*E*)-3,4-dimethoxyphenylprop-2-en-1-one (entry1; parent). The quantify catalyst was raised from 0.05 to 0.5 mg and the quantity of yield was improved from 35 – 88%. The optimal extent quantifiction of catalyst was found as 0.35 mg. Beyond this quantity of catalyst there is no increase yield in the condensation. This catalyst effect on the synthesis was illustrated in Fig. 2.

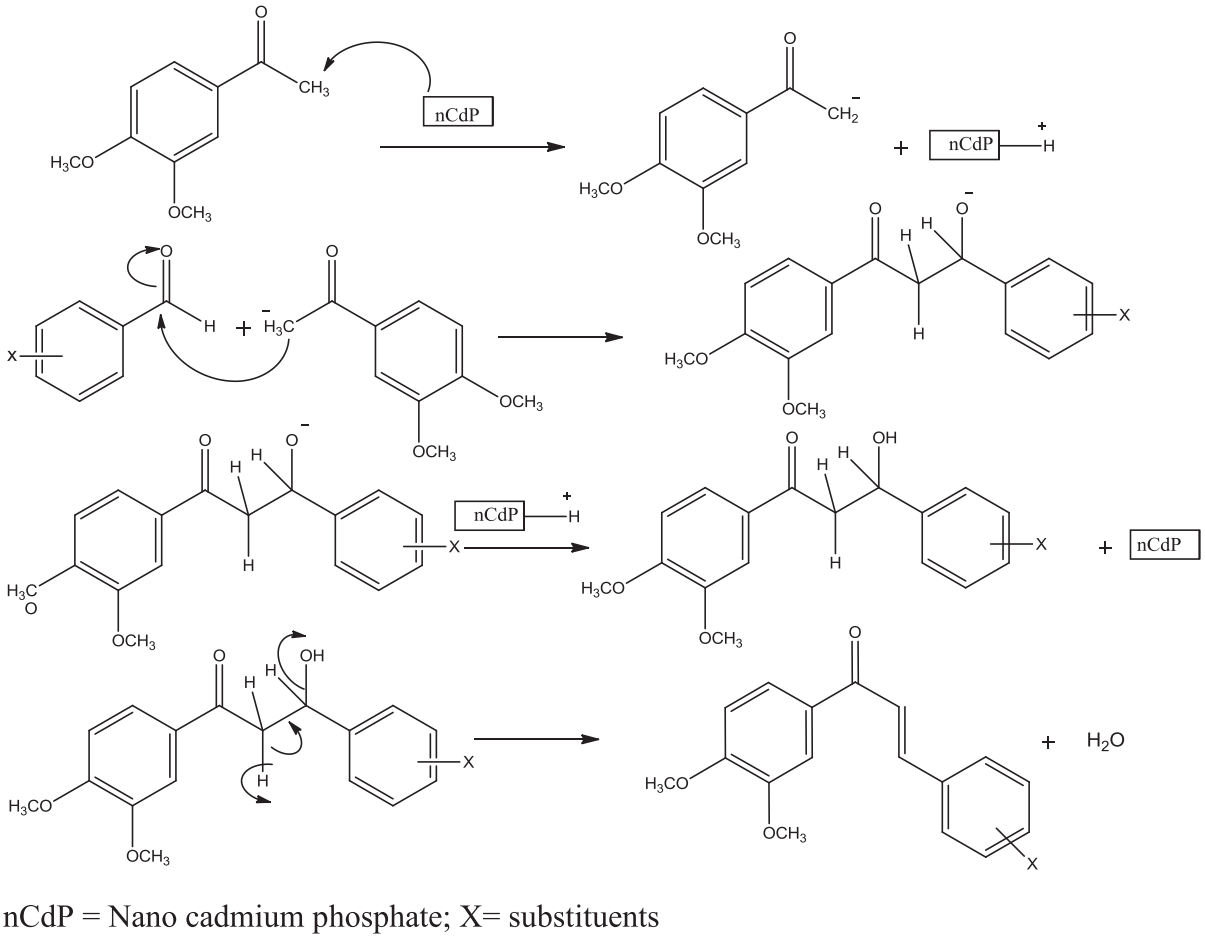

Fig. 1. The plausible mechanistic pathway of nano cadmium phosphate catalyzed Aldol condensation for the synthesis of (*E*)-3,4-dimethoxyphenylprop-2-en-1-ones.

Reusability of the catalytic reagent (entry 1) was investigated up to 6th run. The first 3 runs gave without change a quantity of yield (88%). The 4, 5 and 6th runs gave 87% yields. Here there is no considerable variation of yield in these reaction runs. These are shown in Table 4.

Table 4
Reusability of nano cadmium phosphate catalyst in the synthesis of (*E*)-3,4-dimethoxyphenylprop-2-en-1-ones (for entry 1).

Run	1	2	3	4	5	6
Yield (%)	88	88	88	87	87	87

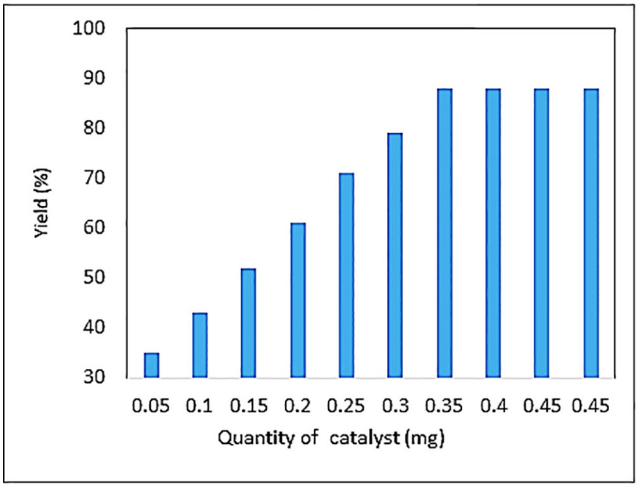

Fig. 2. Effect of catalyst on the yield.

The consequences of solvents on the yield (entry 1) was studied under conventional heating process with various solvents such as acetonitrile, dichloromethane, dioxane, ethanol, methanol and tetrahydrofuran within the same quantities of substrates, catalyst and 15 mL of solvents. In this conventional heating experiment, the ethanol medium gave higher yield (72%) and dioxane gave least yield (43%). The consequences of solvents on the yield of this experiments was shown in Table 5.

Both the solvent-free and conventional synthetic techniques gave more than 43% yields. Therefore, the nano cadmium phosphate is good and suitable catalyst for the synthesis of enones by aldol condensation. All the synthesized enones were analyzed using their physico-chemical parameters, yield, micro analysis and spectroscopic statistics data. In infrared spectral analysis these enones exhibits *s-cis* and *s-trans* conformers and these absorptions are observed in the range of 1600.36 – 1664.23 cm^{-1} and the consistent conformers are exposed in Fig. 3.

In NMR analysis, the observed hydrogen and carbon-13 chemical shifts are accepted and are fully supported for the formation of enones.

Table 5
Effect of solvents on the synthesis of(*E*)-3,4-dimethoxyphenylprop-2-en-1-ones with nano cadmium phosphate catalyst in conventional heating process (for entry 1).

Technique	Conventional						MW
Solvent	ACN	DCM	DO	EtOH	MeOH	THF	
Yield (%)	61	58	43	72	63	55	88

ACN: Acetonitrile; DCM: Dichloromethane; DO: Dioxane; EtOH: Ethanol; MeOH: Methanol; THF: Tetrahydrofuran.

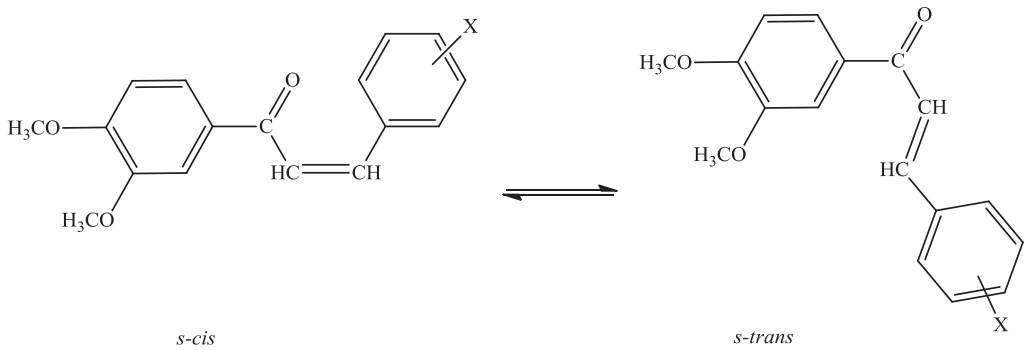

Fig. 3. The *s-cis* and *s-trans* conformers of 3,4-dimethoxyphenyl enones.

4. Conclusion

The catalytic effect of nano cadmium phosphate was investigated by the synthesis of 3,4-dimethoxyphenyl enones under microwave and conventional heating methods. In this investigation, the observed maximum yield is 88 and the minimum of 43%. The reusability of the catalyst was found to be good from the observed yield was not appreciably change up to 6th run of reactions. The effect of catalyst was studied on the synthesis with this catalyst under conventional heating. The ethanol medium gave high yield and not more than microwave method. All the synthesized enones were analyzed using their physico-chemical parameters, CHN analysis and spectroscopic data. Above obtained data were fully reinforced for the construction of enones. Therefore, the nano cadmium phosphate catalyst was good and suitable for synthesis of enones through Aldol Condensation both microwave as well as conventional heating process.

CRediT authorship contribution statement

V. Mala: Conceptualization, Methodology, Validation. **I. Muthuvel:** Data curation, Writing - original draft. **G. Thirunarayanan:** Supervision, Writing - review & editing. **V. Usha:** Visualization, Investigation.

Declaration of Competing Interest

The authors declare that they have no known competing financial interests or personal relationships that could have appeared to influence the work reported in this paper.

Acknowledgment

Authors thank IIT, Madras, Chennai-60025 for measuring NMR spectra of all synthesized enones.

References

[1] P. Olivera-Pastor, P. Maireles-Torres, E. Rodríguez-Castellón, A. Jiménez-López, T. Cassagneau, D.J. Jones, J. Rozière, Nanostructured Inorganically Pillared Layered Metal(IV) Phosphates, Chem. Mater. 8 (8) (1996) 1758–1769, https://doi.org/10.1021/cm960156r.
[2] C.N.R. Rao, S. Natarajan, A. Choudhury, S. Neeraj, A.A. Ayi, Aufbau Principle of Complex Open-Framework Structures of Metal Phosphates with Different Dimensionalities, Acc. Chem. Res. 34 (1) (2001) 80–87, https://doi.org/10.1021/ar000135+.
[3] R. Murugavel, A. Choudhury, M.G. Walawalkar, R. Pothiraja, C.N.R. Rao, Metal Complexes of Organophosphate Esters and Open-Framework Metal Phosphates: Synthesis, Structure, Transformations, and Applications, Chem. Rev. 108 (9) (2008) 3549–3655, https://doi.org/10.1021/cr000119q.
[4] J.P. Pocostales, M.M. Sein, W. Knolle, C. von Sonntag, T.C. Schmidt, Degradation of Ozone-Refractory Organic Phosphates in Wastewater by Ozone and Ozone/Hydrogen Peroxide (Peroxone): The Role of Ozone Consumption by Dissolved Organic Matter, Environ. Sci. Technol. 44 (21) (2010) 8248–8253, https://doi.org/10.1021/es1018288.
[5] G. Liu, Q. Tang, Y. Zhou, X. Cao, J. Zhao, D. Zhu, Photo-induced phosphate released from organic phosphorus degradation in deionized and natural water, Photochem. Photobiol. Sci. 16 (4) (2017) 467–475, https://doi.org/10.1039/C6PP00313C.
[6] X.T. Hong, X.H. Wu, Q.Y. Zhang, M.F. Xiao, G.L. Yang, M.R. Qiu, G.C. Han, Hydroxyapatite supported Ag_3PO_4 nanoparticles with higher visible light photocatalytic activity, Appl. Surf. Sci. 258 (2012) 4801–4805.
[7] M. Elobeid C. Göbel I. Feussner A. Polle Cadmium interferes with auxin physiology and lignification in poplar 63 3 2012 2012 1413 1421 10.1093/jxb/err384
[8] G. Wang, B. Huang, X. Ma, Z. Wang, X. Qin, X. Zhang, Y. Dai, M.-H. Whangbo, $Cu_2(OH)PO_4$, a Near-Infrared-Activated Photocatalyst, Angew. Chem. Int. Ed. 52 (18) (2013) 4810–4813, https://doi.org/10.1002/anie.201301306.
[9] S.-Y. Guo, S. Han, Constructing a novel hierarchical 3D flower-like nano/micro titanium phosphate with efficient hydrogen evolution from water splitting, J. Power Sources 267 (2014) 9–13, https://doi.org/10.1016/j.jpowsour.2014.05.011.
[10] T. Yan, W. Guan, L. Cui, Y. Xu, J. Tian, Immobilization of cadmium ions to synthesis hierarchical flowerlike cadmium phosphates microspheres and their application in the degradation of organic pollutants under light irradiation, RSC Adv. 5 (54) (2015) 43756–43764, https://doi.org/10.1039/C5RA07224G.
[11] E.R. Burkhardt, R.D. Rieke, The direct preparation of organocadmium compounds from highly reactive cadmium metal powders, J. Org. Chem. 50 (3) (1985) 416–417, https://doi.org/10.1021/jo00203a036.
[12] E. Ortiz-Islas, T. López, R. Gomez, J. Navarrete, Effect of phosphate ions in the properties of titania sol-gel, J Sol-Gel Sci Technol 37 (3) (2006) 165–168, https://doi.org/10.1007/s10971-005-6622-1.
[13] Z.G. Yi, J.H. Ye, N. Kikugawa, T. Kako, S.X. Ouyang, H. Stuart-Williams, H. Yang, J.Y.H. Cao, W.J. Luo, Z.S. Li, Y. Liu, R.L. Withers, An orthophosphate semiconductor with photooxidation properties under visible-light irradiation, Nat. Mater. 9 (2010) 559–564.
[14] J. Guo, S. Ouyang, P. Li, Y. Zhang, T. Kako, J. Ye, A new heterojunction Ag_3PO_4/Cr-$SrTiO_3$ photocatalyst towards efficient elimination of gaseous organic pollutants under visible light irradiation, Appl. Catal. B. 286 (2013) 134–135.
[15] A.I. Ahmed, S.A. El-Hakam, M.A. Abd-Elghany, W.S. Abo El-Yazeed, Synthesis and characterization of new solid acid catalysts, $H_3PW_{12}O_{40}$ supported on nanoparticle tin oxide: An efficient catalyst for the preparation of 7-hydroxy-4-methylcoumarin, Appl. Catal. A: General. 407 (2011) 40–48.
[16] R. FENG, X. YANG, W. JI, Y. CHEN, C. AU, VPO catalysts supported on H_3PO_4-treated ZrO_2 highly active for *n*-butane oxidation, Journal of Catalysis 246 (1) (2007) 166–176, https://doi.org/10.1016/j.jcat.2006.11.027.
[17] M. Ghiaci, A. Abbaspur, R.J. Kalbasi, Vapor-phase Beckmann rearrangement of cyclohexanone oxime over H_3PO_4/ZrO_2–TiO_2, Applied Catalysis A: General 287 (1) (2005) 83–88, https://doi.org/10.1016/j.apcata.2005.03.045.

[18] M. Ghiaci, R.J. Kalbasi, M. Mollahasani, H. Aghaei, Vapor phase acylation of phenol with ethyl acetate over H_3PO_4/TiO_2-ZrO_2, Applied Catalysis A: General 320 (2007) 35–42, https://doi.org/10.1016/j.apcata.2006.12.013.
[19] M. Ghiaci, A. Abbaspur, R. Kalbasi, Internal versus external surface active sites in ZSM-5 zeolitePart 1. Fries rearrangement catalyzed by modified and unmodified H_3PO_4/ZSM-5, Appl. Catal. A: Gene. 298 (2006) 32–39, https://doi.org/10.1016/j.apcata.2005.09.015.
[20] M. Ghiaci, A. Abbaspur, M. Arshadi, B. Aghabarari, Internal versus external surface-active sites in ZSM-5 zeolite Part 2: Toluene alkylation with methanol and 2-propanol catalyzed by modified and unmodified H_3PO_4/ZSM-5, Appl. Catal. A: Gene. 316 (2007) 32–46.
[21] M. Ghiaci, A. Abbaspur, R. Kia, C. Belver, R. Trujillano, V. Rives, M.A. Vicente, Vapor-phase alkylation of toluene by benzyl alcohol on H_3PO_4-modified MCM-41 mesoporous silicas, Catal. Commun. 8 (1) (2007) 49–56, https://doi.org/10.1016/j.catcom.2006.05.003.
[22] M. Ghiaci, R.N. Esfahani, H. Aghaei, Efficient dehydration of cinnamaldoxime to cinnamonitrile over H_3PO_4/Al-MCM-41, Catal. Commun. 10 (6) (2009) 777–780, https://doi.org/10.1016/j.catcom.2008.11.036.
[23] 23. B. Khoualdia, M. Loungou, E. Elaloui, Adsorption of organic matter from industrial phosphoric acid (H3PO4) onto activated bentonite, Arabian J. Chem. (2013) xxx, xxx–xxx, article in Press, http://dx.doi.org/10.1016/j.arabjc.2013.01.014.
[24] A. Abbaspourrad, R.J. Kalbasi, F. Zamani, Vapor phase alkylation of toluene using various alcohols over H_3PO_4/MCM-41 catalyst: influence of reaction parameters on selectivity and conversion, Turk. J. Chem. 34 (2010) 875–885.
[25] K. Ranganathan, D. Kamalakkannan, R. Suresh, S.P. Sakthinathan, R. Arulkumaran, R. Sundararajan, V. Manikandan, G. Thirunarayanan, Synthesis, Hammett spectral correlation and evaluation of antimicrobial activities of some substituted styryl 4′-piperidinophenyl ketones, Indian J. Chem. 58B (2019) 1131–1143.
[26] A.M. Maharramov, Y.V. Mamedova, M.R. Bayramov, I.G. Mamedov, Chalcone Derivatives as Corrosion Inhibitors for Mild Steel in Brine-Kerosene Solution, Russian J. Phys. Chem. A 92 (2018) 2154–2158.
[27] S. Rajasri, B. Krishnakumar, A.J.F.N. Sobral, S. Balachandran, M. Swaminathan, I. Muthuvel, Development of $Cd_3(PO_4)_2$/rGO Coupled Semiconductor System for Effective Mineralization of Basic Violet 10 (BV 10) under UV-A Light, Mater. Today Proc. 15 (2019) 471–480.
[28] M. Zhang, J.K. Liu, R. Miao, G.M. Li, Y.J. Du, Preparation and characterization of fluorescence probe from assembly hydroxyapatite nanocomposite, Nanoscale Res. Lett. 5 (2010) 675–679.
[29] M. Thomas, S.K. Ghosh, K.C. George, Characterization of nanostructured silver orthophosphate, Mater. Lett. 56 (2002) 386–932.
[30] H. Deng, J. Wang, R. Callender, W.J. Ray, Relationship between bond stretching frequencies and internal bonding for [16O4]- and [18O4] phosphates in aqueous solution, J. Phys. Chem B. 102 (1998) 3617–3623.

SCREENING OF ANTHELMINTIC ACTIVITY OF *Cassia alata* FLOWER EXTRACTS

G. Akilandeswari[1], R.Suja Pandian[2*], D. Meharaj begum[1],M.Dinesh Kumar[1]

[1]Department of Microbiology, Annai College of Arts and Science, Kumbakonam,Tamilnadu, 612503-India

[2]Department of Biochemistry, Annai College of Arts and Science, Kumbakonam,Tamilnadu, 612503-India

Corresponding author

R.Suja Pandian

sruthivelan@gmail.com

ABSTRACT:

The aim of this presentstudy was to screen the anthelmintic activity of *Cassia alata* flowers on adult earthworm E. eugeniae. The standard drug taken for anthelmintic action was albendazole. The flower extract was found to paralyze and destroy worms, indicating that it has antihelmintic properties.

KEYWORDS: E. eugeniae, *Cassia alata* Linn,flowers,anthelmintic

Introduction:

In livestock production, the issue of helminth parasites is a significant limiting factor. Anthelmintic medications are often used to treat helminth infections in domestic animals. Because of its long-term use, it has resulted in the development of anthelmintic resistance in livestock, which has become a constant source of concern (Kundu et al., 2014).

Because of their negative impact on growth, gastrointestinal nematodes have been found to be of great economic significance in domesticated livestock all over the world. The use of anthelmintics in the management of livestock parasitosis has traditionally provided significant benefits to livestock producers (Anbu et al., 2015). Small-scale farmers in developing countries have limited access to commercially accessible anthelmintics and veterinary services due to lack of supply or high costs. As a result, most farmers, like those in other parts of the world, must rely on ethnoveterinary medicine. Since control programs rely on a small number of compounds, drug resistance becomes much more of a problem, necessitating careful monitoring of those that are available.

Cassia alata Linn. (Fam: Caesalpiniaceae) is a large, attractive shrub with thick, downy branches that can be found growing wild almost anywhere in India. The lower leaflets are oblong-elliptic, while the upper leaflets are broadly obovate. In English, it's called ringworm shrub or winged senna; in Sanskrit, it's called Dadrughna or Dvipagsti; and in Tamil, it's called semaiagathi or Vandugolli.Cassiaalata (C. alata) has been used in herbal medicine for antimicrobial, antifungal, purgative, anti-inflammatory, analgesic, antitumor, and hypoglycemic properties for decades (Kunduet al., 2014). Analgesic, antibacterial, anti-inflammatory, fungicidal, hypoglycemic, laxative, oxytocic, and wound-healing properties have been identified in C. alata leaf extracts.(Mohideen et al.,2005). Furthermore, it has recently been discovered that anthelmintic substances with high human toxicity are found in livestock-derived foods, posing a significant threat to human health (Anbu et al., 2015).

As a result, new chemical substances for helminth regulation are desperately needed, which has prompted research into commonly used anthelmintic drugs, which are widely considered to be essential sources of bioactive substances (Hamondet al.,1997). Medicinal plants, according to the World Health Organization, will be the safest source of a variety of medicines. As a result, such plants should be studied further in order to gain a better understanding of their protection and efficacy (Nascimento et al., 2000). The anthelmintic activity of aqueous and methanolic extracts of Cassia alata flowers was evaluated in this research.

MATERIALS AND METHODS:

Preparation of Flowers Extract: The flowers of Cassia alata were cleaned, shade dried and coarsely powdered. The extracts were concentrated under reduced pressure to obtain solid residues. Cassia alata flowers were washed, shade dried, and coarsely powdered for the preparation of the flowers extract.

Thecoarse powder was then exhaustively extracted in a Soxhlet apparatus. The dried powder material (50 g) was subjected to soxhlet extraction with methanol and water for 6 h. To obtain solid residues, the extracts were concentrated at a lower pressure.

Because of its anatomical similarity to human intestinal roundworm parasites, all of the experiments were conducted on the African adult earth worm E. eugeniae (Annelida). The earthworms were all roughly the same size. They were gathered, washed, and placed in a container of water.

Screening of Anthelmintic Activity:

Extract doses of 10, 50, and 100 mg/ml were chosen at random for anthelmintic activity testing. In a nine-cm petri dish, E. eugeniae was put in three separate concentrations of extract (10, 50, and 100 mg/ml). When no movement of any kind could be detected, even when the worm was shaken vigorously, mean times for paralysis (in minutes) were taken; mean times for worm death (in minutes) were taken after worms did not move when shaken vigorously or dipped in warm water (50°C). The worms died because they lost their motility, which was followed by the fading of their body colors. The reference compound used was albendazole (10 mg/ml).

Table 1: Anthelmintic activity of aqueous and methanolic extract of *Cassia alata* L. flowers. **on earthworm** E. eugeniae

Groups	Treatment	Dose (mg/ml)	Time taken for paralysis (min)	Time taken for death (min)
I	Control (Normal saline)	-	-	-
II	Albendazole	10	0.40±0.03	1.32±0.01
III	Aqueous extracts	10	0.48±0.02	1.48±0.07
IV	Aqueous extracts	25	0.49±0.06	1.41±0.06
IV	Aqueous extracts	50	0.50±0.01	1.32±0.00
V	Methanolic extract	10	0.47±0.00	1.42±0.02
VI	Methanolic extract	25	0.43±0.00	1.40±0.04
VI	Methanolic extract	50	0.37±0.00	1.30±0.06

Each value is represented as mean ± standard deviation (n = 5). Data are found to be significant by testing through one way ANOVA at 5 % level of significance ($p < 0.05$).

RESULTS AND DISCUSSION:

The antihelmintic activity of aqueous and methanolic extracts of Cassia alata flowers was dose-dependent, with efficacy for worms at 10, 25, and 50 mg/ml concentrations. The anthelmintic activity of the aqueous and methnolic extracts was significant. Table 1 shows the results of the anthelmintic activity of C. alata flower extract on earthworms.

The anthelmintic activity of aqueous extracts of C. alata flowers peaked at 50 mg/ml concentrations. The crude extract contained tannins, among other chemical constituents, according to phytochemical analysis.

Tannins have been shown to have antihelmintic properties. Tannins are polyphenolic compounds that can attach to free proteins in the gastrointestinal tract of the host animal or glycoprotein on the parasite's cuticle, potentially killing the parasite (Adnaiketal., 2011).

According to Maqbool et al. (2004), Fumaria parviflora's anthelmintic behavior may be attributed to alkaloids that have the ability to intercalate with parasite DNA synthesis.

Albendazole kills worms by increasing chloride ion conductance in the worm muscle membrane, resulting in hyperpolarization and reduced excitability, resulting in muscle relaxation and flaccid paralysis (Athanasiadou et al., 2001).

In comparison to the regular drug albendazole, methanolic and aqueous extracts of C. alata flowers not only demonstrated paralysis, but also induced worm death in a shorter period.

Delaquis et al. (2002) reported that naturally occurring combinations of plant compounds are synergistic, resulting in crude extracts with higher antimicrobial activity than purified individual constituents.

In developing countries, such plant-based treatments could be part of an integrated management strategy for helminth regulation. To determine the mechanism of action, further research is needed to isolate and reveal the active compound found in the crude extracts.The current research concluded that the aqueous extract had significantly higher anthelmintic activity than the methanolic extract as compared to the standard drug (Albendazole).

CONCLUSION:

We can deduce from the results of this analysis that Cassia alata flower extract has important anthelmintic activity. As a result, it's worth looking into Cassia alata's potential for treating helminthic infections. More research is needed to pinpoint the chemical constituents of this plant that are responsible for its anthelmintic properties.

REFERENCES

Kundu S, Roy S, Lyndem LM. Broad spectrum anthelmintic potential of Cassia plants. Asian Pac J Trop Biomed. 2014 May;4(Suppl 1):S436-41.

Anbu, Jayaraman & Murali, Anita & Sathiya, R & Gr, Saraswathy &Azamthulla, Mohammad. (2015). In Vitro Anthelmintic Activity of Leaf Ethanolic Extract of Cassia Alata and Typha Angustifolia. 41.

Hamond J.A., Fielding D., Bishop S.C., (1997) Prospects for plant anthelmintics in tropical veterinary medicine, Vet Res Comm., 21, pp. 213-228.

Nascimento GG, Locatelli J, Freitas PC, Silva GL. Antibacterial activity of plant extracts and phytochemicals on antibiotic resistant bacteria. Braz J Microbiol 2000; 31: 247-256.

Mohideen S., Sasikala E., Arun A., (2005) Pharmacognosy of Cassia Alata Linn –leaves, Anc Sci Life, XXIV (4), pp. 192-198.

Athanasiadou, S., Kyriazakis, I., Jackson, F. and Coop, R.L. 2001. Direct anthelmintic effects of condensed tannins towards different gastrointestinal nematodes of sheep: in vitro and in vivo studies. Vet. Parasitol. 99, 205-219.

Adnaik, Rahul & Bhagwat, Dr. Durgacharan & Raut, I.D. & Mohite, S.K. &Magdum, Chandrakant. (2011). Laxative and anthelmintic potential of Cassia alata flower extract. Research Journal of Pharmacy and Technology. 4. 98-100.

Maqbool A, Hayat CS, Tanveer A. Comparative efficacy of various indigenous and allopathic drugs against fascioliasis in buffaloes. Vet Arch 2004; 74: 107-114.

Delaquis PJ, Stanich K, Girard B, Mazza G. Antimicrobial activity of individual and mixed fractions of dill, cilantro, coriander and eucalyptus essential oils. Int J Food Microbiol 2002; 74: 101-109

EVALUATION OF MID-GUT BACTERIA PRESENT IN THE LARVA OF RICE MOTH, CORCYRA CEPHALONICA (STAIN.) (GALLERIIDAE: LEPIDOPTERA) FED ON DIFFERENT GRAINS USING 16S RDNA SEQUENCE BASED CULTURE DEPENDENT TECHNIQUE

Arumugam Dhanalakshmi, Ganesan Sasireka, Palaniappan Suresh, Panagal Mani, Palanisamy Chella Perumal, Kalimuthu Ayyakalai Marikannu Karthikeyan*

Abstract— *Corcyra cephalonica* (Stainton) (Lepidoptera: Pyralidae) is a factitious host extensively used for rearing egg parasitoids. The present study attempt to investigate mid-gut bacteria present in larva of *Corcyra cephalonica (C. cephalonica).* The mid-gut bacteria were collected from the *C. cephalonica* fed on eight different grains were identified and characterized by 16S rDNA sequence based culture dependent method. The results revealed that, 16 bacterial species where presented in mid-gut of *C. cephalonica* larva which are belonging to 11 bacterial genera included in three phyla namely Firmicutes, Proteobacteria and Actinobacteria. Among the three phyla Firmicutes was the most dominant phylum with a record of 7 bacterial species, followed by Proteobacteria with 5 species and Actinobacteria with 4 species. Phylum Firmicutes, was dominated by members of Class Bacilli. The genus *Staphylococcus* was the largest genus represented by 4 species namely *Staphylococcus* sp., *S. saprophyticus*, *Staphylococcus pasteuri* and *Staphylococcus warneri* and also the most prevalent genus which was recorded in the mid-gut of *C. cephalonica* fed on 4 grains. No single bacterium was found in all the mid-gut samples. This record of varied mid-gut bacterial composition could be attributed to the feeding behaviour/pattern of the larvae and further intensive large scale research like extensive sampling and deep-sequencing are needed to ascertain it.

Index Terms— Grains, *C. cephalonica*, mid-gut bacteria, 16S rDNA sequencing.

1 INTRODUCTION

Corcyra cephalonica (C. cephalonica) is commonly known as rice meal moth or rice moth which belongs to the family of Pyralidae. It is a destructive insect and infects cereals, cereal products, oilseeds, pulses, dried fruits, nuts and spices [1-3]. The adult *C. cephalonica* is nocturnal, grey in colour and does not feed. Generally the female lays about 100-200 eggs near food source. Eggs hatch after an incubation period of about 5 days [4,5]. The larva however, constructs a feeding tube gallery, consisting of silken web and food particles, to stay, feed and grow inside it. After larval period of 23-25 days fully-grown larvae form dense white cocoons to pupate. Pupae are usually found in food or they may be found between pellets and sacks [6]. Adults emerge from pupae after pupal period of 4-8 days and lives for about a week. One *C. cephalonica* alone can feed up to 32.9 mg. While feeding, it forms web on the stored grains, thus leads to the quality loss of the stored products [7,8]. The infestation of this stored product pest is limited to the grains in the storage locations like godowns, warehouses, retail shops and local storage areas like houses and the successful establishment of this pest species is attributed to the poor storage facilities [9].

Besides the destructive properties of *C. cephaionica*, it has some good aspects as well, as it acts as an alternate host for some egg parasitoids which are used for biological control programmes of different destructive pests like sugarcane borers in many countries of the world [10-14]. It is one of the most used factitious hosts and is being utilized in various bio-control research, developmental and extension units for mass production of number of natural enemies in several countries [15,16]. Therefore present study aimed to screen the bacteria present in mid-gut of *C. cephaionica* larva using 16S rDNA sequence based culture dependent technique.

2 MATERIALS AND METHODS

2.1 Insect sample collection

The infested grains such as rice (*Oryza sativa*), red rice (*Oryza punctata*), groundnut (*Arachis hypogaea* L.), pearl millet (*Pennisetum glaucum* (L.)), red sorghum (*Sorghum bicolour* L.), white sorghum (*Sorghum vulgare*), sesame black (*Sesamum indicum*) and almond (*Prunus dulcis*) were collected from the godowns of Regulated Trade Centre, Villupuram, Tamilnadu, India and white sorghum and dry nuts were collected from local godowns in Madurai, Tamilnadu, India. The actively feeding sixth instar larvae of *C. cephalonica* were isolated from the infested grains and were used for the determination of gut microbiota study.

C

- *Arumugam Dhanalakshmi and Kalimuthu Ayyakalai Marikannu Karthikeyan: Department of Zoology, N.M.S.S. Vellaichamy Nadar College, Madurai-625 019, Tamil Nadu, India.*
- *Ganesan Sasireka: Department of Zoology, Sri Meenakshi Government Arts College for Women, Madurai-625 002, Tamil Nadu, India.*
- *Palaniappan Suresh: Department of Zoology, Thiagarajar College, Madurai-625 009, Tamil Nadu, India.*
- *Panagal Mani: Department of Biotechnology, Annai College of Arts and Science, Kovilacheri-612503, Tamil Nadu, India.*
- *Palanisamy Chella Perumal: Department of Plant Science, University of the Free State, QwaQwa Campus, South Africa.*
- ***Corresponding Author: K.A.M. Karthikeyan, Email: karthikeyaan@gmail.com; Mobile No. +91-9865578847*

2.2 Mid-gut dissection

The collected larvae of *C. cephalonica* were sacrificed and surface sterilized with 70% of ethanol for 5 min followed by washing in 0.85% normal saline (phosphate buffered saline (PBS)) twice. The mid-gut was dissected out in a sterile condition and placed in 2ml microcentrifuge tube containing 300µl of 0.85% saline (PBS) and homogenized with micro-pestle. The 0.85% saline (PBS) after second wash in all the samples were collected and used as a negative control to check the sterility of the procedure. Scissors, forceps, needle, glasswares, plasticwares, buffers and solutions/reagents used in the dissection process were sterilized in autoclave and UV treatment. About 10 insect specimens were used for single midgut sample preparation and three replicates (positive controls) were maintained.

2.3 Isolation of mid-gut bacteria

The mid-gut homogenates were centrifuged for a brief period of 2min. at 2,000g and the supernatant was collected. 100µl each of the supernatant was spread on Nutrient Agar plate and incubate at 30ºC for 48hrs. The resulting bacterial colonies obtained on the spread plate were differentiated according to their colony morphology like shape, size, colour, margin, opacity, elevation etc. and morphologically distinct colonies were selected for repeated subculture on nutrient agar plates until a presumably pure colony was obtained. The pure colonies were transferred to nutrient broth and incubated at 30ºC.

2.4 Extraction of Genomic DNA from bacterial samples

1.5 ml of overnight grown bacterial isolates maintained in nutrient broth were transferred to 2 ml of microcentrifuge tube and centrifuged at 10,000g for 2 min and pellet was collected. The same was repeated for another 1.5 ml of culture to harvest enough quantity of cells (100 mg). The pellet was resuspended in 1.5ml of sterile distilled water and centrifuged at 10,000g for 2min. The pellet was then collected and ground with 300µl of CTAB (cetyltrimethyl ammonium bromide) DNA extraction buffer (1% W/V CTAB; 1.4M NaCl; 10mM EDTA, pH 8.0; 100mM Tris-HCl, pH 8.0; 0.2% V/V ß-mercaptoethanol) in a glass homogenizer. The mixture was emulsified with equal volume of phenol:chloroform (1:1). It was centrifuged at 10,000rpm for 5min. at room temperature. The aqueous phase was collected and mixed with equal volume of chloroform:isoamyl alcohol (24:1). The mixture was then centrifuged at 10,000g for 5min. at room temperature. The aqueous phase collected was then added with equal volume of cold absolute ethanol and the DNA was allowed to precipitate by keeping the tubes in -20ºC for overnight. DNA pellets were obtained by centrifugation at 10,000g for 5min. and the ethanol was air-dried. The pellet was dissolved in 50µl of TE buffer (Tris 10mM, pH 8.0 and EDTA 1mM, pH 8.0) and stored at 4ºC. The quality of the isolated genomic DNA was tested by agarose gel electrophoresis [17].

2.5 PCR amplification of 16S rDNA

The Universal Primers for the amplification of the 16S rDNA region of approximately 1,550bp were Forward primer 27F: $^{5'}$AGAGTTTGATCCTGGCTCAG$^{3'}$ and Reverse primer 1492R: $^{5'}$GGTTACCTTGTTACGACT$^{3'}$ used [18]. The primer set used in the PCR reactions resulted in the amplification of the homologous fragments from all the bacterial isolates. The PCR reaction mix was prepared in a total volume of 30ul with 10ng of genomic DNA, a 2.5mM concentration each of dATP, dTTP, dCTP and dGTP, 100ng each of the Forward primer and Reverse primer, 3U of Taq DNA polymerase enzyme and 1X Taq DNA polymerase assay buffer (10X) and the remaining volume with glass distilled water (Bangalore Genei, India). The PCR reactions were conducted MJ Mini-BIO RAD Thermal Cycler. The PCR reaction cycles consisted of initial denaturation for 5 minutes at 94ºC, 40 cycles of 94ºC for 30 seconds (denaturation), 55ºC for 45 seconds (annealing) and 72ºC for 30 seconds (extension) and followed by the final extension of 72ºC for 10 minutes. The amplicons were run through 1% agarose gel electrophresis along with 100bp DNA ladder (Bangalore Genei, India) and purified for sequencing process using the DNA elution kit (Bangalore Genei) as per manufacturer's protocol [19].

2.6 Sequencing of 16S rDNA

The amplified 16S rDNA region of the bacterial samples are sequenced by the dideoxy chain termination method (Sanger et al., 1977), using the Big Dye Terminator Version 3.1" Cycle Sequencing Kit in the ABI 3130 Genetic Analyzer in accordance with the manufacturer's instructions (Polymer & Capillary Array: POP_7 polymer, 50cm Capillary Array; Analysis protocol: BDTv3-KB-Denovo_v5.2; Data Analysis Software: Seq Scape_v 5.2; Reaction Plate: Applied Biosystem Micro Amp Optical 96-Well Reaction Plate) [20].

2.7 Sequencing of Sequence analysis of 16S rDNA for Bacterial species identification

The sequence of 16S rDNA of the bacterial samples obtained were analysed for the bacterial species identification by carrying out NCBI-BLAST. After identification of the bacterial species, each species have been deposited in the NCBI-GenBank through BlankIt tool [21].

3 RESULTS

As demonstrated *C. cephalonica* infesting different grains namely rice, red sorghum, sesame black, pearl millet, red rice, groundnut, almond and white sorghum were sacrificed and the mid-guts were isolated for the study of mid-gut microbiota. A total of twenty species of bacteria were recorded in the midgut samples of *C. cephalonica* infesting eight different grains with an average of 2.5 bacterial species per mid-gut sample (Table 1). In this present study no fungal colony was recorded in the mid-gut samples of *C. cephalonica*. The twenty bacterial species represent 11 Genera and 16 species of bacteria (Table 2), which include *Staphylococcus saprophyticus*, *Enterococcus gallinarum*, *Staphylococcus* sp., *Alcaligenes faecalis*, *Luteimonas* sp., *Oceanobacillus* sp., *Kocuria palustris*, *Brevibacterium* sp., *Kocuria flava*, *Brevundimonas* sp., *Staphylococcus pasteuri*, *Kytococcus* sp., *Staphylococcus warneri*, *Pseudomonas* sp. and *Pseudomonas stutzeri* belong to the phyla Firmicutes, proteobacteria and Actinobacteria. The *C. cephalonica* fed on rice (*oryza sativa*) harbored maximum number of bacteria of five species namely *Paenibacillus* sp., *S. saprophyticus*, *E. gallinarum*, *Staphylococcus* sp. and *A. faecalis*. Three bacterial species was found in the gut of *C. cephalonica* fed on pearl millet (*K. palustris*, *E. gallinarium* and *Brevibacterium* sp.) and ground nut (*S. pasteuri*, *K. palustris* and *Kytococcus* sp.). Two species of bacteria was recorded in the midgut of red sorghum (*S. saprophyticus* and *E. gallinarum*), sesame black (*Luteimonas* sp. and *Oceanobacillus* sp.) red rice (*Kocuria*

flava and *Brevundimonas* sp.) and white sorghum (*Pseudomonas* sp. and *P. stutzeri*).

The most common genus of bacteria found in the gut was *Staphylococcus* which had four species; and *Kocuria* and *Pseudomonas* recorded two species of bacteria each. *E. gallinarum* was the bacterium which was commonly found in the gut of *C. cephalonica* fed with rice, red sorghum and pear millet and *S. saprophyticus* was found in the gut of rice and red sorghum fed *C. cephalonica*. The bacterial genus *Pseudomonas* was exclusively present in the midgut of white sorghum fed *C. cephalonica*. Diet dependent gut flora was clearly exhibited in the present study and no single bacterium was found in all the midgut samples of *C. cephalonica* fed with different grains.

4 DISCUSSION

The bacteria species identified from the mid-gut larval samples of *C. cephalonica* fed on six different grains comprising 11 Genera and 16 species and 3 phyla (Firmicutes, proteobacteria and Actinobacteria). The most dominant species of bacteria is *Staphylococcus saprophyticus* which was present in the mid-gut of fed *C. cephalonica*. From the present study it was observed that the predominant phyla in the mid-gut of larvae of *C. cephalonica* was Firmicutes representing 43.75%. The gut of the insect provides suitable microbiome to many gut-associated microorganisms like bacteria, fungi and viruses, amongst which bacteria dominate in most insect groups [22]. The association between insect and bacteria are significant and the gut of insect species harbor highly diverse bacteria comprising of different Phyla, Class, Order, Family, Genus, species and strains. 16S rDNA gene, which is present in all nucleoid of bacteria have been widely used to determine the diversity of the insect gut bacterial microbiota [23]. Recently 16S rDNA sequence based identification and characterization of insect intestinal bacteria was carried out. They are having well symbiotic association which leads to the enhancement in the nutrition supply, increased physiological activities and behavioral changes in the host insect [24]. Apart from that some bacteria confers resistance of host insect species to particular pesticides and some bacteria plays antagonistic role. The insect pests of household like housefly and cockroach are very common in possessing some pathogenic bacteria in their gut environment and serves as a vector of diseases [25].

The classical way of biochemical based identification of bacterial species, which is usually mentioned as culture dependent method, is cumbersome, laborious and time consuming and needs expertise in bacterial taxonomy, in addition only cultivable bacteria can be identified. The technological advancement in the field of biotechnology made it simple, easy, rapid and uncultivable bacterial species can be identify by sequencing 16S rRNA region and subsequent blast of the query sequence in the NCBI [26]. This culture independent method need less effort in the bacterial species identification as the species is identified purely based on the similarity of the 16S rRNA gene sequences. This method of identification of bacterial species at its current form enables to identify more number of bacterial species due to the pyrosequencing or Next Generation Sequencing [27]. The study on the gut microbiota of the economically important insect pests provide valuable information about the total gut bacterial community and any economically important bacterial species which could be cultured and potent compounds

TABLE 1

IDENTIFICATION OF MID-GUT BACTERIAL SPECIES

Sl. No.	Bacterial Species with GenBank Accession number	Length (bp)	Closely related bacterial species	16S rRNA gene similarity (%)	Max. Score	Query Coverage (%)
1.	*Paenibacillus* sp. MK005262	1399	*Paenibacillus uliginis* NR117012	100	2357	97
2.	*Staphylococcus saprophyticus* MK005263	1399	*Staphylococcus saprophyticus* NR_115607	100	2584	100
3.	*Enterococcus gallinarum* MK005265	1402	*Enterococcus gallinarum* NR_104559	99	2573	100
4.	*Staphylococcus* sp. MK841609	479	*Staphylococcus warneri* NR_025922	96	1408	79
5.	*Alcaligenes faecalis* MK005266	1378	*Alcaligenes faecalis* NR_113606	92	1953	97
6.	*Staphylococcus saprophyticus* MK005267	1394	*Staphylococcus saprophyticus* NR_115607	100	2575	100
7.	*Enterococcus gallinarum* MK005268	1408	*Enterococcus gallinarum* NR_104559	100	2579	100
8.	*Luteimonas* sp. MK005269	1402	*Luteimonas padinae* NR_153744	99	2475	98
9.	*Oceanobacillus* sp. MK005270	1412	*Oceanobacillus oncorhynchi* subsp. *incaldanensis* NR_042257	99	2603	100
10.	*Kocuria palustris* MK005272	1348	*Kocuria palustris* NR_026451	99	2486	100
11.	*Enterococcus gallinarum* MK005273	1383	*Enterococcus gallinarum* NR_104559	95	2165	100
12.	*Brevibacterium* sp. MK005274	1366	*Brevibacterium casei* NR_041996	99	2484	100
13.	*Kocuria flava* MK005275	1352	*Kocuria flava* NR_044308	99	2481	100
14.	*Brevundimonas* sp. MK005276	1388	*Brevundimonas diminuta* NR_113602	92	2032	99
15.	*Staphylococcus pasteuri* MK005277	1396	*Staphylococcus pasteuri* NR_024669	99	2540	100
16.	*Kocuria palustris* MK005278	1355	*Kocuria palustris* NR_026451	100	2503	100
17.	*Kytococcus* sp. MK005279	1344	*Kytococcus sedentarius* NR_074714	99	2471	100
18.	*Staphylococcus warneri* MK005280	1379	*Staphylococcus warneri* NR_025922	99	2543	100
19.	*Pseudomonas* sp. MK005282	1389	*Pseudomonas fluorescens* NR_113647	99	2549	100
20.	*Pseudomonas stutzeri* MK005282	1381	*Pseudomonas stutzeri* NR_041715	99	2543	100

extracted from it.

5 CONCLUSION

In the present study, evaluated the presence of mid-gut bacteria in the larva of C. cephalonica and it showed 16 bacterial species which are belonging to 11 bacterial genera included in three phyla namely Firmicutes, Proteobacteria and Actinobacteria. Among the three phyla Firmicutes was the most dominant phylum with a record of 7 bacterial species, followed by Proteobacteria with 5 species and Actinobacteria with 4 species. Phylum Firmicutes, was dominated by members of Class Bacilli. None of the single bacterium was found in all the mid-gut samples. Together this study can conclude that, C. cephalonica could be serve as factitious hosts and might be utilized in various bio-control research, developmental and extension units for large-scale production of natural enemies. However, further studies such as, extensive sampling and deep-sequencing are warranted to determine the current findings.

TABLE 2
LIST OF BACTERIAL SPECIES IDENTIFIED

Sl. No.	Grains	Collection area or location of the grains	Total number of bacterial species/ isolates	Bacteiral species
1.	Rice (*Oryza sativa*)	Madurai	5	*Paenibacillus* sp. *Staphylococcus saprophyticus* *Enterococcus gallinarum* *Staphylococcus* sp. *Alcaligenes faecalis*
2.	Red Sorghum (*Sorghum bicolor*)	Salem	2	*Staphylococcus saprophyticus* *Enterococcus gallinarum*
3.	Sesame black (*Sesamum indicum*)	Villupuram	2	*Luteimonas* sp. *Oceanobacillus* sp.
4.	Pearl millet (*Pennisetum glaucum*)	Villupuram	3	*Kocuria palustris* *Enterococcus gallinarum* *Brevibacterium* sp.
5.	Red Rice (*Oryza punctata*)	Ramnad	2	*Kocuria flava* *Brevundimonas* sp.
6.	Ground nut (*Arachis hypogoea*)	Madurai	3	*Staphylococcus pasteuri* *Kocuria palustris* *Kytococcus* sp.
7.	Almond (*Prunus dulcis*)	Madurai	1	*Staphylococcus warneri*
8.	White sorghum (*Sorghum vulgare*)	Villupuram	2	*Pseudomonas* sp. *Pseudomonas stutzeri*

ACKNOWLEDGMENT

The authors are thankful to the management of N.M.S.S. Vellaichamy Nadar College, Madurai, Tamil Nadu, India for providing facilities and encouragement to complete this research work finefulfilment.

REFERENCES

[1] Rasool A., Zubair R., Rasheed R., Gull S., Ahmed A. Mass production of rice meal moth (*Corcyra cephalonica*) on different food media under laboratory conditions. J Res Dev. 2018; 74-80.
[2] Chakravorty S., Das HC. Egg laying behaviour of *Corcyra cephalonica* (Stain.). Rev Appl Ent. 1985; 73 (4): 222.
[3] Suchiung C., Wikang P., Se C., Wk P. Emergence and longevity of the rice moth, *Corcyra cephalonica* (Stain.) (Pyralidae: Lepidoptera). Chinese J Ent. 1998; 18(2): 135-140.
[4] Yaui Chu., Menping T., Wenyi C. Effect of photoperiodism on the larval development, adult emergence, and fecundity of the rice moth, *Corcyra cephalonica* (Stain.) (Galleriidae: Lepidoptera) at constant temperature. Ent. Abs. 1994; 25(6): 74.
[5] Islam MN. Studies on the biology and control of rice meal moth, *Corcyra cephalonica* (Stain.) on stored wheat. M.Sc.(Ag) thesis, Bangladesh Agricultural University, Mymensingh. 1971; 76 pp.
[6] Mbata GN. Studies on some aspect of the biology of Corcyra cephalonica (Stain.). Rev. Appl. Ent. 1989; 78 (7): 793.
[7] Mukhukrishnan N., Venugopal MS., Hamurougu K., Janathan R. Recycling of spent larval food of *Corcyra cephalonica* for fuel gas production. Rev Agril Ent. 1996; 85(12): 1418.
[8] Pajni HR., Rose HS., Gill KM. Some observation of the biology of *Corcyra cephalonica* (Stain.). Rev Appl Ent. 1980; 68 (12): 824.
[9] Ray R. Life table and intrinsic rate of increase of *Corcyra cephalonica* (Stain.) on maize. Ent Abs. 1994; 25(10): 95.
[10] Seshagiri AD. Seshagiri Notes on rice moth, *Corcyra cephalonica* (Stain.) (Galleriidae: Lepidoptera). Indian J Ent. 1954; 16(2): 95-114.
[11] Padamshali S., Ganguli JL. Evaluation of life-cycle of rice meal moth, *Corcyra cephalonica* stainton larvae reared on different diets. Int J Chem Stud. 2019; 7(3): 4279-4282.
[12] Jalali SK., Singh SP. Effect of infestation of sorghum grains by different dosage of *Corcyra cephalonica* on adult emergence pattern. Entomon. 1992; 17(1-2):117-119.
[13] Kumar S., Murthy KS. Mass production of corcyra. in: training manual of the second training on mass production of biological control agents. National Centre for Integrated Pest Management, New Delhi, India, 2000, 10-20.
[14] Chaudhuri N., Ghosh A., Ghosh J. Variation in biological parameters of *Corcyra cephalonica* Stainton (Lepidoptera: Pyralidae) with quality of rearing media. Int J Curr Res Acad. 2015; 3(4):373-380.
[15] Sahayaraj K., Sathiamoorthi P. Influence of different diets of *Corcyra cephalonica* on life history of a reduviid predator *Rhynocoris marginatus* (Fab.). J Centr Eur Agric. 2002; 3:53D61.
[16] Sowjanya KC., Thippaiah M., Mohan K. Gender associated differences in developmental parameters of *Corcyra cephalonica* (Stainton) (Lepidoptera: Pyralidae). Int J Curr Microbiol App Sci. 2018; 7(9):2534-2539.
[17] Smith K., Diggle MA., Clarke SC. Comparison of commercial DNA extraction kits for extraction of bacterial genomic DNA from whole-blood samples. J Clin Micro. 2003; 2440–2443.
[18] Jiang H., Dong H., Zhang G., Yu B., Chapman LR., Fields MW.

Microbial diversity in water and sediment of lake chaka, an Athalassohaline lake in Northwestern China. App Environ Microbiol. 2006; 72 (6): 3832–3845.

[19] Clarke SC. Nucleotide sequence-based typing of bacteria and the impact of automation. Bioessays. 2002; 24: 858–862.

[20] Woo PCY., Lau SKP., Teng JLL., Tse H., Yuen KY. Then and now: use of 16S rDNA gene sequencing for bacterial identification and discovery of novel bacteria in clinical microbiology laboratories. Clin Microbiol Infec. 2008; 14 (10): 908-934.

[21] Wagner K., Springer B., Pires VP., Keller PM. High-throughput screening of bacterial pathogens in clinical specimens using 16S rDNA qPCR and fragment analysis. Diagnos Microbiol Infec Dis. 2019; 93(4): 287-292.

[22] Douglas AE. Multiorganismal insects: diversity and function of resident microorganisms. Annu Rev Entomol. 2015; 60: 17–34.

[23] Gill EE., Brinkman FS. The proportional lack of archaeal pathogens: Do viruses/phages hold the key? BioEssays. 2011;33:248–54.

[24] Sabree ZL., Kambhampati S., Moran NA. Nitrogen recycling and nutritional provisioning by Blattabacterium, the cockroach endosymbiont. Proc Natl Acad Sci USA. 2009; 106: 19521–19526.

[25] Köhler T., Dietrich C., Scheffrahn RH., Brune A. High-resolution analysis of gut environment and bacterial microbiota reveals functional compartmentation of the gut in wood-feeding higher termites (Nasutitermes spp.). Appl Environ Microbiol. 2012; 78(13): 4691-4701.

[26] Wong AC., Chaston JM., Douglas AE. The inconstant gut microbiota of Drosophila species revealed by 16S rRNA gene analysis. ISME J. 2013; 7: 1922–1932.

[27] Akman L., Yamashita A., Watanabe H., Oshima K., Shiba T., et al. Genome sequence of the endocellular obligate symbiont of tsetse flies, Wigglesworthia glossinidia. Nat Genet. 2002; 32: 402–407.

Environmental Technology & Innovation 20 (2020) 101176

Contents lists available at ScienceDirect

Environmental Technology & Innovation

journal homepage: www.elsevier.com/locate/eti

Nanoremediation of dimethomorph in water samples using magnesium aluminate nanoparticles

Tentu Nageswara Rao [a], A.P.B. Balaji [b], Mani Panagal [c,*], Botsa Parvatamma [d], Bharathi Selvaraj [e], Saravanan Panneerselvam [f], Wilson Aruni [g,h], Kumaran Subramanian [g,i,**], Pugazhvendan Sampath Renuga [j,l,***], Sivakumar Pandian [k]

[a] Department of Chemistry, Krishna University, Machilipatnam, Andhrapradesh, India
[b] Ecoysus Lifescience, Chennai, India
[c] Department of Biotechnology, Annai College of Arts&Science, Kumbakonam, Tamil Nadu, India
[d] Department of Organic Chemistry, Gayathri P.G. Courses, Gotlam, Vizianagaram, India
[e] Department of Microbiology, Sri Sankara Arts and Science College, Kanchipuram- 631561, Tamil Nadu, India
[f] Research and Development Centre, Chennai Petroleum Corporation Limited, Chennai- 600068, India
[g] Department of Biotechnology, School of Bio and Chemical Engineering, Sathyabama Institute of Science and Technology, Chennai- 600119, Tamil Nadu, India
[h] US Department of Veteran affairs, Loma Linda, CA, USA
[i] Centre for Drug Discovery and Development, Sathyabama Institute of Science and Technology, Chennai, Tamil Nadu, India
[j] Department of Zoology – Arignar Anna Government Arts College, Cheyyar, Tamil Nadu, India
[k] School of Petroleum Technology, Pandit DeenDayal Petroleum University, Gandhinagar, Gujarat, India
[l] Department of Zoology, Annamalai University, Annamalainagar, Cuddalore District, Tamil Nadu, India

ARTICLE INFO

Article history:
Received 16 July 2020
Received in revised form 8 September 2020
Accepted 22 September 2020
Available online 25 September 2020

Keywords:
Magnesium aluminate nanoparticles
Water samples
Dimethomorph
Liquid chromatography mass spectrometry
Solid phase extraction

ABSTRACT

The present work aims to prepare magnesium aluminate nanoparticles ($MgAl_2O_4$ NPs) using aluminum isopropoxide and magnesium ethoxide by hydrolysis reaction and to investigate them as new adsorbent materials for the extraction and clean-up of dimethomorph pesticide from tap water. The $MgAl_2O_4$ NPs were characterized by X-ray powder diffraction (XRD), Fourier-transform infrared spectroscopy (FTIR), field emission scanning electron microscopy (FESEM), and high-resolution transmission electron microscopy (HRTEM). The XRD result confirmed the formation of the spinal cubic structure in the fabricated sample. A solid-phase extraction (SPE) cartridge packed with $MgAl_2O_4$ NPs was used to extract dimethomorph pesticide from water samples. The extracted pesticide solution was quantified using a validated liquid chromatography mass spectrometry (LC-MS-MS) method. The limit of quantification (LOQ) was found to be 1—g/L, signifying the sensitivity of the LC-MS-MS. The water samples were passed through the cartridges and investigated to find the adsorption strength of the pesticides under the influence of temperature, volume of sample, flow rate, pH and ionic strength on the efficiency of the cartridge. The extraction efficiency of the developed $MgAl_2O_4$ NPs SPE was found to be higher than that of commercially available SPE-C_{18}cartridge. The average recoveries of the pesticides ranged from 90%–94% which was obtained at two different fortification levels of 1 and 10 —g/L using $MgAl_2O_4$ NPs SPE.

* Corresponding author.
** Correspondence to: Sathyabama Institute of Science and Technology, Chennai.
*** Corresponding author at: Department of Zoology, Annamalai University, Annamalainagar, Cuddalore District, Tamil Nadu, India.
E-mail addresses: master.maniji@gmail.com (M. Panagal), kumarun23@gmail.com (K. Subramanian), pugazhvendan@gmail.com (P. Sampath Renuga).

https://doi.org/10.1016/j.eti.2020.101176
2352-1864/

1. Introduction

Chemical pesticides are used predominantly to protect crops from dreadful diseases among which fungicides play a major role in protecting crops from oomycete disease and fungal pathogens. To protect crops against fungal pathogens, mancozeb and chlorothalonil are commonly used. However, these fungicides have several drawbacks, like carcinogenic effect, as reported by Environmental Protection Agency (EPA) and this has led to its restricted usage (Damalas and Eleftherohorinos, 2011). As an alternative to this, dimethamorph is found to be a benign fungicide with higher antifungal efficacy having no carcinogenic effects in mice up to 1000 mg/kg body weight/day (Aktar et al., 2009).

Dimethamorph [(E, Z)-4-[3-(4-chlorophenyl)-3-(3, 4 dimethoxyphenyl) acryloyl] morpholine] is a derivative of cinnamic acid belonging to the category of morpholine fungicides which comprise an approximately equal mixture of *E* and *Z* isomers (Kuhn et al., 1991). The antifungal efficacy of dimethomorph was first reported by (Stout et al., 1996). The toxicity of dimethomorph was executed by infiltrating into the leaf surface and translocating inside to exert defensive action by interrupting the development of fungal cell walls. Dimethomorph was found to be effective when used as a foliar spray and in protecting several fruits and vegetables from mildew disease (Moraes et al., 2003; Duvenhage and Köhne, 1995). American Cyanamid (Princeton, NJ) is a commercial producer of dimethomorph that controls velvety mildews of hops (Sharma et al., 2016).

In India, dimethomorph is primarily used to protect grapes, potatoes, cucurbits from Downy mildew, and Late blight disease. As dimethomorph is known to exert higher efficacy, it has been continuously used in agricultural practices. Owing to the continual and prolonged exposure of dimethomorph, fungal species have developed resistance and have become insensitive to lower concentrations (Lan et al., 2009). In order to fight fungal infection, a higher concentration of dimethomorph is sprayed in fields. resulting in an increased amount of dimethamorph in agricultural runoff (Blankenberg et al., 2007), which infiltrates into the groundwater, whereby it is mixed with drinking water (Zou et al., 2016). In addition, bioaugmentation can also increase the levels of dimethomorph alarmingly causing higher toxicity levels (Yang et al., 2020)

However, recent trends in nanotechnology have given rise to key concepts in engineering the nanoparticles towards their specific roles and functions (Hasnain et al., 2013). Several nanoparticles have been used to detoxify or transform contaminants specifically by enabling chemical reduction or catalysis (Karn et al., 2009). It is a new trend that has emerged in the field of nanoremediation, which is the process of utilizing nanoparticles for environmental remediation (Cecchin et al., 2017). Nanosystems having immense capacity to detoxify pesticides (Bapat et al., 2016; Kaur et al., 2014; Pang et al., 2015) and being environmentally benign (Balaji et al., 2017, 2015) are of great importance.

This research synthesized the novel nanocomposite material composed of magnesium oxide, high-density polyethylene, tricalcium phosphate and hydroxyapatite by being in agreement with this concept. The same nanocomposite was already proven to be a non-induction of inflammation and toxicity in human osteoblast cells and has the potential to be used in orthopedic applications (Pourdanesh et al., 2014). Magnesium aluminate nanoparticles are commonly used as polycrystalline materials. The material has good physical properties, including a high melting point, good mechanical strength, low dielectric constant and good resistance to increasing alkali as acid (Chandradass and Kim, 2010). In the present study, $MgAl_2O_4$NPs are used as a stationary phase in the development of SPE cartridges which are then used for the extraction and cleanup of dimethomorph pesticides from water samples. The pesticide residues are quantified by LC-MS-MS system. This study reports the detection of a low level of this pesticide in the tap water sample and optimizes the conditions for the SPE method in comparison with the commercial SPE–C_{18} Sigma product.

2. Experimental

2.1. Materials

The analytical standard of dimethomorph (97.9%) was obtained from Sigma Aldrich, dichloromethane and n-hexane from Rankem, New Delhi, analytical grade solvents i.e., acetonitrile, aluminum isopropoxide, magnesium ethoxide, methanol and isopropanol were supplied by Merck Limited and tap water was collected from our laboratory.

2.2. Methods

2.2.1. Synthesis of $MgAl_2O_4$ NPs

$MgAl_2O_4$ NPs were synthesized by hydrolysis reaction using high-purity aluminum isopropoxide and magnesium ethoxide raw materials. Initially, 6.2 g of aluminum isopropoxide was dissolved in 1540 mL of isopropanol and 12.5 g of magnesium ethoxide was dissolved in 550 mL of methanol thereby making two distinct solutions. Both solutions were then mixed together in a 5 L beaker and heated at 70 °C for 2 h. The mixture solution was then added with 330 mL of water and stirred at 200 rpm. Finally, the solution was filtered, and the precipitate obtained was dried for 24 h at 120 °C.

2.2.2. Characterization of $MgAl_2O_4$ NPs

The XRD profile of the MgAl2O4 NPs was studied using "Debye Scherrer" equation for the crystal structure and the sample phase purity of the crystallite size was determined from XRD spectra. FESEM's characterization of $MgAl_2O_4$ NPs (TESCAN, CZ/MIRA I LMH) showed MgO's production on the Al_2O_3 matrix. The particle size was found to be 4–5 nm by HRTEM. FTIR (PerkinElmer) was used for the identification of functional groups.

Table 1
DMRM conditions for LCMS/MS analysis.

Precursor m/z	Product m/z	Collision energy
387.90	301.15 (Quantifier)	−22.0
387.90	165.00 (Qualifier 1)	−32.0
387.90	139.05 (Qualifier 2)	−35.0

2.2.3. Preparation of dimethomorph calibration solutions and sample

The reference standard of dimethomorph was prepared in a 100 mL volumetric flask by adding 10.02 mg of dimethomorph (purity 97.9%) in acetonitrile. The solution was sonicated and made with the same solvent up to the mark. The standard solutions (1.0, 10, 25, 50, 100, and 200.0 μg/L) were prepared by diluting the above stock solution in acetonitrile. A representative 50.0 mL of the tap water sample was fortified with 50 μL of working standard solution and the samples were kept in a refrigerator at 8 °C till analysis.

2.2.4. LCMS– MS analysis — dimethomorph

LCMS–MS analysis of lower concentration samples 1 μg/L–250 μg/L was performed using an Agilent Technologies 6460-triple quadrupole mass spectrometer. Dimethomorph was detected using Jetstream electrospray ionization (ESI) in positive mode as ionization intensity was higher in FIA mode (Flow injection analysis). The method conditions were set with nitrogen drying gas temperature at 350 °C, nitrogen drying gas flow 10 L/min, nitrogen sheath gas temperature at 400 °C, nitrogen sheath gas flow 11 L/min, nebulizer pressure 55 psi, capillary and nozzle voltage at 5000 V and 1000 V respectively. The mobile phase was set at a ratio of 5% v/v (0.1% v/v formic acid in water as aqueous phase) and 95% v/v (acetonitrile) consisting of a flow rate of 0.6 mL/min. The rinse port consisted of 50% v/v water and 50% v/v acetonitrile. The injection volume was set at 0.5 μL. The parental m/z was evaluated and auto-optimization of the dynamic multiple reaction monitoring (dMRM) for MS/MS conditions was performed in FIA mode (Flow injection analysis) as represented in Table 1. Further more, the optimized method was assessed for the calibration standards using an Agilent Poroshell 120 EC C_{18} column with a 4.6 mm column ID X 50 mm column length and particle size of 2.7 μm. Weighing method $1/c^2$was used as the data algorithm by Mass Hunter Software for performing the calibration and quantifying the unknown concentrations.

Method validation confirms the reliability. In this work, the parameters assay-accuracy, method precision, linearity and quantification (LOQ) were deliberated (Daraghmeh et al., 2007; Apparao et al., 2015). The assay accuracy was determined by recovery tests using the samples fortified at two different concentration levels of 1 and 10 μg/L. The linearity curve was established using different known concentrations of analytical standards. The quantification limit (LOQ, μg/L) was calculated as the lowest concentration of a fungicide with a response of 10 times the baseline noise.

2.2.5. Extraction procedure

50 mL of the homogenized representative pesticide containing a water sample was taken in a bottle. The sample was added to 100 ml acetonitrile and both were properly mixed for 30 min using an orbital shaker followed by filtration. The process was repeated using 50 ml of acetonitrile. The final extract was transferred to a 500 ml separating funnel, which was then mixed with a solution of 25 mL saturated sodium chloride and partitioned with 75 ml of dichloromethane. The separating funnel was shaken vigorously for 10 min to obtain the organic and aqueous phases. The organic phase was separately collected after which the aqueous phase was again partitioned with 75ml of dichloromethane. The combined dichloromethane fraction was concentrated to near dryness under a vacuum flash evaporator and the residue was taken in 10 ml of elution mixture for $MgAl_2O_4$ NPs SPE.

2.2.6. $MgAl_2O_4$NPs SPE for the clean-up procedure

500 mg of $MgAl_2O_4$ NPs was wetted with n-hexane and packed in a plastic syringe having a column of 0.5 cm diameter, a length of 10 cm and 1 cm glass wool plug at the lower end where the top was covered with 0.5 g sodium sulfate (Na_2SO_4). The residue obtained from the partition step (Section 2.2.5) was transferred into the column and eluted with 10 mL of elution mixture (25: 75, acetonitrile: n-hexane). The initial 5 mL eluate was discarded and the remaining eluate was collected, concentrated to near dryness and reconstructed with a 10 mL mobile phase for HPLC analysis.

2.2.7. Amount of sorbent effect ($MgAl_2O_4$ NPs)

The effect of the sorbent amounts investigated in the range of 100–2000 mg of $MgAl_2O_4$ NPs were used for the determination of the recovery % of 1 μg/L spiked sample solution.

2.2.8. Effect of flow rate

Pre-concentration of 1 μg/L spiked sample solution recoveries were investigated under the influence of different flow rates at 1–2 mL, 3–4 mL, 5–6 mL and 7–8 mL/min.

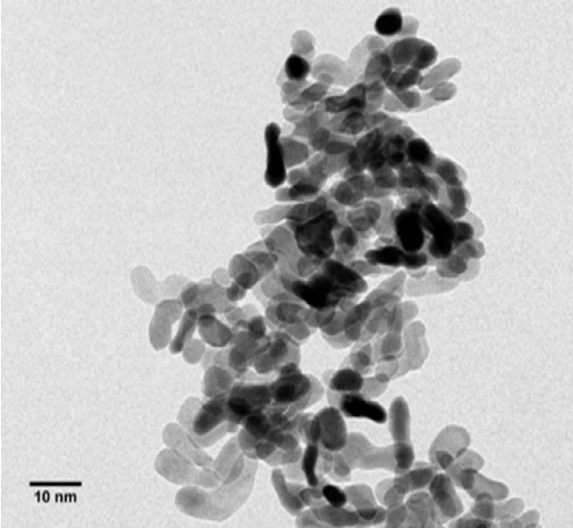

Fig. 1. HRTEM micrograph of $MgAl_2O_4$ NPs.

2.2.9. Effect of pH

The influence of pH in the pre-concentration 1 μg/L spiked sample solution recoveries was investigated by adjusting the pH of the water samples using 0.1 molar hydrochloric acid and 0.1 molar sodium hydroxide solutions.

2.2.10. Effect of ionic strength

The effect of ionic strength was monitored by a standard pesticide solution of 1 μg/L in 0.1% and a solution of 1 percent sodium chloride in distilled water at 20 ± 2 °C.

3. Result and discussion

Due to their low cost, negligible toxicity, higher stability, higher surface area and increased chemical reactivity to environmental contaminants, metal aluminum nanoparticles are widely used in various environmental remediation applications

3.1. Synthesis and characterization of $MgAl_2O_4$ NPs

$MgAl_2O_4$ NPs were synthesized by hydrolysis reaction and were found to possess an average particle size of 5 nm by HR-TEM (Fig. 1). FE-SEM micrograph revealed the presence of particles of different shapes and sizes (Fig. 2). A comparative study of the SEM images of the samples synthesized by three separate ion-pair complex precursors specifies that both agglomeration degree and particle size are lower for the sample synthesized by the precursor [Al(sal)2(H2O)2]2[Mg(dipic)2]. The SEM illustration of the spinel synthesized by [Al(sal)2(H2O)2]2[Mg(dipic)2] precursor showed smooth, distinct particles. The particles were interconnected in some regions causing the agglomerated region of the sample. Thus, it is speculated here that some particles within the sample act as nucleation centers around which condensation of the smaller particles occurs thereby giving rise to agglomeration (Paorici et al., 2003). With a narrow size distribution in the range of 13–20 nm, the SEM images for the other two samples (especially for the sample synthesized by [Mg(H2O)6][Al(ox)2(H2O)2]2•5H2O precursor) show aggregated particles and broad agglomerates. Flake morphology is one of the most common MgO morphologies that can be obtained via Zhang et al. (2014), using different methods of synthesis.

The XRD profile of the $MgAl_2O_4$synthesized sample at room temperature is depicted in Fig. 3. Which shows the formation of a cubic spinel phase in the fabricated sample. These consciences results were similar to (Tian et al., 2015). The lattice parameter for the cubic structure was obtained from the XRD pattern using powder-x software which was found to be 8.08 Å. There were no additional peaks in the XRD indicating the formation of phase pure material (Tian et al., 2015). The peaks in magnesium oxide nanoparticles XRD pattern were consistent with JCDS 75–1525 which express the cubic structure of Rao et al. (2014) synthesized nanoparticles. The presence of sharp peaks in the magnesium oxide samples XRD spectrum verified the development of nanoparticles and the increase in peak width reflected a decrease in nanoparticles scale.

The FT-IR spectrum revealed a band at 523 cm^{-1} related to the Al–O stretching vibration that corresponds to the AlO_6 groups that build up the $MgAl_2O_4$ composition (Fig. 4). The strong absorption at 3445 cm^{-1} is the stretching vibration

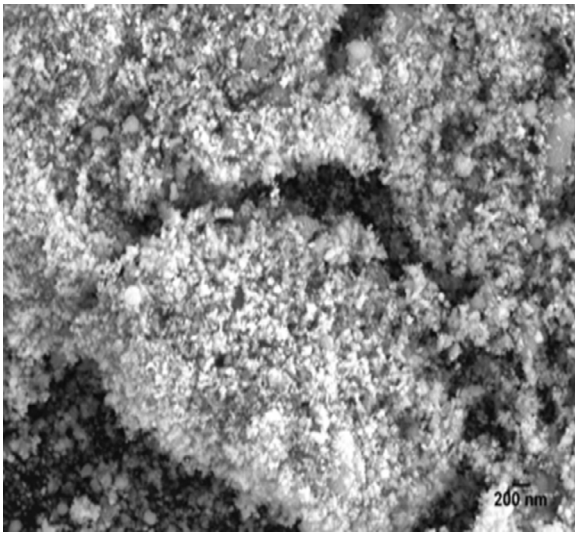

Fig. 2. FESEM image of $MgAl_2O_4$ NPs.

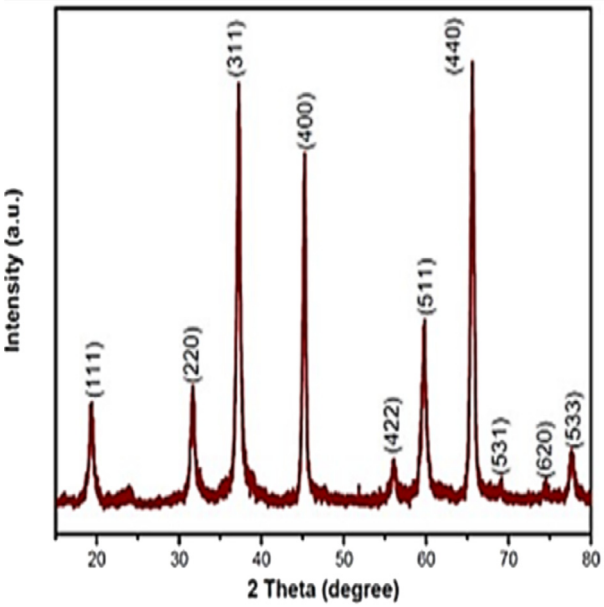

Fig. 3. XRD pattern of $MgAl_2O_4$ NPs.

of hydroxyl (OH) and a peak at 1645 cm^{-1} is due to the bending vibration of the adsorbed water molecule. The major peak at 702 cm^{-1} shows the presence of Mg–O vibrations. The weak band at 1462 cm^{-1} proves the presence of organic content due to C–O stretching vibration. In the IR spectra of the materials, Nakamoto (2009) vibration bands about 3515 and 1680 cm-1 could be attributed to the stretching and bending vibrations of the adsorbed molecular surface water interacting with MgAl2O4 materials and the width of these bands could be due to hydrogen bonding O–H.

3.2. LCMS analysis

The LCMS method was developed by merging the mixture of *E* and *Z* isomers to quantify the trace level in the water matrix. The developed method was found to possess higher accuracy and precision for the detection of dimethomorph, which possesses no buffer salts affecting the column and instrument efficiency. The parental m/z was for dimethomorph which was found to be 387.90. The auto MRM transition for the dimethomorph parent ion yielded the transition as follows: 387.90 > 301.15, 387.90 > 165.00 and 387.90 > 139.50 (Fig. 5). Here, 387.90 > 301.15 was used as the quantifier,

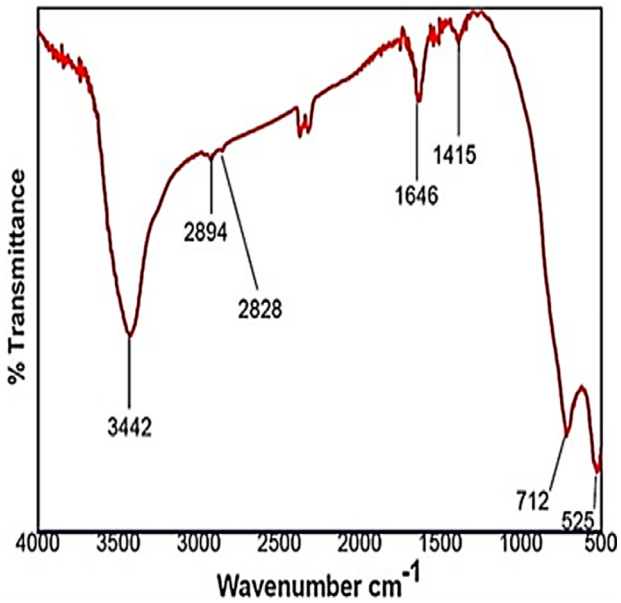

Fig. 4. FTIR spectra of $MgAl_2O_4$ NPs.

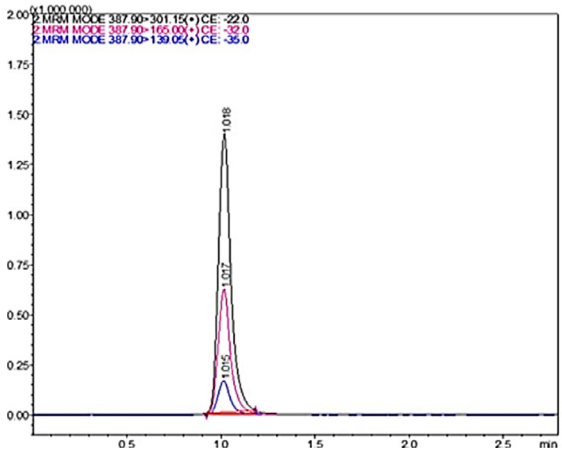

Fig. 5. MRM chromatogram of dimethomorph. Displaying the transition of 387.90 > 301.15, 387.90 > 165.00 and 387.90 > 139.05.

possessing good peak shape and sensitivity. The LOQ of the method was determined to be 1 μg/L for an injection volume of 0.5 μL. The linear regression (r^2) goodness of fit for the linearity calibration standard 1 μg/L to 250 μg/L was found to be 0.9999 (Fig. 6). which ensured the peak height ratio on concentration (Chandradass and Kim, 2010).

To determine the specificity standard solution of dimethomorph, spiking sample solution, water control, mobile phase and extracted solvents were assayed. No matrix peaks interfered with the main peak. The parental m/z was evaluated and auto-optimization of the MRM (Multiple Reaction Monitoring) for MS/MS conditions was performed in FIA mode (Flow injection analysis) as represented in Table 1 and Fig. 7.

The quantification limit was found to be 1.0 μg/L. The quantitative limit was defined as the lowest level of fortification evaluated at which the acceptable mean recoveries (82%–94% RSD<2%) were obtained. This quantitation limit also represents the level of fortification at which the chromatogram reliably produces an analyte peak at approximately ten times the baseline noise. The detection limit was set at 0. 3 μg/L, three times that of the control injection around the retention time of the peak of interest.

3.3. $MgAl_2O_4$ NPs SPE extraction and recovery

Recovery studies were performed at 1.0 and 10 μg/L spiked levels for dimethomorph in water samples using $MgAl_2O_4$ NPs packed SPE cartridge (Fig. 8) and SPE–C_{18} Sigma product. Tables 2 and 3 show the recovery data and the relative

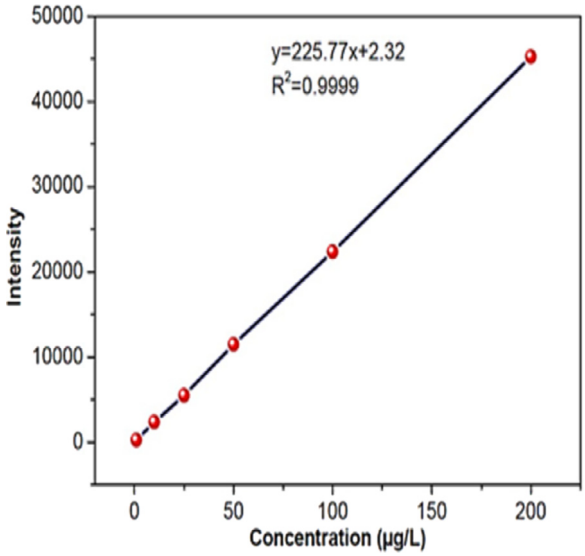

Fig. 6. Representative calibration curve of dimethomorph.

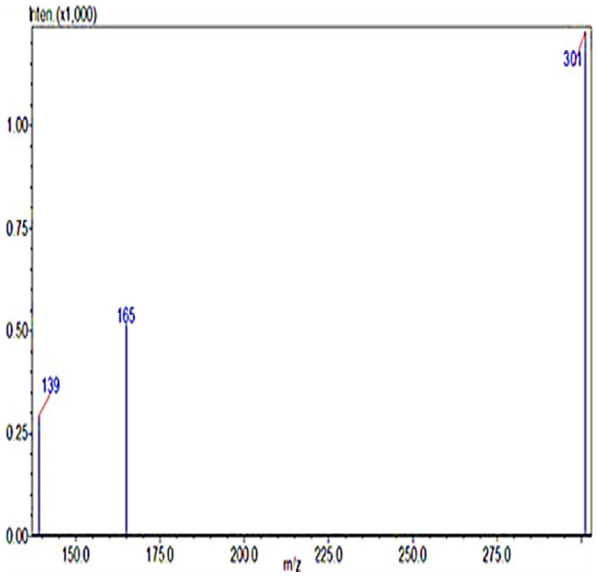

Fig. 7. LCMS–MS Spectral profile of dimethomorph.

standard deviation values. The values were calculated using six replicates for dimethomorph analysis by a single analyst on one day. The recovery at 1 µg/L yielded a mean recovery percentage of 88.33, a standard deviation of 1.83% and a relative standard deviation of 2.07%. However, for 10.0 µg/L, the mean recovery % was found to be 94.06 with standard deviation recovery of 1.65% and relative standard deviation recovery of 1.76%. Hence, the repeatability RSDs<3% of the method was found to be satisfactory.

3.4. Amount of sorbent effect ($MgAl_2O_4$ NPs)

For this investigation, 100, 500, 1000 and 2000 mg of $MgAl_2O_4$ NPs packed with SPE cartridges were used. At concentrations of 500, 1000 and 2000 mg were allowed for maximum recovery of the analyte of interest. Lower recovery values were recorded when lower amounts, such as 100 mg was used that shows the part of the analyte was not retained in the stationary phase. However, when 500 mg, 1000 mg and 2000 mg were used, satisfactory average recovery rate was obtained. Therefore, we used in the subsequent experiments to lower the amount of stationary phase used and consequentially decrease the cost of the SPE procedure.

Table 2
Recoveries of the pesticide from fortified water sample using $MgAl_2O_4$ NPs.

Fortified concentration −g/L	Recovered concentration −g/L	Recovery %	Mean recovery %	Standard deviation of recovery %	The relative standard deviation of Recovery %
1.0	0.027	90.00			
1.0	0.026	86.67			
1.0	0.027	90.00	88.33	1.83	2.07
1.0	0.026	86.67			
1.0	0.026	86.67			
1.0	0.027	90.00			
10.0	0.276	92.00			
10.0	0.279	93.00			
10.0	0.289	96.33	94.06	1.65	1.76
10.0	0.279	93.00			
10.0	0.286	95.33			
10.0	0.284	94.67			

Table 3
Recoveries of the pesticide from fortified water sample using SPE-C18 Sigma product.

Fortified concentration −g/L	Recovered concentration −g/L	Recovery %	Mean recovery %	Standard deviation of recovery %	The relative standard deviation of Recovery %
1.0	0.025	83			
1.0	0.024	80			
1.0	0.025	83	82.00	1.54	1.88
1.0	0.024	80			
1.0	0.025	83			
1.0	0.025	83			
10.0	0.274	91			
10.0	0.269	90			
10.0	0.280	93	91.83	1.16	1.27
10.0	0.278	93			
10.0	0.277	92			
10.0	0.275	92			

The results are shown in graphical Fig. 9. Also, confirmed the absence of extra peaks in the synthesized nanoparticles in their high purity. Usually, traditional SPE procedures require centrifugation or sample solution filtration to remove the adsorbent from the sample. However, an external supermagnet can be used to quickly and rapidly isolate magnetic NPs from the sample. The effect of extraction and desorption times on the recovery of target ions was investigated to get the optimum experiment time. The experimental results show that 10 min is adequate to achieve both quantitative adsorption and desorption of metal ions with > 90 percent recovery. Because of its super paramagnetism property, the magnetic adsorbent can detach completely from the solution in less than 1.0 min. The entire SPE procedure can be carried out within approximately 30 min, effectively shortening the conventional SPE-passing column.

3.5. Effect of flow rate, pH and ionic strength

The effect of flow rate on the pre-concentration of the residues of dimethomorph was tested. The study result reveals that an increase in flow rate decreases the pre-concentration of SPE cartridges. The recovery of dimethomorph was higher with flow rates of 1 to 2 mL/min and the nominal flow rate for the pre-concentration was established as 3 to 4 mL/min. While increasing the flow rate to greater than 5 mL/min, the recovery percentage decreased significantly with $MgAl_2O_4$ NPs based SPE cartridges (Fig. 10).

The effect of pH in pre-concentration residues was studied by adjusting the pH of the water sample using 0.1% hydrochloric acid or 0.1% sodium hydroxide solution. The study found that the nominal pH for the pre-concentration of residues was 5 to 8. A drastic reduction in recovery percentage was observed at pH < 5 and > 8. The recoveries were high with $MgAl_2O_4$ NP-packed cartridges. The average recoveries of dimethomorph residues in $MgAl_2O_4$ NPs-based SPE cartridges were found to be 83.45% at pH 4.0, 91.34% at pH 5.0, 97.45% at pH 6.0, 98.21% at pH 7.0, 90.07% at pH 8.0 and 85.67% at pH 9.0, with the tested concentration 1 μg/L level (Fig. 11).

The influence of ionic strength in the pre-concentration of residues using NPs-SPE cartridges was studied. From the results it was observed that there was significant change in the pre-concentration capacity of residues due to variation in the ionic strength. The recovery percentage was found to be 82.35% and 98.44% of recoveries were found in 0.1% and 1% sodium chloride solution respectively (Fig. 12). The study concluded that varying the flow rate, pH and ionic strength exerted the least effect on the system. The pHZPC may explain the effect of the solution pH on the surface charge of the

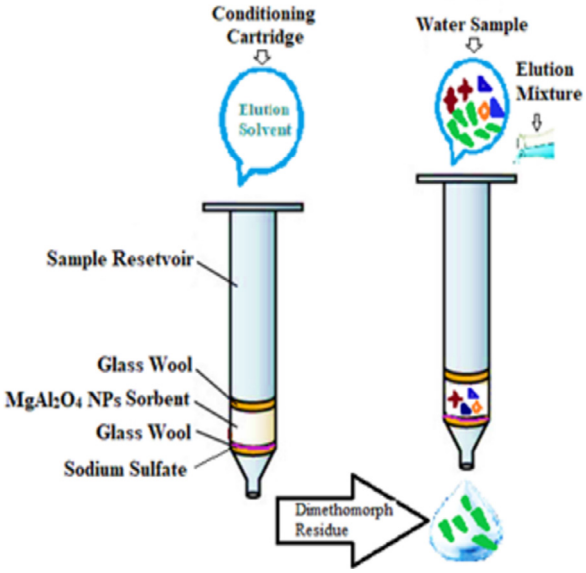

Fig. 8. $MgAl_2O_4$ NPs SPE of dimethomorph Pesticide Residues.

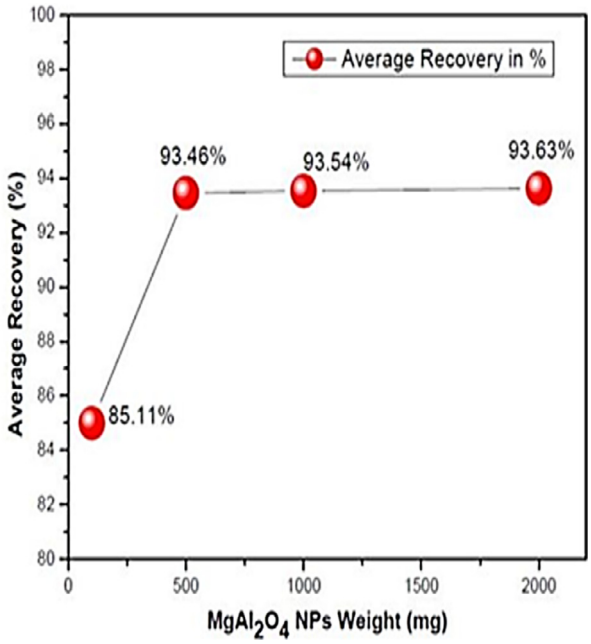

Fig. 9. Effect of sorbent in pre-concentration of dimethomorph.

medium. The adsorbent would also have a positive or negative charge on its surface, respectively, below or above pHzpc. The results of this analysis have shown that the pHzpc value of the adsorbent used was 5.5 as shown. The results of this analysis have shown that the pHzpc value of the adsorbent used was 5.5 as solution pH is an important parameter that can affect the medium surface charge and the solute ionization equilibrium.

4. Conclusion

The superior efficacy of dimethomorph against plant–fungal infections and its continual usage have led to contamination of ground and surface water systems. Most of the commercial formulations of dimethomorph are water-soluble and wettable powders, possessing water solubility and surface runoff because of which the mobility in water during

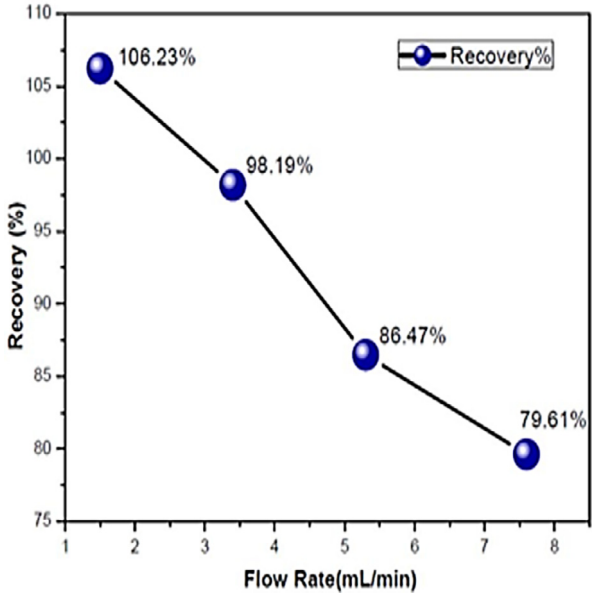

Fig. 10. Effect of flow rate in pre-concentration of dimethomorph.

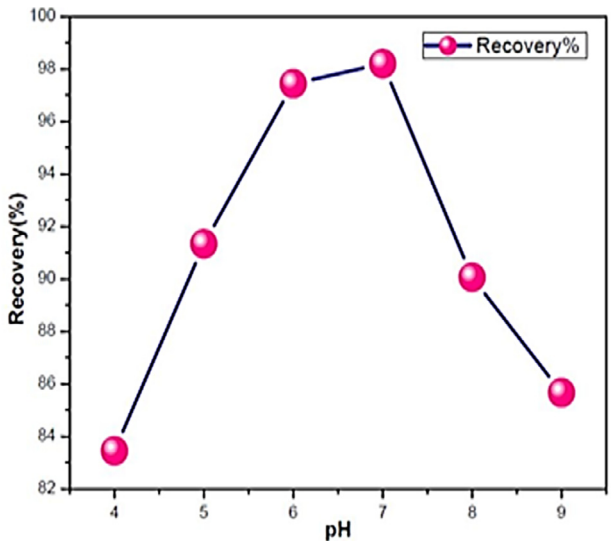

Fig. 11. Effect of pH in pre-concentration of dimethomorph.

agricultural practices increases drastically. The remediation of dimethomorph is inevitable to hinder biomagnification. In the present study, $MgAl_2O_4$ NPs were used for the nanoremediation of dimethomorph. To the best of our knowledge, we report for the first time the determination and extraction of dimethomorph residues in water using a $MgAl_2O_4$ NPs-packed cartridge. The use of the $MgAl_2O_4$ NPs-packed cartridge showed improved results when compared with the commercially available SPE-C18 cartridge. The developed method was found to possess higher accuracy and precision for the detection of dimethomorph, which possesses no buffer salts affecting the column and instrument efficiency. In future prospects, more insights on the surface morphology studies of $MgAl_2O_4$ will add more insights into the effective removal of pesticides such as dimethomorph.

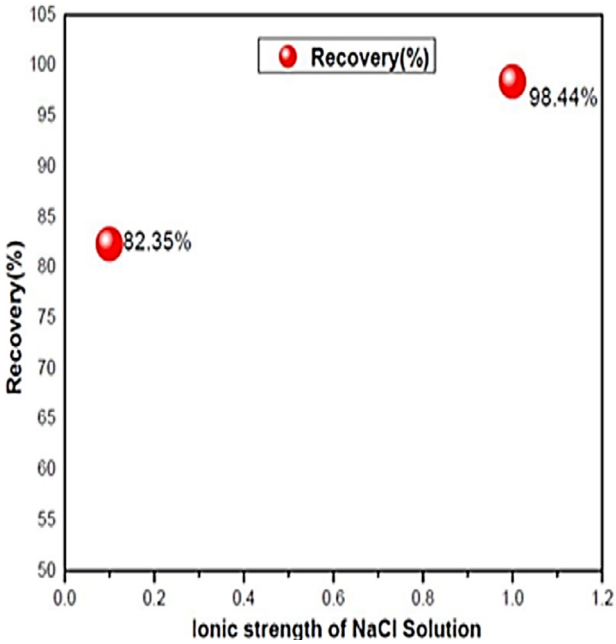

Fig. 12. Effect of ionic strength in pre-concentration of dimethomorph.

CRediT authorship contribution statement

Tentu Nageswara Rao: Conceptualization, Data curation, Visualization, Formal analysis, Investigation, Methodology, Resources, Software. **A.P.B. Balaji:** Conceptualization, Data curation, Visualization, Formal analysis, Investigation, Methodology, Resources, Software. **Mani Panagal:** Conceptualization, Data curation, Visualization, Formal analysis, Investigation, Methodology, Resources, Software. **Botsa Parvatamma:** Conceptualization, Data curation, Visualization, Formal analysis, Investigation, Methodology, Resources, Software. **Bharathi Selvaraj:** Methodology, Resources and Software Supervision, Project administration, Writing - original draft, Writing - review & editing. **Saravanan Panneerselvam:** Methodology, Resources and Software Supervision, Project administration, Writing - original draft, Writing - review & editing. **Wilson Aruni:** Methodology, Resources and Software Supervision, Project administration, Writing - original draft, Writing - review & editing. **Kumaran Subramanian:** Methodology, Resources and Software Supervision, Project administration, Writing - original draft, Writing - review & editing. **Pugazhvendan Sampath Renuga:** Methodology, Resources and Software Supervision, Project administration, Writing - original draft, Writing - review & editing. **Sivakumar Pandian:** Methodology, Resources and Software Supervision, Project administration, Writing - original draft, Writing - review & editing.

Declaration of competing interest

The authors declare that they have no known competing financial interests or personal relationships that could have appeared to influence the work reported in this paper.

Acknowledgment

The Authors express their heart full thanks to Management of Sathyabama Institute of Science and Technology, Chennai, for constant support.

References

Aktar, W., Sengupta, D., Chowdhury, A., 2009. Impact of pesticides use in agriculture: Their benefits and hazards. Interdiscip. Toxicol. 2, 1–12.

Apparao, K., Surendra Babu, M.S., Nageswara Rao, T., Basaveswara Rao, M.V., 2015. A. novel method for determination of topramezone residues in maize. Orient. J. Chem. 31.

Balaji, A.P.B., Mishra, P., Suresh Kumar, R.S., Ashu, A., Margulis, K., Magdassi, S., Mukherjee, A., Chandrasekaran, N., 2015. The environmentally benign form of pesticide in hydrodispersive nanometric form with improved efficacy against adult mosquitoes at low exposure concentrations. Bull. Environ. Contam. Toxicol. 95, 734–739.

Balaji, A.P.B., Sastry, T.P., Manigandan, S., Mukherjee, A., Chandrasekaran, N., 2017. Environmental benignity of a pesticide in soft colloidal hydrodispersive nanometric form with improved toxic precision towards the target organisms than non-target organisms. Sci. Total Environ. 579, 190–201.

Bapat, G., Labade, C., Chaudhari, A., Zinjarde, S., 2016. Silica nanoparticle based techniques for extraction, detection, and degradation of pesticides. Adv. Colloid Interface Sci. 237, 1–14.
Blankenberg, A.G.B., Haarstad, K., Braskerud, B.C., 2007. Pesticide retention in an experimental wetland treating non-point source pollution from agriculture runoff. Water Sci. Technol. 55, 37–44.
Cecchin, I., Reddy, K.R., Thomé, A., Tessaro, E.F., Schnaid, F., 2017. Nanobioremediation: Integration of nanoparticles and bioremediation for sustainable remediation of chlorinated organic contaminants in soils. Int. Biodeterioration Biodegrad. 119, 419–428.
Chandradass, J., Kim, K.H., 2010. Effect of precursor ratios on the synthesis of $MgAl_2O_4$ nanoparticles by a reverse microemulsion method. J. Ceram. Process. Res. 11, 96–99.
Damalas, C.A., Eleftherohorinos, I.G., 2011. Pesticide exposure, safety issues, and risk assessment indicators. Int. J. Environ. Res. Public Health 8, 1402–1419.
Daraghmeh, A., Shraim, A., Abulhaj, S., Sansour, R., Ng, J.C., 2007. Imidacloprid residues in fruits, vegetables and water samples from Palestine. Environ. Geochem. Health 29, 45–50.
Duvenhage, J.A., Köhne, J.S., 1995. Efficacy of dimethomorph against phytophthora root rot of avocado. South Afr. Avocado Grow. Assoc. Yearb 18, 41–42.
Hasnain, S., Ali, S.S., Uddin, Z., Zafar, R., 2013. Application of nanotechnology in health and environmental research: A review. Res. J. Environ. Earth Sci. 5, 160–166.
Karn, B., Kuiken, T., Otto, M., 2009. Nanotechnology and in situ remediation: A review of the benefits and potential risks. Environ. Health Perspect. 117, 1823–1831.
Kaur, R., Hasan, A., Iqbal, N., Alam, S., Saini, M.K., Raza, S.K., 2014. Synthesis and surface engineering of magnetic nanoparticles for environmental cleanup and pesticide residue analysis: A review. J. Sep. Sci. 37, 1805–1825.
Kuhn, P.J., Pitt, D., Lee, S.A., Wakley, G., Sheppard, A.N., 1991. Effects of dimethomorph on the morphology and ultrastructure of phytophthora. Mycol. Res. 95, 333–340.
Lan, G.X., Xiao, M.Q., Yang, B., Fei, W.P., Li, L.X., 2009. Baseline sensitivity and laboratory mutants of Phytophthora capsici resistant to dimethomorph. Acta Phytopathol. Sinica 39 (6), 630–637.
Moraes, S.L., Rezende, M.O.O., Nakagawa, L.E., Luchini, L.C., 2003. Multiresidue screening methods for the determination of pesticides in tomatoes. J. Environ. Sci. Health B 38, 605–615.
Nakamoto, K., 2009. Infrared and Raman Spectra of Inorganic and Coordination Compounds. Part B: Applications in Coordination, Organometallic, AndBioinorganic Chemistry, sixth ed. Wiley-Interscience, USA.
Pang, Z., Hu, C.M.J., Fang, R.H., Luk, B.T., Gao, W., Wang, F., Chuluun, E., Angsantikul, P., Thamphiwatana, S., Lu, W., et al., 2015. Detoxification of organophosphate poisoning using nanoparticle bioscavengers. ACS Nano 9, 6450–6458.
Paorici, C., Lovergine, N., Prete, P., 2003. Progress in crystal growth and characterization of materials: Preface. Prog. Cryst. Growth Charact. Mater 47, 63–64.
Pourdanesh, F., Jebali, A., Hekmatimoghaddam, S., Allaveisie, A., 2014. In vitro and in vivo evaluation of a new nanocomposite, containing high density polyethylene, tricalcium phosphate, hydroxyapatite, and magnesium oxide nanoparticles. Mater. Sci. Eng. C 40, 382–388.
Rao, K.G., Ashok, C.H., Rao, K.V., 2014. Structural properties of MgO nanoparticles: synthesized by co-precipitation technique. Int. J. Sci. Res. 3 (12), 43–46.
Sharma, A.K., Tiwari, R.K., Gaur, M.S., 2016. Nanophotocatalytic UV degradation system for organophosphorus pesticides in water samples and analysis by Kubista model. Arab. J. Chem. 9, 1755–1764.
Stout, S.J., DaCunha, A.R., Allardice, D.G., 1996. Microwave-assisted extraction coupled with gas chromatography/electron capture negative chemical ionization mass spectrometry for the simplified determination of imidazolinone herbicides in soil at the ppb level. Anal. Chem. 68, 653–658.
Tian, J., Tian, P., Ning, G., Pang, H., Song, Q., Cheng, H., Fang, H., 2015. Synthesis of porous $MgAl_2O_4$ spinel and its superior performance for organic dye adsorption. RSC Adv. 5, 5123–5130.
Yang, L., Zheng, Q., Lin, S., Wang, Y., Zhu, Q., Cheng, D., Chen, J., Zhang, Z., 2020. Dissipation and residue of dimethomorph in potato plants produced and dietary intake risk assessment. Int. J. Environ. Anal. Chem. 1–13.
Zhang, Y., Ma, M., Zhang, X., Wang, B., Liu, R., 2014. J. Alloys Compd. 590, 373.
Zou, N., Gu, K., Liu, S., Hou, Y., Zhang, J., Xu, X., Li, X., Pan, C., 2016. Rapid analysis of pesticide residues in drinking water samples by dispersive solid-phase extraction based on multiwalled carbon nanotubes and pulse glow discharge ion source ion mobility spectrometry. J. Sep. Sci. 39, 1202–1212.

Saudi Journal of Biological Sciences 27 (2020) 975–984

Contents lists available at ScienceDirect

Saudi Journal of Biological Sciences

journal homepage: www.sciencedirect.com

Original article

Isolation, purification and characterization of naturally derived Crocetin beta-D-glucosyl ester from *Crocus sativus* L. against breast cancer and its binding chemistry with ER-alpha/HDAC2

Mudasir A. Mir [a,*], Shabir Ahmad Ganai [b], Sheikh Mansoor [c], Sumira Jan [d], P. Mani [e], Khalid Z. Masoodi [a], Henna Amin [f], Muneeb U. Rehman [g], Parvaiz Ahmad [h,*]

[a] Division of Biotechnology, Sher-e-Kashmir University of Agricultural Sciences and Technology of Kashmir, Shalimar, Srinagar 190025, Jammu and Kashmir, India
[b] Division of Basic Sciences and Humanities, Faculty of Agriculture, SKUAST-Kashmir, Wadura, Sopore 193201, Jammu & Kashmir, India
[c] Division of Biochemistry, Sher-e-Kashmir University of Agricultural Sciences and Technology, Jammu 180009, J&K, India
[d] Division of Basic Science and Humanities, Sher-e-Kashmir University of Agricultural Sciences and Technology of Kashmir, Shalimar, Srinagar 190025, Jammu and Kashmir, India
[e] Department of Biotechnology, Annai College of Arts & Science, Kumbakonam, Tamil Nadu 612503, India
[f] Department of Pharmaceutical Sciences, Faculty of Applied Science and Technology, University of Kashmir, Srinagar, J&K 190006, India
[g] Department of Clinical Pharmacy, College of Pharmacy, King Saudi University, P. O. Box. 2460, Riyadh 11451, Saudi Arabia
[h] Botany and Microbiology Department, College of Science, King Saudi University, P. O. Box. 2460, Riyadh 11451, Saudi Arabia

ARTICLE INFO

Article history:
Received 7 December 2019
Revised 15 January 2020
Accepted 16 January 2020
Available online 27 January 2020

Keywords:
Saffron
Floral biowastes
Antioxidant
Crocetin beta-D-glucosyl ester
Breast cancer
Molecular docking

ABSTRACT

Saffron plant (*Crocus sativus* L.) is being used as a source of saffron spice and medicine to cure or prevent different types of diseases including cancers. We report the isolation, characterization of bioactive small molecule ([crocetin (β-D-glucosyl) ester] from the leaf biowastes of saffron plant of Kashmir, India. MTTC assay and Bio-autography aided approach were used to assess anti-oxidant activity and anti-cancer properties of crocin (s) against DPPH free radical and breast cancer cell line respectively. Crocetin beta-D-glucosyl ester restrained proliferation of human breast adeno-carcinoma cell model (MCF-7) without significantly affecting normal cell line (L-6). Further studies involving molecular mechanics generalized born surface area and molecular docking showed that crocetin beta-D-glucosyl ester exhibits strong affinity for estrogen receptor alpha and histone deacetylase 2 (crucial receptors involved in breast cancer signalling) as evidenced by the negative docking score and binding free energy (BFE) values. Therefore, crocetin beta-D-glucosyl ester from *Crocus sativus* biowastes showed antiproliferative effect possibly by inhibiting estrogen receptor alpha and HDAC2 mediated signalling cascade.

1. Introduction

Breast cancer has implications in excess women mortality rates, the main reasons of it being lack of safer, effective, non-toxic and potent treatment options (Latosińska and Latosińska, 2013). In the United States, there were 40,290 breast cancer related deaths seen during 2015, more than 2.8 million breast cancer women cases were identified during 2016, among which 40,610 were estimated to die at the end of 2017, and around 255,180 new cases will be diagnosed (Bray et al., 2018). Breast cancer majorly occurs due to genetic mutations (85%) specifically mutations of *BRCA1* and *BRCA2* genes. There are mounting evidences that natural products that are currently used in traditional medicinal system, possess a wider range of chemical diversity and potential to be the source for modern drug discovery (Gilbert et al., 1997), because natural bioactive molecules are curative as compared to inherently

Abbreviations: DPPH, 2,2-diphenyl-1-picrylhydrazyl; MTT, 3-(4,5–dimethyl thiazol–2–yl)–5–diphenyltetrazolium bromide; FBS, Fetal Bovine serum; DMEM, Dulbecco's Modified Eagle's Medium; UV, Ultra violet; TLC, Thin layer chromatography; FTIR, Fourier-transform infrared spectroscopy; NMR, Nuclear magneticresonance; LC-MS/MS, Liquid chromatography–mass spectrometry.

* Corresponding authors.
E-mail addresses: mudasirbt@gmail.com (M.A. Mir), parvaizbot@yahoo.com (P. Ahmad).

Peer review under responsibility of King Saud University.

Production and hosting by Elsevier

https://doi.org/10.1016/j.sjbs.2020.01.018
1319-562X/

destructive chemotherapy and cytotoxic drugs (Sodde et al., 2015). This has lead deep passion among scientists towards identification of pharmaceutically important novel plant based compounds as compared to synthetic drugs that could intervene to modulate different signalling cascades so as to circumvent breast cancers (Bishayee et al., 2011; Sodde et al., 2015). Although, breast cancer related mortality incidences have declined to some extent due to currently employed therapies such as selective radiotherapy, chemotherapy, estrogen receptor modulators (or SERMs) in the form of tamoxifen, raloxifene and class of aromatase inhibitors (letrozole, exemestane, anastrozole). However, not all races are getting benefitted from such aggressive therapies because, the patients generally relapse or suffer from side effects such as menopausal complications, blood clots, osteoporosis, etc (Cuzick et al., 2013). It is an established fact that an alternative mode of treatment is vital either singly or in combinatorial drug regimen against breast cancers (Bray et al., 2018). These grim facts and figures tempt scientists to desperately look for newer, safer, cheaper and potent natural sources of anticancer drugs that were being used in different ethno-medicinal systems from past several centuries due to their better tolerability (Tiwari, 2011). These measures if proved scientifically will result to tackle this unmet medical condition using alternative natural drug therapy.

Crocus sativus L. (*Crocus sativus* var. Cashmerianus Royle) is considered as a legendary, highly remunerative cash crop, being source of luxury spice known as saffron. Among the world's total saffron production of 205 tons, Iran contributes 160 tons (~80%), Jammu and Kashmir, India contributes around 8–10 tons (~5%), Greek 4–6 tons (~3%), Morocco 0.8–1 ton (~0.5%), Spain 0.3 to 0.5 ton (~0.25%) and rest is contributed by other countries (Fernández, 2004). It is economically very important medicinal spice, possessing fabulous ethno-pharmacological potential. Saffron plant has a rich history of being used in various folk medicinal systems (Traditional Indian, Iranian and Azerbaijani) to cure or prevent different types of diseases including cancer (Samarghandian and Borji, 2014; Mollazadeh et al., 2015; Hire et al., 2017; Khorasanchi et al., 2018). The production of small quantity of saffron leave behind huge quantities of least priced bio-wastes in the form of tepals, leaves, stamen etc. These biowastes could play source of lead compounds for food and pharmaceutical industries, as they have potential medicinal properties including cytotoxic, antioxidant, antifungal etc. (Mir et al., 2014). The outcome of proper scientific evaluation of different organs of this species is anticipated to find new bioactive molecules against various cancer types, as they possess different types of yellowish carotenoids (Crocins). Crocin molecules being the main constituent of saffron extract is a family of carotenoids that constitutes 6–30% in terms of saffron total dry matter, the concentration of which depends upon growing conditions**,** variety and processing methods (Melnyk et al., 2010; Mollazadeh et al., 2015). Apart from stigmatic portion of *C. sativus* which is an important source of bioactive constituents, there is a growing zeal among natural product researchers to study other least explored tissue types of this plant species including leaves so as to isolate the potential phytocompounds responsible for anticancer properties (Mousavi et al., 2009; Lu et al., 2015).

There are marvellous biological properties attributed towards crocin(s) such as antioxidant, as it increases glutathione peroxidase and superoxide dismutase activity that helps in the detoxification of free radicals (Bathaie and Sajjadi, 2017) also these molecules act as chemo preventive agents (Bathaie and Sajjadi, 2017). Moreover, crocins reported much effective against wide range of malignant cells both *in-vitro* and *in-vivo* e.g. HeLa, HL60 (Ashrafi et al., 2005; Jalili et al., 2015; Jiang et al., 2018), MCF-7, MDA-MB-231, adenocarcinoma HT-29 (Melnyk et al., 2010), AGS-gastric adenocarcinoma (Bhandari, 2015), HT-29, Caco-2, CEM/ADR5000, HepG2, LAPC-4, CWR22, DU145, L1210/P3888 Leukemia, Sarcoma S-180, HT-29, C26 colon carcinoma, BxPC-3, TC-1, SKOv3, A549 (Bathaie et al., 2014; Bathaie and Sajjadi, 2017). Hence, crocins molecules possess important biological properties such as antioxidant, anticancer, chemo prevention etc. (Liakopoulou-Kyriakides and Kyriakidis, 2002; Melnyk et al., 2010; Bathaie et al., 2014; Kim et al., 2014). Crocins do not compromise safety of normal cells as they are non-toxic and non-mutagenic agents with potential to treat different cancer types by modulating various signalling pathways (Abdullaev and Espinosa-Aguirre, 2004; Bhandari, 2015; Milajerdi et al., 2016).

Crocin and crocetin exist in *Crocus*. They are the chemical components with antioxidative properties primarily responsible for the color of the stigmas of *Crocus sativus* L. (Saffron). Crocetin is a carotenoid dicarboxylic acid with 20 carbon atoms and it is the core of crocin. Crocin, in general term, includes Crocin-I (Crocetin-di-beta -D-gentiobiosyl ester), Crocin-II (Crocetin-beta-D-gentiobiosyl-beta-D-glucosyl ester), Crocin-III (Crocetin-mono-beta-D-gentiobiosyl ester), Crocin-IV (beta-D-monoglucoside ester of monomethyl alpha-crocetin), Crocetin-di-(beta-D-glucosyl) ester, Crocetin-mono-beta -D-glucosyl ester. Crocin mainly exists in *trans*-form, but can also present in *cis*-form in minor amount. Crocetin beta-D-glucosyl ester has antioxidant properties, (Bathaie and Sajjadi, 2017) also these molecules act as chemo preventive agents (Bathaie and Sajjadi, 2017). Moreover, Crocetin have been reported to act against malignant cells both *in-vitro* and *in-vivo* e.g. HeLa, HL60 (Ashrafi et al., 2005; Jalili, et al., 2015; Jiang, et al., 2018),

Estrogen receptor alpha has potent implications breast cancer which is quite evident from the fact that it is over-represented in majority of such cancers. Estrogen provoked breast cancer signalling is mediated by estrogen receptor alpha and due to these reasons this receptor has remained the central focus in anti-estrogen breast cancer therapy. Besides breast cancer signalling is epigenetically fuelled by HDAC2 over activity. On the whole these findings suggest that estrogen receptor alpha and HDAC2 are the promising targets for breast cancer drugs and therapy. Taking these grim facts into account we selected these two receptors for our molecular docking and binding affinity studies.

It is important to validate the ethno-medicinal properties of plant derived drugs, because there is a huge scientific and industrial interest mushrooming within pharmaceutical domain to isolate and characterize plant based bioactive compounds including carotenoids (Crocins) that could open up novel ways to treat and prevent cancer incidences specifically breast cancers (Sajjadi and Bathaie, 2017). Saffron plant has a rich history of being used as a folklore medicine to prevent and treat different diseases including cancers which has been recently studied through various scientific evidences (Melnyk et al., 2010; Khorasanchi et al., 2018). Therefore, the current study attempted to isolate and characterize crocin(s) from leaves of *Crocus sativus* which are considered to be the major and cheaper biowastes of saffron industry. The antioxidant and antiproliferative properties were undertaken using *in-vitro* and *in-silico* based combinatorial approach.

2. Materials and methods

2.1. Plant material collection, authentication and processing

The leaves of *Crocus sativus* var. *Cashmerianus* were collected from saffron karewas of Pampore Kashmir, India (1574 m above sea level) during March 2019 and were shade dried. The authentication of sample was done by an expert taxonomist and the voucher specimen of the same was deposited at Kashmir university herbarium (KASH) under accession number KASH-1733. The dried samples were subjected to grinding into fine powder and phyto-

chemical extraction through maceration was carried out using petroleum ether as an organic solvent (Tiwari, 2011).

2.2. Chemicals and solvents

The chemicals and reagents including 2,2-diphenyl-1-picrylhydrazyl (DPPH), 3-(4,5–dimethyl thiazol–2–yl)–5–diphenyl tetrazolium bromide (MTT) were procured from Sigma Aldrich, USA. Pre-coated TLC aluminum sheets from Analtech, Inc, Germany. 60–120 mesh size silica gel, Fetal Bovine serum (FBS), Phosphate Buffered Saline (PBS), Dulbecco's Modified Eagle's Medium (DMEM), Trypsin. EDTA, Glucose, MHA medium, PDB medium, solvents and antibiotics were procured from Hi-Media Laboratories Ltd., Mumbai. UV–Vis spectrophotometer (Chemito Technologies, India), FT-IR spectrums (Perkin Elmer, MA, USA), NMR spectrometer (Bruker) and mass spectra's were recorded using WATERS-Q-TOF Micromass.

2.3. Biological materials and culture medium

MCF-7 (Human breast carcinoma cell line) and L-6 (Normal rat muscle cell line) were obtained from National Centre for Cell Sciences (NCCS), Pune, India. DMEM medium containing 10% inactivated Fetal Bovine Serum (FBS), streptomycin (100 g/ml), amphotericin B (5 g/ml) and penicillin (100 IU/ml) with humidified atmosphere of 5% CO_2 was maintained at 37 °C until confluent and was used for the culture of cell stock. Later, the dissociation of the cells was done using TPVG (Trypsin Phosphate Versene Glucose) solution containing 0.2% trypsin, 0.02% EDTA, 0.05% glucose in PBS and 25 cm^2 culture flasks were used to grow the stock cultures.

2.4. Localization, isolation and purification of Crocin (s)

Bioautography: The identification of biologically active compounds was localized by DPPH/antioxidant TLC bioautography assay (Cannell, 1998; Sarker et al., 2006). Briefly extract was applied on TLC plates as a spot using capillary tube at the concentration of 100 μg/ml. The plates were dried, immersed in 0.2% DPPH solution in methanol and left for half an hour. The appearance of white, yellow spots against a purple background indicates antioxidant activity. The isolation of crocetin beta-D-glucosyl ester using column chromatography, followed by preparative thin layer chromatography on pre-coated TLC plates of 20 × 20 cm (Kalimuthu et al., 2011). Briefly, a glass column of 5 cm diameter and 70 cm length was packed with activated 400 g silica gel slurry (Silica gel was dried at 100 C with mesh size of 60–120; Merk India) dissolved in petroleum ether. The crude extract (10 g) was dissolved in minimum quantity of toluene, followed by adsorption onto 20 g of silica gel, the solvent was allowed to evaporate and then the silica bound sample was placed at the top of the already packed silica gel column. The mobile phase toluene: acetone: water: acetic acid (16:2:2:2) was allowed to elute the column using increase in polarity in different ratios at fraction of 5 ml volume were collected, evaporated using rotary evaporator at controlled temperature of 40–50 °C. The identity of the fractions was examined by TLC on silica gel coated aluminum sheets (UV 254, Macherey/Nagel GmbH & co. Duren Germany). The developed plate was dried, exposed to iodine vapors (spots marked) and finally derivatized with anisaldehyde reagent (10 ml sulphuric acid + ice cooled mixture of methanol & 20 ml acetic acid + 1 ml anisaldehyde). The fractions that showed the same UV/Vis spectrum (Cannell, 1998) as well as same TLC development profiles (Color and RF Value) were pooled together and concentrated to dryness under reduced pressure using rotary evaporator. The column sub fractions were purified using preparative pre-coated TLC plates via bioautography approach. The experiment was repeated several times till the purity of the compound was assured by aiming that compound is present as a single spot.

The identification of biologically active compounds were localized by DPPH-Antioxidant TLC Bioautography assay (Cannell, 1998; Sarker et al., 2006). The isolation of crocetin beta-D-glucosyl ester was carried out using preparative thin layer chromatography on pre-coated TLC plates of 20 × 20 cm and also by silica gel based column chromatography (Kalimuthu et al., 2011). All the scrapped spots were collected and dissolved in highly soluble solvents (ethanol, methanol and DMSO). The solution was subjected to centrifugation to remove silica gel pellet, supernatant was collected and solvent evaporated using rotary evaporator. The physical properties of purified compounds were noted down e.g. color, solubility &R_f values.

2.5. Structural elucidation of Crocin(s)

The purified molecule was characterized for structural elucidation using various spectroscopic hyphenated techniques such as FT-IR (Assimiadis et al., 1998), UV–Vis (Cossignani et al., 2014), NMR (Yilmaz et al., 2010), MS-MS (Kalimuthu et al., 2011; Montoro et al., 2012) and the data was compared with previously published literature.

2.6. Free radical scavenging (DPPH) bioautography assay

The antioxidant activity of isolated compound was further tested using TLC based qualitative assay described by Sarker et al. (2006) with minute modifications. Briefly, respective compounds were applied on TLC plates as a spots using capillary tubes at the concentration of 100 μg/ml. The plates were dried, immersed in 0.2% of DPPH solution in methanol and left for half an hour. The appearance of white-yellow spots against a purple background indicates antioxidant activity.

2.7. Antiproliferative assay

Cytotoxicity studies were performed by MTT assay as described in the previous literature (Sarker et al., 2006). Briefly, Crocetin beta-D-glucosyl ester small molecule was dissolved in distilled DMSO (0.1%) and stock solution of 1 mg/ml concentration was made using DMEM supplemented with 2% inactivated FBS. The solution so obtained was sterilized by filtration. The serial dilutions were made to prepare different concentrations of the extract (31.25, 62.5, 125, 250, 500, 1000 μg/ml) to carry out cytotoxic studies. The monolayer cell culture was trypsinized and using DMEM containing 10% FBS, the cell count was adjusted to 1.0×10^5 cells/ml. 0.1 ml of the diluted cell suspension (approximately 10,000 cells) was added to each well of the 96 well microtitre plate, and DMSO (0.1%) without crocetin beta-D-glucosyl ester was considered as negative control, the cell suspension was kept at 37 °C for 24 h. The supernatant was flicked off and monolayer so obtained was once washed with medium followed by addition of 100 μl of different test concentrations to the partial monolayer in microtitre plates (Tarsons India Pvt. Ltd., Kolkata, India). The plates were then incubated at 37 °C for 72 h in 5% CO_2 atmosphere and observations were noted every 24 h interval using microscopic examination (20×). The solution in the wells was discarded after 3 days of incubation and to each well 50 μl of MTT in PBS was added. The plates were then gently shaken and incubated for 3 h at 37 °C in 5% CO_2 atmosphere. The supernatant obtained was discarded first and then 100 μl of propanol was added. In order to solubilise the formed formazan, the plates were gently shaken and absorbance was measured using a microplate reader at a wavelength of 540 nm. The percentage growth inhibition was calculated

using the following formula and the concentration of test sample needed to inhibit cell growth by 50% (IC_{50}) values was generated from the dose–response curves for both the cell lines (MCF-7 and L-6). All the experiments were carried out in triplicates (n = 3)

$$\% \text{ Growth inhibition} = 100 - \left(\frac{\text{Mean OD of individual test group}}{\text{Mean OD of control group}} \times 100\right)$$

2.8. Ligand preparation

All the ligand molecules were retrieved from PubChem with PubChem CID of 449,459 for 4-hydroxytamoxifen and10368299 for crocetin beta-D-glucosyl ester. The ligand molecules were prepared using the LigPrep of Maestro v11.0 of Schrodinger tool (Van Den Driessche and Fourches, 2017; Van Den Driessche and Fourches, 2018). The ligands were minimized and protonation states were generated using the Epik (Shelley et al., 2007). Moreover, the ligand molecules were desalted and specified chiralities were retained (Ganai et al., 2015). For ligands going to be docked against metalloenzyme HDAC2, metal binding states were also generated.

2.9. Protein preparation

The crystal structures of estrogen receptor alpha and HDAC2 were retrieved from Protein Data Bank with PDB ID 3ERT (Shiau et al., 1998) and 4LY1 respectively (Lauffer et al., 2013). The protein preparation was done by Shrodinger package (Protein Preparation wizard) to certify correctness of the structure (Kalyaanamoorthy and Chen, 2013; Sastry et al., 2013). The hydrogen atoms which were missing were added to these structures and bond orders were properly assigned. The Shrodinger package was utilized to fill the side chains and loops which were missing in the protein (Mir et al., 2014; Lu et al., 2015). Every molecule of water beyond 5 Å was deleted. In the subsequent steps, the redundant protein chains and heteroatoms were also removed. However, the cocrystallized ligands were retained in both structures for subsequent use in grid generation (Mir et al., 2014). Moreover, in HDAC2, the heteroatom Zinc was retained as it serves as a cofactor for the given enzyme. In the next step the structures were optimized, water molecules making less than 3 hydrogen bonds with non-waters were deleted and the structures were subjected to minimization where heavy atoms were converged to 0.30 Å (Harder et al., 2015). In case of both structures grid was specified using the co-crystallized ligand as centroid.

2.10. Pose validation by self-docking

The Protein preparation wizard was employed to prepare estrogen receptor alpha along with its cocrystallized ligand until minimization. Then the separation of the ligand was done and the ligand was redocked to estrogen alpha receptor using the protocol of extra precision flexible docking and the calculation of the root mean square deviation (RMSD) between the native and docked pose was carried out (Sándor et al., 2010).

2.11. Molecular docking

The ligands that were prepared were docked against the grid specified receptors using the extra precision flexible docking protocol. Glide (Grid-based Ligand Docking with Energetics) program of Schrödinger package (Glide v7.3) was used to perform molecular docking (Friesner et al., 2006). The docked scores were obtained from the pose viewer files of docked complexes.

2.12. Molecular mechanics generalized born surface area (MMGBSA)

The binding free energy (BFE) of inhibitors was calculated by using an implicit solvation model, MMGBSA. The docked complexes were used as input and no flexibility was given to receptor (frozen condition. Prime MM-GBSA makes five important energy calculations namely optimized free receptor (Receptor), optimized free ligand (Ligand), optimized complex (complex), receptor from optimized complex, ligand from optimized complex (Lyne et al., 2006). From these energies, MMGBSA free energy of binding is calculated as:

$$\text{MMGBSA dG Bind} = \text{Complex} - \text{Receptor} - \text{Ligand}.$$

3. Results

3.1. Isolation and characterization of [crocetin (β-D-glucosyl) ester]/ Crocetin beta-D-glucosyl ester

Analytical thin layer chromatography (TLC) lead identification of ideal mobile phase (Toluene: acetone: water: acetic acid in the ratio of 16:2:2:2) which gave maximum separation of bands in the crude leaf extracts of *Crocus sativus* (Fig. 1A). The crude petroleum ether extract was subjected to column chromatography using solvents of differential polarities starting from non-polar towards molar polarity index. The polarity of the solvent was increased step up step by 10% towards more polarity index. Seven different fractions so obtained were tested for antioxidant activity, however only one fraction showed marked antioxidant activity against DPPH free radical (Fig. 1B) Post preparative TLC, the study ended up with isolation of a yellow coloured compound from the leaves of *C. sativus.* The weight of compound so obtained was found as 17 mg with R_f value as 0.53. The solubility of purified compound was verified using ethanol, methanol and DMSO, it dissolves completely in all these solvents.

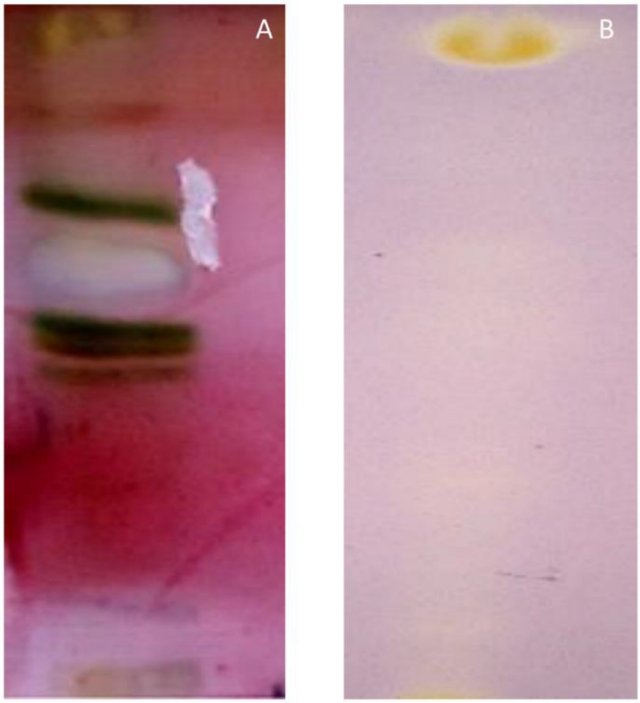

Fig. 1. (A) TLC separation of petroleum ether leaf extract of *Crocus sativus* using mobile phase Toluene: acetone: water: acetic acid (16:2:2:2), (B) Antioxidant TLC Bio autography assay of crocetin beta-D-glucosyl ester using DPPH as free radical.

UV–Vis-spectral data has showed various characteristics absorption bands (Fig. 2A) between 226 and 500 nm i.e. λmax at 260 nm and 437 corresponds to glucosyl ester bonds and all-*trans*-carotenoids respectively. The FT-IR showed bands at wavelength of 3432 cm^{-1} assigned to hydroxyl groups (—OH), 2921, 1463 and 1376 cm^{-1} for C—H, 1728 cm^{-1} for carbonyl group (C=O), 1623 cm^{-1} for C=C group, 1071 cm^{-1} for C—O sugar groups (Fig. 2B). The ^{1}H NMR spectrum of molecule in DMSO solution showed the presence of terminal methyl groups by exhibiting signals at δ 0.89, methylene groups at δ 1.29 and methyl groups attached to the double bonds by exhibiting signals at δ 1.56. Further the bunch of signals between δ 3.00 and 4.00 are due to protons present in the sugar residue. The signals at δ 4.5 and 5.5 are due to the anomeric protons. The couple of signals between δ 6.0 and 7.5 are due to unsaturated protons of crocins. In ^{1}H–^{13}C heteronuclear single quantum coherence (HSQC), signals at δ 14.00 for methyl carbon, between δ 20 and 40 for the carbon atoms attached to the double bond, between δ 50 and 80 for the sugar carbons (Fig. 2C and D). The scan for mass spectrum was run in positive ion mode and molecular mass of isolated compounds was found as 490. Molecular ion EI-MS^{+} (Mass spectroscopy) was observed at m/z = 513 ($[M+Na]^{+}$) along with an additional signal at m/z 328 $[(M+H)\text{-}Glc]^{+}$ (Fig. 2E). The molecule (Fig. 3-PubChem CID-10368299) is identified as crocetin beta-D-glucosyl ester/[crocetin (β-D-glucosyl)ester].

3.2. Crocetin beta-D-glucosyl ester as a significant antioxidant and anticancer agent

The antioxidant activity has revealed appearance of white-yellow spots against purple background on TLC antioxidant bioautographic plates, indicating significant antioxidant property (Sarker et al., 2005). The antiproliferative activity of crocetin beta-D-glucosyl ester against MCF-7 cell line has showed statistically significant inhibitory effect in a dose dependent way with IC_{50} value of 628.36 ± 15.52 μg/ml ($P < 0.001$) (Table 1). The percentage cytotoxicity effect ranged from 18.5 ± 0.8% to 61.57 ± 1.90% at different concentrations of crocetin beta-D-glucosyl ester molecule (31.25–1000 μg/ml). The microscopic examination has revealed that crocetin beta-D-glucosyl ester treated MCF-7 cells have showed cellular apoptotic characteristics such as cell shrinkage, reduced cytoplasm, cytoplasmic vacuole like areas, pyknotic nuclei, nuclear condensation and fragmentation (altered nuclear morphology), while as L-6 cell line has intact cell distribution along with no-marked apoptotic or anti-proliferative characteristics (Figs. 4 and 5).

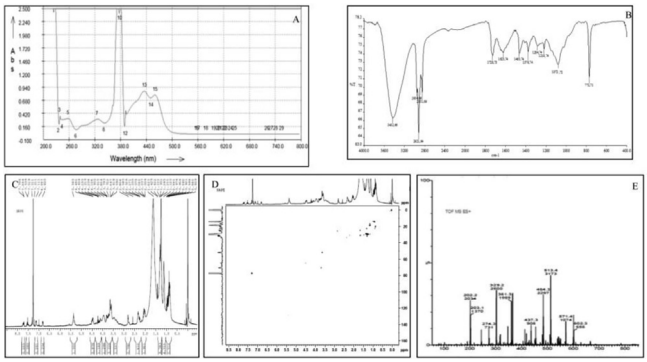

Fig. 2. A Spectrums of crocetin beta-D-glucosyl ester based on hyphenated spectroscopic techniques (A) UV–Vis (B) FT-IR (C) ^{1}H NMR (D) ^{13}C NMR (E) Mass spectrum (ESI^{+}). The interpretation of the obtained data along with its comparison with literature data has characterized the compound as [crocetin (β-D-glucosyl) ester] (Molecular formula = $C_{26}H_{34}O_{9}$).

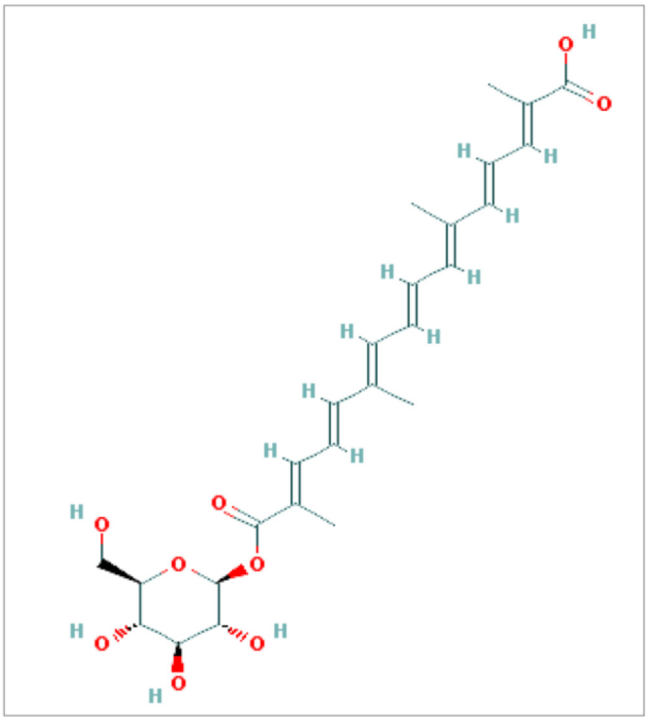

Fig. 3. Structure of crocetin (β-D-glucosyl) ester retrieved from Pubchem (CID-10368299).

3.3. Molecular docking simulation studies showed crocetin beta-D-glucosyl ester shows stronger affinity against estrogen receptor alpha

Before performing molecular docking studies, it is mandatory to validate algorithm for reproducing the crystal pose of ligand. We performed self-docking as described in methods and computational details. The redocked and native pose presented and RMSD of 1.9341 Å thus validating the accuracy of our algorithm to generate correct pose (Ganaiet al., 2015) (Fig. 6). Molecular docking is regarded as the central facet in drug discovery. Our studies showed crocetin beta-D-glucosylester inhibits the defined receptor as evidenced by the docking score of −6.9 against the defined receptor (Table 2). Crocin −1 showed affinity towards HDAC2 receptor as determined by a docking score of −6.61.

3.4. Binding free energy calculation confirmed the predictions of molecular docking

The relative binding affinity of ligands especially of a congeneric series is calculated by MMGBSA, an implicit solvation model (Ganai et al., 2015; Kalyaanamoorthy and Chen, 2013). Crocin −1 showed BFE value of −80.3 Kcal/mol towards estrogen receptor alpha. The binding free energy value of (−61.7441 Kcal/mol) against HDAC2 was shown by the defined inhibitor (Table 2).

3.5. Crocetin beta-D-glucosyl ester shows similar but not identical interaction profile as that of 4-hydroxytamoxifen

In order to gain insights regarding the interaction profile of crocetin beta-D-glucosyl ester against estrogen receptor alpha we generated ligand–protein contacts up to 4 Å from docked complexes. While 4-hydroxytamoxifen showed 3 hydrogen bonding interactions with Arg 394, Glu 353, Asp 351, crocetin beta-D-glucosyl ester portrayed 4 hydrogen bonding interactions with Arg 394, Leu 536

Table 1
Cytotoxicity effect of *Crocus sativus* derived Crocetin beta-D-glucosylesteron on MCF-7 cell line.

Compound name	Test conc. (μg/ml)	% Cytotoxicity* MCF-7	IC_{50}(μg/ml)* MCF-7	% Cytotoxicity* L-6	IC_{50}(μg/ml)* L-6
[crocetin (β-D-glucosyl) ester]	1000	61.57 ± 1.90	628.36 ± 15.52	21.80 ± 0.90	>1000
	500	47.89 ± 2.0		21.45 ± 1.2	
	250	40.78 ± 0.95		20.8 ± 0.75	
	125	35.46 ± 1.2		20.45 ± 0. 5	
	62.5	24.34 ± 1.0		17.89 ± 1.32	
	31.25	18.5 ± 0.8		17.20 ± 0.45	

* **% Cytotoxicity**: The statistically significant percentage of cell toxicity ($p < 0.05$) in MCF-7 cells upon progressive increase of dose (31.25, 62.5, 125, 250, 500, 1000 μg/ml). **IC_{50}**: Effective concentration of molecules in μg/ml required to achieve 50% growth inhibition of breast cancer cells (MCF-7). Data are representative of three independent experiments (mean ± SD).

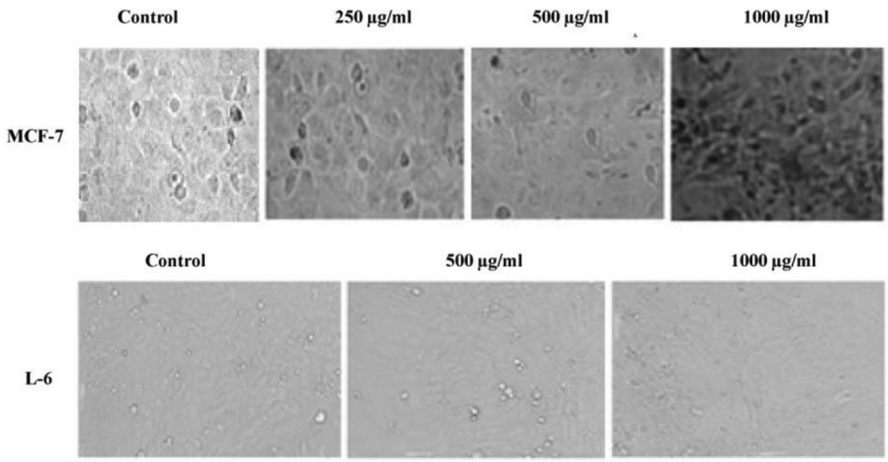

Fig. 4. Cytotoxicity effect of [crocetin (β-D-glucosyl) ester] on cells from MCF-7 cell line. The cells were seeded in 96-well plate (10,000 cells/well) for 24 h, then exposed to 0.1% DMSO based extract of [crocetin (β-D-glucosyl) ester] 1 for 72 h at different concentrations (31.25, 62.5, 125, 250, 500, 1000 μg/ml). The statistically significant concentration dependent cytotoxicity (*P* value = 0.0019) was observed with IC_{50} as 628.36 μg/ml. Data are representative of three independent experiments (mean ± SD). Representative slides of MTT assay for MCF-7 cell line upon treatment with [crocetin (β-D-glucosyl) ester]. The prominent morphological changes are seen in treated cells at concentration gradient of 250, 500, 1000 μg/ml, representing apoptosis. L-6 cell line has not demonstrated any significant levels of cytotoxicity upon treatment by [crocetin (β-D-glucosyl) ester] at 500, 1000 μg/ml concentrations with IC_{50} > 1000 μg/ml. Untreated MCF-7 and L-6 cells act as negative control without any morphological variations. Data are representative of three independent experiments (mean ± SD).

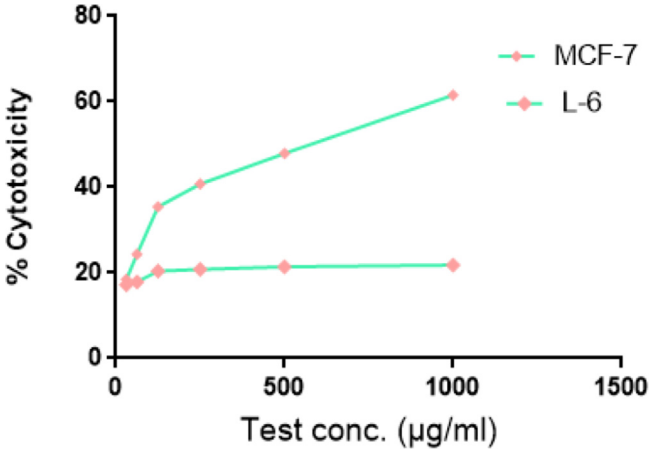

Fig. 5. Relationship between dose of [crocetin (β-D-glucosyl) ester] and % cytotoxicity against MCF and L-6 cell lines at different concentrations (31.25, 62.5, 125, 250, 500, 1000 μg/ml). The statistically significant concentration dependent cytotoxicity (*P* value = 0.0019) was observed with IC_{50} as 628.36 μg/ml. Non-significant levels of cytotoxicity was observed in L-6 cell line.

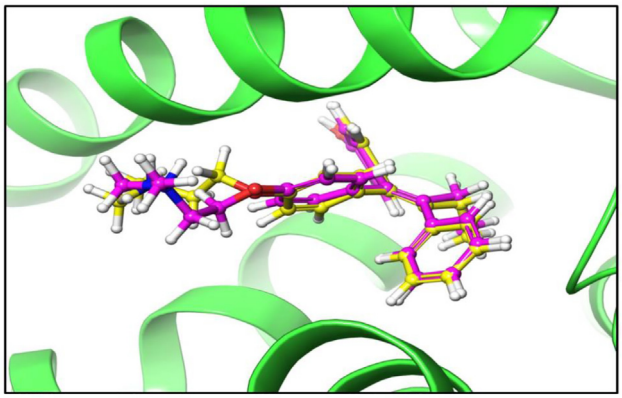

Fig. 6. Pose validation by self-docking. The native ligand of crystal structure was redocked to its host receptor using extra precision flexible docking protocol. The RMSD between native (pink) and redocked (yellow) pose of ligand was found to be 1.9341 Å clearly suggesting that docking algorithm is working correctly.

and Glu 380 (Figs. 6–8). In case of HDAC2 crocetin beta-D-glucosyl ester formed one hydrogen bonding interaction with Pro 211 and one salt bridge with Arg 39 (Fig. 9).

4. Discussion

Globally, breast cancer is the most common cancer type causing cancer related deaths in huge numbers among women and this is the second most cancer type in general. Since 2008 onwards breast

Table 2
Docking scores of Crocetin beta-D-glucosyl esteragainst estrogen receptor alpha and HDAC2.

Ligand	Receptor	Docking score	dGBind(Kcal/mol)
4-hydroxytamoxifen	Estrogen	−14.58	−134.1
Crocin-1	receptor alpha	−6.53	−80.3
Crocin-1	HDAC2	−6.61	−61.7441

cancer induced mortality rate has increased by 14%. Although several dozens of synthetic anticancer drugs have been discovered till date like tamoxifen, raloxifene and class of aromatase inhibitors. Nevertheless, with these treatments patients generally relapse or suffer from side effects such as menopausal complications, blood clots, osteoporosis etc (Cuzick et al., 2013). In contrary, natural products are generally seen as lesser toxic, effective and cheap. The screening of such potential bioactive molecules against breast cancer can open up novel gateway to tackle such therapeutically challenging disease.

There are many plant based potential molecules currently being used in the pharmaceutical industry and about 60% of anti-tumor and anti-infectious drugs which are prescribed worldwide come from plants like vincristrine/vinblastine from *Catharanthus roseus* (Rates, 2001). *Crocus sativus* is source of saffron which is a repository of complex molecules like carotenoids (Crocin, picrocrocin and safranal), glycosides, monoterpenes, aldehydes, anthocyanins, flavonoids, vitamins, amino acids, starch, mineral matter, proteins, gums (Fernández, 2006), chitinase Safchi A (Castillo et al., 2007) and other compounds present in saffron could be responsible for different properties including antioxidant, anticancer, antibacterial, antidiabetic, analgesic, aphrodisiac, sedative, anti-alzheimer's, anti-tussive, anti-convulsant (Bhargava, 2011; Mir et al., 2012; Alhakmani et al., 2013). There are no toxicity reports associated with proper usage of saffron or its extracts because hematological and biochemical studies on the toxicity of saffron has showed that there are no signs of any toxicity found in kidney, liver or bladder (Hamidpour et al., 2014). The previous studies have specified the importance of *Crocus sativus* in traditional and modern therapy including its major components in the form of crocin (s) (Sajjadi and Bathaie, 2017; Khorasanchi et al., 2018; Mykhailenko et al., 2019). However, the biologically active crocin (s) have been isolated from stigmatic portion of saffron plant which is economically a costlier source. The current study therefore attempted to isolate and characterize a bioactive molecule from leaves of saffron plant in the form of crocetin beta-D-glucosyl ester which is a cheaper source. UV–Vis, FT-IR, NMR and mass spectrum of isolated molecule were compared with previous studies which confirmed this molecule as Crocetin beta-D-glucosyl ester (Cossignani et al., 2014; Cagliani et al., 2015). Based on the interpretation of obtained spectral data along with its comparison with literature data, we proposed the molecular formula of isolated compound as $C_{26}H_{34}O_9$ (Fig. 2). This small molecule of crocetin beta-D-glucosyl ester is identified and characterized for the first time from cheaper sources (leaves) of *C. sativus* using hyphenated spectroscopic techniques (Fig. 3). Crocetin beta-D-glucosyl ester has demonstrated significant inhibitory activity against MCF-7 cell line without affecting normal cell line (L-6). Strong strong inhibitory effect of saffron crude extracts against MCF-7 cell lines has been observed earlier with IC_{50} value between 350 and 400 μg/ml (Chryssanthi et al., 2007) which could be due to synergistic effect of multiple compounds present in crude extract. The current investigation has successfully been able to prove that the main chemical player responsible against breast cancer cell lines is Crocetin beta-D-glucosyl ester. The intricate molecular mechanism of crocin molecules against breast cancer is globally still enigmatic, but the most accepted mechanism is that the sugar moiety of crocin(s) plays a vital role in its chemical activities due to in-tense electrostatic potential terminals which makes it as a trap for free radicals. There are other proposed mechanisms of crocin acting against different malignant human cell lines e.g. it strongly binds to histone H1 which induce unknown conformational changes that decreases the interaction between H1 protein with DNA (Ashrafi et al., 2005). Crocin increases tubulin polymerization and microtubule nucleation rate in a concentration dependent manner and it showed downregulation of cyclin D1, p21 and p53 which occurs in breast tumor induced by NMU injection in female rat. They also induce tumor cell apoptosis by down regulating the expression of B-cell lymphoma/leukemia-2 (Bcl-2), survivin, cyclin D1 and up regulating the expression of Bax (decrease Bcl-2/Bax ratio). The action of saffron extract on breast cancer cell line MCF-7 could be by induction of caspase-dependent pathway and exerts proapoptotic effects (Friesner et al., 2006). The evidence of antiproliferative activity of saffron derived crocin molecule against breast cancer cell lines indicates its ethno- pharmacological potential to prevent and treat cancer owing its strong antioxidant potential (Rates, 2001; Samarghandian and Borji, 2014; Harder et al., 2015). Crocin as a candidate chemopreventive agent against HCC. Crocin exhibited anti-inflammatory properties where NF-κB, among other inflammatory markers, was inhibited (Amin, et al., 2016). The folklore medicinal properties of saffron could be thus attributed due to strong radical scavenging activities incoherence

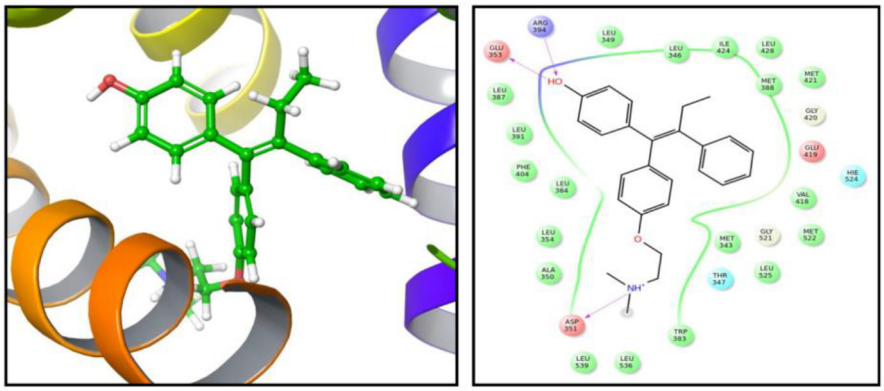

Fig. 7. Residues of estrogen alpha receptor targeted by 4-Hydroxytamoxifen. This inhibitor targets Arg 394, Glu 353 and Asp 351 by forming hydrogen bonding interactions with them.

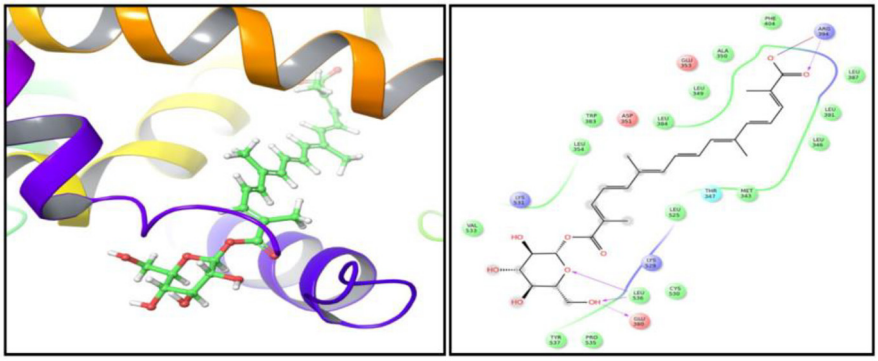

Fig. 8. Residues targeted by Crocetin beta-D-glucosyl ester in estrogen receptor alpha. [crocetin (β-D-glucosyl) ester]-1 forms hydrogen bonding interaction with residues Glu 380, Leu 536 and Arg 394. Moreover, the defined inhibitor forms a salt bridge with Arg 394.

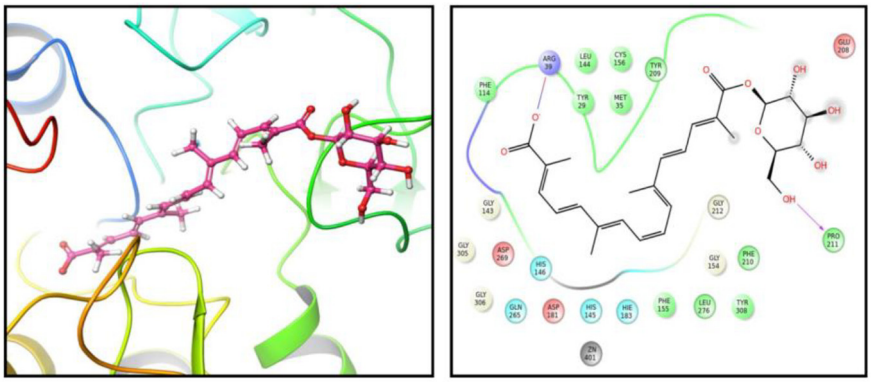

Fig. 9. Crocetin beta-D-glucosyl ester targets HDAC2 residue Pro 211 by forming hydrogen bonding interaction with it and Arg 39 by forming salt bridge.

with proapoptotic effects. The further evaluation of its clinical use would ameliorate saffron demand which will motivate farmers or traditional healers to promote its cultivation at a large scale, an opportunistic approach would lead its constructive conservation and usage sustainably, a way to assure biodiversity preservation. Structure based drug designing studies showed that crocetin beta-D-glucosyl ester has stronger affinity against estrogen receptor alpha, while as binding free energy calculation confirmed the predictions of molecular docking. Molecular docking is regarded as the central facet in drug discovery. It predicts the conformation and orientation of ligand within a target binding site (Ganai et al., 2015). Moreover, accurate structural modelling and correct prediction of activity are its two main aims. We performed molecular docking simulations against estrogen alpha receptor using 4-hydroxytamoxifen as positive control and crocetin beta-D-glucosyl ester as experimental molecule. Moreover, HDAC-2 over-expression is also seen in breast cancer so performed docking studies against this enzyme also (Müller et al., 2013). Thus our molecular docking simulations and binding free energy calculations clearly suggest that crocetin beta-D-glucosyl ester indeed shows affinity towards estrogen receptor alpha and HDAC2 as determined by the negative values of docking score and BFE (Kalyaanamoorthy and Chen, 2013). Crocetin beta-D-glucosyl ester shows similar but not identical interaction profile as that of 4-hydroxytamoxifen and thus it is quite evident that crocetin beta-D-glucosyl ester shows similar but not identical interaction profile against estrogen receptor alpha. The results of this study could act as a base to provide an alternative natural therapy for mitigation of breast cancer incidences.

This study involved the combinatorial stragey for proving the cytotoxic effect of Crocin-1 against breast cancer model along with the possible underlying mechanism being involved. However, this study shedded no light on the higher order clinical studies which will further support the promsing effect of defined molecules. Thus capacious clinical studies are required to facilitate this molecule from bench to bedside.

5. Conclusions

Based on the facts and information provided in the current research article, it is concluded that *Crocus sativus* leaf derived crocetin beta-D-glucosyl ester small molecule is effective against DPPH free radical and against MCF-7 breast cancer cell line. The results of this study could also offer an opportunity to use leaves of *Crocus sativus* as cheap source of crocetin beta-D-glucosyl ester for pharmaceutical industry, this would open up new dimensions to prevent and tackle therapeutically challenging breast cancer cases naturally, economically and elegantly compared to conventional drug therapies. It is recommended here that further *in-vitro* and *in-vivo* vigorous studies regarding dose, safety and toxicity of crocetin beta-D-glucosyl ester molecule needs to be undertaken before they could enter into different phases of clinical trials, as a potential alternative against breast cancer.

Acknowledgments

Shabir Ahmad Ganai thanks DST-SERB for financial help in the form of Start Up Grant (YSS/2015/001267). The authors would also like to

extend their sincere appreciation to Researchers Supporting Project Number (RSP-2019/116), King Saud University, Riyadh, Saudi Arabia.

Declaration of Competing Interest

All the authors confirm that there is no conflict of interest.

References

Abdullaev, F., Espinosa-Aguirre, J., 2004. Biomedical properties of saffron and its potential use in cancer therapy and chemoprevention trials. Cancer Detect. Prev. 28, 426–432.

Alhakmani, F., Kumar, S., Khan, S.A., 2013. Estimation of total phenolic content, in–vitro antioxidant and anti–inflammatory activity of flowers of *Moringa oleifera*. Asian Pacific J. Trop. Biomed. 3, 623–627.

Amin, A., Hamza, A.A., Daoud, S., Khazanehdari, K., Al Hrout, A., Baig, B., Chaiboonchoe, A., Adrian, T.E., Zaki, N., Salehi-Ashtiani, K., 2016. Saffron-based crocin prevents early lesions of liver cancer: in vivo, in vitro and network analyses. Recent Patents Anti-Cancer Drug Discovery 11 (1), 121–133.

Ashrafi, M., Bathaie, S., Taghikhani, M., Moosavi-Movahedi, A., 2005. The effect of carotenoids obtained from saffron on histone H1 structure and H1–DNA interaction. Int. J. Biol. Macromol. 36, 246–252.

Assimiadis, M.K., Tarantilis, P.A., Polissiou, M.G., 1998. UV-Vis, FT-Raman, and 1H NMR spectroscopies of cis-trans carotenoids from saffron (*Crocus sativus* L.). Appl. Spectrosc. 52, 519–522.

Bathaie, S., Sajjadi, M., 2017. Comparative study on preventive effect of saffron carotenoids, crocin and crocetin, in NMU-induced breast cancer in rat. Cell J. 19, 94.

Bathaie, S.Z., Bolhassani, A., Tamanoi, F., 2014. Anticancer effect and molecular targets of saffron carotenoids. In: The Enzymes. Elsevier, pp. 57–86.

Bhandari, P.R., 2015. *Crocus sativus* L. (saffron) for cancer chemoprevention: a mini review. J. Trad. Complement. Med. 5, 81–87.

Bhargava, V., 2011. Medicinal uses and pharmacological properties of *Crocus sativus* Linn (Saffron). Int. J. Pharm. Pharm. Sci 3, 22–26.

Bishayee, A., Ahmed, S., Brankov, N., Perloff, M., 2011. Triterpenoids as potential agents for the chemoprevention and therapy of breast cancer. Front. Biosci.: J. Virtual Library 16, 980.

Bray, F., Ferlay, J., Soerjomataram, I., Siegel, R.L., Torre, L.A., Jemal, A., 2018. Global cancer statistics 2018: GLOBOCAN estimates of incidence and mortality worldwide for 36 cancers in 185 countries. CA Cancer J. Clin. 68, 394–424.

Cagliani, L.R., Culeddu, N., Chessa, M., Consonni, R., 2015. NMR investigations for a quality assessment of Italian PDO saffron (*Crocus sativus* L.). Food Control 50, 342–348.

Cannell, R.J., 1998. Natural Products Isolation. Springer Science & Business Media.

Castillo, R., Gómez-Gómez, L., Fernandez, J., 2007. SafchiA is a new class of defence chitinase from saffron (*Crocus sativus* L.). Acta Hortic. 739, 195.

Chryssanthi, D.G., Lamari, F.N., Iatrou, G., Pylara, A., Karamanos, N.K., Cordopatis, P., 2007. Inhibition of breast cancer cell proliferation by style constituents of different Crocus species. Anticancer Res. 27, 357–362.

Cossignani, L., Urbani, E., Simonetti, M.S., Maurizi, A., Chiesi, C., Blasi, F., 2014. Characterisation of secondary metabolites in saffron from central Italy (Cascia, Umbria). Food Chem. 143, 446–451.

Cuzick, J., Sestak, I., Bonanni, B., Costantino, J.P., Cummings, S., DeCensi, A., Dowsett, M., Forbes, J.F., Ford, L., LaCroix, A.Z., 2013. Selective oestrogen receptor modulators in prevention of breast cancer: an updated meta-analysis of individual participant data. Lancet 381, 1827–1834.

Fernández, J.-A., 2004. Biology, biotechnology and biomedicine of saffron. Recent Res. Dev. Plant Sci. 2, 127–159.

Fernández, J.-A., 2006. Anticancer properties of saffron, *Crocus sativus* Linn. Adv. Phytomed. 2, 313–330.

Friesner, R.A., Murphy, R.B., Repasky, M.P., Frye, L.L., Greenwood, J.R., Halgren, T.A., Sanschagrin, P.C., Mainz, D.T., 2006. Extra precision glide: docking and scoring incorporating a model of hydrophobic enclosure for protein− ligand complexes. J. Med. Chem. 49, 6177–6196.

Ganai, S.A., Shanmugam, K., Mahadevan, V., 2015. Energy-optimised pharmacophore approach to identify potential hotspots during inhibition of Class II HDAC isoforms. J. Biomol. Struct. Dyn. 33, 374–387.

Gilbert, B., Ferreira, J.L., Almeida, M.B.S., Carvalho, E.S., Cascon, V., Rocha, L.M., 1997. The official use of medicinal plants in public health. Ciênc. cult. (Säo Paulo) 49, 339–344.

Hamidpour, R., Hamidpour, S., Hamidpour, M., Shahlari, M., 2014. Chemistry, pharmacology and medicinal property of sage as a viable agent in the treatment of prostate, pancreatic or other types of cancer. Global J. Med. Res.

Harder, E., Damm, W., Maple, J., Wu, C., Reboul, M., Xiang, J.Y., Wang, L., Lupyan, D., Dahlgren, M.K., Knight, J.L., 2015. OPLS3: a force field providing broad coverage of drug-like small molecules and proteins. J. Chem. Theory Comput. 12, 281–296.

Hire, R.R., Srivastava, S., Davis, M.B., Konreddy, A.K., Panda, D., 2017. Antiproliferative activity of crocin involves targeting of microtubules in breast cancer cells. Sci. Rep. 7, 44984.

Jalili, C., Tabatabaei, H., Kakaberiei, S., Roshankhah, S., Salahshoor, M.R., 2015. Protective role of Crocin against nicotine-induced damages on male mice liver. Int. J. Preventive Med. 6.

Jiang, Z., Gu, M., Liu, J., Li, H., Peng, J., Zhang, Y., 2018. Anticancer activity of crocin against cervical carcinoma (HeLa cells): Bioassessment and toxicity evaluation of crocin in male albino rats. J. Photochem. Photobiol., B 180, 118–124.

Kalimuthu, S., Latha, S., Selvamani, P., Rajesh, P., Balamurugan, B., Chandrasekar, T., 2011. Isolation, characterization and antibacterial evaluation on long chain fatty acids from *Limnophila polystachya* Benth. Asian J. Chem. 23, 791.

Kalyaanamoorthy, S., Chen, Y.P.P., 2013. Energy based pharmacophore mapping of HDAC inhibitors against class I HDAC enzymes. Biochim. Biophys. Acta (BBA)-Proteins Proteomics 1834, 317–328.

Khorasanchi, Z., Shafiee, M., Kermanshahi, F., Khazaei, M., Ryzhikov, M., Parizadeh, M.R., Kermanshahi, B., Ferns, G.A., Avan, A., Hassanian, S.M., 2018. Crocus sativus a natural food coloring and flavoring has potent anti-tumor properties. Phytomedicine 43, 21–27.

Kim, S.H., Lee, J.M., Kim, S.C., Park, C.B., Lee, P.C., 2014. Proposed cytotoxic mechanisms of the saffron carotenoids crocin and crocetin on cancer cell lines. Biochem. Cell Biol. 92, 105–111.

Latosińska, J.N., Latosińska, M., 2013. Anticancer drug discovery—from serendipity to rational design. Drug Discovery. IntechOpen.

Lauffer, B.E., Mintzer, R., Fong, R., Mukund, S., Tam, C., Zilberleyb, I., Flicke, B., Ritscher, A., Fedorowicz, G., Vallero, R., 2013. Histone deacetylase (HDAC) inhibitor kinetic rate constants correlate with cellular histone acetylation but not transcription and cell viability. J. Biol. Chem. 288, 26926–26943.

Liakopoulou-Kyriakides, M., Kyriakidis, D., 2002. *Croscus sativus*-biological active constitutents. In: Studies in Natural Products Chemistry. Elsevier, pp. 293–312.

Lu, P., Lin, H., Gu, Y., Li, L., Guo, H., Wang, F., Qiu, X., 2015. Antitumor effects of crocin on human breast cancer cells. Int. J. Clin. Exp. Med. 8, 20316.

Lyne, P.D., Lamb, M.L., Saeh, J.C., 2006. Accurate prediction of the relative potencies of members of a series of kinase inhibitors using molecular docking and MM-GBSA scoring. J. Med. Chem. 49, 4805–4808.

Melnyk, J.P., Wang, S., Marcone, M.F., 2010. Chemical and biological properties of the world's most expensive spice: Saffron. Food Res. Int. 43, 1981–1989.

Milajerdi, A., Djafarian, K., Hosseini, B., 2016. The toxicity of saffron (*Crocus sativus* L.) and its constituents against normal and cancer cells. J. Nutrit. Intermed. Metabol. 3, 23–32.

Mir, M., Rameashkannan, M., Raj, J., Malik, A., Rajesh, T., 2012. Phytochemical and pharmacological profile of *Crocus sativus* L. by-products found in Kashmir. IV International Symposium on Saffron Biology and Technology, 1200, pp. 213–226.

Mir, M.A., Rameashkannan, M., Pala, R.A., 2014. Screening of *Crocus sativus* L. (Saffron) Bio-residues from kashmir as a source of phenols and flavonoids with antioxidant potential. Adv. Biotechnol. Patent. 303.

Mollazadeh, H., Emami, S.A., Hosseinzadeh, H., 2015. Razi's Al-Hawi and saffron (*Crocus sativus*): a review. Iranian J. Basic Med. Sci. 18, 1153.

Montoro, P., Maldini, M., Luciani, L., Tuberoso, C.I., Congiu, F., Pizza, C., 2012. Radical scavenging activity and LC-MS metabolic profiling of petals, stamens, and flowers of *Crocus sativus* L. J. Food Sci. 77, C893–C900.

Mousavi, S.H., Tavakkol-Afshari, J., Brook, A., Jafari-Anarkooli, I., 2009. Role of caspases and Bax protein in saffron-induced apoptosis in MCF-7 cells. Food Chem. Toxicol. 47, 1909–1913.

Müller, B.M., Jana, L., Kasajima, A., Lehmann, A., Prinzler, J., Budczies, J., Winzer, K.-J., Dietel, M., Weichert, W., Denkert, C., 2013. Differential expression of histone deacetylases HDAC1, 2 and 3 in human breast cancer-overexpression of HDAC2 and HDAC3 is associated with clinicopathological indicators of disease progression. BMC Cancer 13, 215.

Mykhailenko, O., Kovalyov, V., Goryacha, O., Ivanauskas, L., Georgiyants, V., 2019. Biologically active compounds and pharmacological activities of species of the genus Crocus: a review. Phytochemistry 162, 56–89.

Rates, S.M.K., 2001. Plants as source of drugs. Toxicon 39, 603–613.

Sajjadi, M., Bathaie, Z., 2017. Comparative study on the preventive effect of saffron carotenoids, crocin and crocetin, in NMU-induced breast cancer in rats. Cell J. (Yakhteh) 19, 94.

Samarghandian, S., Borji, A., 2014. Anticarcinogenic effect of saffron (*Crocus sativus* L.) and its ingredients. Pharmacognosy Res. 6, 99.

Sándor, M., Kiss, R., Keserű, G.r.M., 2010. Virtual fragment docking by Glide: a validation study on 190 protein− fragment complexes. J. Chem. Inf. Model. 50, 1165–1172.

Sarker, S.D., Latif, Z., Gray, A.I., 2006. Natural product isolation. In: Natural products isolation. Springer, pp. 1–25.

Sastry, G.M., Adzhigirey, M., Day, T., Annabhimoju, R., Sherman, W., 2013. Protein and ligand preparation: parameters, protocols, and influence on virtual screening enrichments. J. Comput. Aided Mol. Des. 27, 221–234.

Shelley, J.C., Cholleti, A., Frye, L.L., Greenwood, J.R., Timlin, M.R., Uchimaya, M., 2007. Epik: a software program for pK a prediction and protonation state generation for drug-like molecules. J. Comput. Aided Mol. Des. 21, 681–691.

Shiau, A.K., Barstad, D., Loria, P.M., Cheng, L., Kushner, P.J., Agard, D.A., Greene, G.L., 1998. The structural basis of estrogen receptor/coactivator recognition and the antagonism of this interaction by tamoxifen. Cell 95, 927–937.

Sodde, V.K., Lobo, R., Kumar, N., Maheshwari, R., Shreedhara, C., 2015. Cytotoxic activity of *Macrosolen parasiticus* (L.) Danser on the growth of breast cancer cell line (MCF-7). Pharmacognosy Mag. 11, S156.

Sarker, S.D., Kumarasamy, Y., Shoeb, M., Celik, S., Yucel, E., Middleton, M., Nahar, L., 2005. Antibacterial and antioxidant activities of three Turkish species of the genus. Centaurea, Oriental Pharmacy and Experimental Medicine 5, 246–250.

Tiwari, P., Kumar, B., Kaur, M., Kaur, G., Kaur, H., 2011. Phytochemical screening and extraction: a review. Int. Pharm. Sci. 1, 98–106.
Van Den Driessche, G., Fourches, D., 2017. Adverse drug reactions triggered by the common HLA-B* 57: 01 variant: a molecular docking study. J. Cheminf. 9, 13.
Van Den Driessche, G., Fourches, D., 2018. Adverse drug reactions triggered by the common HLA-B* 57: 01 variant: virtual screening of DrugBank using 3D molecular docking. J. Cheminf. 10, 3.
Yilmaz, A., Nyberg, N.T., Mølgaard, P., Asili, J., Jaroszewski, J.W., 2010. 1 H NMR metabolic fingerprinting of saffron extracts. Metabolomics 6, 511–517.

ISSN 2515-8260 Volume 07, Issue 09, 2020

DIABETES DETECTION USING TONGUE IMAGE USING EXTRACTION OF GLOBAL FEATURES AND DECISION TREE

Dr.S.Bhuvaneswari,

Asst.Prof.,Dept.of BCA., Annai College of Arts and Science. Kumbakonam, Tamil Nadu.
E-mail:drbhuvanamagesh@gmail.com
(Affiliated to Bharathidasan University, Tiruchirappalli)

Abstract:

In the day to day working of people, the tongue plays a significant role.The tongue is an organ connected to each other parts.Diabetics classification using tongue images are described in this study. Diabetes detection using tongue image using extraction of texture and random forestis described in this study.Initially, the input tongue images are given to global feature for feature extraction and finally, the decision treeclassifieris used for classification. Experimental results show the performance of proposed system using texture and RFC.

Keywords:Diabetes detection, Tongue images, Decision tree Classifier, Global feature

Introduction:

Tongue images for feature extraction and diagnostic statistical analysis [1]. A relationship between tongue color and different tongue color distributions can be obtained with various typological tongue characteristics, such as red points or petechial points. Color distributions. Diabetes identification diabetic diabetic retinopathy with tongue tone, texture and geometry characteristics [2].Eight blocks' texture values strategically placed on the tongue surface are used to describe the nine language texture characteristics by an extra mean of all eight blocks.

System of tongue therapies for successful area extraction and tongue coating classification [3]. Local minimum over tongue shading, local miniatures or color difference detection edges, and smoothing edges where downsampling is done to decrease calculation time, histogram balancing and edge enhancement, which produces the segmented area, and then color components of the region are saturated into hues.Medical optical tongue image analysis with a new ColorChecker language [4]. A color gamut is defined on the basis of a broad image tongue dataset.

Colorimetric functional research in language diagnostic teaching [5]. The cluster analysis approach was used to obtain various forms of tongue color from the cluster centers. Tongue contours automated selection and monitoring [6]. In an established location without disturbing speech to stabilize the head and assist the transducer under the chin.

In this study, diabetes detection using tongue image using extraction of global feature and decision tree classifieris discussed. The rest of the paper is organized as follows; Section 2 describes the materials and methods. Experimental results and discussion are described in section 3. The last section concludes the proposed system.

Methods and Materials:

The input tongue images are given to global featurefor extraction of features and for the prediction of normal and abnormal tongue images for diabetes detection using decision tree classifier.

Global feature extraction:

A feature is a piece of information on the quality of an image in computer vision and image processing; usually if any aspect of the image has certain properties. Unique images structures like dots, edges or artefacts can be features.Texture provides information on the colors or intensity of an image in the spatial arrangement. Texture is defined by the spatial intensity distribution in a district.The extraction of features improves the accuracy of learned models by eliminating features from input data. The general system process reduces data dimensionality by deleting the redundant information. Naturally, preparation and speed of inference are improved.

Texture analysis refers to the texture content characterization of the regions in an image. Texture analyse aim to measure intuitive consistency defined as a function of spatial variations in pixel intensities, in terms of such as rough, smooth, silky or bumpy.

Decision Tree Classification:

Decision Tree is one of the most understandable and common classification algorithms. It can be used for classification as well as regression problems. Decision trees are splitting a node by several algorithms into two or more subnodes. The formation of subnodes increases their homogeneity. The decision tree divides the nodes into all variables and selects the division which results in most homogenous subnodes.

Usually, a decision tree begins with one node that branches into potential outcomes. Each of these results leads to more nodes that link to other possibilities. There was a mistake. A decision node, represented by a square, shows an option and the final result of a decision path shows an end node.

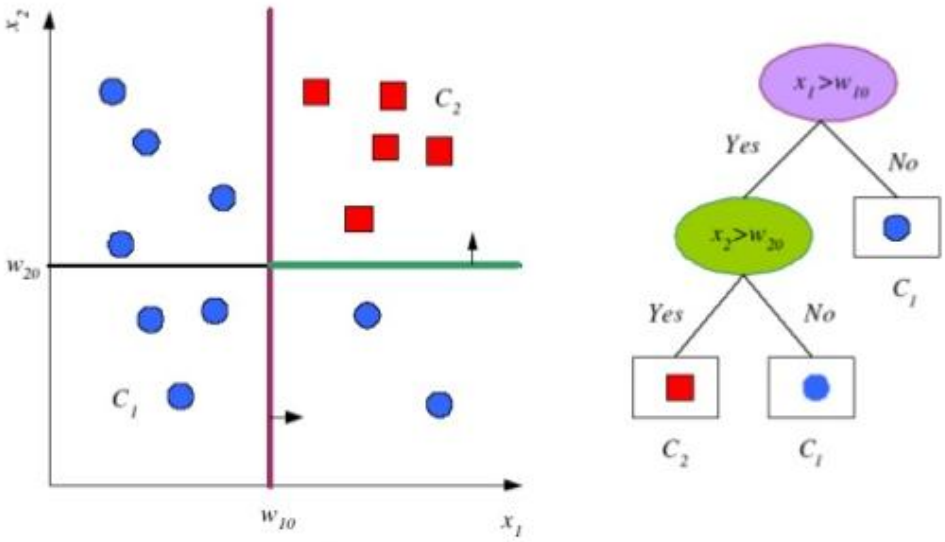

Figure 1 Workflow of Decision tree classifier

Results and Discussion:

The performance of diabetes detection is made by using tongue images. The sample tongue images in the database are shown in figure 2.

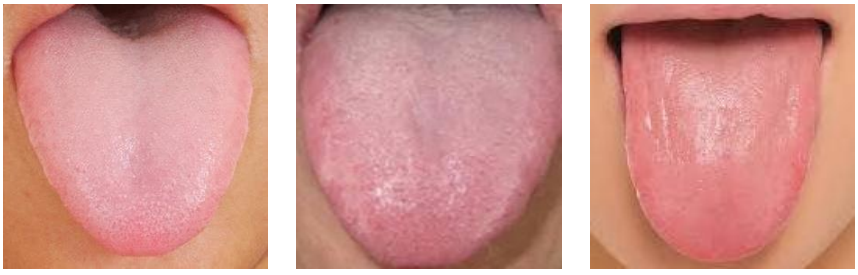

(a) Normal Tongue images

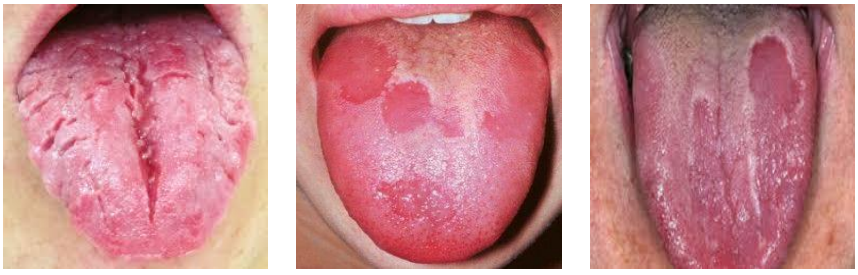

(b) Abnormal Tongue images

Figure 2Sample tongue images

Initially, the tongue images are given to global feature extraction method for the detection of diabetes. The colour of different tongue images predicts the presence of diabetes in patients. Figure 3 shows the performance of diabetic detection using tongue images.

(a) Original image

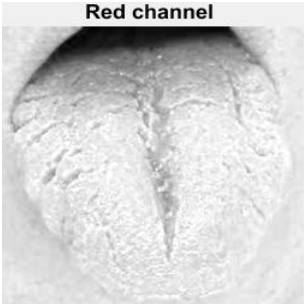

(b) Red Channel

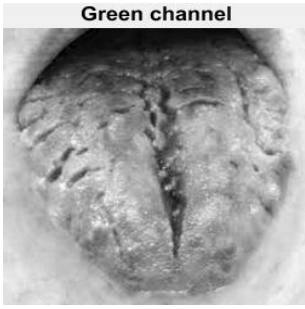

(c) Green Channel

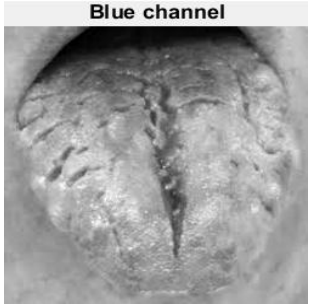

(d) Blue Channel

Figure 3Performance of diabetes detection using tongue images

Initially, the global features are used for feature extraction. The color of the tongue identifies the diabetes detection in the human. Finally,decision tree classifier is used for classification. Table 1 shows the performance of proposed system.

Table 1 Performance of diabetic detection using texture features and RFC

	Accuracy (%)	**Sensitivity (%)**	**Specificity (%)**
Normal images	95	94	93
Abnormal images	93	92	91

From the above table, it is observed that the classification accuracy of normal tongue image is 95% and also its sensitivity and specificity are 94% and 95%. Whereas, the classification accuracy of abnormal tongue images is 93% and its sensitivity and specificity are 92% and 91% by using global features and decision tree classifier.

Conclusion:

Diabetes detection using tongue image using extraction of global and decision tree is presented in this study. The texture features and decision treeareused for the prediction of diabetes using tongue images. The colour of tongue is used to identify the diabetes. Initially, the normal and abnormal images are given to feature extraction by using global features. Then the prediction is made by using decision tree classifier for the identification of diabetes using tongue images. Finally, the colour of the tongue identifies the diabetes. Then the classification accuracy of normal abnormal tongue images is 95% and 93% using RFC.

Reference:

[1] Wang, X., Zhang, B., Yang, Z., Wang, H., & Zhang, D. (2013). Statistical analysis of tongue images for feature extraction and diagnostics. IEEE Transactions on Image Processing, 22(12), 5336-5347.

[2] Zhang, B., Kumar, B. V., & Zhang, D. (2013). Detecting diabetes mellitus and nonproliferative diabetic retinopathy using tongue color, texture, and geometry features. IEEE transactions on biomedical engineering, 61(2), 491-501.

[3] Kim, K. H., Do, J. H., Ryu, H., & Kim, J. Y. (2008, November). Tongue diagnosis method for extraction of effective region and classification of tongue coating. In 2008 First Workshops on Image Processing Theory, Tools and Applications (pp. 1-7). IEEE.

[4] Zhao, Q., Zhang, D., & Zhang, B. (2016, October). Digital tongue image analysis in medical applications using a new tongue ColorChecker. In 2016 2nd IEEE International Conference on Computer and Communications (ICCC) (pp. 803-807). IEEE.

[5] Liang, R., Wang, Z. P., Yang, X. Y., Ren, Y. J., Zhang, Y., & Yao, X. Y. (2012, August). Applied research of colorimetric in the teaching of tongue diagnosis. In 2012 International Symposium on Information Technologies in Medicine and Education (Vol. 1, pp. 426-429). IEEE.

[6] Akgul, Y. S., Kambhamettu, C., & Stone, M. (1999). Automatic extraction and tracking of the tongue contours. IEEE Transactions on Medical Imaging, 18(10), 1035-1045.

[7] Ranganathan, S. (2019). Rain Removal in the Images Using Bilateral Filter. International Journal of MC Square Scientific Research, 11(1), 9-14.

[8] Manahoran, N., & Srinath, M. V. (2017). K-Means Clustering Based Marine Image Segmentation. International Journal of MC Square Scientific Research, 9(3), 26-29.

sciendo

DOI: 10.2478/auoc-2020-0024

Ovidius University Annals of Chemistry Volume 31, Number 2, pp. 152 - 157, 2020

Ultrasound assisted synthesis and pharmacological evaluation of some (*E*)-1,2,3-triphenylprop-2-en-1-ones

Veerendiran MALA,[1] Inbasekaran MUTHUVEL,[2,3] Ganesamoorthy THIRUNARAYANAN[*],[2] Saravanan Palanivel SAKTHINATHAN,[4] Ranganathan ARULKUMARAN,[4] Venkatesan MANIKANDAN,[4] Rajasekaran SUNDARARAJAN,[4] Dakshnamoorthy KAMALAKKANNAN,[4] Ramamurthy SURESH,[4] and Veeramalai USHA[5]

[1]*Department of Chemistry, Annai College of Arts and Science, Kovilacheri, Kumbakonam-612 503, India*
[2]*Department of Chemistry, Annamalai University, Annamalainagar-608 002, India*
[3]*Department of Chemistry, MR Government Arts College, Mannargudi-614 001, India*
[4]*Postgraduate and Research Department of Chemistry, Government Arts College, C-Mutlur-608102, Chidambaram, India*
[5]*Department of Chemistry, University College of Engineering, Panruti-607 106, India*

Abstract. More than 85% yield of (*E*)-1,2,3-triphenylprop-2-en-1-ones were synthesized using disodium hydrogen phosphate (Na_2HPO_4) catalyzed ultrasound assisted aldol condensation of 1,2-diphenylethanone and various substituted benzaldehydes. Synthesized (*E*)-1,2,3-triphenylprop-2-en-1-ones were examined by their spectroscopic data, yield, micro analysis and physical constants. The effect of solvent on the yield was investigated. The pharmacological effects such as antibacterial and antifungal activities of synthesized enones were evaluated with Bauer-Kirby disc diffusion method.

Keywords: triphenyl enones; ultrasonication; disodium hydrogen phosphate; aldol condensation; solvent effect; antimicrobial activity.

1. Introduction

Now-a-days scientist and chemists paid much more attention to ultrasound assisted organic synthesis due to this technique obeyed twelve principle of green chemistry [1, 2]. Conventional synthetic methods need prolonged time for completion of reaction, required expensive catalysts and lower yield obtained. Due to this inconvenient, ultrasound or microwave irradiation are used as alternate source of energy for applied organic synthesis. Application of ultrasound is very vast visible such as chemical synthesis, bio-leaching, chemical leaching of metals and non-metals, polymer degradation, polymerization, luminance, bio-metabolites production and bio-degradation [3, 4]. In industrial views, ultrasound was used for cleaning, welding of melts and plastics, cutting, forming separating, degassing, mixing localizing and atomizing [5]. About 20-100 kHz frequency range of ultrasound was utilized for microbial growth and 24-25 kHz frequency range of ultrasound was suitable for biodegradation and fermentation. Sonication at 1 MHz is suitable for electron spin resonance study with free radicals. Nucleation of protein was done with 100 kHz frequency range of ultrasound. About 0.02 – 20 MHz frequency range of ultrasound was used to therapeutics and enhancement of microbial enzymatic activities [6, 7]. Enones are important basic units for organic building construction, pharmaceutical and industrial applications including non-corrosiveness [8, 9]. Enones exhibits *s-cis* and *s-trans* conformers and possessing *E* and *Z* configurations. These structural conformations are confirmed by infrared and nuclear magnetic resonance spectroscopy [8, 10]. Numerous catalysts employed for ultrasound assisted organic synthesis such as Lewis acids for synthesis of pyrimidine [11], Pd/C assisted Heck reaction for alkenes[12], palladium acetate and Cu assisted biphenyl and heterocycle synthesis [13, 14], $Pd(PPh_3)_4$ catalyst used for alkene synthesis by cross coupling reaction [15], $PdCl_2$ catalyst applied for synthesis of alkenes including ferrocenyl alkenes through Sonogashira coupling [16], phase transfer catalyst employed for amino acid synthesis by Strecker technique [17], Mg metal assisted trimethyl silane synthesis [18], Zn/CH_2I_2 and NaOH assisted cyclopropanation of alkenes [19], I_2 in Zn dust catalyst for β-hydroxy esters [20], Al_2O_3-KCN supported Diels-Alder arylation [21], sulphamic acid catalyzed β-aminocarbonyl compound synthesis [22], Li catalyzed naphthol synthesis from *o*-allyal benzamides [23] and ZSM-5 zeolite catalyzed acrolein synthesis by dehydration of glycerol [24]. Recently, Usha et al. reported good yields of 3-chloro-4-nitrophenyl chalcones synthesized by NaOH catalyzed ultrasound assisted aldol condensation [25]. Literature review shows that, there is no report availed for disodium hydrogen phosphate (Na_2HPO_4) catalyzed ultrasound assisted synthesis of (*E*)-1,2,3-triphenylprop-2-en-1-ones in the past. Hence, the authors taken efforts for the

[*] Corresponding author. *E-mail address*: drgtnarayanan@gmail.com (G. Thirunarayanan)

synthesis of above enones and studied the pharmacological effects by Bauer-Kirby [26] disc diffusion method.

2. Experimental

2.1. Materials and methods

Chemicals and solvents used in this research work were procured from Sigma-Aldrich Chemical company Bangalore India. Nutrient broth, Mueller Hinton agar, potato dextrose agar, Tween-80 solution and other materials required have been purchased from Himedia, Mumbai, India. Melting points of synthesized enones are found in Raga Tech. make electrical melting point apparatus and are uncorrected. The UV λ_{max} (nm) absorption was measured in spectral grade methanol using Shimadzu-1650 UV spectrophotometer. Avatar–Nicolet-330 FT-IR spectrophotometer was used for recording infrared spectra of all enones in KBr discs. NMR Spectra of all α, β-unsaturated ketones under investigation were recorded using Bruker 400MHz Spectrometer. Frequencies range of 400 and 125 MHz was applied for recording ^{1}H and ^{13}C spectra in deuterated $CDCl_3$ solvent and TMS as standard. Thermo Fennigan CHN analyzer was used for micro analysis estimation. Shimadzu mass spectrometer was used for recording mass spectra of all compounds.

Microorganisms such as *Bacillus subtilis, Micrococcus luteus, Staphylococcus aureus, Escherichia coli, Pseudomonas aeruginosa, Aspergillus niger* and *Trichoderma viride* were received and maintained at the Research laboratory, Post Graduate and Research Department of Chemistry, Government Arts and Science College, Chidambaram. Ampicillin and Michanazole are employed as standard drug for this measurement. The stock cultures have been stored in the cooler machine for further studies.

2.2. General procedure for synthesis of (E)-1,2,3-triphenylprop-2-en-1-ones

A mixture of equimolar quantities of substituted benzaldehydes (1 mmol) and 1,2-diphenylethanone (1 mmol), 1 M Na_2HPO_4 (0.3 mL) and 10 mL of ethanol were ultrasonication in ultrasound bath at 40 Hz (Citizen Ultra Sonicator, 40 Hz, 120W, 240V, AC) for 10-15 minutes (Scheme 1) in room temperature. After the completion of the reaction, as monitored by thin layer chromatogram, the resulting precipitate was filtered and washed with cold water. The product appeared as pale-yellow solid. Then this was recrystallized using ethanol afforded glittering solids and kept in a desiccator.

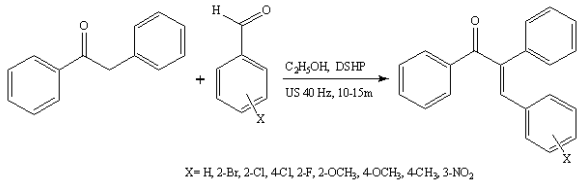

Scheme 1. Synthesis of (*E*)-1,2,3-triphenylprop-2-en-1-ones by ultrasonication.

2.3. Evaluation of antimicrobial activities

Antimicrobial activities such as antibacterial and antifungal activities of synthesized (*E*)-1,2,3-triphenylprop-2-en-1-ones were measured using the standard Bauer-Kirby [26] disc diffusion method by means of measurement of the diameter (mm) of zone of inhibition as reported in our earlier work [27].

3. Results and discussion

In our synthetic organic chemistry research laboratory, we attempt to synthesis some (*E*)-1,2,3-triphenylprop-2-en-1-ones by ultrasonicated aldol condensation of 1,2-diphenylethanone and substituted benzaldehydes in presence of Na_2HPO_4. In this condensation, electron-donating substituted benzaldehydes gave higher yields than electron-withdrawing substituted benzaldehydes. For this condensation, the authors studied the effect of solvents on the yield in both ultrasonication and conventional heating method. Various solvents such as acetonitrile, dichloromethane, dioxane, ethanol, methanol and tetrahydrofuran employed in this condensation under the same condition as mentioned in the experimental section. Both the methods, ethanol medium gave higher yields than other solvents. Dioxane and acetonitrile medium gave lower yields in ultrasonication and conventional heating methods.

Table 1. Effect of solvents on the yields (%) in ultrasonication and conventional heating aldol-condensation methods.

Entry	X	ACN		DCM		DO		EtOH		MeOH		THF	
		USM	CHM	USM	CHM	USM	CHM	USM	CHM	USM	CHM	USM	CHM
1	**H**	66	44	72	56	63	52	86	74	73	58	74	69
2	**2-Br**	64	40	69	52	60	52	81	76	68	50	72	68
3	**2-Cl**	64	46	68	57	62	48	82	75	69	54	73	70
4	**4-Cl**	61	44	68	56	54	47	84	71	69	53	70	67
5	**2-F**	62	41	70	58	60	53	82	70	68	50	69	66
6	**2-OCH_3**	68	45	76	61	58	49	88	80	74	59	77	73
7	**4-OCH_3**	68	44	75	61	60	52	87	79	74	58	76	72
8	**4-CH_3**	62	43	73	59	55	46	85	77	71	57	74	71
9	**3-NO_2**	44	37	55	41	40	38	80	69	63	46	67	65

ACN: Acetonitrile; DM: Dichloromethane; DO: Dioxane; EtOH: Ethanol; MeOH: Methanol; THF: Tetrahydrofuran
USM: Ultrasonication method (Time: 10-15 minutes); CHM: Conventional heating method (Time: 5 hours)

The effect of solvents on the yield was presented in Table 1. Both the methods gave more than 37% yields. From this observation, Na_2HPO_4 is suitable catalyst for the aldol-condensation of substituted benzaldehydes and 1,2-diphenylethanone. All synthesized enones were characterized by their physico-chemical constants, yield, micro analysis and spectroscopic data. From the infrared spectra, the νCO *s-cis* and *s-trans* stretches of enones absorbed in the frequency range of 1691.16 - 1594.62 cm^{-1} and corresponding conformers are shown in Figure 1.

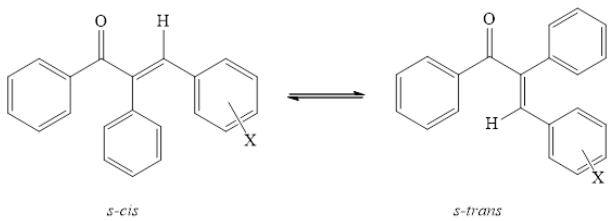

Figure 1. The *s-cis* and *s-trans* conformers of (*E*)-1,2,3-triphenylprop-2-en-1-ones.

Similarly, the deformation modes of νCH_{ip}, CH_{op} and $C{=}C_{op}$ stretches absorbed in the frequency ranges of 1089.78 - 1179.82, 756.21 - 761.88 and 495.71 - 569.75 cm^{-1}. The chemical shifts δH_β proton of all enones obtained in the range of 7.511 - 8.53 ppm. The chemical shifts of δCO, C_α and C_β carbons of (*E*)-1,2,3-triphenylprop-2-en-1-ones appeared in the range of 197.04 - 202.83, 133.07 - 137.35 and 139.47 - 142.29 ppm. The complete characterization data of synthesized (*E*)-1,2,3-triphenylprop-2-en-1-ones (**1-9**) are furnished as below.

(*E*)-1,2,3-Triphenylprop-2-en-1-one (1): Pale yellow glittering solid; Yield: 86%; m.p. 103-104 (100-101) °C [28]; UV λ_{max} (nm): 296; IR (ν, cm^{-1}): 1668.43 ($CO_{s\text{-}cis}$), 1597.06 ($CO_{s\text{-}trans}$), 1089.78 (CH_{ip}), 761.88 (CH_{op}), 495.71 ($C{=}C_{op}$); ^1H NMR (δ, ppm): 7.051 (s, 1H, H_β), 6.944 - 7.492 (m, 15H, Ar-H); ^{13}H NMR (δ, ppm): 197.04 (CO), 134.07 (C_α), 140.09 (C_β), 125.73 - 139.93 (Ar-C); Anal (%). Calcd. for M.F. $C_{21}H_{16}O$ (284): C, 88.70; H, 5.57. Found: C, 88.73; H, 5.52; Mass (m/z): 284 [M^+], 207, 179, 130, 118, 105, 102, 91, 77, 53, 41, 28, 24.

(*E*)-3-(2-Bromophenyl)-1,2-diphenylprop-2-en-1-one(2): Yellow solid; Yield: 81%; m.p. 90-91 °C; UV λ_{max} (nm): 330; IR (ν, cm^{-1}): 1654.35 ($CO_{s\text{-}cis}$), 1594.62 ($CO_{s\text{-}trans}$), 1173.31 (CH_{ip}), 760.54 (CH_{op}), 569.65 ($C{=}C_{op}$); ^1H NMR (δ, ppm): 7.713 (s, 1H, H_β), 7.023-7.504 (m, 14H, Ar-H); ^{13}H NMR (δ, ppm): 196.05 (CO), 136.022 (C_α), 141.99 (C_β), 124.33-138.90 (Ar-C); Anal (%). Calcd. for M.F. $C_{21}H_{15}BrO$ (363): C, 69.44; H, 4.16. Found: C, 69.46; H, 4.12; Mass (m/z): 363[M^+], 365 [M^{2+}], 285, 283, 257, 207, 180, 178, 168, 156, 130, 118, 105, 102, 91, 77, 53, 41, 28, 24.

(*E*)-3-(2-Chlorophenyl)-1,2-diphenylprop-2-en-1-one(3): Pale yellow solid; Yield: 82%; m.p. 76-77 °C; UV λ_{max} (nm): 298; IR (ν, cm^{-1}): 1653.23 ($CO_{s\text{-}cis}$), 1594.92 ($CO_{s\text{-}trans}$), 1176.65 (CH_{ip}), 756.62 (CH_{op}), 547.22 ($C{=}C_{op}$); ^1H NMR (δ, ppm): 8.053 (s, 1H, H_β), 7.431-7.792 (m, 14H, Ar-H); ^{13}H NMR (δ, ppm): 197.46 (CO), 133.82 (C_α), 142.29 (C_β), 125.03-139.83 (Ar-C); Anal (%). Calcd. for M.F. $C_{21}H_{15}ClO$ (319): C, 79.12; H, 4.74. Found: C, 79.08; H, 4.71; Mass (m/z): 319 [M^+], 321 [M^{2+}], 283, 213, 207, 194, 164, 124, 111,102, 91, 77, 53, 41, 35, 28, 24.

(*E*)-3-(4-Chlorophenyl)-1,2-diphenylprop-2-en-1-one(4): Pale yellow solid; Yield: 84%; m.p. 76-77 °C; UV λ_{max} (nm): 304; IR (ν, cm^{-1}): 1646.12 ($CO_{s\text{-}cis}$), 1618.54 ($CO_{s\text{-}trans}$), 1179.82 (CH_{ip}), 757.12 (CH_{op}), 567.63 ($C{=}C_{op}$); ^1H NMR (δ, ppm): 7.871 (s, 1H, H_β), 7.031-7.791 (m, 14H, Ar-H); ^{13}H NMR (δ, ppm): 197.13 (CO), 133.07 (C_α), 142.30 (C_β), 123.230-139.905 (Ar-C); Anal (%). Calcd. for M.F. $C_{21}H_{15}ClO$ (319): C, 79.12; H, 4.74. Found: C, 79.16; H, 4.69; Mass (m/z): 319 [M^+], 321 [M^{2+}], 283, 241, 213, 207, 194, 164, 154, 124, 111, 105, 102, 91, 77, 53, 41, 35, 28, 24.

(*E*)-3-(2-Fluorophenyl)-1,2-diphenylprop-2-en-1-one(5): Pale yellow solid; Yield: 82%; m.p. 81-82 °C; UV λ_{max} (nm): 311; IR (ν, cm^{-1}): 1674.32 ($CO_{s\text{-}cis}$), 1648.37($CO_{s\text{-}trans}$), 1176.41 (CH_{ip}), 758.75 (CH_{op}), 548.04 ($C{=}C_{op}$); ^1H NMR(δ, ppm): 7.734 (s, 1H, H_β), 7.183-7.7102 (m, 14H, Ar-H); ^{13}H NMR (δ, ppm): 202.83 (CO), 137.35 (C_α), 140.68 (C_β), 124.11-139.02 (Ar-C); Anal(%). Calcd. for M.F. $C_{21}H_{15}FO$ (302): C, 83.43; H, 5.00. Found: C, 83.46; H, 4.94; Mass (m/z): 302 [M^+], 304 [M^{2+}], 285, 225,207, 197, 194, 178, 148, 108, 105, 102, 95, 91, 77, 53,48, 24, 19

(*E*)-3-(2-Methoxyphenyl)-1,2-diphenylprop-2-en-1-one (6): Pale yellow solid; Yield: 88%; m.p. 189-190 °C; UV λ_{max} (nm): 330; IR (ν, cm^{-1}): 1667.28 ($CO_{s\text{-}cis}$), 1644.62 ($CO_{s\text{-}trans}$), 1177.68 (CH_{ip}), 752.65 (CH_{op}), 525.56($C{=}C_{op}$); ^1H NMR (δ, ppm): 7.921 (s, 1H, H_β), 1.832 (s, 3H, OCH_3), 7.262-7.790 (m, 14H, Ar-H); ^{13}H NMR (δ, ppm): 198.21 (CO), 133.71 (C_α), 141.54 (C_β), 64.38 (OCH_3), 124.02-137.92 (Ar-C); Anal(%). Calcd. for M.F. $C_{22}H_{18}O_2$ (314): C, 84.05; H, 5.77. Found: C, 84.12; H, 5.72; Mass (m/z): 314 [M^+], 299, 283, 207, 194, 132, 120, 107, 105, 91, 77, 53, 48, 31, 24, 15

(*E*)-3-(4-Methoxyphenyl)-1,2-diphenylprop-2-en-1-one(7): Pale yellow solid; Yield: 87%; m.p. 180-181 °C; UV λ_{max} (nm): 325; IR (ν, cm^{-1}): 1691.16 ($CO_{s\text{-}cis}$), 1664.49 ($CO_{s\text{-}trans}$), 1176.47 (CH_{ip}), 753.43 (CH_{op}), 548.79 ($C{=}C_{op}$); ^1H NMR (δ, ppm): 7.952 (s, 1H, H_β), 1.824 (s, 3H, OCH_3), 7.213-7.780 (m, 14H, Ar-H); ^{13}H NMR (δ, ppm): 202.87 (CO), 136.63 (C_α), 141.07 (C_β), 64.51 (OCH_3), 123.22-139.90 (Ar-C); Anal (%). Calcd. for M.F. $C_{22}H_{18}O_2$ (314): C, 84.05; H, 5.77. Found: C, 84.07; H, 5.70; Mass (m/z): 314 [M^+], 299, 283, 237, 209, 207, 194, 160, 132, 120, 107, 105, 91, 89, 77, 53, 48, 31, 24, 15

(*E*)-3-(4-methylphenyl)-1,2-diphenylprop-2-en-1-one(8): Yellow solid; Yield: 85%; m.p. 118-119 °C; UV λ_{max} (nm): 299; IR (ν, cm^{-1}): 1654.14 ($CO_{s\text{-}cis}$), 1630.87 ($CO_{s\text{-}trans}$), 1112.92 (CH_{ip}), 756.21 (CH_{op}), 559.26 ($C{=}C_{op}$); ^1H NMR (δ, ppm): 7.536 (s, 1H, H_β), 2.064 (s, 3H, CH_3), 7.012-7.487 (m, 14H, Ar-H); ^{13}H NMR (δ, ppm): 1697.86 (CO), 136.85 (C_α), 141.36 (C_β), 24.91 (CH_3), 123.22-139.90 (Ar-C); Anal (%). Calcd. for M.F. $C_{22}H_{18}O$ (298): C, 88.56; H, 6.08. Found: C, 88.52; H, 6.02; Mass (m/z): 298 [M^+], 283, 221, 207, 193, 134, 117, 105, 104, 91, 77, 53, 48, 24, 15

(*E*)-3-(3-nitrorophenyl)-1,2-diphenylprop-2-en-1-one(9): Yellow solid; Yield: 80%; m.p. 120-212°C; UV λ_{max} (nm): 320; IR (ν, cm^{-1}): 1672.39 ($CO_{s\text{-}cis}$), 1642.75 ($CO_{s\text{-}trans}$), 1174.23 (CH_{ip}), 756.32 (CH_{op}), 542.91 ($C{=}C_{op}$); ^1H NMR (δ, ppm): 7.821 (s, 1H, H_β), 7.254-7.763 (m, 14H, Ar-H); ^{13}H NMR (δ, ppm): 199.75 (CO), 134.07 (C_α), 139.47 (C_β), 124.70-138.90 (Ar-C); Anal(%). Calcd. for M.F. $C_{21}H_{15}NO_3$ (329): C, 76.58; H, 4.59; N, 4.25. Found: C, 76.62; H, 4.53; N, 4.19; Mass (m/z): 329 [M^+], 283, 252, 224, 207, 194, 178, 135, 122, 105, 104, 91, 77, 54, 48, 24.

3.1. Antibacterial activity

The measured antibacterial activities of substituted (*E*)-1,2,3-triphenylprop-2-en-1-one compounds are shown in Figure 2.

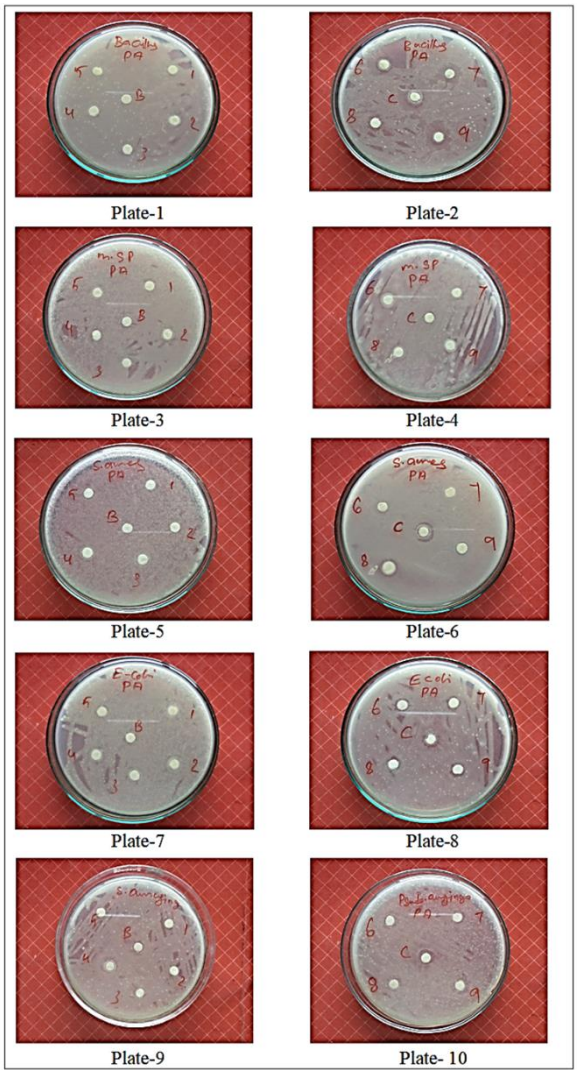

Figure 2. Antibacterial activities of (*E*)-1,2,3-triphenylprop-2-en-1-ones on Petri plates.

The diameter of zone of inhibition (mm) values of antibacterial activity is given in Table 2.

Table 2. Measured antibacterial activities (diameter of zone of inhibition) of (*E*)-1,2,3-triphenylprop-2-en-1-ones

Entry	X	Zone of inhibition (mm)				
		Gram positive bacteria			Gram negative bacteria	
		B. subtilis	*M. luteus*	*S. aureus*	*E. coli*	*P. aeruginosa*
1	H	6	-	-	7	7
2	2-Br	-	6	6	7	-
3	2-Cl	8	8	8	-	-
4	4-Cl	-	-	7	7	8
5	2-F	7	6	6	-	-
6	4-CH_3	10	7	-	7	7
7	2-OCH_3	9	-	6	7	7
8	4-OCH_3	7	7	8	9	8
9	3-NO_2	9	8	9	8	10
Standard	Ampicillin	14	12	12	11	13
Control	DMSO	-	-	-	-	-

Analysis of the zone of inhibition diameter values reveals that the 4-CH_3 substituted compounds shown good antibacterial activity against *B. subtilis* strain. Here the mesomeric and hyper conjugation effects of methyl group enhance the antibacterial activity.

Six more compounds with H (parent), 2-Cl, 2-F, 2-OCH_3, 4-OCH_3 and 3-NO_2 substituents have shown moderate antibacterial activity. Here the +I, -I and F electronegativity of substituents were slightly influences their effects.

Remaining enones have shown poor antibacterial activity. The (*E*)-1,2,3-triphenylprop-2-en-1-ones with 2-Br, 2-Cl, 2-F, 4-CH_3, 4-OCH_3 and 3-NO_2 substituents have shown moderate antibacterial activity against *Micrococcus luteus* stain as similar with above.

The parent (H), 2-OCH_3 and 4-CH_3 substituents shows poor antibacterial activity. Here the mesomeric effect was completely absent.

The enone with 3-NO_2 substituent has shown good antibacterial activity against *Staphylococcus aureus* stain. Here the +I effect of the nitro group enhance the antibacterial activity.

Compounds with 2-Br, 2-Cl, 4-Cl, 2-F, 2-OCH_3 and 4-OCH_3 substituents have shown moderate antibacterial activity. The parent H and 4-CH_3 substituted enones shows poor antibacterial activity. This means that the mesomeric and hyper conjugation effects of methyl group was dies off completely.

The 4-OCH_3 substituted enone shows good antibacterial activity against *Escherichia coli* stain. Here the +R effect of methoxy group enhances the antibacterial activity.

Compounds with H (parent), 2-Br, 4-Cl, 4-CH_3, 2-OCH_3 and 3-NO_2 substituents have shown moderate antibacterial activity. The 2-F and 4-CH_3 substituted enones have no antibacterial activity. This is due to the absence of F, electronegativity, mesomeric and hyper conjugative effects of methyl groups.

The 3-NO_2 substituted compound showed good antibacterial activity against *Pseudomonas aeruginosa* stain. The H (parent), 4-Cl, 4-CH_3, 2-OCH_3 and 4-OCH_3 substituted compounds have shown moderate antibacterial activity. The enones containing 2-F and 4-CH_3 substituents no antibacterial activity and the reason is already stated earlier.

3.2. Antifungal activity

The antifungal activities of the substituted (*E*)-1,2,3-triphenylprop-2-en-1-one compounds are shown in Figure 3.

The diameter of zone of inhibition (mm) values of antifungal activity is given in Table 3.

Analysis of the diameter of zone of inhibition values reveals that the compounds with H (parent), 2-Br, 2-Cl, 2-F, 4-CH_3, 4-OCH_3 and 3-NO_2 substituents have shown moderate antifungal activity against *Aspergillus niger* stain. Here the electronic effects of the substituents such as inductive, electronegative, field and resonance are not delicately reflected. The 4-Cl and 4-CH_3 substituted compounds are inactive and this is due to the +I effect of chlorine atom, hypercoagulation and mesomeric effects of methyl groups are absent.

Synthesized (*E*)-1,2,3-triphenylprop-2-en-1-ones with 2-Cl and 4-Cl substituents have shown good antifungal activity. Here, the +I effect of the choro-

substituents actively enhanced the antifungal activity against *Trichoderma viride* fungal stain.

Compounds with 2-Br, 2-F, 4-CH_3, 4-OCH_3 and 3-NO_2 substituents shows moderate antifungal activity. This is due to the inductive, F, electronegativity, hyper conjugation, mesomeric and resonance effects of the substituents are slightly active. The parent H and 4-OCH_3 substituted ketones inactive and the reason for inactiveness is stated earlier.

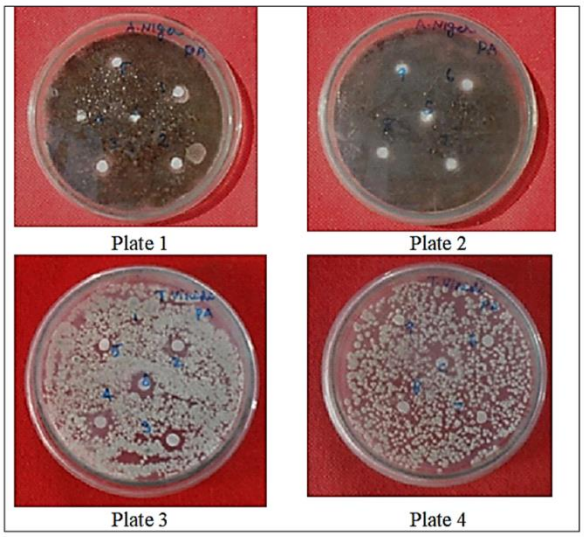

Figure 3. Antifungal activity of (*E*)-1,2,3-triphenylprop-2-en-1-ones on Petri plates.

Table 3. Zone of inhibition(mm) values of antifungal activities of substituted (*E*)-1,2,3-triphenylprop-2-en-1-ones

Entry	X	Zone of inhibition (mm)	
		A. niger	*T. viride*
1	H	8	-
2	2-Br	8	8
3	2-Cl	9	9
4	4-Cl	-	9
5	2-F	7	7
6	4-CH_3	8	7
7	2-OCH_3	-	-
8	4-OCH_3	8	7
9	3-NO_2	9	8
Standard	Miconazole	14	13
Control	DMSO	-	-

4. Conclusions

Authors demonstrated the ultrasonicated aldol condensation for the synthesis of (*E*)-1,2,3-triphenylprop-2-en-1-ones. More than 88% yield was obtained in this condensation. The influence of solvents on then yields were investigated with various solvents in both ultrasonication and conventional heating methods. Overall, the minimum of 37% yield was obtained and hence this condensation was suitable for enone synthesis. The antimicrobial activities of these enones were measured by disc diffusion method. The enones have 4-CH_3, 4-OCH_3 and 3-NO_2 substituted enones showed good antibacterial activities against *B. subtilis*, *E. coli* and *P. aeruginosa* stains. The 2-Cl and 4-Cl substituted enones shows good antifungal activity against *T. viride* fungal stain. Remaining compounds are shown moderate antimicrobial activities. The reason for good, moderate and poor or inactive antimicrobial activities was stated in terms of their electronic effects.

Acknowledgment

Authors thank DST NMR facility, Department of Chemistry, Annamalai University, Annamalainagar-608 002 for recording NMR spectra of all compounds.

Conflict of interest

The authors declare that there is no conflict of interest regarding this research article.

References

[1]. B. Banerjee, Recent developments on ultrasound assisted catalyst-free organic synthesis, Ultrason. Sonochem. 35 (2017) 1–14.

[2]. M.S. Singh, S. Chowdhury, Recent developments in solvent-free multicomponent reactions: a perfect synergy for eco-compatible organic synthesis, RSC Adv. 2 (2012) 4547.

[3]. S. Hatanaka, H. Mitome, K. Yasui, S. Hayashi, Single-bubble sonochemiluminescence in aqueous luminol solutions, J. Am. Chem. Soc. 124 (2002) 10250–10251.

[4]. K.M. Swamy, K.L. Narayana, V.N. Misra, Bioleaching with ultrasound, Ultrason. Sonochem. 12 (2005) 301–306.

[5]. D. Chen, S.K. Sharma, A. Mudhoo, Handbook on applications of ultrasound: sonochemistry for sustainability, CRC Press, 2011.

[6]. S. Vyas, Y.P. Ting, A Review of the application of ultrasound in bioleaching and insights from sonication in (bio)chemical processes, Resources 7 (2018) 3. Doi:10.3390/resources7010003.

[7]. G. Ter Haar, Therapeutic applications of ultrasound, Prog. Biophys. Mol. Biol. 93 (2007) 111–129.

[8]. K. Ranganathan, D. Kamalakkannan, R. Suresh, S. P. Sakthinathan, R. Arulkumaran, R. Sundararajan, V. Manikandan, G. Thirunarayanan, Synthesis, Hammett spectral correlation and evaluation of antimicrobial activities of some substituted styryl 4′-piperidinophenyl ketones, Indian J. Chem. 58B (2019)1131-1143.

[9]. S. Balaji, V. Manikandan, M. Rajarajan, V. Usha, S. Rajalakshmi, P. Venkatachalam, I. Muthuvel, G. Thirunarayanan, Investigation of catalytic activity of solid acidic $FeCl_3$/Bentonite catalyst on the synthesis of some (*E*)-1-(2,4-Dimethylthiazol-5-yl)-3-phenylprop-2-en-1-ones by solvent-free technique, Mat. Today Proc. 22 (2020) 931-936.

[10]. K. Ranganathan, D. Kamalakkannan, R. Suresh, S.P. Sakthinathan, R. Arulkumaran, R. Sundararajan, V. Manikandan, P. Venkatachalam, S. Rajalakshmi, I. Muthuvel, G. Thirunarayanan, Cu^{2+}/Zeolite catalyzed aldol condensation: Greener synthesis of 4′-piperidinophenyl enones, Mat. Today Proc. 22 (2020) 1196-1199.

[11]. D.K. Yadav, M.A. Quraish, Choline chloride. $ZnCl_2$: green effective and reusable ionic liquid for synthesis of 7-amino-2,4-dioxo-5-phenyl-2,3,4,5-

tetrahydro-1H-pyrano[2,3-d]pyrimidine-6-carbonitrile derivatives, J. Mater. Environ. Sci. 5 (2014) 1075-1078.

[12]. S. Bhavani, M.A. Ashfaq, D. Rambabu, M.V. Basaveswara Rao, M. Pal, Ultrasound assisted Mizoroki–Heck reaction catalyzed by Pd/C: Synthesis of 3-vinyl indoles as potential cytotoxic agents, Arabian J. Chem. 12 (2019) 3836-3846.

[13]. N. Basavegowda, K. Mishra, Y.R. Lee, Ultrasonic-assisted green synthesis of palladium nanoparticles and their nanocatalytic application in multicomponent reaction, New J. Chem. 39 (2015) 972-977.

[14]. M.A.P. Martins, C.P. Frizzo, D.N. Moreira, L. Buriol, P. Machado, Solvent-free heterocyclic synthesis, Chem. Rev. 109 (2009) 4140–4182

[15]. S. Puri, B. Kaur, A. Parmar, H. Kumar, Applications of ultrasound in organic synthesis - A green approach, Current Org. Chem. 17 (2013) 1790-1828.

[16]. A.R. Gholap, K. Venkatesan, R. Pasricha, T. Daniel, R.J. Lahoti, K.V. Srinivasan, Copper- and ligand-free Sonogashira reaction catalyzed by Pd(0) Nanoparticles at Ambient Conditions under ultrasound irradiation, J. Org. Chem. 70 (2005) 4869–4872.

[17]. D. Paprocki, A. Madej, D. Koszelewski, A. Brodzka, R. Ostaszewski, Multicomponent Reactions Accelerated by Aqueous Micelles, Front. Chem. 6 (2018) 502. Doi: 10.3389/fchem.2018.00502.

[18]. J.D. Sprich, G.S. Lewandos, Sonochemical removal of adsorbed water and alcohol from magnesium surfaces, Inorg. Chim. Acta 76 (1983) l241-l242.

[19]. O. Repič, S. Vogt, Ultrasound in organic synthesis: cyclopropanation of olefins with zinc-diiodomethane, Tetrahedron Lett. 23 (1982) 2729-2732.

[20]. N.A. Ross, R.A. Bartsch, High-intensity ultrasound-promoted Reformatsky reactions, J. Org. Chem. 68 (2003) 360–366.

[21]. T. Ando, T. Kimura, Ultrasonic organic synthesis involving non-metal solids, Advances in Sonochemistry, ed. T. J. Mason, JAI Press, London, 1991, vol. 2, p. 211.

[22]. H. Zeng, H. Li, H. Shao, One-pot three-component Mannich-type reactions using sulfamic acid catalyst under ultrasound irradiation, Ultrason. Sonochem. 16 (2009) 758–762.

[23]. J. Einhorn, C. Einhorn, J.L. Luche, Ultrasound in organic synthesis 15. Radical cyclisation of o-allyl benzamides via the sono chemically generated radical anions, Tetrahedron Lett. 29 (1988) 2183-2184.

[24]. L. Huang, F. Qin, Z. Huang, Y. Zhuang, J. Ma, H. Xu, W. Shen, Hierarchical ZSM-5 zeolite synthesized by an ultrasound-assisted method as a long-life catalyst for dehydration of glycerol to acrolein, Ind. Eng. Chem. Res. 55 (2016) 7318–7327.

[25]. V. Usha, V. Thangaraj, G. Thirunarayanan, Antimicrobial potent (2E)-3-chloro-4-nitrophenyl chalcones, Indian J. Chem. 56B (2017) 1094-1102.

[26]. A.W. Bauer, W.M.M. Kirby, J.C. Sherris, M. Truck, Antibiotic susceptibility testing by a standardized single disk method, Am. J. Clin. Pathol. 45 (1996) 493-498.

[27]. R. Suresh, S.P. Sakthinathan, D. Kamalakkannan, I. Muthuvel, G. Thirunarayanan, Synthesis and pharmacological evaluation of some benzylidene-4-nitroanilines, Ovidus Univ. Annal. Chem. 31 (2020) 55-59.

[28]. C. Wang, T. Morimoto, H. Kanashiro, H. Tanimoto, Y. Nishiyama, K. Kakiuchi, L. Artok, Rhodium(I)-catalyzed carbonylative arylation of alkynes with arylboronic acids usisng formaldehyde as a carbonyl source, Synlett 25 (2014) 1155-1159.

Received: 08.07.2020
Received in revised form: 20.11.2020
Accepted: 21.11.2020

International Journal of Botany Studies
ISSN: 2455-541X; Impact Factor: RJIF 5.12
Received: 09-10-2020; Accepted: 24-10-2020: Published: 10-11-2020
www.botanyjournals.com
Volume 5; Issue 6; 2020; Page No. 137-140

Evaluation of *in vitro* anticancer activity of *Trianthema decandra* extract

P Suriya[1], R Shalini[2], K Shibula[3], A Amargeetha[4]
[1] Head and Assistant Professor, Department of Biochemistry, Annai College of Arts and Science (Affiliated to Bharathidasan University), Kovilacheri, Kumbakonam, Tamil Nadu, India
[2] Assistant Professor, Department of Biochemistry, Annai College of Arts and Science (Affiliated to Bharathidasan University), Kovilacheri, Kumbakonam, Tamil Nadu, India
[3] Lecturer, Department of Biomedical, Shivaji College of Engineering and Technology, Neyattinkara, Trivandrum, Kerala, India
[4] Assistant professor, Department of Chemistry, Bon Secours College for Women, Affiliated to Bharathidasan University, Vilar Bypass, Thanjavur, Tamil Nadu, India

Abstract
Medicinal plants and its products have been the backbone of traditional system of medicine throughout the world for over thousands of year. It is continued to provide new remedies to human being without any side effects. In the present study, ethanol extract of *Trianthema decandra* leaves were evaluated for their *in-vitro* anticancer activity by making use of cancer cell line (MCF-7 cell line) cytotoxicity by MTT assay. The results obtained indicated that the plant extracts has potent cytotoxic activity on MCF-7. The results of the present findings strengthen the potential of the selected plants as a resource for the discovery of novel anticancer agents.

Keywords: *Trianthema decandra*, leaf, anticancer, MTT assay

1. Introduction

Cancer is one of the most life-threatening diseases, with more than 100 different types occurring due to some molecular changes within the cell. It is the third leading cause of death worldwide following cardiovascular and infectious diseases. It is estimated that more than 1300 Indians die due to cancer. Mortality rate due to cancer is was increased up to 6% (Rajan *et al* 2011) [1]. Breast cancer is the most common cancer among women worldwide. It is a type of cancer where cells in the breast divide and grow without normal control. The incidence of breast cancer has doubled during the past 30 years. 50 to 75 per cent of breast cancers begin in the ducts, 10 to 15 per cent begin in the lobules and a few begin in other breast tissues (Dillon *et al* 2010) [2]. Fortunately, the mortality rate from breast cancer has decreased in recent years with an increased emphasis on early detection and more effective treatments (Sunil *et al* 2014) [3].

Several commonly used herbs have been identified by the National Cancer Institute as possessing cancer-preventive properties. These include members of the Allium sp. [garlic, onions and chives], members of the Lamiacea family [basil, mints, oregano, rosemary, sage, and thyme], members of the Zingiberaceae family [turmeric and ginger] and members of the Umbelliferae family (anise, caraway, celery, chervil, cilantro, coriander, cumin, dill, fennel, and parsley). In addition, many herbs contain a variety of phytosterols, triterpenes, flavonoids, saponins, and carotenoids, present in the plants are also prevent to be cancer chemoprotective Jaikumar and Jasmine (2016) [4]. Present study aimed to investigate ethanolic extract of *Trianthema decandra* leaf (Tamil: Sakthi saranai) for their potential anticancer activity against human breast cancer cell line viz.MCF-7.

2. Materials and Methods

Collection, identification, and authentication of the selected medicinal plants

Trianthema decandra leaf was collected from the nearby regions of Kumbakonam, Thanjavur district (Tamil Nadu). The plants were identified and authenticated by Dr. John Britto, Director, Rabinath Herbarium, St. Josephs College, Tiruchirappalli. India. Voucher specimens of the collected plants were deposited in the herbarium center of the host institute. The plant materials were dried under shade at room temperature pulverized by a mechanical blender and sieved through 40 meshes then stored in airtight closed bottle until required.

Extraction

The shade-dried, powdered leaf sample (100 g) was extracted in ethanol by using Soxhlet apparatus. The resultant extracts were filtered by using Whatman No 1 filter paper and then concentrated in a rotary evaporator and were stored in a refrigerator at 4ºC in small sterile glass bottles for further analysis.

Anticancer assay

Anticancer assay was evaluated by the MTT reduction assay [3-(4, 5- dimethylthiazol-2-yl)-2, 5-diphenyltetrazolium] (Mosmann 1983; Monks *et al* 1991) [5, 6]. The monolayer cells were detached and single cell suspensions were made using trypsin-ethylenediamine tetraacetic acid (EDTA). A hemocytometer was used to count the viable cells and the cell suspension was diluted with a medium containing 5% FBS in order to obtain final density of 1x105 cells/ml. 96-well plates at plating density of 10,000 cells/well were seeded with one hundred microlitres per well of cell

suspension and incubated for cell attachment at 37° C, 5% CO_2, 95% air and 100% relative humidity. Aliquots of 100 µl of different concentrations of leaf and bark extracts (25, 50, 100 and 200µg/ml) dissolved in DMSO (1%) were added to the appropriate wells already containing 100 µl of medium, resulted the required final sample concentrations for 48h at 37°C, 5% CO_2, 95% air and 100% relative humidity. After 48h of incubation, to each well 20µl/well (5mg/ml) of 0.5% 3-(4,5-dimethyl-2- thiazolyl)-2,5-diphenyl--tetrazolium bromide (MTT) phosphate- buffered saline solution was added and incubated at 37°C for 4 h. Then, 100µl of 0.1% DMSO is added to each well to dissolve the MTT metabolic product. Then the plate is shaken at 150 rpm for 5 min. Viable cells were determined by the absorbance at 570nm. Measurements were performed and the concentration required for inhibition Concentration (IC_{50}) was determined graphically. The absorbance at 570nm was measured with a UV- Spectrophotometer. The medium without samples served as control and triplicate was maintained for all concentrations. The effect of the samples on the proliferation of MCF-7 was expressed as the % cell viability & % Cell growth inhibition using the following formulas: % Cell viability = Abs 570 of treated cells / Abs 570 of control cells × 100%.

% of Cytotoxicity = [100 - Abs (sample) /Abs (control)] x100.

3. Results and Discussion

Michigan Cancer Foundation-7 (MCF-7) is a human breast cancer cell line and useful for *in vitro* breast cancer studies because the cell line has retained several ideal characteristics particular to the mammary epithelium. These include the ability for MCF-7 cells to process estrogen via estrogen receptors. The cell growth inhibition of *Trianthema decandra* leaf extract and AgNPs the tested against MCF-7 cell line at different concentrations (25, 50, 100 and 200µg/ml). The results of the study observed that the concentrations increases there are an increase in the cell growth inhibition (Cytotoxicity) and represent in table 1 and figure 1. The cell growth inhibition of *Trianthema decandra* leaf extract was found to be lowest growth inhibition was 9.92 % at 25µg/ml and highest growth inhibition was 67.25% at 200 µg/ml. Photomicrograph of MCF-7 cell line at various concentrations (25, 50, 100 and 200µg/ml) of *Trianthema decandra* leaf extract are shown in Plate1. The IC_{50} value was more than 142.18µg/ml.

Table 1: Percentage cell growth inhibition of *Trianthema decandra* extract on MCF 7cell line by MTT assay

S.No.	Concentrations (µg/ml)	Absorbance (Optical density)	Cell Viability (%)	Cytotoxicity (%)
1.	25	0.342	90.07	9.92
2.	50	0.311	81.91	18.08
3.	100	0.224	59.17	40.82
4.	200	0.124	32.74	67.25
	Cell Control	0.379	100	0
Half Inhibition Concentration (IC_{50})				142.18µg/ml

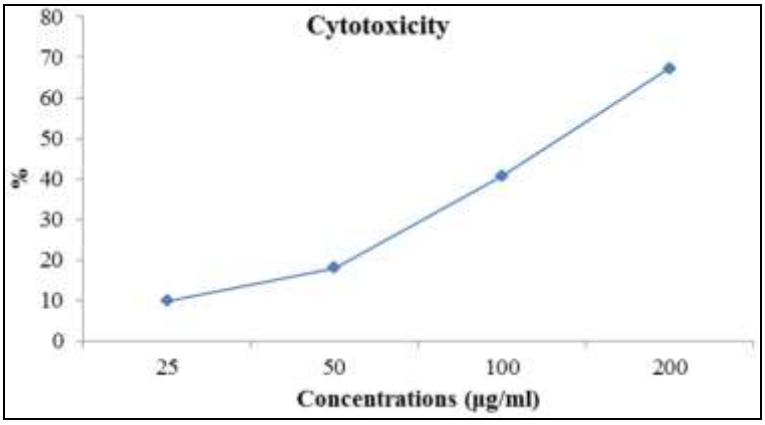

Fig 1: Percentage of cell growth inhibition (Cytotoxicity) of *Trianthema decandra* extract on MCF 7cell line by MTT assay

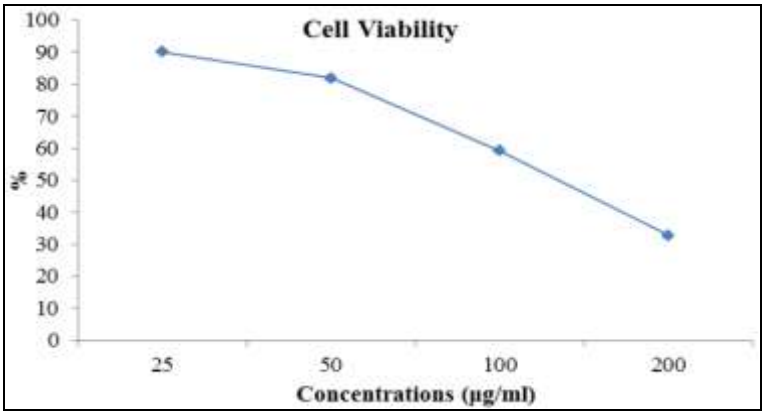

Fig 2: Percentage of cell viability of *Trianthema decandra* extract on MCF 7cell line by MTT assay

Normal cells showing surface architecture. Cytotoxic cells shows the cells became rounder, shrunken and showed signs of detachment from the surface of the wells denoting cell death (Round pebbles).

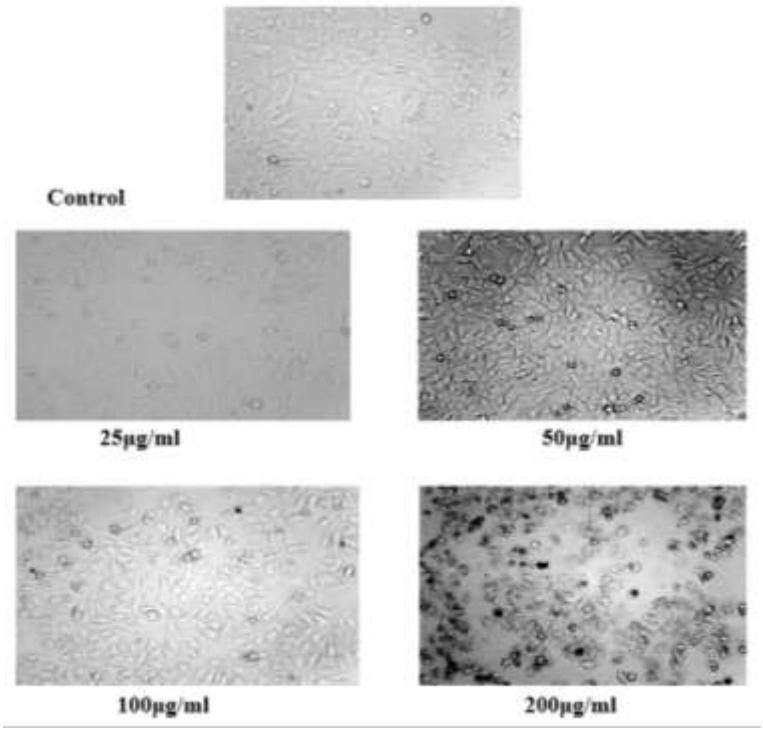

Plate 1: Photomicrograph of MCF-7 cell line of plant extract

MCF-7 is a breast cancer cell line isolated in 1970 from a 69-year-old Caucasian woman. MCF-7 is the acronym of Michigan Cancer Foundation-7, referring to the institute in Detroit where the cell line was established in 1973 by Herbert Soule and co-workers (Mosmann 1983) [5]. The Michigan Cancer Foundation is now known as the Barbara Ann Karmanos Cancer Institute (Nagamine *et al* 2009) [7].

Michigan Cancer Foundation-7 (MCF-7) is a human breast cancer cell line that was first isolated in 1970 from the malignant adenocarcinoma breast tissue of a 69-year old woman. MCF-7 cells are useful for in vitro breast cancer studies because the cell line has retained several ideal characteristics particular to the mammary epithelium. These include the ability for MCF-7 cells to process estrogen via estrogen receptors. MCF-7 cells are also sensitive to cytokeratin. When grown *in vitro*, the cell line is capable of forming domes and the epithelial like cells grow in monolayers. Growth can also be inhibited using tumor necrosis factor alpha (TNF alpha) (Son *et al*., 2009) [8].

These results are in agreement with those reported by Ranjit *et al* (2015) [9] who observed a significant anti-cancer property of various ornamental flowers (*Ixora coccinia, Allamanda cathartica, Hibuscus rosa-sinensis* and *Tecoma stans*) against MCF-7 cell lines by using MTT assay. Umapriyatharshini *et al* (2018) [10] studied the anti-cancer effects *Garcinia quaesita* Pierre and *Garcinia zeylanica* on breast cancer stem cells isolated from MCF-7. Hexane and chloroform extracts of *Garcinia quaesita* and *Garcinia zeylanica* barks showed dose dependent reduction in proliferation and stemness in MCF-7 cells.

Earlier reports explained that phenolic compounds and its congeners are known to show cytotoxicity against various cancer cell lines and capable of inducing caspase-mediated apoptosis activity (Owen *et al* 2000; Nandi *et al* 2007) [11, 12]. The mechanism of action of anticancer activity of phenolics could be by disturbing the cellular division during mitosis at the telophase stage. It was also reported that phenolics reduced the amount of cellular protein and mitotic index, and the colony formation during cell proliferation of cancer cells. The presence of a 4-carbonyl group of the flavonoid molecule also contributes to anticancer activity. In addition, the presence of 2,3-double bond in flavonoid molecules correlates with mitochondrial damage and cancer cell death (Plochmann *et al* 2007) [13]. The main objective of this assay is to check the cytotoxicity brought about by the extract and to find the toxicity levels in terms of IC_{50} dose when live and dead cell percentages are equal, which is considered as the optimum dose for the various assays. It has been shown that the ethanolic extract of *Trianthema decandra* leaf possesses activity at higher concentration.

Data of the results indicate that the cytotoxic effect strengthens with increase in the concentration of the extracts. Due to the mitochondrial enzyme in living cells, succinate dehydrogenase, cleaves the tetrazolium ring and converts the MTT to an insoluble purple formazan and the amount of formazan produced is directly proportional to the number of viable cells. Polyphenol (flavonoid) compounds might inhibit cancer cells by xenobiotic metabolizing enzymes that alter metabolic activation of potential carcinogens, while some flavonoids could also alter hormone production and inhibit aromatase to prevent the development of cancer cells (Wali *et al* 2019) [14].

4. Conclusion

Chemoprevention studies are underway to identify promising candidates for reduced cancer risk. Based on the results obtained in this study, in which the *in vitro* cytotoxicity assay of MCF 7 was used. It is concluded that

the ethanolic extract of *Trianthema decandra* leaf possess cytotoxic efficacy against breast carcinoma MCF-7 cell line. Results of the present study provided new evidence for anticancer activity of *Trianthema decandra* leaf which could be useful for developing new anticancer therapies.

5. References

1. Rajan S, Mahalakshmi S, Deepa M, Sathya K, Shajitha S, Thirunalasundari T, *et al*. Antioxidant potentials of *Punica granatum* fruit rind extracts. IJPPS. 2011; 3(3):82-88.
2. Dillon DA, Guidi AJ, Schnitt SJ. Chapter 28: Pathology of Invasive Breast Cancer, in Harris JR, Lippman ME, Morrow M, Osborne CK. Diseases of the Breast, 4th edition, Lippincott Williams &Wilkins, 2010.
3. Sunil R, Abhishek K, William J. Economic burden of cancer in India: Evidence from cross sectional nationally representative household survey, 2014 PLOS ONE, 2018, 1-17
4. Jaikumar B, Jasmine RPG. A Review on a few medicinal plants possessing anticancer activity against human breast cancer. International Journal of Pharm Tech Research. 2016; 9(3):333-365.
5. Mosmann T. Rapid colorimetric assay for cellular growth and survival: application to proliferation and cytotoxicity assays. Journal of Immunological Methods. 1983; 65:55-63.
6. Monks A, Scudiero D, Skehan P, Shoemaker R, Paull K, Vistic D, *et al*. Feasibility of high flux anticancer drug screen using a diverse panel of cultured human tumour cell line. Journal of the National Cancer Institute. 1991; 83:757-766.
7. Nagamine MK, Silva TC, Matsuzaki P, Pinello KC, Cogliati B, Pizzo CR, *et al*. Cytotoxic effects of butanolic extract from *Pfaffia paniculata* (Brazilian ginseng) on cultured human breast cancer cell line MCF-7, Experimental Toxicology of Pathology. 2009; 61:75-82.
8. Son YO, Kim J, Lim JC, Chung Y, Chung GH, Lee JC, *et al*. Ripe fruits of *Solanum nigrum* L. inhibits cell growth and induces apoptosis in MCF-7 cells, Food Chem Toxicol. 2009; 4:1421-1428.
9. Ranjit Nagarani T, Swathi V, Pahni Kumar K, Chowdary YA, Siva Reddy CH, Girijasankar G, *et al*. Evaluation of phytochemical content and In vitro cytotoxic activity of various ornamental plant flower extracts against MCF-7 Cell lines. International Journal of Current Research in Life Sciences. 2015; 4(3):172-176.
10. Umapriyatharshini R, Sameera R Samarakoon, Kamani H Tennekoon, Neelika Malavige, ED de Silva. Screening of five Sri Lankan endemic plants for anti-cancer effects on breast cancer stem cells isolated from MCF-7 and MDA-MB-231 cell lines. Tropical Journal of Pharmaceutical Research September. 2018; 17(9):1825-1832.
11. Owen RW, Giacosa A, Hull WE, Haubner R, Spiegelhalder B, Bartsch H, *et al*. The antioxidant/anticancer potential of phenolic compounds isolated from olive oil. Eur J Cancer. 2000; 36:1235-47.
12. Nandi S, Vracko M, Bagchi MC. Anticancer activity of selected phenolic compounds: QSAR studies using ridge regression and neural networks. Chem Biol Drug Design. 2007; 70:424-436.
13. Plochmann K, Korte G, Koutsilieri E, Richling E, Riederer P, Rethwilm A, *et al*. Structure-activity relationships of flavonoid-induced cytotoxicity on human leukemia cells, Arch. Biochem. Biophysics. 2007; 460(1):1-9.
14. Wali AF, Majid S, Rasool S, *et al*. Natural products against cancer: Review on phytochemicals from marine sources in preventing cancer. Saudi Pharmaceutical Journal: SPJ: the Official Publication of the Saudi Pharmaceutical Society. 2019; 27(6):767-777.